UNIVERSITY OF SOUTHAMPTON
FACULTY OF PHYSICAL SCIENCES AND ENGINEERING
Department of Electronics and Computer Science

Modelling and Analysis of the Sinoatrial Node

Jianhao Xiong

Thesis for the degree of Doctor of Philosophy

June 2017

Abstract

The contraction of the heart is achieved by the regulation of the sinoatrial node (SAN), the natural pacemaker. The SAN cells are capable of initiating action potentials, i.e. the electrical signals which produce the contraction of cardiac muscle. The generation of action potentials are governed by ion channels where various types of ion currents flow through. Computational models characterized by ordinary differential equations (ODE) have been published to explain the deterministic behavior of SAN cells.

In this thesis, we investigate the effects of the ion channels of these models by both local and global sensitivity analysis. The local sensitivity analysis identifies the impact of ion channels by means of partial derivatives. The global sensitivity analysis uses the variance of model outputs as an indicator to investigate the influence of ion channels. The results show that there are common roles of ion channels on action potentials among several models. Additionally, we propose stochastic single cell SAN models to explain the cellular-level variability in action potentials. Novel one-dimensional SAN models of coupled SAN cells are developed to explain the action potential variability at a tissue level. These models capture the stochastic behavior of ion channels, cell-to-cell coupling and SAN cell heterogeneity. By this analysis we are able to computationally compare two models of coupled cells (heterogeneity of cell population versus identical cells with graded coupling strength), regarded as an open problem in the literature. Our results suggest that the SAN heterogeneity decreases the tissue level variability of action potentials. Based on the experimental observation that the variability of intact SAN is greatly smaller than the variability of single cell, our results support the hypothesis of the SAN cell heterogeneity. New insights are provided by the models to further understand the influence of heterogeneity and the coupling strength on determining the stochastic behavior of the intact SAN.

Declaration of Authorship

I, Jianhao Xiong, declare that that the thesis entitled *Modelling and Analysis of the Sinoatrial Node* and the work presented in it are my own and has been generated by me as the result of my own original research. I confirm that:

• This work was done wholly or mainly while in candidature for a research degree at this University;

• Where any part of this thesis has previously been submitted for a degree or any other qualification at this University or any other institution, this has been clearly stated;

• Where I have consulted the published work of others, this is always clearly attributed;

• Where I have quoted from the work of others, the source is always given. With the exception of such quotations, this thesis is entirely my own work;

• I have acknowledged all main sources of help;

• Where the thesis is based on work done by myself jointly with others, I have made clear exactly what was done by others and what I have contributed myself;

• None of this work has been published before submission.

Signed: _____ Date: _____

List of Acronyms

ANOVA Analysis of variance

AP Action Potential

APA Action Potential Amplitude

APDR Action Potential Duration Restitution

APO Action Potential Overshoot

ATP Adenosine Triphosphate

AVN Atrioventricular Node

CL Cycle Length

CICR Calcium Induced Calcium Release

DDR Diastolic Depolarization Rate

DI Diastolic Interval

DP Dome Peak

ECC Excitation-contraction Coupling

ECG Electrocardiography

FAST Fourier Amplitude Sensitivity Test

HH Hodgkin-Huxley

L Length

MDP Maximum Diastolic Potential

MC Markov Chain

ODE Ordinary Differential Equation

1D One-dimensional

SA Sensitivity Analysis

SAN Sinoatrial Node

SDE Stochastic Differential Equation

SLOP Slope of the Action Potential Duration Restitution Curve

Contents

List of Figures

List of Tables

Acknowledgements

I have many individuals to thank for supporting me during my PhD.

First and foremost, I would like to gratefully acknowledge my supervisor Prof. Mahesan Niranjan. He gave me the opportunity to explore and discover the exciting field of computational biology and machine learning. He was always supportive along every step of the way. He has been an excellent supervisor, offering an extra push whenever I get stuck. It would have been impossible for me to finish my work without his supervision. His excitement in his research set a strong example for me.

I also want to thank my colleagues (in alphabetical order): Dr. Abdullah Alrajeh, Benjamin Jesty, Bingchen Guo, Boriboon Deeka, Dr. Chathurika Dharmagunawardhana, Daniel Martinho-Corbishley, Enrique Marquez, Luis Montesdeoca, Muhammad S. S. Kassim, Dr. Jing Liu, Dr. Jonathan Mayo, Dr. Ke Yuan, Steven Squires, Sisi Wu, Dr. Shaobai Li, Dr. Tayyaba Azim, Tanyakul Deeka, Thabiso M. Maupong, Dr. Wanmu Liu, Dr. Wei Liu, Dr. Xin Liu, Xiaoru Sun, Xuan Wang, Dr. Yawwani Gunawardana, Yan Sun and Zheng Cui.

I would like to thank my friends Hongming Zhang, Sze Tan Fion Wu and Chen Wang. My thanks go to my English teacher Lauren Dampier for her tireless efforts and patience on my spoken English.

Finally, it is a great opportunity to express my feelings to my parents Xingzhi and Zhiqun. Their love and support helped me on every step of the way.

To my parents Xinzhi and Zhiqun

Like a lamp, a cataract, a star in space, an illusion, a dew drop, a bubble, a dream, a cloud, a flash of lightning; view all created things like this.

The Diamond Sutra (Red Pine, Trans.)

Chapter 1

Introduction

1.1 Problem statement

The variability of heart rate is an important indicator of the physiological state of the heart. The rhythmic beating of the heart originates in the natural pacemaker, the SAN which generates spontaneous action potentials. Action potentials in the SAN cells are triggered by inward and outward currents of various ions via transmembrane ion channels. The spread of the SAN action potentials is achieved via cell-to-cell coupling, which excites atrial and ventricular cells and initiates the atrium and ventricle to contract. If the SAN does not function properly, the heart rate may be too slow (bradycardia) or too fast (tachycardia). Ionic mechanisms of the SAN cells are revealed by computational models (Zhang et al., 2000) (Kurata et al., 2002). These models provide a procedural and interactive view of the mechanisms as a function of ion channel states which is often formulated as ordinary differential equations (ODEs). The system of ODEs is deterministic and can be solved by standard integrators. The cardiac cell electrophysiology can also be represented as Markov models or stochastic differential equations (SDEs) which model the ionic behave in a stochastic manner (Wilders and Jongsma, 1993) (Goldwyn et al., 2011a). Such deterministic and stochastic models typically have complex structures with a large number of parameters. Some parameter values have large variation among different experimental conditions, and the confidence on the parameter is limited due to the uncertainties of the parameters. Markov models have been associated with high computational cost due to their large number of state variables and parameters, which presents an obstacle for multicellular SAN simulation for capturing the variability of intrinsic heart rate (Fink and Noble, 2009). Hence, it is changeling in determining the significance of model parameters and modeling variability of SAN action potential efficiently. In this work, we focus on the two problems.

The SAN is a complex heterogeneous tissue (Boyett et al., 2000), and the heterogeneous pacemaker structure may determine its functions. Experimental observations show grad-

ual morphological changes in SAN action potentials from its centre to periphery, which results in the regional difference of single SAN action potential characters (e.g. the action potential cycle length (CL) and its variability). Kodama and Boyett (1985) showed that the CL of isolated central SAN tissue is 331 ± 13 ms while CL of peripheral SAN tissue is 298± 8 ms. However, the intact SAN behavior is distinct from the regional SAN tissues. Yaniv et al. (2014) showed that the CL of the intact rabbit SAN is 324 ± 11 ms. However, these observations are not well understood. Two distinct hypotheses were proposed to explain the intact SAN heterogeneity:

(1) there are two specific SAN cell types (central cells and peripheral cells) with distinct characteristics (Boyett et al., 2000). Therefore, the heterogeneity is due to the distinct characteristics of central and peripheral cells.

(2) there is no regional difference in SAN cells. All SAN cells are assumed to be central SAN cells. The experimentally measured regional difference is due to cell-to-cell coupling effects, especially the effects from the atrium (Michaels et al., 1987) (Verheijck et al., 1998).

Various SAN models have been proposed based on the two hypotheses. To support the first hypothesis, Zhang et al. (2000) first proposed SAN models of central and peripheral SAN cells, The 1D model is a non-uniform model which consists of two different types of SAN models, the central and peripheral SAN models. Oren and Clancy (2010) proposed a uniform model (containing only central SAN cells), and compared the model with non-uniform model. Their results support the second hypothesis. Parameter values for these models describe SAN cells with differences in capacitances (cell size), ion channel densities, ion pumps, and exchangers (Boyett et al., 2007a). Individual types of ion channels, ion pumps and exchangers play a unique role in characterising action potentials. The influence of these ion channels attracted considerable interest in the literature, which has been review by Wilders (2007). Furthermore, a recent research discovered the physical interactions of ion channels. Guo et al. (2011) found a physical interaction between two potassium ion channels, the rapid and slow delayed rectifying K^+ ion channel, in human ventricular myocyte cells. Their experimental results suggested that the interaction is the results of a macrocomplex which is formed by the K^+ channels at the membrane. The quantification of the roles of ion channels should based on a large number of samples on model inputs, because ion channel parameters are estimated from experimental data in which there is measurement error and inherent variability. These show that a systematical way is needed to quantify roles of ion channels and their interactions, which is one of the issues addressed in this thesis.

Sensitivity analysis has be applied to test systems biology models to present not only the individual effects of each ion channel but also their interactions (see Zi (2011) for

a review of the application in other areas of biology). Global sensitivity analysis is capable of assessing the impact of parameters over the entire parameter space. As global approaches could be model independent, the results of the sensitivity analysis enable us to understand the intrinsic roles of parameters among various models. If there is a common roles of an ion channels among various models, the models are in agreement with the ion channel behavior. If not, there is an intrinsic difference among these models, which could difficult to be observed from model outputs. The understanding derived from sensitivity analysis is helpful in model development, and it can further explain whether the SAN model is dependent on model assumptions (e.g. the differential equations) or parameter estimation (e.g. the parameter values). Sensitivity analysis is also useful in simplifying model by the quantification of the relationship between model inputs and outputs. The insensitive parameters can be fixed or eliminated. Thus, the the modelling of ionic mechanism may be simplified. Furthermore, the most sensitive model parameters and their influencing model outputs could be valuable for further experimental analysis.

Most of the published SAN models are described by a system of ordinary differential equations (ODE), and therefore there is no variability of of action potentials presented by these models, but variability of single SAN cells carries important biological information. As we introduced before, there is controversy about the regional difference of the action potentials of SAN cells. In the literature, this open problem was discussed with deterministic models (Zhang et al., 2001) (Oren and Clancy, 2010). However, the action potential variability also carries important information about single SAN cells and SAN tissue, which could further our understanding of the SAN heterogeneity. For examples, Yaniv et al. (2014) observed that the action potential variability of the intact SAN tissue is largely different from isolated single SAN cells, which could possibly be the result of SAN cell heterogeneity. In order to understand the SAN heterogeneity by the means of variability, stochastic SAN models which capture the variability is required. In this work, we started the work with single SAN ODE models. Then we converted the single cell ODE models to stochastic differential equation (SDE) models to present the action potential variability. Based on the single cell stochastic models, novel one-dimensional SAN models are proposed to capture the stochastic behavior of the intact SAN. The novel one-dimensional SAN models give insight to how SAN cell heterogeneity impact the action potential variability, and a further discussion of the controversial SAN regional difference can be given. These discussion of the SAN stochastic modelling and the regional difference (or SAN cell heterogeneity) is shown in Chapter 5.

Based on the challenges outlined above, aims of the thesis are

- Identify the key parameters of single cell SAN models.
- Quantify the roles of ion channels and their interactions.
- Build multi-scale stochastic SAN models by using SDEs.

- Analyse the effect of SAN cell heterogeneity in determining action potential variability by employing multi-scale models.

1.2 Thesis organisation

The remainder of this report is organized as follows. In Chapter 2, a literature review of the cardiac physiology and various cardiac action potential models is introduced, which prepares the reader for the results chapters. The quantification of action potential features, the backgrounds of sensitivity analysis and of SDE are given in this chapter. In Chapter 3, we implement local sensitivity analysis on single cell SAN models. The results of these models are compared to show model inner mechanisms. In this chapter, we explain why it is essential to use global sensitivity analysis. Chapter 4 investigates global sensitivity analysis of single cell cardiac models. The roles and interactions of ion channels are quantified and discussed in this chapter. We further explain how the ion channel conductances have greater effects on action potentials than model formulations of ion channel (e.g. the number of ion gates or the expression of voltage threshold), which answers the questions of roles of ion channels and their interactions. In Chapter 5, we illustrate the reformulation of single cell SDE models and 1D SDE models, and the analysis of a 1D SDE model is carried out in order to present the SAN cell heterogeneity. In this chapter, we compare our simulation results with published experimental observations and give our explanations to the the SAN cell heterogeneity. Chapter 6 concludes of the thesis, and outlines future work.

Chapter 2

Physiological Background and Literature

This chapter introduces the cardiac physiology background of this work and some related works on modelling of cardiac cells.

2.1 Cardiac Physiology

2.1.1 The SAN and generation of action potential

The heart is a hollow organ located at the thoracic cavity. It serves as the pump which generates the pressure gradient for the flow of the blood to different parts of body. The heart is a crucial organ in animals as it transports the nutrients and wastes to different organs and tissues with long distance by driving the circulation system (Sherwood, 2008).

Heart rate is an important reflection of the body's physical and mental states, and is influenced by oxygen concentration, carbon dioxide concentration, anxiety, stress and illness. Abnormal heartbeat behaviour may be caused by many diseases, which can produce serious symptoms of dizziness and fainting. Heartbeat can be measured using electrocardiography (ECG) on the surface of the body. For normal heartbeat, the coordinated contraction starts from the Sinoatrial node (SAN), which is located at the right atrium of the heart as shown in Figure 2.1. As shown in Figure 2.1, cardiac activity begins with the firing of the SAN. The SAN (rabbit) contains a number of cells of various sizes: the length of central and peripheral cells is around 51 and 88 μm respectively (Boyett et al., 2007a). These cells generate regular and spontaneous electrical signals the action potential (AP), to regulate the contraction of the heart. The intrinsic frequency of the pacemaker is 100 to 120 beats per minute (bpm) (Clifford, 2002). The SAN does not contain the only cardiac cells capable of auto-rhythmicity. The atrioventricular (AV)

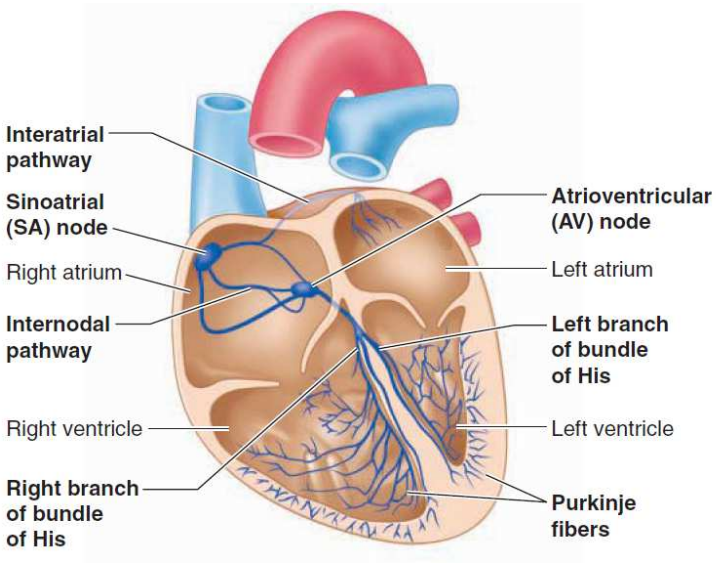

FIGURE 2.1: Conduction system of the heart, taken from (Sherwood, 2008). The conduction path way is made up with SAN, internodal pathway, AV node, bundle of His and Purkinje fibres. The internodal pathway connects the SAN and AV nodes. The bundle of his is the collection between the AV node and Purkinje fiber cells.

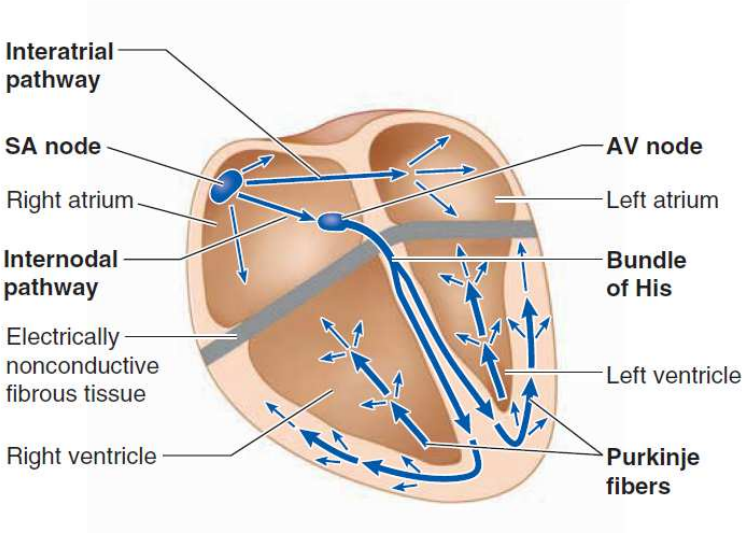

FIGURE 2.2: Conduction of action potential, taken from (Sherwood, 2008). SAN cells initiate action potentials (electrical stimulus). The action potentials released from SAN cells pass through the atrial cells (internodal pathway) to AV node. Then the stimulus is delayed briefly so that the atria contracts under the control of action potentials. The action potentials reach bundle of His and then Purkinje fibres, and eventually cause the contraction of ventricles.

node the Purkinje fibers are all able to generate action potentials at different rates as shown in Table 2.1. The AV node is located on the border of the right atrium and the right ventricle and Purkinje fibres are located within the ventricular walls, then the simulation reaches AV node, a connection to a group of fibers in the ventricles.

After the AV node, the action potential spreads throughout the ventricles along the Purkinje fibers to produce ventricular contraction, as shown in Figure 2.2. For normal

pacemaker activity, the SAN is the primary pacemaker, and the rate of the heartbeat is controlled by SAN. The resulting heart rate is often lower than the firing rate of the SAN due to the complex chemical exchanges that occur in subsequent cardiac tissues (Clifford, 2002). As indicated in Table 2.1, autorhythmic tissues have distinct intrinsic

Tissue	**Action Potentials (pulse per min)**
SAN (primary pacemaker)	70-80
AV node	40-60
Purkinje fibers	20-40
Human heart rate	60-100

TABLE 2.1: Normal rate of human action potentials in autorhythmic tissues of the heart (Sherwood, 2008). SAN is the fastest engine of the heart which drives the heart rate at round 70 - 80 beat per minute (bpm). If the SAN breaks down, the AV node drives the heart rate at 40-60 bpm. If the AV node is nonfunctional, ventricular tissues are driven by the Purkinje fibres at around 30 bpm.

rates. If the primary pacemaker, the SAN, breaks down, the pacemaker activity can be assumed by the AV node at around 50 beats per minute (Sherwood, 2008). If the AV node becomes non-functional, the ventricular tissues cannot receive the action potential from it and will be driven by the Purkinje fibres at a rate of around 30 bpm, while the SAN still keeps the normal rate at 70 beats per minute. To the best of our knowledge, the contribution of auto-rhythmic tissues to heart rate variability has not been reported in the literature up to now.

Occasionally, any pacemaker of the heart can become over-excited, for example the Purkinje fiber may depolarizes more rapidly than the SAN. This abnormal pacemaker, an ectopic focus, generates the action potential which spreads to the rest of the heart. The ectopic pacemaker may be caused by the innervation of parasympathetic nervous system and over stimulation from drugs (Rozanski, 1991a). The ectopic focus can occur also due to SAN dysfunction and SAN blockage (Phibbs, 1963). This kind of abnormal behaviour may occur in ventricular tissue and initiate a premature ventricular contraction, which involves heartbeat initiation from Purkinje fibres rather than the SAN. Abnormal heartbeat initiation can occur in healthy hearts because of various stimulations, such as increased local parasympathetic nervous system activity, elevated sympathetic nervous system output and over stimulation from excess caffeine, nicotine or alcohol (Rozanski, 1991b) (Port, 2005) (Maupoil et al., 2007).

2.1.2 Generation of Action Potential in the SAN

The contraction of the heart is generated by the regulation of electrical signals and action potentials from the pacemakers of the heart. Pacemaker tissue is composed of auto- rhythmic cells which are capable to initiate and conduct action potentials. By contrast, contractile cells do not initiate their own action potentials but receive action potentials from the auto- rhythmic cells and produce contractions. When an external

stimulus delivered to a contractile cell, the membrane potential rises up. Once the membrane potential reach a threshold, the activation of ion channels depolarizes the membrane and initiates an action potential.

The action potential of auto-rhythmic cells is produced by complex interactions of ionic mechanisms, which are regulated by ion channels, ion pumps and ion exchangers across the membrane of the cardiac cells. An ion channel is composed of embedded protein molecules in the membrane which is composed of a tunnel with gates which regulate the flow of ions. An ion exchanger is a molecule which uses potential energy in electrochemical gradients to move one type of ions into a cell and to move another type of ion out of the cell. An ion pump consumes energy in the form of adenosine triphosphate (ATP) to move ions against their electrochemical gradients (Bronzino and Peterson, 2014). Ion pumps are active transports while ion channels and ion exchangers are passive transports.

Figure 2.3 shows the structure of a single SAN cell. The opening and closing of each ion channel periodically produce the rise and fall of membrane voltages, which affect the contraction of the heart. Figure 2.4 shows the gating time and flow volume of ion

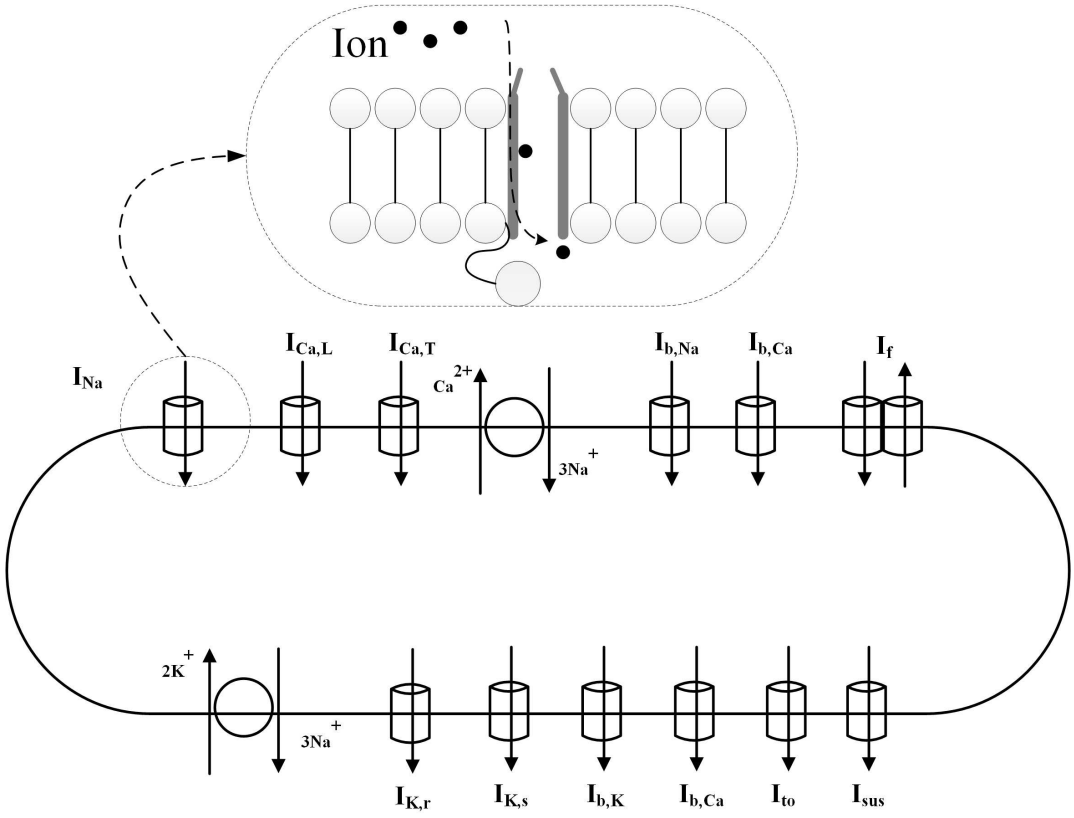

FIGURE 2.3: Schematic diagram of a single SAN cell (adapted from Zhang et al. (2000)). I_{Na}, $I_{Ca,L}$, $I_{Ca,T}$, $I_{K,r}$, $I_{K,s}$, I_f, $I_{b,Na}$, $I_{b,K}$, $I_{b,Ca}$, I_{to} and I_{sus} are the ion currents across ion channels. Na^+/Ca^{2+} is an ion exchanger. Na^+/K^+ is a ion pump.

currents which is gated by ion channel at various stages of a membrane potential period. The number of ion channels can be estimated from total ion channel conductances and

single ion channels conductances. Table 2.2 gives an estimation of the number of ion channels in a SAN cell. In Chapter 5, the estimation of the number of ion channels is further discussed.

TABLE 2.2: The estimated number of ion channels in a single SAN cell. The ion channels listed are the key ion channels which are involved in the stochastic gating of ion currents. The results are obtained from Wilders and Jongsma (1993). The definitions of corrects (I_{h}, $I_{\mathrm{Ca,L}}$, $I_{\mathrm{Ca,T}}$, $I_{\mathrm{K,r}}$ and I_{Na}) are given in Table A.4.

Ion Channel	Number of ion channel
I_{h}	24000
$I_{\mathrm{Ca,L}}$	10000
$I_{\mathrm{Ca,T}}$	4400
$I_{\mathrm{K,r}}$	1000
I_{Na}	625

The auto-rhythmic cells repeat cycles, and this periodical firing initiates action potentials which spread across the heart and produce heart contractions. The ionic mechanisms underlying the initiation and propagation of action potential was first described by Hodgkin and Huxley (Hodgkin and Huxley, 1952). The scheme used in their model to de- scribe ionic currents was applied to cardiac cell modelling and became the most popular modelling scheme in this field. Mathematical models to describe the mechanisms are introduced in the next section.

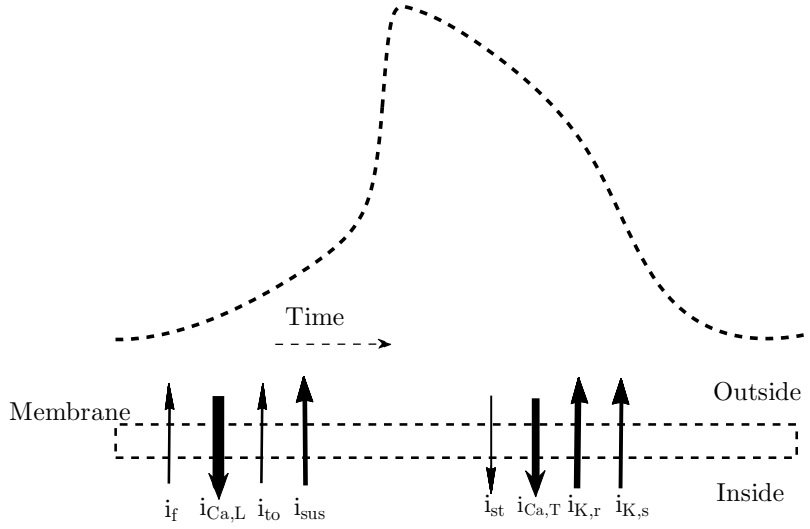

FIGURE 2.4: The inward and outward of ion currents of the Kurata model (Kurata et al., 2002). The arrows show the main activation time of of ion currents. The direction and the strength are shown by the arrows and weights respectively. The definitions of the inward and outward corrects are listed in Table A.4.

Cardiac contractile cell undergos contraction via excitation-contraction coupling (ECC). ECC is dependent on a process named Calcium Induced Calcium Release (CICR). Action

potential travels down T tubules, a deep invagination of contractile cell membrane. L-type Ca^{2+} channels lie in the T tubules. The Ca^{2+} ions from action potential enter through the Ca^{2+} ion channels. The influx of Ca^{2+} ion triggers further release of Ca^{2+} ions from intracellular stores into cytosol (a liquid found inside cells). The extra release of Ca^{2+} ions is responsible for long period of cardiac contraction. Ca^{2+} ions bind to troponin and the troponin is moved away from actin binding site, which frees the actin to be bound by myosin and adenosine triphosphate to initiates the muscle contraction. Intracellular Ca^{2+} ion is later removed by sarcoplasmic reticulum. The decrease of Ca^{2+} ion concentration returns the actin to its position of the active site of actin and ends the contraction. The excitation-contraction coupling between an action potential and cardiac contraction is shown as Figure 2.5. The action potential in contractile cell has a longer refractory period than the SAN action potential, which ensure the duration of contraction and relaxation of for pumping blood. As shown by Figure 2.5, the refractory period is associated with the contraction duration.

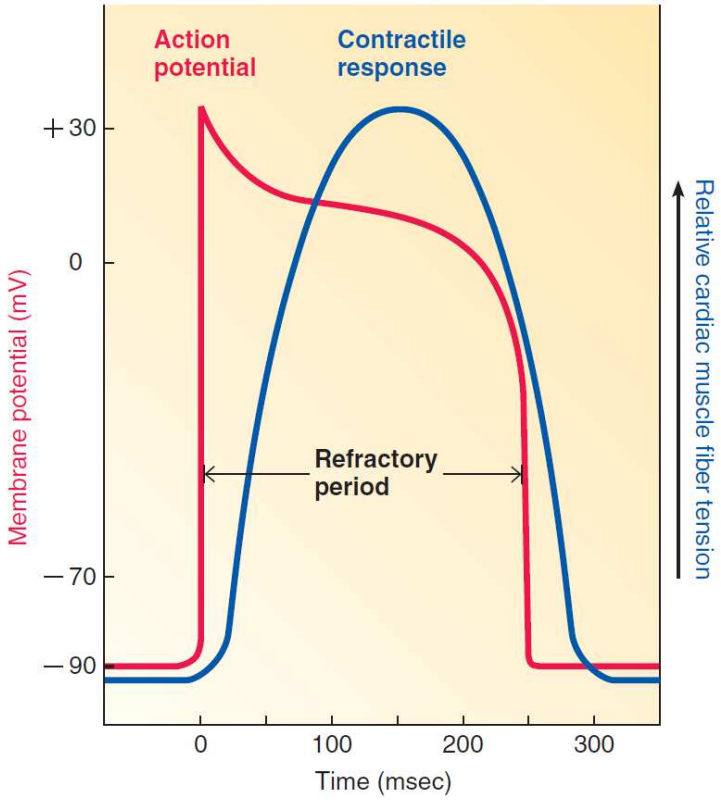

FIGURE 2.5: Relationship of an action potential and cardiac muscle contraction. Taken from (Sherwood, 2008).

2.2 Modelling of Cardiac Cells

The Hodgkin-Huxley model was published in 1952 by Alan Lloyd Hodgkin and Andrew Fielding Huxley (Hodgkin and Huxley, 1952). This model is the first use of a mechanistic

mathematical model to explain physiological function. The model was the result of a pioneering study in biophysics at systems level and was also the first to uncover the interactions among different molecular components. The Hodgkin-Huxley model of the squid nerve action potential explains the ionic mechanism of the action potential. This model was the outcome of early applications of the voltage clamp technique on electrophysiology. The technique was deployed to record ionic currents in neurons to study the principles of the action potential. The mathematical model explains the movement of ions and the function of ion channels and its success encouraged many researchers to apply it to other fields.

The Hodgkin-Huxley model was employed to create the cardiac action potential model with certain modifications as shown in Figure 2.6. Because the cardiac action potential has a depolarization stage (a long lasting large voltage value near the peak) compared to the action potential in neurons, Noble directly formulated the Hodgkin-Huxley model to achieve the cardiac depolarization. (Noble, 1962). The Noble model succeeded in

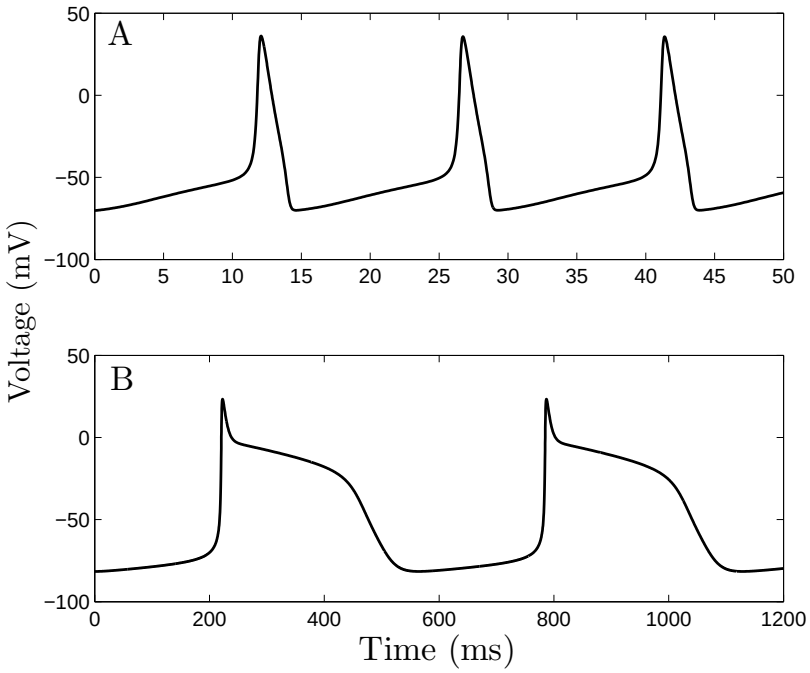

FIGURE 2.6: A. Nervous action potential of Hodgkin-Huxley model. B. Cardiac action potentials of Noble model . By certain modifications of the Hodgkin-Huxley model, the cardiac action potentials with long lasting large value near the peak are achieved by Noble (1962).

generating a long lasting depolarization stage of Purkinje fibre action potential with new ion channels base on new experiment results. In addition, the model includes a chloride current as a leak current. This work proves that with certain modifications, the Hodgkin- Huxley formulation can be easily applied to models of cardiac cells. The deficiency of the model is the absence of many important ion currents. For example, the sodium current is the only inward current in the model and calcium currents is not

included. This is due to the limitations of the early experimental work. At that time, many properties of cardiac cells had not yet been discovered.

Many experiential discoveries have resulted in the development of new cardiac models. Voltage clamp is an experimental method which is widely used in cardiologist and neuroscientist to measure the ion currents of excitable cells, such as neurons and cardiac cells. Voltage clamp technique led to the discovery of the calcium current of cardiac cells (Reuter, 1967). In addition, the discoveries of multiple components of the potassium current and different slow gated currents in the plateau range of potentials showed that the modelling of action potentials in ventricular tissue needed to be improved (Noble and Tsien, 1967). A model from a large range of experimental results and better accuracy was proposed (McAllister et al., 1975). In 1977, a first numerical simulation model of the ventricular myocardial action potential was proposed (Beeler and Reuter, 1977). This model created the cardiac ventricular action potential from transmembrane ionic currents by modifying the Hodgkin-Huxley equations. This work became the framework of many later models and is still extensively used.

The ion exchangers were considered in the DiFrancesco-Noble model (DiFrancesco and Noble, 1985). Ion exchangers are transmembrane proteins that move ions across the membrane against their concentration gradient by using energy. The incorporation of ion exchangers, for instance Na-K exchange and Na-Ca exchange, is a great advance of the cardiac model and this work is an important part to study the cardiac disease states. However, the main deficiency of the model was the absence of intracellular calcium buffering. The problem was tackled by modelling the atrial action potential (Hilgemann and Noble, 1987). The Hilgemann-Noble model considered intracellular calcium buffering and provided a basis for modelling ventricular cells. The model incorporates the inward sodium-calcium exchange current flowing during the action potential and makes great progress regarding the calcium balance.

Based on the new experimental findings, Luo-Rudy models of the ventricular cell were proposed (Luo and Rudy, 1994a) (Luo and Rudy, 1994b). In the previous models, while the ion concentrations inside the cell is unchanged, the Luo-Rudy models demonstrate the change of ion concentrations by using ion exchangers to return back ions after action potential. Luo-Rudy models not only include ion exchangers but also introduce a non-specific calcium-activated channel, the L-type calcium channel, the delayed rectifier potassium current and the inward rectifier potassium current. Therefore, the important ion currents are reformulated to provide us with more reliable results.

All the models demonstrated above employ the traditional Hodgkin-Huxley scheme (Hodgkin and Huxley, 1952). In this scheme, the simulation of the action potential derives from a macroscopic description of transmembrane ionic currents generated by a great number of ion channels. Hence, the randomness in a single or several channels cannot be represented by the deterministic Hodgkin-Huxley scheme models. As the heart

contraction rate is regulated by action potentials, the randomness of the action potential also contributes to heart rate variability. To the best of our knowledge, the influence of randomness on heart rate variability is still known. The state-specific Markov model of a single cardiac sodium channel was proposed (Clancy and Rudy, 1999). A single channel based on the Markov scheme is a major difference from the Hodgkin-Huxley scheme because the Markov chain can allow for complex state transitions. Figure 2.7 shows a brief introduction to the development of mathematical cardiac models. The

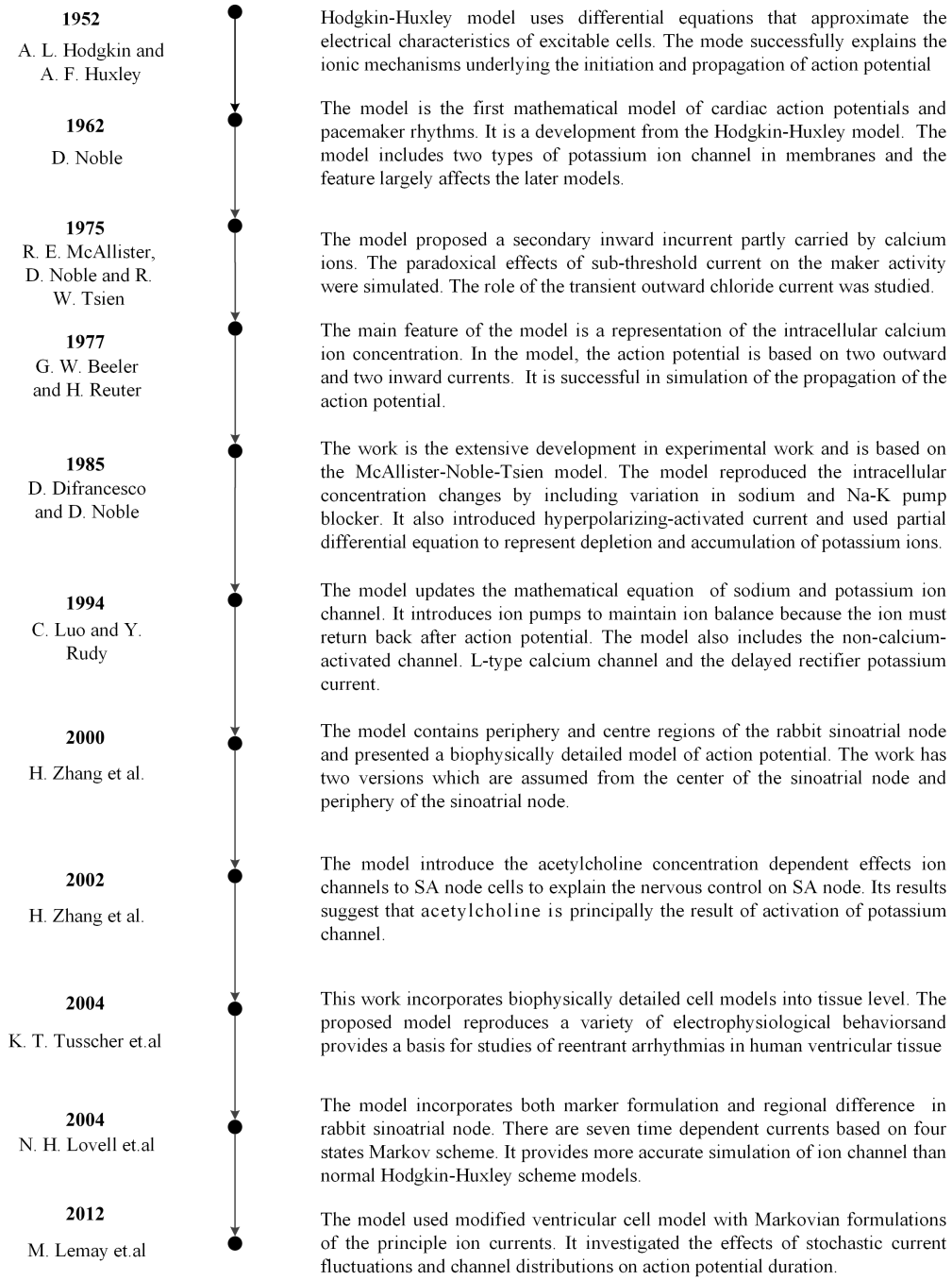

FIGURE 2.7: Chronological development of mathematical cardiac models.

models of the heart have been created from the genes to the cells and to the whole organ

(Noble, 2002). Models have been developed at the genetic level to reconstruct the effects of particular mutations of proteins in ion channels. A single channel-based Markovian model was applied to simulate the genetic defects in membrane ion channels (Clancy and Rudy, 1999). This work successfully explains its arrhythmogenic consequences at the cellular level. The effective treatment of cardiac diseases demands the mathematical understanding of cardiac mechanisms. The understanding faces the challenges at several levels of integration and complexity from the ion channel to the cardiac cell to the heart as a whole organ. All of the models are only partial representations of the cardiac mechanism at certain levels. Hence, choosing a the right model and reconstructing the model it is essential in many cases.

The models of rabbit SAN cells are chosen by us to perform sensitivity analysis and stochastic modelling because of the rich literature available. The SAN models are discussed in Section 2.5. Wilders (2007) highlighted that 16 out of 43 second generation cardiac models (advanced models with ion pumps and exchangers) were in fact rabbit cardiac models. These advanced cardiac models are based on the Hodgkin-Huxley model. In the following section, the Hodgkin- Huxley modelling of the action potential mechanism is introduced.

2.3 Hodgkin-Huxley Description of Ion Currents

The Hodgkin-Huxley model (Hodgkin and Huxley, 1952) for the generation of the nerve action potential is one of the most successful mathematical models. The basic concepts of the model have proved invaluable in the study of bio-electrical activity. The approach underlies the development of mathematical cardiac models. Hodgkin and Huxley used the voltage clamp procedure to analyse the action potential of the squid giant axon.

The starting point of the original model is that the nerve membrane, specifically the membrane of the squid giant axon, contains three types of ion currents: sodium ion current I_{Na}, potassium current I_K and leakage current I_L. The currents I_K and I_{Na} are voltage-dependent so total conductance is a function of the voltage across the membrane. Their work showed that action potentials are initiated by the voltage-dependent activation of the inward sodium current I_{Na}, and that after a 1-2 ms delay, outward potassium current I_K carries K^+ ion across the membrane. The leakage current I_L has a relatively low and constant conductance. The leakage channels are mainly responsible for the resting membrane potential. The schematic diagram of the model is given in Figure 2.8. Each voltage-dependent channel can be pictured as a tunnel with a small number of gates arranged one after another. All the gates are responsible for the opening and closing of the ion channel. When a channel opens, all of the gates within it must be open. On the other hand, the whole channel is shut even if a single gate is shut. The schematic diagram of a ion channel is shown in Figure 2.9. The channel is

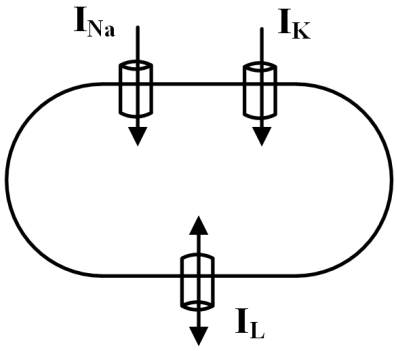

FIGURE 2.8: A schematic diagram of the Hodgkin-Huxley model (Hodgkin and Huxley, 1952) describing the currents flows across the cell membrane. The Hodgkin-Huxley model incorporates I_{Na}, I_K and I_L currents. I_{Na} and I_K are inward currents. I_L flows across the membrane in both directions.

conducting ions only when the gate m and the gate h open simultaneously. If any of the two gates are closed, the ion channel remains shut. In the Hodgkin-Hoxley description,

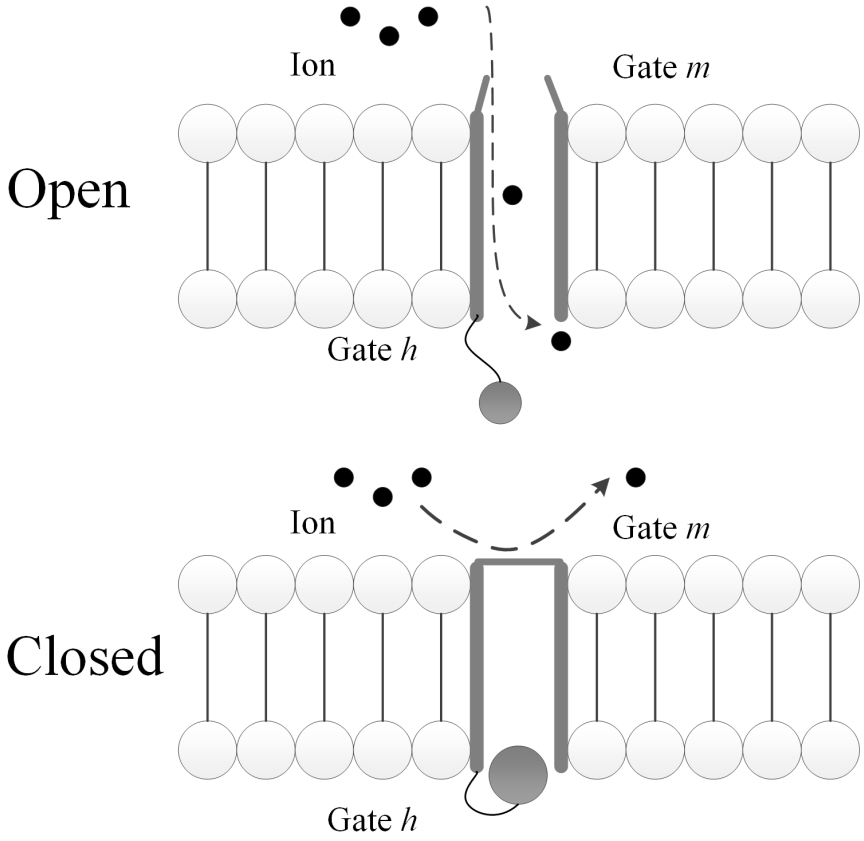

FIGURE 2.9: A schematic diagram of a ion channel. The gate of a ion channel can block ion currents and therefore changes the membrane voltage. The an ion channel is open only under the condition that two ion gates open simultaneously.

the transition between opening and closing can be described by Equation 2.1

$$\text{Shut} \underset{\beta}{\overset{\alpha}{\rightleftharpoons}} \text{Open}, \tag{2.1}$$

where factors α and β are the transition rate constants. α is the number of times per second that a gate in the shut state opens, and β is the number of times per second that a gate in the open state shuts.

In the Hodgkin-Huxley description, the gating variable is x. x is the proportion of gates in open state, while 1-x is the proportion in close state. At a given time, the fraction of gates opening is $\alpha(1-x)$, and similarly the fraction of gates shutting is βx. The variable x changes with time as

$$\frac{\mathrm{d}x}{\mathrm{d}t} = \alpha(1-x) - \beta x. \tag{2.2}$$

The Hodgkin-Huxley description hypothesises that α and β instantaneously change with the membrane voltage. The difference of x is equal to the difference in the rate of gates opening and closing. The relationship between the current I and the conductance the gating variable x can be given as

$$I = g_{\max} x (V_{\mathrm{m}} - E_{\mathrm{eq}}), \tag{2.3}$$

where $g_{\max}$ is the maximal conductance of the ion channel and E_{eq} is the equilibrium potential at which the flow of ions is zero. The potential V_{m} is the voltage difference across the membrane. The driving force of an ion is $V_{\mathrm{m}} - E_{\mathrm{eq}}$ which is a measure of how far the membrane potential is from the equilibrium potential.

The equation can be understood as follows. If we assume that the membrane voltage is fixed as a constant voltage for a long time, then the x is at a equilibrium value x_{eq}. When the membrane voltage is suddenly changed, the α and β immediately change to new values. If a system is in equilibrium, the proportion of gates in open states is a not changing, and this proportion must equal to the ratio of gates in close state. At equilibrium state, Equation 2.6 is equal to zero. The equation is rearranged as

$$\alpha(1-x) = \beta x, \tag{2.4}$$

The variable x starts to approach a new equilibrium value x_∞. Based on the rearrangement of Equation 2.4, the new equilibrium value x_∞ is given as

$$x_\infty = \frac{\alpha}{\beta + \alpha}, \tag{2.5}$$

The time constant of activation τ_∞ is defined as

$$\tau_\infty = \frac{1}{\beta + \alpha}, \tag{2.6}$$

As constants τ_∞ and x_∞ can be derived from experimental measurements, therefore the α and β can be estimated.

As an examples, the Hodgkin-Hoxley description of the Na^+ channel is presented here. The Na^+ channel consists of two type of ion gates, gate h and gate m. The gating variable m can be described with following equation:

$$\frac{\mathrm{d}m}{\mathrm{d}t} = \alpha_m(1-m) - \beta_m m, \tag{2.7}$$

where α_m and β_m are the rate constants of gate m. The another gating variable h can also be shown as

$$\frac{\mathrm{d}h}{\mathrm{d}t} = \alpha_h(1-h) - \beta_h h, \tag{2.8}$$

where α_h and β_h are the rate constants of gate h. In the Hodgkin-Hoxley description, a Na^+ channel contains three activation m-gates and one inactivation h-gate. The Hodgkin-Hoxley modeling of the Na^+ channel was later proved by experimental observation of the ion channel structure. The mechanism of the inactivation h-gate has been well understood with clear structural evidence. The protein of Na^+ channel consists of a α subunit of 260 kDa and a smaller subunit β of 30-40 kDa (Beneski and Catterall, 1980). The h-gate is formed by an intracellular loop confecting two domains (domain III and IV) of the α subunit (Catterall, 2012). The S4 region of α subunit is responsible for the activation gating (m-gate) in HH scheme (Goldin, 2003). The sodium conductance can be given as

$$g_{\mathrm{Na}} = \bar{g}_{\mathrm{Na}} m^3 h, \tag{2.9}$$

where $\bar{g}_{\mathrm{Na}}$, the channel conductance at the a given voltage is decided by the maximum conductance $\bar{g}_{\mathrm{Na}}$ and the ratio of open channels m^3h. As we introduced before, the m-gate and h-gate should open simultaneously to let channel conduct, the ratio of the open ion channel is the product of the two open gates which is m^3h. Therefore, the sodium current across the membrane can be calculated if $\bar{g}_{\mathrm{Na}}$ is given. According to Equation 2.3, the Na^+ current across the membrane is

$$I_{\mathrm{Na}} = g_{\bar{\mathrm{Na}}} m^3 h (V_{\mathrm{m}} - E_{\mathrm{Na}}), \tag{2.10}$$

where E_{Na} is equilibrium potential which is equilibrium potential which can be calculated using the Nernst equation. The Equation2.7, Equation2.8 and Equation2.10 explain the mechanism of the Na^+ channel. The corresponding graphs of the Na^+ channel behavior are shown by Figure 2.10. Figure 2.10 shows the regulation of gating variables and the Na^+ channel conductance according to the Equation 2.9. The gating variables regulate the current conductance and therefore vary the ion current, which indirectly changes the membrane voltage by the regulation of ion currents. The sodium ion current and the sodium ion conductance show a large similarity due to the modulation of gating variables. The complete equations are given in the next section.

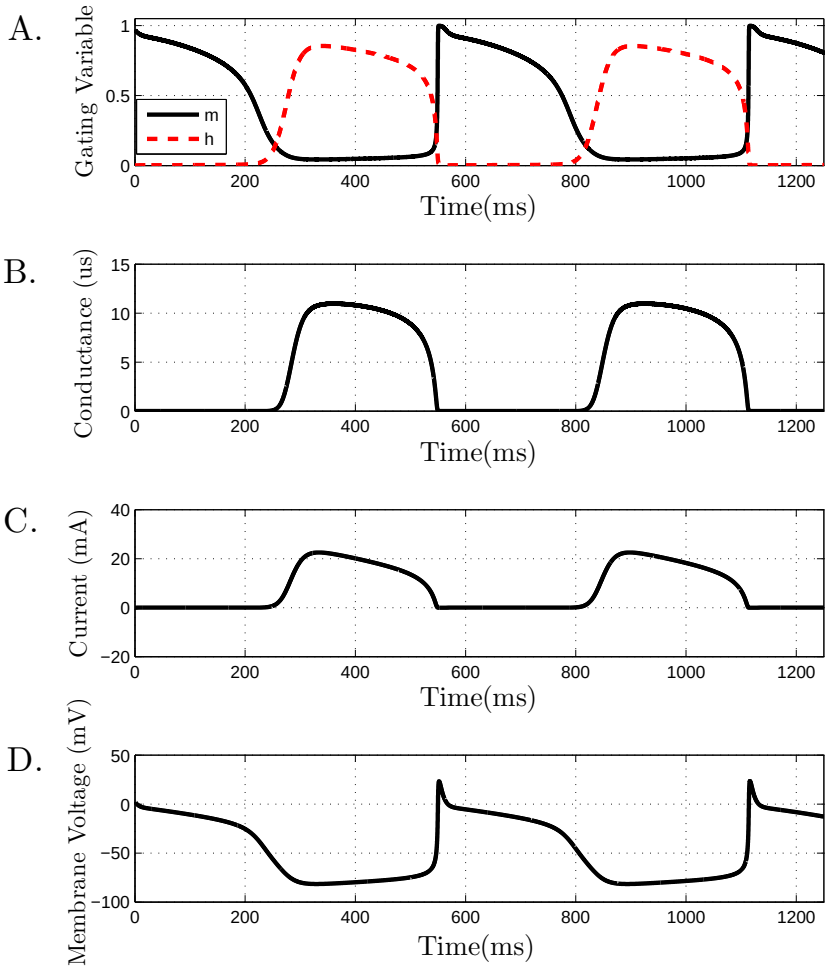

FIGURE 2.10: Gating variables exhibit the fluctuation of ion channel gates which control the ion channel conductance and in addition affect the ion current value. (A) The value of gating variable m and h of a Na^+ channel (B) The Na^+ channel conductance (C) The Na^+ current (D) The membrane voltage (Noble, 1962).

2.4 Noble Model

In this section, the Noble model is introduced as an example of Hodgkin-Hoxley description. The Noble model is a Purkinje fibre action potential model (Noble, 1962). This model is one of the earliest applications of the Hodgkin-Huxley description on cardiac action potentials. It shows that with certain modifications the Hodgkin-Huxley description of the nerve impulse can also create long plateau of the cardiac action potential. It is formed of a simple mathematical cardiac model and includes three currents and four variables. In Figure 2.11, two types of K^+ currents are shown. The current, I_{K1}, is an instantaneous current which instantly falls when the membrane is depolarized, while slow current I_{K2} gradually activates during the depolarization. The Hodgkin-Huxley

model described the conductance of Na^+ channel is determined by two variables m and h and this formulation is also employed in the Noble model.

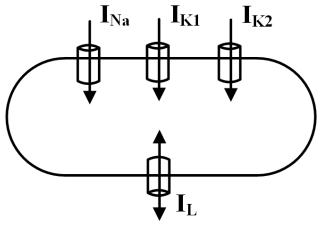

FIGURE 2.11: A schematic diagram of the Noble model describing the currents flows across the cell membrane. The Noble model incorporates three inward current I_{Na}, I_{K1} and I_{K2}. The current I_L flows across the membrane inwardly and outwardly.

1. The Sodium Current

   The following equations are an explanation of the sodium current from the rate constant of a single ion gate in the sodium current,

$$\alpha_m = \frac{0.1(V_m + 48))}{1 - \exp[-(V_m + 48))/15]} \tag{2.11}$$

$$\beta_m = \frac{0.12(V_m + 8))}{\exp[(V_m + 8))/5] - 1} \tag{2.12}$$

$$\alpha_h = 0.17 \exp(-(V_m + 90)/20) \tag{2.13}$$

$$\beta_h = \frac{1}{1 + \exp[-(V_m + 42))/10]} \tag{2.14}$$

$$\tag{2.15}$$

   where α_m is the rate constant of the opening of closed m gates, and β_m is the rate constant of the closing of open m gates. The variable m is the proportion of open m gates and is based on the differential equation in the above equations. The gating variable h is another type of ion gate and also follows the same scheme.

$$\frac{dm}{dt} = \alpha_m(1 - m) - \beta_m m \tag{2.16}$$

$$\frac{dh}{dt} = \alpha_h(1 - h) - \beta_h h \tag{2.17}$$

$$I_{Na} = (400m^3h + 0.14)(V_m - 40), \tag{2.18}$$

   The two variables also vary with membrane voltage in inverse directions. The change in membrane potential exerts a dual effect on the sodium conductance g_{Na}, because at the initial stage of depolarization, g_{Na} can greatly rise but quickly fall to a low value when depolarization is maintained. The equations can be explained by Figure 2.10.

2. The Potassium Current

$$\alpha_{\mathrm{n}} = \frac{0.1000(V_{\mathrm{m}} + 50))}{1 - \exp[-(V_{\mathrm{m}} + 50))/10]]} \tag{2.19}$$

$$\beta_{\mathrm{n}} = 0.002\exp[-(V_{\mathrm{m}} + 90))/80] \tag{2.20}$$

$$\frac{\mathrm{d}n}{\mathrm{d}t} = \alpha_{\mathrm{n}}(1 - n) - \beta_{\mathrm{n}}n \tag{2.21}$$

$$g_{\mathrm{K_1}} = 1.2\exp[(-V_{\mathrm{m}} - 90)/50] + 0.015\exp[(V_{\mathrm{m}} + 90)/60] \tag{2.22}$$

$$g_{\mathrm{K_2}} = 1.2n^4 \tag{2.23}$$

$$I_{\mathrm{K}} = (g_{\mathrm{K_1}} + g_{\mathrm{K_2}})(V_{\mathrm{m}} + 100). \tag{2.24}$$

There are two K^+ channels of different kinds incorporated in the model. In one channel, K^+ conductance g_{K1} is an instantaneous function. The corresponding inward rectifier, I_{K1}, is energy saving and reduces the K^+ ion flow during depolarization. During depolarization, g_{K1} experiences a rapid decrease, while g_{K2} only has a slight incasement. In Figure 2.11, we present the current I_{K} independently as I_{K1} and I_{K2}.

3. The Anion Current

$$I_{\mathrm{An}} = g_{\mathrm{An}}(V_{\mathrm{m}} - E_{\mathrm{An}}). \tag{2.25}$$

A leak current I_{An} is incorporated into the model to describe the flow of chloride ions. The anion conductance is regarded as a constant since it is independent from the time and membrane voltage, and therefore, the current is only regulated by V_{m}.

4. The Membrane Voltage

$$\frac{\mathrm{d}V_{\mathrm{m}}}{\mathrm{d}t} = \frac{1}{C_{\mathrm{m}}}(I_{\mathrm{m}} - I_{\mathrm{Na}} - I_{\mathrm{K}} - I_{\mathrm{An}}), \tag{2.26}$$

where cell capacitance ($\mathrm{C_m}$) represents the bilayer membrane of cardiac cells. The capacitance is associated with cell size. From SAN centre to SAN periphery, the cell capacitance increases from 20 pF to 65 pF with respect to growth of cell size. The change of the membrane potential, V_{m}, is under the regulation of the three ion currents (I_{Na}, I_{K} and I_{An}) and the total membrane current (I_{m}). If there is any applied current from outside of the cell, the current flowed into the membrane, I_m, should be non-zero. Without any applied currents, I_{m} is zero. The implementation details, such as ODE initial values and parameter values, of the Noble model is given in Table A.1 and A.2 (Appendix). The Noble model is an early application of the Hodgkin-Huxley formulation, so it is a variant of the classic model. The work shows that the Hodgkin-Huxley formulation can be applied to the modelling of cardiac cell behaviour. The Noble model successfully predicts that the inward currents in the heart differ from that in nerve and modelled a steady plateau sodium current.

TABLE 2.3: Glossary for Purkinje model (Noble, 1962). A complete glossary is given in Appendix (Table A.4).

Parameter Name	Meaning
E_{Na}	Equilibrium potential for Na^+
E_{K}	Equilibrium potential for K^+
E_{An}	Equilibrium potential for leak current
V_{m}	Membrane potential
I_{Na}	Na^+ current
I_{K}	K^+ current
I_{An}	Leak current
I_{m}	Total membrane current
C_{m}	Cell capacitance
m	Gating variable m
n	Gating variable n
h	Gating variable h
g_{An}	Conductance of leak current

As shown in Figure 2.6, the Noble model action potential has a long pulse duration which is achieved by certain modification of the Hodgkin-Huxley model parameters. For example, the Noble model has smaller ion channel conductance and rate constants (e.g. α_n and β_n are divided by 100). However, the model is largely incomplete because many cardiac ion currents and exchangers, such as Ca^{2+} current and funny current I_f, are not incorporated. I_f is an important mixed Na^+K^+ current which activates on hyperpolarization. These ion currents were later discovered and modeled. In the following section, the incorporation of these new ion currents in SAN models is presented.

2.5 The Single SAN Cell Model

A great deal of research has been conducted on the modelling of excitable cardiac cells, as shown in Figure 2.7, However, the modelling of SAN cells has received much less attention. SAN cells are auto-rhythmic cardiac cells which is the primary pacemaker. The rate of SAN cells (human) is 70-80 beat per minute, which is the fastest rate of auto-rhythmic cardiac cells. In this section, the development of single cell SAN models is presented.

In early 1980s, the SAN model was constructed by modifying a Purkinje fibre model (Bristow and Clark, 1982). In late 1980s, because of the progress made in cardiac cellular electrophysiology and in computer science, several cardiac cell models, especially SAN cell models, were developed. The later generation models have time- varying ion concentrations that are regulated by pumps and exchangers. Table 2.4 shows the development and incorporation of ion channel of single cell SAN models.

TABLE 2.4: The development of the incorporation of ion currents in single cell SAN models. ✓ stands for the incorporation of an ion current. In 1980s, the Ca^{2+} current, I_{Ca}, was developed into a T type component $I_{Ca,T}$ and a L type component $I_{Ca,L}$. Ca^{2+} handling was modeled in late 1980s. I_{sus}, I_{to} and I_{st} were introduced in 2000s. The delayed rectifier K^+ current, I_K, was modeled independently into rapid component ($I_{K,r}$) and slow component ($I_{K,s}$) respectively. ✓*: $I_{b,Na}$ is not incorporated.

	I_{Na}	I_{Ca}		I_K		I_{sus} & I_{to}	Ca^{2+} handling	I_{NaK}	I_{NaCa}	I_{st}	$I_{b,K}$ $I_{b,Na}$ $I_{b,Ca}$	I_f
Bristow and Clark (1982)	✓	✓		✓								✓
Irisawa and Noma (1982)	✓	✓		✓								✓
	I_{Na}	$I_{Ca,L}$	$I_{Ca,T}$	I_K		I_{sus} & I_{to}	Ca^{2+} handling	I_{NaK}	I_{NaCa}	I_{st}	$I_{b,K}$ $I_{b,Na}$ $I_{b,Ca}$	I_f
Noble et al. (1989)	✓	✓		✓			✓	✓	✓		✓	✓
Wilders et al. (1991)	✓	✓	✓	✓			✓	✓	✓		✓	✓
Demir et al. (1994)	✓	✓	✓	✓			✓	✓	✓		✓	✓
Dokos et al. (1996)	✓	✓	✓	✓			✓	✓	✓		✓*	✓
	I_{Na}	$I_{Ca,L}$	$I_{Ca,T}$	$I_{K,r}$	$I_{K,s}$	I_{sus} & I_{to}	Ca^{2+} handling	I_{NaK}	I_{NaCa}	I_{st}	$I_{b,K}$ $I_{b,Na}$ $I_{b,Ca}$	I_f
Zhang et al. (2000) central SAN		✓	✓	✓	✓	✓		✓	✓	✓	✓	✓
Zhang et al. (2000) peripheral SAN	✓	✓	✓	✓	✓	✓		✓	✓	✓	✓	✓
Kurata et al. (2002)		✓	✓	✓	✓	✓	✓	✓	✓	✓	✓	✓
Sarai et al. (2003)		✓	✓	✓			✓	✓	✓		✓	✓

There are two disparate hypotheses on the modelling of SAN cells.

1. The SAN has specific cell types with distinct action potential characteristics

2. The SAN cells have no significant variations in action potential

The first hypothesis considers SAN as a complex heterogeneous tissue. Zhang et al. (2000) constructed two models, a central cell model and a peripheral cell model, based on the first hypothesis. The second hypothesis suggests that all the observed SAN heterogeneity are due to electrotonic coupling effects - membrane voltage of SAN cells are strongly affected by voltages of adjacent cells, especially the voltage coupling from atrial cells. The SAN model described the SAN heterogeneity is known as the non-uniform SAN model. Based on the second hypothesis, Oren and Clancy (2010) used the Kurata model (Kurata et al., 2002) to construct 1D SAN model. This type of model is known as the uniform SAN model. In the following section, the single cell SAN model based on the two hypothesises are presented.

2.5.1 Zhang SAN Cell Models

The Zhang SAN cell models incorporate periphery and center regions of the rabbit sinoatrial node. The models aim to present a biophysically detailed model of action potentials with respect to regional difference (Zhang et al., 2000). The model was developed on the basis of published results and the resulting simulation results have good agreement with the published experimental work. The following shows the differential equations of membrane voltage. The two models incorporate 13 ion currents or exchangers as shown by Figure 2.12 (the central SAN model set the Na^+ current as zero). Figure 2.12 demonstrates that the periphery and centre version of the model incorporate the models of the hyperpolarization-activated current, the L-type and T-type of calcium currents, the ion exchangers, the rapid and slow delayed rectifying K^+ currents and the 4-Aminopyrine sensitive current. The equations, the parameter values and the details of the model are

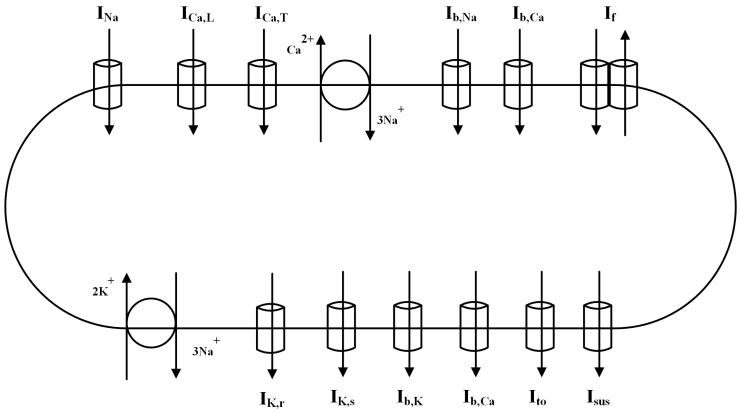

FIGURE 2.12: A schematic diagram of the central and peripheral SAN cell models (Zhang et al., 2000) model with demonstration of ion currents and their directions.

given in the Appendix. In contrast with the Noble model, the sinoatrial node model provides better simulation results according to experimental discoveries. This work has two versions. Small SAN cells, with a membrane capacitance of 20 pF, are assumed to originate from the centre of the SAN. Large cells, with a membrane capacitance of 65 pF, are hypothesised to be the periphery of the sinoatrial node.

2.5.2 Kurata SAN Cell Model

As discussed, one type of the SAN tissue models is the uniform model. Oren and Clancy (2010) constructed a one-dimensional SAN uniform model based on the single cell Kurata SAN model (Kurata et al., 2002). The Kurata SAN cell model was also used as the basis for the uniform model in our work. This mode incorporates 1). a new pacemaker current I_{st}, 2). a novel activation mechanism of L-type Ca^{2+} channel, 3). intracellular Ca^{2+} dynamics. The Kurata model incorporates 13 ion currents or ion exchangers, the schematic diagram of the model is shown in Figure 2.13. The action

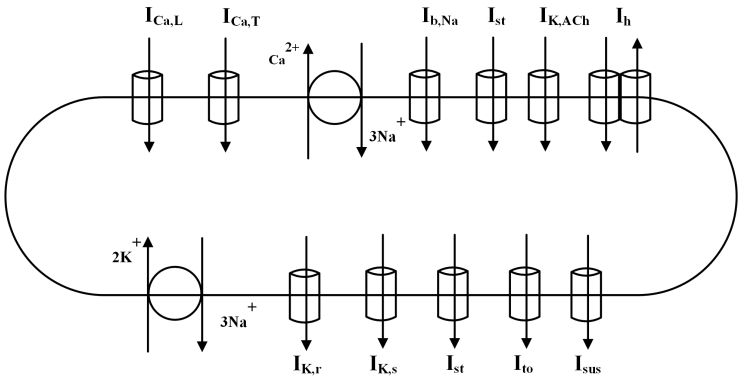

FIGURE 2.13: A schematic diagram of the Kurata SAN cell model (Kurata et al., 2002).

potentials of the Kurata SAN model, the Zhang central and peripheral SAN model are illustrated in Figure 2.14.

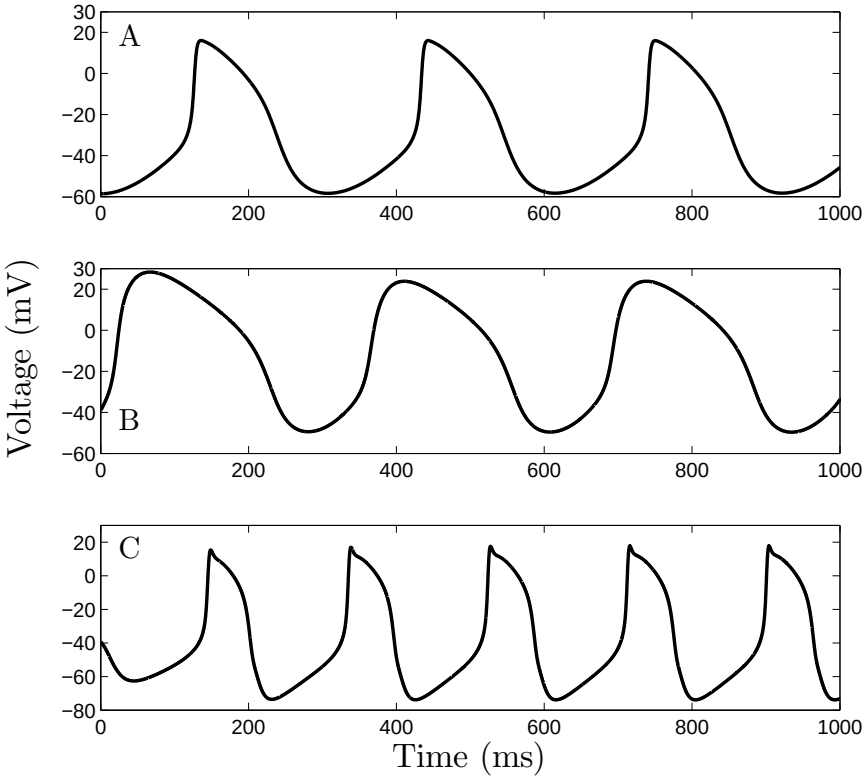

FIGURE 2.14: SAN action potential waveforms. A. Kurata SAN model, B. Zhang central SAN model, C. Zhang peripheral SAN model.

2.6 Excitable Cardiac Cell Models

2.6.1 Atrial Cell Model

In order to model the SAN electrophysiological behavior at the tissue level, an atrial cell model needed to be included into the 1D SAN model. Garny et al. (2003) published a 1D rabbit SAN model based on the Zhang central and peripheral SAN model and Hilgemann-Noble atrial model (Hilgemann and Noble, 1987). The Hilgemann-Noble atrial model describes the rabbit atrial cell action potentials. We incorporate the Hilgemann atrial model into our 1D modeling of the SAN tissue. The schematic diagram of the model is shown in Figure 2.15. Action potentials of the Hilgemann-Noble atrial

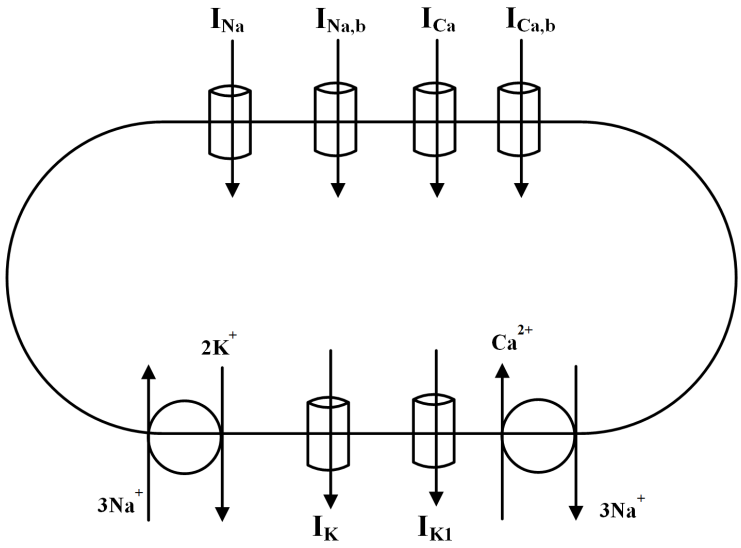

FIGURE 2.15: A schematic diagram of the atrial cell model (Hilgemann and Noble, 1987) with demonstration of ion currents and their directions.

model are illustrated in Figure 2.17.

2.6.2 Ventricular Cell Model

A strong ion channel interaction was observed in the ventricular cell behavior (Chang et al., 2015). In order to analyze the interaction effects of excitable cells, A Luo-Rudy ventricular cell model is used in our global sensitivity analysis. The schematic diagram of the ventricular cell model is given as Figure 2.16. The action potentials of the Hilgemann-Noble atrial model are given in Figure 2.17.

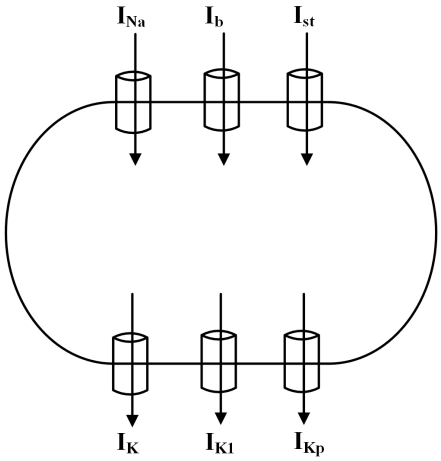

FIGURE 2.16: A schematic diagram of a ventricular cell model (Luo and Rudy, 1991) with demonstration of ion currents and their directions. This mode is presented to test and to quantify the interactions of ion channels.

2.7 One Dimensional Sinoatrial Node Model

As discussed, there are two hypothesis on the SAN tissue. The first hypothesis considers SAN as a complex heterogeneous tissue. This complexity is on the regional difference of action potential conduction, ion channel densities, expression of gap junction proteins, autonomic regulation, and ageing (Boyett et al., 2000). The action potential characteristics are dependent on the size of the SAN cell in the rabbit (Boyett et al., 2007b). Based on this hypothesis, the SAN is considered as **a gradient model** (or a non-uniform model) which has a gradual change from the SAN centre to periphery. The electrophysiological distinction of the two models are regulated by the cell size (the capacitance of the cell membrane).

The second hypothesis suggests that all the observed SAN heterogeneity are due to electrotonic coupling effects, especially the coupling effects from the atrial cells. The hypothesis is supported by experiments that indicate that the morphologically distinct SAN cells have no significant variations in action potentials, channel expression and firing period (Lyashkov et al., 2007). Moreover, other researchers failed to observe a size-dependent difference in isolated SAN cells (Michaels et al., 1987) (Verheijck et al., 1998). Oren and Clancy (2010) constructed **a uniform model** based on the second hypothesis.

2.7.1 Non-uniform 1D SAN Model

The pacemaker SAN cells generate spontaneous action potentials that spread via gap junctions, which allows the diffusion of ions. The spread of ions allows the potentials of cells to interact, and SAN action potentials can be further spread to excitable cells,

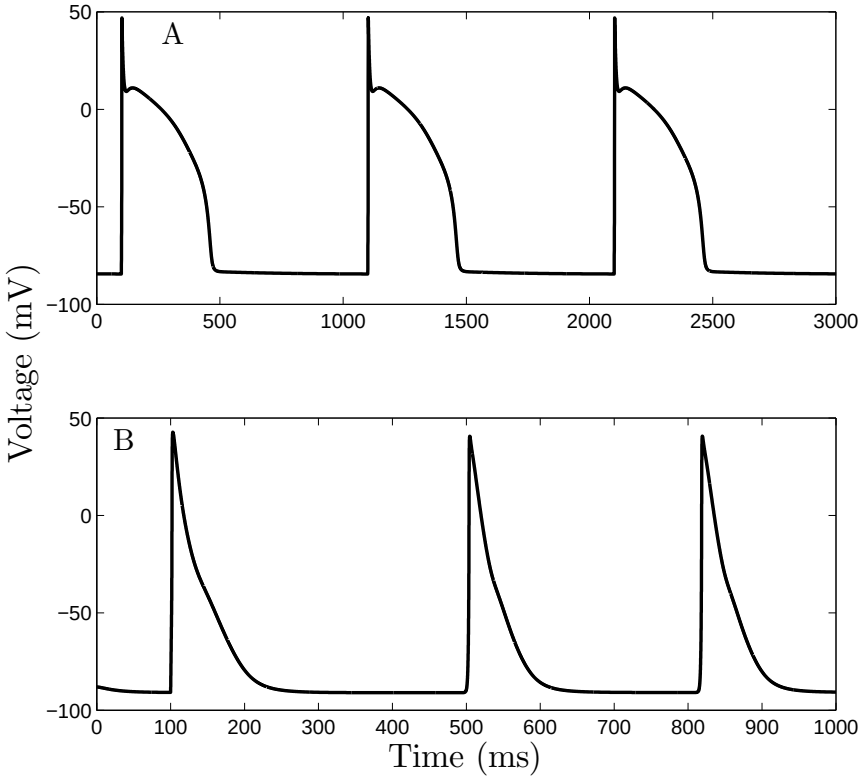

FIGURE 2.17: The action potentials of ventricular cell and atrial cell. A. Luo-Rudy ventricular model action potentials. B. Hilgemann-Noble atrial model action potentials.

e.g. atrial cells. The atrial cells consequently start to fire after the stimulus of the SAN action potential. The excitations of atrial cells are stimulated by the depolarization in SAN cells when the atrial cells reach the excitation threshold. An one-dimensional (1D) model is presented by Zhang et al. (2000) to describe the cell to cell interaction and AP spread between SAN and atrial cells. The Zhang 1D SAN model was improved by Garny et al. (2003), and be further extended into a two-dimensional and three-dimensional SAN and atrial cell model (Garny et al., 2005).

Zhang et al. (2000) proposed a gradient 1D model of the SAN based on the central and peripheral SAN cell models. In this model, the SAN tissue is considered to have a length (L) of 12.6 mm. The 1D tissue contains 3 mm SAN tissue and 9.6 mm atrial tissue. The differential equations of the Zhang 1D SAN model are given as follows: For x = 0 - 3 mm

$$\frac{\mathrm{d}V^s}{\mathrm{d}n} = 0, \text{ for x} = 0, \tag{2.27}$$

$$C^s(x) = 20 + \frac{1.07(x - 0.1)}{L^s[1 + 0.7747 \exp -(x - 2.05)/(0.295)]}(65 - 20) \tag{2.28}$$

$$g^s(x) = \frac{[65 - C_m^s(x)]g_c + (C_m^s - 20)g_p}{65 - 20} \tag{2.29}$$

$$\frac{\mathrm{d}V^s(x)}{\mathrm{d}t} = -\frac{1}{C_m^s(x)}[i_{tot}^s(x) + D^s\frac{\mathrm{d}^2V^s(x)}{\mathrm{d}x^2}], \tag{2.30}$$

where $V^s(x)$ is the SAN cell voltage with a distance x from SAN centre. D^s is a scale of the conduction velocity of action potential in the SAN cells. A gradient is present in the SAN capacitance and conductance from central to peripheral SAN cells. The capacitance $C^s(x)$ is defined by Equation 2.28, and $C^s(x)$ is allowed to change from 20 pF to 65 pF. The conductance $g^s(x)$ at a given distance x is shown by Equation 2.29, and the conductance value of $g^s(x)$ varies with respect to $C^s(x)$. For x = 3 - 12.6 mm

$$\frac{\mathrm{d}V^s}{\mathrm{d}n} = 0, \text{ for x = L,} \tag{2.31}$$

$$\frac{\mathrm{d}v^a(x)}{\mathrm{d}t} = -\frac{1}{C_m^a}[i_{tot}^a(x) + D^a\frac{\mathrm{d}^2V^a(x)}{\mathrm{d}x^2}], \tag{2.32}$$

where $V^a(x)$ is the atrial cell voltage with a distance x from SAN centre. D^a is a scale of the conduction velocity of action potential in the atrial cells. Equation 2.27 and Equation 2.31 are the non-flux boundary conditions, which consider that there is no ion exchange between the 1D tissue and the outside environment of 1D tissue at the two ends of the 1D model. The non-flux boundary condition implies no flux and thus no concentration gradient at the boundary. Therefore, there is no ions (or voltage) exchange between the SAN and outside.

The 1D Zhang SAN model consider the diffusion rates D^a and D^a as constants in the SAN tissue and atrial tissue. (Garny et al., 2003) modified the parameters of the Zhang 1D model and considered diffusion rate D^a (or conductivity) as a gradient (from 7.5 nS to 75 nS) from the central SAN to peripheral the SAN according to the experimental observation of cell-to-cell coupling (Bleeker et al., 1980). The Zhang 1D SAN model is a space based 1D model, whose simulation accuracy is relevant to the space step Δx. Figure 2.19 is our recreation of the 1D non-uniform model.

2.7.2 Uniform 1D SAN Model

(Oren and Clancy, 2010) proposed a cellular 1D SAN tissue model which addresses the cellular properties of SAN tissue. They examined cellular properties of a non-uniform 1D model and a uniform 1D model based on the Kurata model Kurata et al. (2002). The non-uniform and uniform 1D model both contain 60 cells (30 SAN cells and 30 atrial cells). The non-uniform model achieves stable central pacemaking (the leading pacemaker is located at the SAN centre). If stochastic single cell SAN model is available,

The cellular 1D SAN model can be converted into the stochastic 1D SAN model by incorporation of cell-to-cell coupling. The tissue level variability can be modeled by this cellular structure. In order to couple the SAN and atrial cells together, Equation 2.30 and Equation 2.32 can be rewritten as (Oren and Clancy, 2010)

$$C_m \frac{\mathrm{d}V(i)}{\mathrm{d}t} = G_{Gap}[V(i-1) - V(i) + V(i+1) - V(i)] - I_{tot}(i), \tag{2.33}$$

where $V(i)$ is the membrane voltage of the $\mathrm{i_{th}}$ cell, $I_{tot}(i)$ is the sum of the transmembrane ion currents of the $\mathrm{i_{th}}$ cell, and G_{Gap} is the gap-junction coupling. As shown in Figure

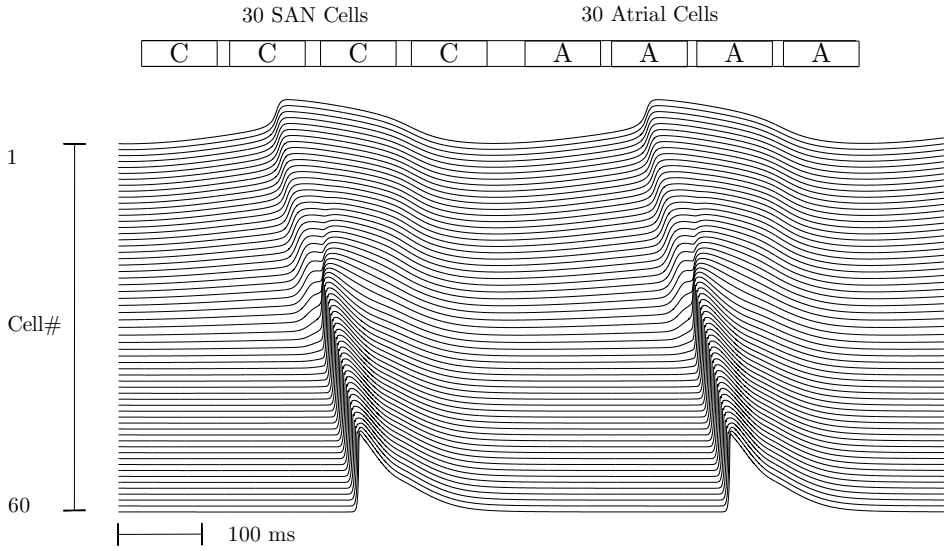

FIGURE 2.18: Uniform 1D SAN-atrial model action potentials. The model involves 30 SAN cells (Kurata central SAN model) and 30 atrial cells (Hilgemann-Noble atrial model).

2.19, we failed to reproduce the published results that the leading pacemaker is located at the SAN centre, not periphery. Oren and Clancy (2010) observed the same phenomenon and stated that the non-uniform model cannot recreate the experimental observation, and discussed the leading pacemaker (the first cell starting the depolarization) location of the uniform and non-uniform model as shown by Figure 2.20 which suggests that the uniform model is robust and can locate the leading pacemaker at the SAN centre with respect to a range of coupling values.

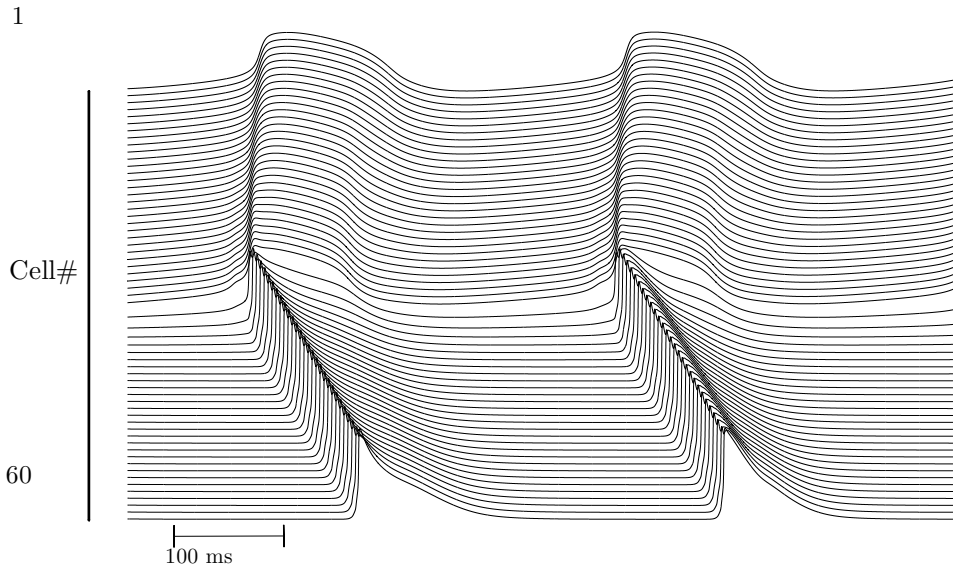

FIGURE 2.19: Non-uniform 1D SAN-atrial model action potentials. The model involves 30 SAN cells (Zhang gradient SAN model, a linear gradient applied from the SAN centre to periphery) and 30 atrial cells (Hilgemann-Noble atrial model).

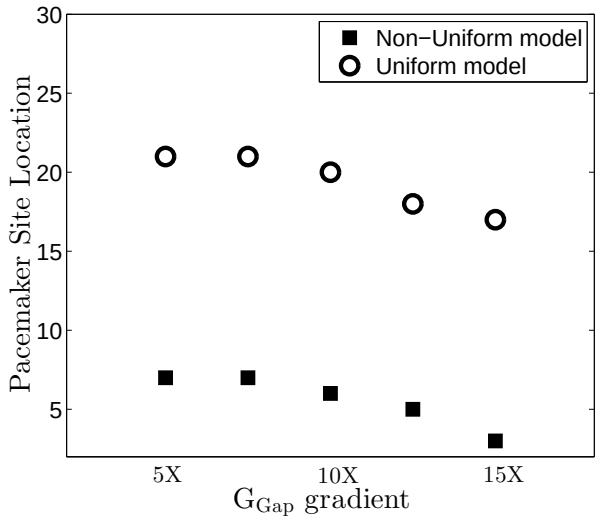

FIGURE 2.20: The pacemaker site location for uniform and non-uniform 1D SAN model with respect to a range of coupling strength values. Recreated from Oren and Clancy (2010).

2.8 Features of Action Potentials

2.8.1 Features of SAN Action Potentials

The characteristics of SAN action potentials can be quantified by several features which are considered as model outputs of sensitivity analysis in the following chapter. The definitions of these features are listed as follows. Cycle length (CL) is the time interval

between two consecutive action potential peaks. Action potential overshoot (APO) is the maximum voltage value of an action potential. Maximum diastolic potential (MDP) is the most negative voltage value in an action potential. Action Potential Amplitude (APA) is the voltage difference between APO and MDP. dv/dt_{max} is the maximum rate change of a rise of an upstroke AP. The measurements of the five features are given in Figure 2.21. APD_{90} and APD_{50} are two features which are related to the duration of

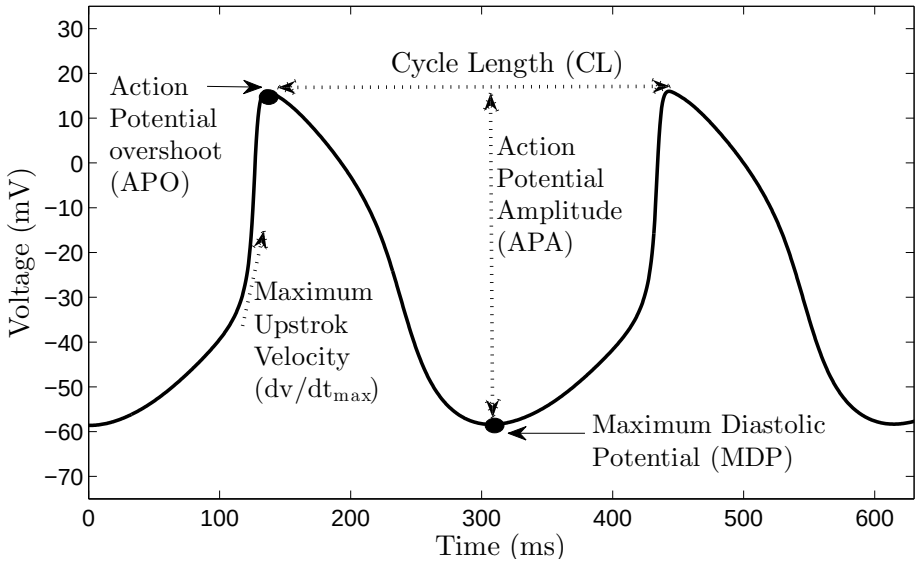

FIGURE 2.21: Graphical illustration of the definitions of CL, APO, MDP, APA and dv/dt_{max} from action potentials.

an action potential pulse. APD_{90} is the duration between a MDP and the consequent 90% popularization of membrane voltage, and APD_{50} is the duration between a MDP and the consequent 50% popularization of membrane voltage. The measurements of APD_{90} and APD_{50} is shown in Figure 2.22. The diastolic depolarization rate (DDR) is the slope of the line segment between MDP and the take off potential. The take off potential Figure 2.23 shows the measurement of the DDR. The take-off potential is at a AP slop rate same with the line joining MDP and APO as shown in Figure 2.23. The Δx and Δy are the intervals between the MDP and the take-off potential. DDR is calculated as a ratio of Δy and Δx. Table 2.5 gives the standard values of these features for the three SAN models. The model is obtained from the Physiome project (http://www.physiomeproject.org/) as Matlab files. The computational models of the Physiome project are often described by CellML language which is primarily designed for biological models. The Physiome project also provides models described by Matlab, Python and C. These feature values are measured at the default model setting given according to codes obtained from the Physiome project. Model details are given in Table 2.6.

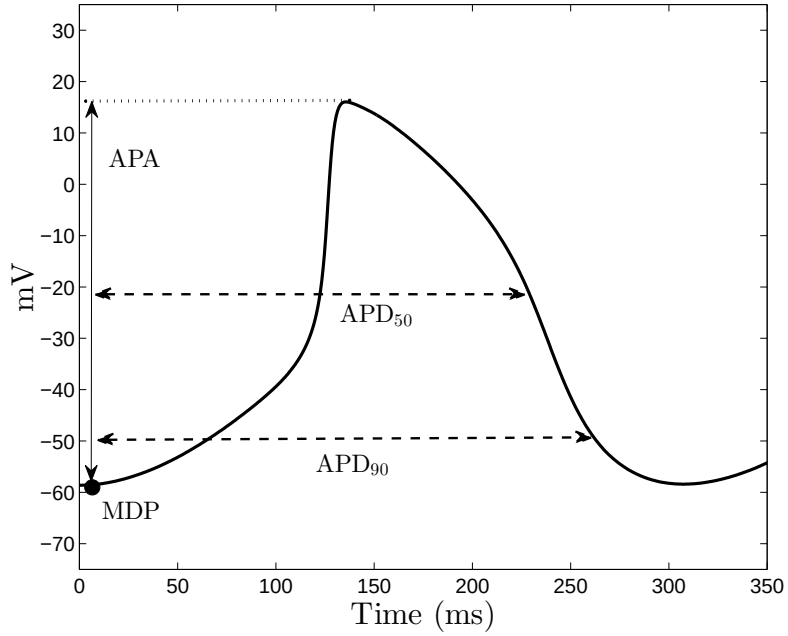

FIGURE 2.22: Measurements of APD_{90} and APD_{50} from an action potential.

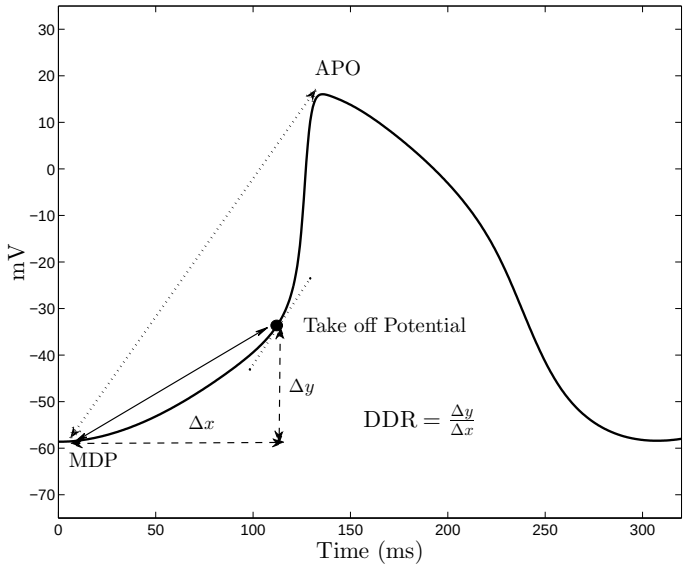

FIGURE 2.23: The measurement of DDR of an action potential.

2.8.2 Features of Ventricular Action Potentials

In the case of the ventricular cell, the CL and DDR are not relevant because the firing rate is determined by the stimulus from outside of the ventricular cell. The definitions of APO, MDP, APD_{90} and dv/dt_{max} for ventricular action potentials are the same as SAN action potentials. A new feature, Dome Peak (DP), is introduced to describe the

TABLE 2.5: Standard outputs of three SAN models. A: Central SAN model Zhang et al. (2000),B: Peripheral SAN model Zhang et al. (2000) , C: SAN model Kurata et al. (2002). The standard outputs are generated with the published parameter values. The output values are measured from the last action potential pulse by running the simulation for 5 s duration and time step of 0.01 ms.

Model	CL (ms)	APO (mV)	MDP (mV)	APA (ms)	APD_{90} (ms)	dv/dt_{max} (mV/ms)	DDR (mV/ms)
A	326.2	23.9	-49.7	73.5	292.9	3.1	0.25
B	188.3	17.7	-73.9	91.6	171.8	11.0	0.37
C	307.3	15.9	-58.2	74.2	264.7	6.1	0.21

TABLE 2.6: The reference of cardiac models. Four cardiac models are obtained from the Physiome Project as Matlab codes. The implementation of these models is based on the default setting of Physiome Project.

Model Name	Code Author	Download Date	Link
Zhang Central SAN	Dr. Alan Garny	11/04/2016	https://models.physiomeproject.org/exposure/b8bcdc147950c7bb4a3a1ac9206ba3f3/garny_kohl_hunter_boyett_noble_2003.cellml/view
Zhang Peripheral SAN	"-"	"-"	"-"
Kurata Model	Dr. Alan Garny	09/12/2015	https://models.physiomeproject.org/exposure/47b969553fcfe6f875d4e38d1fd33986/kurata_hisatome_imanishi_shibamoto_2002.cellml/view
Luo-Rudy Model	Dr. Alan Garny	14/04/2016	https://models.physiomeproject.org/exposure/2d2ce7737b42a4f72d6bf8b67f6eb5a2/luo_rudy_1991.cellml/view

ventricular action potential. The DP is the dome peak of the AP as shown in Figure 2.24. The measurements of MDP, APO, APA, APD_{90}, dv/dt_{max} and DP are shown in Figure 2.24. The features Slope, maximum Action Potential Duration Restitution (APDR) slope, and DI_{min} (minimum Diastolic Interval) are the indicators of dynamic properties of the ventricular AP. The dynamic properties describe how the ventricular cells response to the stimulus. The five outputs APO, MDP, APD_{90}, dv/dt_{max}, DP can be directly measured from the final AP pulse, but the measurements of Slope and DI_{min} need a progressive simulation as follows. The initial values of state variables are obtained from the five AP final variables as above. The stimuli (-25.5 μA cm^{-2} and duration 2 ms) is progressively delivered at shorter CL until the excitation of the second AP beats cannot be elicited. The APD and DI are obtained during this additional stimulation as shown in Figure 2.25. Figure 2.25 shows the response of the ventricular cells after the second stimulus. When we progressively reduce the stimulus time interval between the first and the second stimulus, the DI and APD_{90} vary with respect to it. The relationship between APD_{90}^2 and DI is given as (Chang et al., 2015)

$$\mathrm{APD} = \mathrm{a} - \mathrm{b}\exp\left(-\mathrm{DI}/\mathrm{c}\right). \tag{2.34}$$

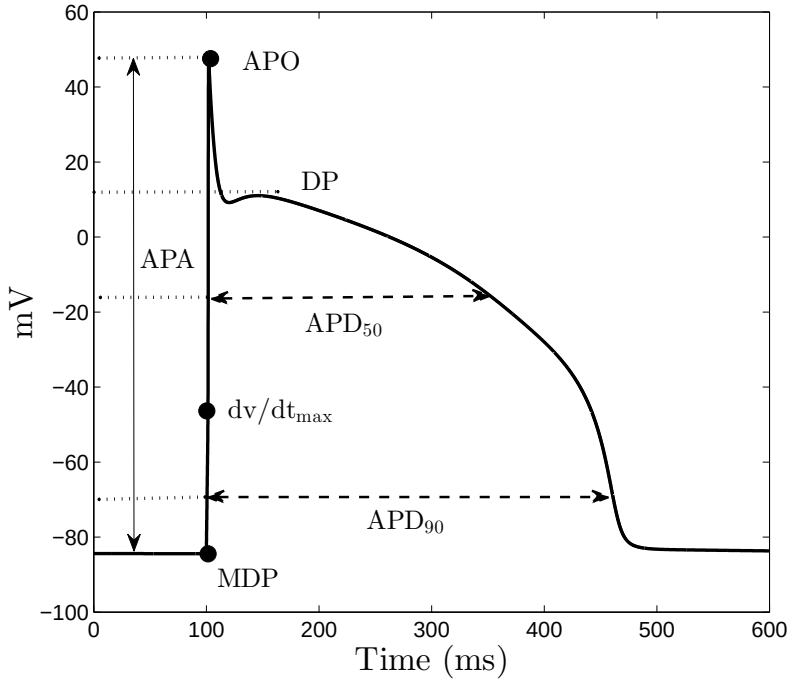

FIGURE 2.24: Measurements of APO, MDP, APA, DP and dv/dt_{max} of an ventricular action potential.

The progressive simulation can produces a number of DI and APD_{90}^2 which can be used to fit the data with Equation 2.34. Following Chang et al. (2015), we used MATLAB function *fmincon* to fit the data with Equation 2.34, and the values of constants a, b and c are obtained from the Equation. DI_{min} is the minimum DI value which is generated from the excitable second AP after the stimuli during the progressive simulation. The slope of the APDr curve can be obtained from the constants a, b, c and DI_{min} by Equation 2.35 (Chang et al., 2015).

$$\text{Slop} = \frac{\text{a}}{\text{b}} \exp\left(\text{DI}_{\text{min}}/\text{b}\right). \tag{2.35}$$

The standard values of all the features are listed in Table 2.7. In the sensitivity analysis,

TABLE 2.7: Standard outputs of the ventricular models. D: Luo-Rudy ventricular cell model (Luo and Rudy, 1991). slope is the APDR slope. DI_{min} is the minimum DI. DP is the dome peak. The output values of APO, MDP, APD_{90}, dv/dt_{max} and DP are measured from the last action potential pulse by running the simulation for 5 s duration and time step of 0.01 ms.

Model	APO (mV)	MDP (mV)	APD_{90} (ms)	dv/dt_{max} (mV/ms)	DP (mV)	Slope (mV/ms)	DI_{min} (ms)
D	46.93	-81.44	236.5	378.7	11.03	1.12	0.64

the features of SAN and ventricular AP are used as function outputs of cardiac models. This is because each feature can be considered as a scalar output with a specific biological meaning as some sensitivity analysis methods assume that the output of the target model

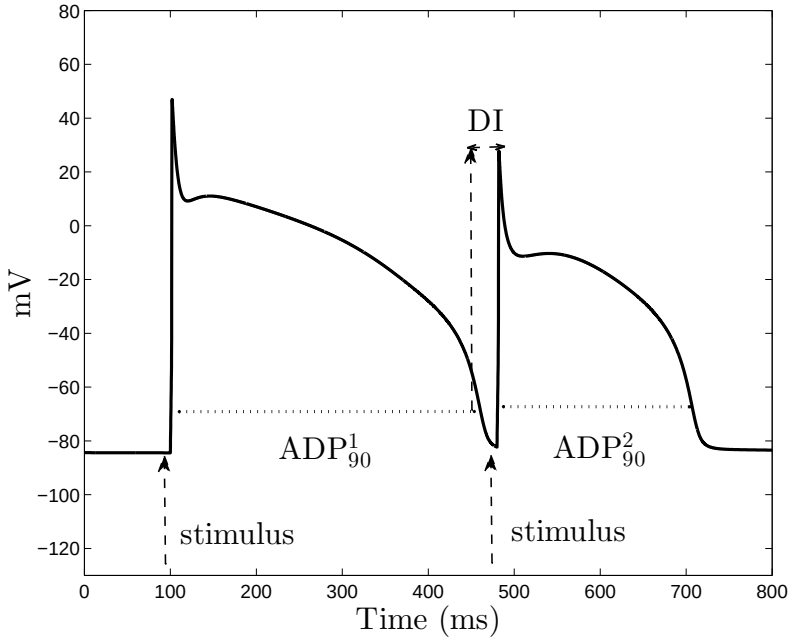

FIGURE 2.25: Measurements of DI and APD_{90} of a ventricular action potential. APD_{90} used for the APDR curve is the APD^2_{90} which is after the second stimulus.

is a scalar.

2.9 Conclusion

Following a review of the development of models of cardiac pacemaker cells, this chapter defined some of the key features defining the properties of the action potential waveform. These properties will be used as the targets whose sensitivities with respect to models will be the subject of analysis in the next chapter.

Chapter 3

Local Sensitivity Analysis in Cardiac Models

In this chapter, we implement local sensitivity analysis to quantify the roles of ion channels. The local sensitivity analysis is to calculate the partial derivatives of model outputs. The results show that ion channels have common functions in various SAN models.

3.1 Sensitivity Analysis and Local Sensitivity Analysis

Systems biology with mathematical models is a powerful tool to study the behaviour of cells and to uncover the principles of biological systems. The development of the models requires parameter estimation from experimental data. However, experimental data supported by theoretical hypotheses may be largely missing (Arkin and Schaffer, 2011), which could make the parameter estimation impossible. There are also large variations of parameter values among different experimental measurement. Individual parameters can be well constrained or poorly constrained in the prediction of their values. Some parameters have no large effects on model outputs although with large perturbations of their values. The dependence of model outputs on inputs can be quantified as parameter sensitivities. Gutenkunst et al. (2007) showed that the parameter sensitivity are evenly distributed over many decades of parameter space in systems biology, which results in multi-parameter fitting problems for these models.

SA can validate if the model reproduces experimental observation or not (Saltelli et al., 2000), and the key parameters which produce large output variation can be identified (Beres and Hawkins, 2001). SA on cardiac models can be helpful to answer the following type of questions:

- Do the cardiac models resemble the cardiac cell system?

- Which parameters exert a significant influence on action potential characters?

- Does the covariation of parameters have a large effects on model outputs, i.e. are there large parameter interactions (Gutenkunst et al., 2007)?

Sensitivity analysis (SA) quantifies how sensitive the model outputs are with respect to the variation of model inputs. In the SA literature, there are local SA and global SA. Local SA assesses the contribution of parameters to outputs at a fixed set of parameter values. Typically, these parameter values are considered as points that fit optimally to experimental data. Global SA refers to an assessment of the contribution of parameters over the entire input space of parameters.

SA has been widely applied in many fields of systems biology. Zheng and Rundell (2006) used both local SA and global SA to test signalling pathway. Their results identified critical reactions and their impact on signal dynamics. In addition, SA also been applied to test multi-scale model of blood glucose homeostasis to understand biological systems at the tissue level (Sumner, 2010). In cardiology, local sensitivity analysis is developed and used for the parameter identification of cardiac models (Sher et al., 2013). This local method is used to identify non-significant and redundant parameters in L-type Ca^{2+} channel and rapid inward rectifier K^+ channel. Kharche et al. (2009) performed a global SA on several cardiac models to demonstrate the influence of ion channels and ion concentrations on action potentials. Their work revealed a common set of parameters influencing action potentials among the models.

In this chapter, we start with local SA to elucidate the roles of cardiac model parameters in published parameter values. Three single cell SAN models are tested by local SA and the results are compared with experimental observations of SAN cells.

3.1.1 systems biology Model and Local Sensitivity Index

There are two types of sensitivity analysis: local and global. They are used to evaluate the effects of inputs on outputs at a local and global level respectively. Local sensitivity analysis can be represented by the first-order partial derivatives of outputs with respect to inputs. Systems biology models are generally described by ODE in the following way.

$$\frac{\mathrm{d}y_i}{\mathrm{d}t} = f_i(y, k), \mathbf{y}(0) = \mathbf{y}^0, \tag{3.1}$$

where i = 1, 2, ..., n. $\mathbf{y}$ is a vector of state variables, $\mathbf{k}$ are the input parameters and $\mathbf{y}^0$ are the initial values of state variables. $y_i(t, \mathbf{k} + \Delta\mathbf{k})$ is the solution with respect to a small parameter perturbation and this solution can be expressed by a Taylor series as

Equation 3.2

$$y_i(t, \mathbf{k} + \Delta\mathbf{k}) = y_i(t, \mathbf{k}) + \sum_{j=1}^{m} \frac{\partial y_i}{\partial k_j}\Delta k_j + \frac{1}{2}\sum_{j=1}^{m}\sum_{l=1}^{m} \frac{\partial^2 y_i}{\partial k_l}\partial k_j \Delta k_j \Delta k_l + \dots \tag{3.2}$$

In Equation 3.2, the difference between $y_i(t, \mathbf{k} + \Delta\mathbf{k})$ and $y_i(t, \mathbf{k})$ is described by the partial differential equation of the right side. The derivative $\partial y_i / \partial k_j$ is known as the first-order local sensitivity coefficient. The sensitivity index $S_{i,j}$ is defined as the following;

$$\mathrm{S_{i,j}(t)} = \frac{\partial y_i}{\partial k_j} \tag{3.3}$$

The sensitivity coefficient $S_{i,j}$ shows the effect of the parameter k_j on the value of y_i at time t around the nominal value $\mathbf{k}$.

3.1.2 Finite Difference Approximation

The simplest way of calculating the local sensitivity index is the finite difference approximation. This is called a brute force method or indirect method. The finite difference approximation calculates the first-order local sensitivity coefficients at a given time t as follows.

$$\mathrm{S_{i,j}(t)} = \frac{\partial y_i}{\partial k_j} = \lim_{\Delta k_j \to 0} \frac{y(t, k_j + \Delta k_j) - y_i(t, k_j)}{\Delta k_j} \tag{3.4}$$

$$\simeq \frac{\Delta y_i}{\Delta k_j} = \frac{y_i(t, k_j + \Delta k_j) - y_i(t, k_j)}{\Delta k_j}, \tag{3.5}$$

This method approximates $\mathrm{S_{i,j}(t)}$, the effect of j_{th} input k_j on i_{th} output y_i. The input k_j is perturbed with an interval $k_j + \Delta k_j$ while the other inputs are held at the nominal values $\mathbf{k}$. The output difference $y_i(t, k_j + \Delta k_j) - y_i(t, k_j)$ is obtained by solving the function with perturbed inputs. The sensitivity coefficient is obtained from a forward difference approximation.

This approximation assumes a local linearity at the nominal values $\mathbf{k}$, and the perturbation size Δk_j should be small enough to hold the linearity. If the perturbation size is not small enough, the partial differential equation cannot be approximated well. Finding the perturbation size is a trial and error process (Saltelli et al., 2000). De Pauw and Vanrolleghem (2003) discussed the influence of perturbation size on the sensitivity index calculation. They found that the optimum step size relevant to both variable and parameter and the optimal perturbation size could not be generalised easily. They also found that the integrator accuracy has a great impact on the sensitivity index value and the optimal perturbation size. The integrator accuracy of numerical integration is greatly affected by ODE solvers and their step sizes. The integrator should be accurate enough to capture the small output difference due at a given perturbation size. Oth-

erwise, the local sensitivity index based on the output difference is inaccurate. We also observed the same problems in the analysis of cardiac models. A discussion of the integrator accuracy and perturbation size is presented later in this chapter.

Despite the drawbacks, finite difference approximation is frequently used for model analysis. Newham et al. (2003) assessed a landscape-based sediment source and transport model by the finite difference approximation. The most important parameters of the model are identified and suggestions for its modification are presented to effectively represent observations. Degenring et al. (2004) applied the finite difference approximation to reduce complex metabolism models.

3.1.3 Direct Differential Method

Direct differential method is the another method to calculate the derivatives. This method was proposed by Dickinson and Gelinas (1976) to show the effects of parameters with respect to time. The method only considers a scalar input k and a n-dimensional output $\mathbf{y}$ according to Equation 3.1. The direct method computes the differential sensitivity coefficient S_i with respect to the model time t.

$$\frac{\partial S_i}{\partial t} = \frac{\partial}{\partial t}\left(\frac{\partial y_i}{\partial k}\right) = \frac{\partial}{\partial k}\left(\frac{\partial y_i}{\partial t}\right) = \frac{\partial f_i(y,k)}{\partial k} \tag{3.6}$$

Equation 3.6 can be expressed as the following according to chain rule.

$$\frac{\partial S_i}{\partial t} = \frac{\partial f_i}{\partial k} + \sum_{j=1}^{n} \frac{\partial f_i}{\partial y_i} \times \frac{\partial y_i}{\partial k} = \frac{\partial f_i}{\partial k} + \sum_{j=1}^{n} \frac{\partial f_i}{\partial y_i} \times S_j \tag{3.7}$$

The equation can be further presented as a equation with Jacobian matrix ($\mathbf{J}$) as the following form.

$$\dot{S} = \begin{bmatrix} \frac{\partial S_1}{\partial t} \\ \frac{\partial S_2}{\partial t} \\ \cdots \\ \frac{\partial S_n}{\partial t} \end{bmatrix} = \begin{bmatrix} \frac{\partial f_1}{\partial k} \\ \frac{\partial f_2}{\partial k} \\ \cdots \\ \frac{\partial f_n}{\partial k} \end{bmatrix} + \begin{bmatrix} \frac{\partial f_1}{\partial y_1} & \frac{\partial f_1}{\partial y_2} & \cdots & \frac{\partial f_1}{\partial y_n} \\ \frac{\partial f_2}{\partial y_1} & \frac{\partial f_2}{\partial y_2} & \cdots & \frac{\partial f_2}{\partial y_n} \\ \frac{\partial f_3}{\partial y_1} & \frac{\partial f_3}{\partial y_2} & \cdots & \frac{\partial f_3}{\partial y_n} \\ \frac{\partial f_4}{\partial y_1} & \frac{\partial f_4}{\partial y_2} & \cdots & \frac{\partial f_4}{\partial y_n} \end{bmatrix} = \mathbf{f}_p + \mathbf{J} \times \mathbf{S} \tag{3.8}$$

where the matrixes $\mathbf{f}_p$, $\mathbf{J}$ and $\mathbf{S}$ are defined as follows:

$$\mathbf{f}_p = \begin{bmatrix} \frac{\partial f_1}{\partial k} \\ \frac{\partial f_2}{\partial k} \\ \cdots \\ \frac{\partial f_n}{\partial k} \end{bmatrix} \tag{3.9}$$

$$\mathbf{J} = \begin{bmatrix} \frac{\partial f_1}{\partial y_1} & \frac{\partial f_1}{\partial y_2} & \cdots & \frac{\partial f_1}{\partial y_n} \\ \frac{\partial f_2}{\partial y_1} & \frac{\partial f_2}{\partial y_2} & \cdots & \frac{\partial f_2}{\partial y_n} \\ \frac{\partial f_3}{\partial y_1} & \frac{\partial f_3}{\partial y_2} & \cdots & \frac{\partial f_3}{\partial y_n} \\ \frac{\partial f_4}{\partial y_1} & \frac{\partial f_4}{\partial y_2} & \cdots & \frac{\partial f_4}{\partial y_n} \end{bmatrix} \tag{3.10}$$

$$\mathbf{S} = \begin{bmatrix} S_1 \\ S_2 \\ \cdots \\ S_n \end{bmatrix} = \begin{bmatrix} \frac{\partial y_1}{\partial k} \\ \frac{\partial y_2}{\partial k} \\ \cdots \\ \frac{\partial y_n}{\partial k} \end{bmatrix} \tag{3.11}$$

The direct differential method avoids the difficulty of selecting perturbation size Δk. The method must solve the Jacobian matrix of the system given by Equation 3.1, so this method requires the solution of Equation 3.1. Several approaches were proposed to solve the equation (Valko and Vajda, 1984), (Dickinson and Gelinas, 1976), (Atherton et al., 1975). The direct method has been frequently applied to systems biology. Yue et al. (2006) performed the direct method to analyse a model of IκB-NF-κB, a signal pathway between NF-κB protein and IκB kinase. This cell communication regulates a range of cell responses including immune and inflammatory reactions. The results show that the interactions from certain pairs of parameters have a large effects on NF-κB oscillations. Liu et al. (2005) used the direct method to identify significant contributors of a network of biochemical reactions. Their work quantitatively revealed the dependence of kinase concentration on individual reaction rate constants and identified the important feature regulating signal output.

3.1.4 Feature Based Sensitivity Analysis

The direct differential method and finite difference approximation discussed above are the sensitivity analysis at a given time point. For cardiac models, it is more likely to use features of an action potential instead of potential values at specific time points as discussed in Chapter 2.

The application of sensitivity analysis is very model specific, so the features can be considered the sensitivity analysis targets. (Frenklach, 1984) suggested that the indirect method could be easily applied to calculate features sensitivity indices. Several studies of systems biology have used features to perform sensitivity analysis (Hetherington et al., 2007) (Ihekwaba et al., 2004).

For the case of SAN models, the variation of ion channel conductances can influence the cycle length of the action potential. Hence, the potentials at a given time point

may locate at different stages of the action potential. The shift of the location can generate a great error in the results. The feature based sensitivity analysis can avoid this problem. It is suggested that in many cases the sensitivity of model features is more interested rather than the sensitivity at a given time (Saltelli et al., 2000). Feature based sensitivities can be easily calculated by the indirect method. The implementation details of the feature based local method are presented in the next section. The feature based sensitivity analysis were implemented on several cardiac models, and the results suggest that feature based sensitivity analysis is a platform for the evaluation among different type cardiac models (Kharche et al., 2009).

3.2 Local Sensitivity Analysis of Cardiac model

The local sensitivity analysis applied here is comprised of feature-based analysis. It is implemented by using an indirect local method. The model we consider here is $y = f(\mathbf{k})$, where $\mathbf{x} = (k_1, \ldots k_n)$ is an n-dimensional input and y is a scalar output. The y is a feature of action potentials which are obtained from solving ODE by using MATLAB function $ODE23$. The inputs $\mathbf{k}$ is a vector which stands for parameters which are listed in the following section. The local sensitivity index can be shown as

$$\mathrm{S_i} = \frac{\partial y}{\partial k_i} = \lim_{\Delta k_i \to 0} \frac{y(k_i + \Delta k_i) - y(k_i)}{\Delta k_i} \tag{3.12}$$

$$\simeq \frac{\Delta y}{\Delta k_i} = \frac{y(k_i + \Delta k_i) - y(k_i)}{\Delta k_i}, \tag{3.13}$$

where $\mathrm{S_i}$ is the sensitivity index for input k_i. The method varies a input value one at a time with a perturbation size Δk_i while other inputs hold at the default values. The first order partial differential equation can be approximated by the forward finite difference. In most cases, it is difficult to have the analytical solution of the ODE cardiac biology models. The local sensitivity indices are approximated by finite difference approximation using Equation 3.13. The approximated sensitivity indices can be further normalised. A ratio of nominal values k_i and y is introduced shown as

$$\widehat{\mathrm{S_i}} = \frac{y(k_i + \Delta k_i) - y(k_i)}{\Delta k_i} \frac{k_i}{y} \tag{3.14}$$

$$= \frac{y(k_i + \Delta k_i) - y(k_i)}{y} \frac{k_i}{\Delta k_i} \tag{3.15}$$

This normalised index denotes relative change of y and k as $\Delta y/y$ and $\Delta k_i/k_i$ instead of absolute difference used in Equation 3.13. Both input and output are denoted by proportional change. Hence, the return sensitivity index is normalized and dimensionless. This index $(\Delta y/y)/(\Delta k_i/k_i)$ shows how far y deviated from a notional value with respect to deviation of k proportionally. This definition is widely used on the implementation of local sensitivity analysis. For example, the normalised index is used for assessment

for a landscape-based sediment source and transport model (Newham et al., 2003).

The accuracy of the indices is determined by the perturbation size Δk_i. The choice of Δk_i is selected by error and trail. The Δk_i is progressively reduced until the the value of local index is converged, under the condition that the ODE solver accuracy (Δt) is small enough to obtain the small variation of outputs with respect to a given Δk_i.

3.2.1 Selection of Input Parameters

Equation 2.3 shows the ion current I is proportional to g_{max} for given x and voltage difference (V_m E_{eq}). As x and V_m are variables, the current is only linearly regulated by g_{max}. Hence, g_{max} is considered as the target parameters (or input parameters) for the local sensitivity analysis. The roles of ion currents can be quantified by the analysis of g_{max}.

Table 3.2.1 shows the input parameters of the four models. In the table, $k_{Na,Ca}$ is a scaling factor of the Na^+ and Ca^{2+} exchanger. The role played by $k_{Na,Ca}$ is equivalent to ion channel conductance so $k_{Na,Ca}$ is considered in the sensitivity tests. The local and global sensitivity test are performed on these inputs.

Parameter	Ion Current	Model
g_{Na}	Na^+ current	B
$g_{Ca,L}$	L type of Ca^{2+} current	A, B, C
$g_{Ca,T}$	T type of Na^+ current	A, B, C
g_{to}	Transient components of 4-AP- sensitive current	A, B, C
g_{sus}	Sustained components of 4-AP- sensitive current	A, B, C
$g_{K,r}$	Conductance of rapid delayed rectifying K^+ current	A, B, C
$g_{K,s}$	Slow delayed rectifying K^+ current	A, B, C
$g_{h,Na}$	Na^+ component of hyperpolarization-activated current	A, B, C
$g_{h,K}$	K^+ component of hyperpolarization-activated current	A, B, C
g_{st}	Sustained current	C
$k_{Na,Ca}$	Scaling factor of Na^+ and Ca^{2+} exchanger current	A, B
$g_{b,Na}$	background Na^+ current	A, B, C
$g_{b,Ca}$	background Ca^+ current	A, B
$g_{b,K}$	background K^+ current	A, B
g_{Na_f}	fast Na^+ current	D
g_{Si}	slow inward current	D
g_K	Time dependent K^+ current	D
g_{K1}	Time independent K^+ current	D
g_{Kp}	Plateau K^+ current	D
g_b	Background current	D

TABLE 3.1: List of sensitivity test parameters involved in sensitivity analysis. The corresponding ion currents and models of the parameters are listed. A: Central SAN model (Zhang et al., 2000), B: Peripheral SAN model (Zhang et al., 2000), C: SAN model (Kurata et al., 2002), D: Ventricular cell model (Luo and Rudy, 1991).

The Kurata model and the Zhang central model address the central SAN cell activity with distinct ODE equation formulations; however, the different ion channel types and formulations of the two models describe the same central SAN pacemaking behaviour.

The sensitivity tests of the two models allow the comparison of SAN model with varying dynamics. The Zhang peripheral SAN has the same equation formulation but with different parameter values more specifically with different ion channel conductance values as discussed in Chapter 2 (Section 5).

3.2.2 Selection of perturbation size

The calculation of the local sensitivity indices requires the Selection of Δk_i. To obtain the best value of Δk_i, we select the response of output feature with respect to different perturbation sizes. We used MATLABs ODE23 function to integrate the differential equations, generating the action potentials with a duration of 4 seconds and a time interval Δ t = 0.0001 ms. We selected a small time interval to perform the sensitivity analysis as simulation accuracy could have large impact the local sensitivity analysis (De Pauw and Vanrolleghem, 2003). The Δ t must be small enough to make the feature values accurate at a small small Δk_i. The results are presented in Table 3.2, In the results, the action potentials contain as least three action potential pulses. The output features are measured from the last action potential pulse.

TABLE 3.2: Local sensitivity indices with respect to various perturbation sizes. The Kurata SAN model (Kurata et al., 2002) is used to perform the test. The input $g_{Ca,L}$ is perturbed with several perturbation sizes Δk_i, each perturbed input is assigned to ODE model solver for outputs while the other inputs are fixed. The local sensitivity index is the calculated by the given input and return output. Thus, one local sensitivity index is only related to one perturbed parameter and the corresponding one ODE simulation. A greater the sensitivity index is, the more critical parameter is for the model. $g_{Ca,L}$ is used to perform the test as $i_{Ca,L}$ is generally considered as a key current on determining SAN cell behaviour, which is shown by Table 4.6, Table 4.7 and Table 4.8. The chosen perturbation size are shown in grey color. The indices represent the ratio of relative difference between output and input as shown by Equation 3.14, therefore they are dimensionless.

Perturbation Size	CL	APO	MDP	APA	APD_{90}	$\frac{dv}{dt}_{max}$
$\Delta k_i = 10^{-3} k_i$	0.04	0.80	0.04	0.20	0.08	1.05
$\Delta k_i = 10^{-2} k_i$	0.05	0.79	0.02	0.19	0.04	1.05
$\Delta k_i = 10^{-1} k_i$	0.05	0.75	0.01	0.17	0.05	1.03
$\Delta k_i = 0.2 k_i$	0.04	0.80	0.04	0.20	0.08	1.05
$\Delta k_i =$ -0.2k_i	0.04	0.92	0.04	0.23	0.03	1.11
$\Delta k_i =$ -$10^{-1} k_i$	0.05	0.85	0.03	0.21	0.04	1.08
$\Delta k_i =$ -$10^{-2} k_i$	0.05	0.80	0.02	0.19	0.04	1.05
$\Delta k_i =$ -$10^{-3} k_i$	0.05	0.80	0.00	0.17	-0.12	1.05

The calculation of local sensitivity indices are based on Equation 3.15. The default parameter values (or inputs) are obtained from publications (Zhang et al., 2000) (Kurata et al., 2002). For examples, the input values of central and peripheral SAN models are given in Table A.3. For a given input k_i, we vary the input with a perturbation size Δk_i as $k_i(1 + \Delta k_i)$, while the other inputs are fixed. The varied input and the other inputs

TABLE 3.3: Local sensitivity indices of the Zhang central SAN model (Zhang et al., 2000) with respect to various perturbation sizes. The input $g_{Ca,L}$ is perturbed with several perturbation sizes Δk_i, each perturbed input is assigned to ODE model solver for outputs while the other inputs are fixed. The local sensitivity index is the calculated by the given input and return output. One local sensitivity index is only related to one perturbed parameter and the corresponding one ODE simulation. A greater the sensitivity index is, the more critical parameter is for the model. $g_{Ca,L}$ is used to perform the test, because $g_{Ca,L}$ is generally considered as the most important current to determine SAN cell behaviour. The chosen perturbation size are shown in grey color. The indices represent the ratio of relative difference between output and input as shown by Equation 3.14, therefore they are dimensionless.

Perturbation Size	CL	APO	MDP	APA	APD_{90}	$\frac{dv}{dt}_{max}$
$\Delta k_i = 10^{-3} k_i$	-0.19	1.47	0.12	0.56	-0.24	2.41
$\Delta k_i = 10^{-2} k_i$	-0.19	1.53	0.12	0.58	-0.23	2.48
$\Delta k_i = 10^{-1} k_i$	-0.13	2.36	0.18	0.80	-0.18	3.39
$\Delta k_i = 0.2 k_i$	0.91	-76.55	0.74	3.83	0.54	15.20
$\Delta k_i = -0.2 k_i$	-0.20	0.87	0.06	0.36	-0.24	1.57
$\Delta k_i = -10^{-1} k_i$	-0.21	1.09	0.08	0.44	-0.24	1.90
$\Delta k_i = -10^{-2} k_i$	-0.19	1.43	0.11	0.54	-0.24	2.35
$\Delta k_i = -10^{-3} k_i$	-0.19	1.48	0.12	0.56	-0.23	2.42

TABLE 3.4: Local sensitivity indices with respect to various perturbation size. The Zhang Peripheral SAN model is used to perform the test (Zhang et al., 2000). The input $g_{Ca,L}$ is perturbed with several perturbation sizes Δk_i, each perturbed input is assigned to ODE model solver for outputs while the other inputs are fixed. The local sensitivity index is the calculated by the given input and return output. Thus, one local sensitivity index is only related to one perturbed parameter and the corresponding one ODE simulation. A greater the sensitivity index is, the more critical parameter is for the model. The chosen perturbation size are shown in grey color. The indices represent the ratio of relative difference between output and input as shown by Equation 3.14, therefore they are dimensionless.

Perturbation Size	CL	APO	MDP	APA	APD_{90}	$\frac{dv}{dt}_{max}$
$\Delta k_i = 10^{-3} k_i$	0.21	1.31	0.12	0.35	0.23	1.40
$\Delta k_i = 10^{-2} k_i$	0.17	1.28	0.12	0.35	0.19	1.36
$\Delta k_i = 10^{-1} k_i$	0.16	1.08	0.10	0.31	0.19	1.19
$\Delta k_i = 0.2 k_i$	0.16	0.92	0.09	0.27	0.18	1.05
$\Delta k_i = -0.2 k_i$	0.16	0.92	0.09	0.27	0.18	1.05
$\Delta k_i = -10^{-1} k_i$	0.16	1.08	0.10	0.31	0.19	1.19
$\Delta k_i = -10^{-2} k_i$	0.17	1.28	0.12	0.35	0.19	1.36
$\Delta k_i = -10^{-3} k_i$	0.14	1.30	0.12	0.35	0.16	1.37

are assigned to ODE solver for outputs. There are six outputs in the test (CL, APO, MDP, APA, APD_{90} , $\frac{dv}{dt}_{max}$). For each output, the corresponding local sensitivity index of the given k_i calculated by Equation 3.15. In this chapter, the calculation of all local sensitivity indices follows the same procedure as we described here. The index values with respect to various perturbation sizes are shown in Table 3.3, Table 3.4 and Table 3.2 in grey.

In the three tables, the local sensitivity values are very close at a perturbation size of

10^{-1}k$_i$, 10^{-2}k$_i$ and 10^{-3}k$_i$. The accuracy of local sensitivity index is determined by the choice of perturbation size Δk_i. Equation 3.13 shows the theoretical value of the index is well approximated if Δk_i approaches 0. From a practical point of view, this cannot be achieved because the limited precision of the calculations (De Pauw and Vanrolleghem, 2003). De Pauw and Vanrolleghem (2003) took Δk_i as $10^{-3} \times k_i$. Table 3.2, Table 3.3 and Table 3.4 show that the local indices at a given $\Delta k_i = 10^{-2} \times k_i$ have a good agreement with the indices $\Delta k_i = 10^{-3} \times k_i$. In addition, Table 3.2 shows that the index value of ADP_{90} is not consistent with other indices when $\Delta k_i = -10^{-3} \times k_i$, because only the index polarity of ADP_{90} at $\Delta k_i = -10^{-3}$ is clearly inconsistent with the other ADP_{90} indices. Selecting $\Delta k_i = 10^{-2} \times k_i$ avoids this problem. This may be due to time interval Δ is fixed as 0.0001 ms which is not small enough to measure the output difference for $\Delta k_i = -10^{-3}$. Hence, we reject the results of $\Delta k_i = -10^{-3}$. $\Delta k_i = 10^{-2} \times k_i$ is considered as a reasonable perturbation size. The sign of a perturbation shows no large effects on the local index values as well. In the following content, we use $\Delta k_i = 10^{-2} \times k_i$ to perform sensitivity analysis on all the model inputs.

3.3 Results of Local Sensitivity Analysis

The results of the local sensitivity analysis are shown in Table 3.5. Table 3.5 (Model A) presents the index values for the Zhang central SAN model. The results show that $g_{Ca,L}$ and $g_{K,r}$ are relevant to the APO and APD_{90} variation. In addition, the effects of all the 13 parameters on the MDP and APA are all comparatively small, while dv/dt_{max} are very sensitive to $g_{Ca,L}$ and $g_{K,r}$.

In Table 3.5 (Model B), there is no input with a large contribution to the CL variance as all the local indices for CL are small. The local indices for MDP, APA, and APD_{90} are all comparatively small. There is no important determinant for APA, DDR, MDP and APD_{90}. $g_{Ca,L}$ variation greatly affects the value of dv/dt_{max}.

Table 3.5 (Model C) gives the local indices for the Kurata's model. The local test returns small value indices of CL, MDP, APA and APD_{90}. No large index values are observed for these outputs. $g_{Ca,L}$ has a great effect on APO with a local index value of 0.79, and dv/dt_{max} is largely determined by $g_{Ca,L}$ as well.

For the Zhang central SAN model and Kurata model, there is a agreement on the role of $g_{Ca,L}$ and $g_{K,r}$. The Zhang peripheral SAN model also has a good agreement on the role of $g_{Ca,L}$, but the role of $g_{K,r}$ in the peripheral model is distinct from the other two models. The results of local sensitivity analysis show that there is no common set of inputs on determining CL, APD_{90} and DDR. The indices for many features (e.g. CL, APD_{90} and MDP) are all comparatively small, which make the roles of ion channels difficult to identify.

TABLE 3.5: Local sensitivity indices for the three SAN models. Each input is perturbed with the perturbation sizes $\Delta k_i = -10^{-2}$, while the other inputs are fixed. The local sensitivity index is the calculated by the given input and return output. Thus, one local sensitivity index is only related to one perturbed parameter and the corresponding one ODE simulation. A greater the sensitivity index is, the more critical parameter is for the model. Model A: Zhang central SAN model. Model B: Zhang peripheral SAN model. Model C: Kurata model. The local index of each input (row) and output (column).

Input	CL	APO	MDP	APA	APD_{90}	$\frac{dv}{dt}_{max}$	DDR
Model A							
$g_{Ca,L}$	-0.19	1.43	0.11	0.54	-0.24	2.35	0.50
$g_{Ca,T}$	-0.16	-0.07	-0.10	-0.09	-0.15	-0.12	0.27
$g_{K,r}$	0.17	1.14	0.73	0.87	0.10	1.86	0.35
$g_{K,s}$	-0.06	-0.03	0.01	-0.01	-0.06	0.01	0.01
g_{to}	0.05	-0.18	0.02	-0.04	0.05	-0.23	-0.15
g_{sus}	-0.09	-0.19	-0.03	-0.08	-0.09	-0.08	-0.01
$g_{h,Na}$	-0.05	0.02	-0.02	0.00	-0.04	0.04	0.08
$g_{h,K}$	0.02	-0.03	0.00	-0.01	0.02	-0.05	-0.05
g_{NaCa}	-0.08	-0.21	-0.05	-0.10	-0.08	-0.19	-0.03
$g_{b,Na}$	-0.06	-0.31	-0.25	-0.27	-0.02	-0.62	0.00
$g_{b,Ca}$	-0.01	-0.08	-0.08	-0.08	0.00	-0.18	-0.02
$g_{b,K}$	-0.04	-0.08	0.01	-0.02	-0.05	-0.01	-0.03
g_{p}	0.00	0.00	0.00	0.00	0.00	0.00	0.00
Model B							
$g_{Ca,L}$	0.17	1.28	0.12	0.35	0.19	1.36	-0.01
$g_{Ca,T}$	-0.11	0.14	0.02	0.04	-0.11	0.16	0.19
$g_{K,r}$	0.02	-0.19	0.11	0.05	0.05	-0.19	-0.07
$g_{K,s}$	-0.01	0.00	0.00	0.00	-0.01	0.00	-0.01
g_{to}	0.06	-0.44	-0.03	-0.10	0.07	-0.26	-0.16
g_{sus}	-0.15	-0.40	-0.07	-0.13	-0.17	-0.13	0.02
$g_{h,Na}$	-0.19	0.08	-0.01	0.01	-0.19	0.07	0.37
$g_{h,K}$	0.04	-0.09	-0.01	-0.02	0.05	-0.09	-0.11
g_{NaCa}	-0.01	-0.02	-0.01	-0.01	-0.01	-0.02	-0.02
$g_{b,Na}$	-0.06	0.02	-0.04	-0.03	-0.06	0.00	0.04
$g_{b,Ca}$	-0.02	0.01	-0.01	-0.01	-0.02	0.00	0.01
$g_{b,K}$	0.00	-0.02	0.00	0.00	0.01	-0.02	-0.01
g_{p}	0.00	0.00	0.00	0.00	0.00	0.00	0.00
Model C							
$g_{Ca,L}$	0.05	0.79	0.02	0.19	0.04	1.05	-0.09
$g_{Ca,T}$	-0.17	-0.09	-0.02	-0.04	-0.19	-0.11	0.30
$g_{K,r}$	-0.18	0.05	0.41	0.33	-0.15	0.29	0.73
$g_{K,s}$	0.00	0.00	0.00	0.00	-0.01	0.00	0.01
g_{to}	0.02	-0.29	-0.01	-0.07	0.02	-0.10	-0.11
g_{sus}	-0.06	-0.19	-0.03	-0.07	-0.06	-0.06	0.02
$g_{h,Na}$	-0.15	-0.05	-0.01	-0.02	-0.14	-0.05	0.21
$g_{h,K}$	0.10	-0.02	0.00	0.00	0.11	-0.03	-0.20
g_{st}	-0.13	-0.07	-0.11	-0.10	-0.16	-0.11	0.15
$g_{b,Na}$	-0.09	-0.13	-0.28	-0.25	-0.04	-0.38	-0.50

3.4 Discussion

Among the three SAN models, the central SAN models (model A and model C) show that $I_{Ca,L}$ and $I_{K,r}$ have great effects on APO, dv/dt_{max} and APA. The peripheral SAN model (model B) also shows that $I_{Ca,L}$ largely contribute to APO and dv/dt_{max}. As shown by the absolute value of sensitivity index, there is no large contributor of the feature CL. Some experimental observation showed that SAN action potential amplitude is sensitive

to $I_{Ca,L}$. The block of $I_{Ca,L}$ by 2 μM nifedipine reduces the the action potential amplitude by 11.4% (from 87.5 mV to 77.5 mV).

However, the local sensitivity failed to show that $i_{Ca,L}$ plays a significant role on determining the CL. Previous experimental observation and simulation work all proved that action potential CL is sensitive to the block of $I_{Ca,L}$. Hagiwara et al. (1988a) reported a 5-15% increase of the cycle length when $I_{Ca,L}$ is blocked by 40 μM Ni^{2+} . Kodama et al. (1997) reported the 21% average rate increase by blocking $I_{Ca,L}$ with 2μM nifedipine in experiment . Model analysis of SA node (Kurata et al., 2008) suggests $I_{Ca,L}$ is the basal peacemaking ion channel. As shown in Table 3.5, there is no large contributor in determining the CL as all CL indices are comparatively small. This failure of local sensitivity analysis may be due to the small number of samples (in terms of the number of the combinations of parameter values) or the small perturbation size.

3.5 Limitation of Local Sensitivity Analysis

As shown in Table 3.2, Table 3.3 and Table 3.4, the converged local indices values can be achieved by a small perturbation size, but the results failed to capture certain experimental observation and simulation results. This demonstrates that the contributions of each input need to be measured accurately at a large number of samples. Marino et al. (2008) stated that true parameter values are often very uncertain in biological systems and local sensitivity analysis cannot test the system over a large range.

The values of maximum ion channel conductances used for local sensitivity indices are estimated values from biological data. The true values of the maximum ion channel conductances can never been known with certainty, which may demand the sensitivity analysis over the whole realistic operating range. In addition, the local sensitivity analysis only vary one parameter at a time while all other parameter are fixed, which fails to quantify the interactions of the parameters with one another (Sumner, 2010). In addition, Dresch et al. (2010) stated that the differential sensitivity (the local sensitivity) is largely dependent on the formulation of mathematical models. This results in model dependent sensitivity index values. This problem can be possibly solved by variance based global sensitivity analysis which offers model free sensitivity index. Hence, it is necessary to use global sensitivity analysis to perform the analysis. The use of global sensitivity analysis should satisfy the following conditions.

- Sensitivity indices are normalised and model independent.
- Sensitivity indices are based on a large number of samples in terms of parameter-value combinations.
- Complex ion channel interactions can be presented accurately over a large range of variation .

Chapter 4

Global Sensitivity Analysis

This chapter is devoted to global sensitivity techniques. Two global methods, the Fourier Amplitude Sensitivity Testing (FAST) and Sobol method, are applied to analyse the roles of ion channels in cardiac models. FAST is used to calculate the first order sensitivity index and the Sobol method is performed for higher order indices. We note that first order effects are the dominant contribution to the total effects index in SAN models. In a ventricular cell model, a strong interaction term is observed and quantified by second order sensitivity indices.

4.1 Global Sensitivity Analysis

As discussed in Section 3.5, the results of local sensitivity analysis suggest that a sensitivity test with a large number of model samples is required. The local sensitivity analysis described is an estimation of derivatives at fixed values of model parameters. However, the values of model parameters are derived from biological data. The true values of these parameters are never known with certainty. Biological model parameters may vary in a large range in different cells and environment (Zi, 2011). In cardiac models, the values of parameters may vary from largely among models. For example, the ion channel conductances of L-type Ca^{2+} current are 18.56 nS and 5.8 nS in the Kurata model and the Zhang central SAN model respectively. This suggests the the analysis should be performed over the possible range of parameters.

Global techniques have been applied in many fields of systems biology. Global sensitivity analysis started to be applied to biological models (Van Riel, 2006) to provide guidance for the design of model based experiments. Zheng and Rundell (2006) tested a singling pathway model based on several global sensitivity methods. Their results revealed critical reactions in singling pathways and provided insights into the regulatory mechanisms. Kim et al. (2010) applied global sensitivity analysis on a cell death model to estimate

the values of the most important parameters to fit experimental data. Variance-based sensitivity analysis is a form of global sensitivity analysis. The analysis decomposes the output variance into fractions which can be attributed to inputs or sets of inputs. The variance-based sensitivity index is defined with the decomposition variance. Dresch et al. (2010) applied a variance based global method to test gene expression models to determine the sensitivity of certain parameters.

In the global sensitivity analysis of cardiac models, (Kharche et al., 2009) performed global sensitivity analysis on several cardiac models (SAN models and excitable cardiac cell model) and suggested that a common set of parameter influencing action potentials exists among the them. Chang et al. (2015) used the Luo-Rudy ventricular model for global sensitivity analysis. They observed that ion channel interactions affect the dynamic property of ventricular cells. Guo et al. (2011) found a physical interaction between $i_{K,r}$ and $i_{K,s}$ in human ventricular myocyte cells. Their experimental results suggested that the interactions between $i_{K,r}$ and $i_{K,s}$ are the result of a macro-complex formed at the membrane. The use of a global method should help us quantify the interactions of ion channels, which allows us to understand their intrinsic coupling. If there are no interaction effects between ion channels, the cardiac models may need to be modified to model the physical interactions.

In this chapter, we present the global sensitivity analysis of several cardiac models to quantify the roles of ion channel in a normalised way and to analyse the effects of ion channel interactions. To do this we used variance-based methods. Variance-based methods partition the total output variance to the uncertainty of input parameters. The sensitivity index of variance based method is well defined by Sobol (Sobol, 1990). Sobol described a multi-variable models with certain assumptions can be expressed as a unique finite expansion of the the variables. Variance based sensitivity indices are defined as a fraction of variance over the total variance. The fraction of variance is an item of the finite expansion. Fourier amplitude sensitivity test (FAST) and the Sobol method are the two main approaches of variance based methods. Marino et al. (2008) stated that variance based approaches are key tools, because the variance based approaches can be more generally used for non-linear and non-monotonic models compared with other global approaches. However, the variance based approaches have one major drawback: computational cost. In this chapter, variance-based methods and their application on cardiac models are presented.

4.1.1 Correlation Ratios

Correlation ratio is a variance based global sensitivity analysis technique. This technique presents uncertainty by using probability distributions. The importance of an input is quantified by the conditional probability distribution of an output conditioned on the input. The conditional distribution of Y at a given input x can be expressed as (Saltelli

et al., 2000).

$$p_Y(y) = \int p_{Y|x}(y|x)p_X(x)dx. \tag{4.1}$$

The general analysis model is defined as

$$y = \mathrm{E}(Y|\mathbf{x}) + \varepsilon, \tag{4.2}$$

where y is a output with respect to a set of k input $\mathbf{x}$. ε is an error term with the assumption that $\mathrm{E}(\varepsilon) = 0$. The variance of Y can be expressed as

$$\mathrm{Var}(Y) = \mathrm{Var}_{\mathbf{x}}([\mathrm{E}(Y|\mathbf{x})]) + \mathrm{E}_{\mathbf{x}}(\mathrm{Var}[Y|\mathbf{x}]) \tag{4.3}$$

The two components on the right side of Equation 4.3 are the variance of the conditional expectation and an error part. The variance of the conditional expectation is a measurement of the effect of $\mathbf{x}$ on the $\mathrm{Var}(Y)$. If $\mathrm{Var}(Y)$ is matched by $\mathrm{Var}_{\mathbf{x}}([\mathrm{E}(Y|\mathbf{x})])$ at a given $\mathbf{x}$, the input set $\mathbf{x}$ is important. If $\mathrm{Var}(Y)$ is matched by the error part $\mathrm{E}_{\mathbf{x}}(\mathrm{Var}[Y|\mathbf{x}])$, the input set $\mathbf{x}$ is unrelated to $\mathrm{Var}(Y)$. The *correlation ratio* (McKay, 1995) is introduced to quantify the effect as

$$\eta^2 = \frac{\mathrm{Var}_{\mathbf{x}}([\mathrm{E}(Y|\mathbf{x})])}{\mathrm{Var}(Y)}. \tag{4.4}$$

This version of the correlation ratio is later found to coincide with Sobol sensitivity index. Saltelli et al. (1993) state that McKays correlation ratio is equivalent to Sobol/FAST first order indices. The Sobol method can further produce high order indices (second order and higher order). Hence, the correlation ratio is not implemented on cardiac models in this work.

4.1.2 ANOVA-like representation and Sobol Method

The Sobol method was published in Russian (Sobol, 1990) and in English (Sobol, 1993). This method aims to decompose the total output variance as a sum of variances which are related to input variables, or combinations thereof. This method is similar to the analysis of variance (ANOVA) technique, which partitions the variance into a different sources of variation. The classic ANOVA is based on a factorial experimental design which consists of two or more factors, and the experimental unit takes on all possible combinations of across all such factors (Winer et al., 1971). The Sobol method represents mathematical model variance in an ANOVA like way. If a mathematical model $y = f(\mathbf{x})$ satisfy the assumption that: 1). y is a scalar. 2). $x \in [0,1]^{\mathrm{n}}$, n input parameters in unit cube (unit cube refers to space [0, 1]), is a vector. 3). function $f(\mathbf{x})$ is square integrable over input space. The mathematical model $f(\mathbf{x})$ can be decomposed into summands of

increasing dimensionality as

$$f(\mathbf{X}) = f_0 + \sum_{i=1}^{k} f_i(X_i) + \sum_{i=1}^{k}\sum_{j=i+1}^{k} f_{ij}(X_i, X_j) + \cdots + f_{12\cdots k}(X_1, X_2, \cdots, X_k), \quad (4.5)$$

where f_i is a function of X_i, and f_{ij} is a function of X_i and X_j, and so forth. The input parameters are defined on the n-dimensional unit hypercube $\mathbf{R}^n$ (We define that R is the unit interval [0, 1]):

$$\mathbf{x} \in \mathbf{R}^n, \quad (4.6)$$

where $\mathbf{x}$: $0 \leq x_i \leq 1$ The equation decomposition of Equation 4.5 is unique, if

$$\int_0^1 f_{i_1 i_2 \cdots i_s}(x_1, x_2, \cdots, x_s) dx_{i_k} = 0, \text{for } k = i_1, \cdots, i_s, \quad (4.7)$$

$$f_0 = \int_{\mathbf{R}^n} f(\mathbf{x}) d\mathbf{x}, \quad (4.8)$$

Where f_0 is a constant and the integrals of every summand function must be zero over the hypercube space. Under the condition of Equation 4.7 and Equation 4.8. The any decomposed function in Equation 4.5 are orthogonal to any other decomposed function. The **orthogonal property** of any two decomposed functions can be shown as

$$\int_{0\ \mathbf{R}^n}^{1} f_{i_1 i_2 \cdots i_s}(x_1, x_2, \cdots, x_s) f_{i_1 i_2 \cdots i_t}(x_1, x_2, \cdots, x_t) = 0, \text{for} [i_1, \cdots, i_s] \neq [i_1, \cdots, i_t] \quad (4.9)$$

All the functions in Equation 4.5 can be obtained via integrals because of the orthogonal property.

$$f_i(X_i) = \int_0^1 \ldots \int_0^1 f(\mathbf{x}) d\mathbf{x}_{\sim \mathbf{i}} - f_0, \quad (4.10)$$

where the $d\mathbf{x}_{\sim \mathbf{i}}$ denotes that the integration is over all inputs except x_i. In the same way, the high order can be calculated by using the first order function from Equation 4.10 as

$$f_{i,j}(X_i, X_j) = \int_0^1 \ldots \int_0^1 f(\mathbf{x}) d\mathbf{x}_{\sim (\mathbf{i},\mathbf{j})} - f_i - f_j - f_0 \quad (4.11)$$

This decomposition can also be used for the variance. The total variance of $f(\mathbf{x})$ in the unit cube $\mathbf{R}^n$ is defined to be

$$\mathrm{D} = \int_{\mathbf{R}^n} f^2(\mathbf{x}) d\mathbf{x} - f_0^2 \quad (4.12)$$

The partial variance of function $f_{i_1,...,i_s}$ can be computed as

$$\mathrm{D_{i_1,...,i_s}} = \int_{\mathbf{R}^n} f^2_{i_1,...,i_s}(x_{i_1},...,x_{i_s})dx_{i_1}...dx_{i_s} \tag{4.13}$$

Equation 4.5 can be expressed as the decomposition of variance by squaring and integrating the $f(\mathbf{x})$ over $\mathbf{R}^n$.

$$\mathrm{D} = \sum_{i=1}^{n} \mathrm{D}_i + \sum_{1\le i<j\le n} \mathrm{D}_{i,j} + ... + \mathrm{D}_{1,2,...,n} \tag{4.14}$$

The Sobol sensitivity is defined as

$$\mathrm{S_{i_1,...,i_s}} = \frac{\mathrm{D_{i_1,...,i_s}}}{\mathrm{D}} \tag{4.15}$$

where $\mathrm{S_{i_1,...,i_s}}$ is the sensitivity index for a set input $[x_{i_1},...,x_{i_s}]$. For single input x_i, the sensitivity index should be expressed as $\mathrm{S_i}$ which is called the first order sensitivity index which measures the individual contribution of x_i. If the input $[x_{i_1},...,x_{i_s}]$ is a two dimensional vector such as $[x_i, x_j]$. The sensitivity index $\mathrm{S_{i,j}}$ is the second order sensitivity index which stands for the interaction effects of inputs x_i and x_j. For higher dimensional inputs, $\mathrm{S_{i_1,...,i_s}}$ represents the effects of all the inputs. If we scale the Equation 4.16 by 1/D, all the partial variance is presented as sensitivity indices, and the sum of these sensitivity indices is

$$1 = \sum_{i=1}^{n} \mathrm{S}_i + \sum_{1\le i<j\le n} \mathrm{S}_{i,j} + ... + \mathrm{S}_{1,2,...,n}. \tag{4.16}$$

Here, we use an example function $f(\mathbf{x})$ (obtained from Saltelli et al. (2008)) to illustrate Sobol decomposition.

$$f(\mathbf{x}) = f(x_1, x_2, x_3) = \sin x_1 + a \sin^2 x_2 + b x_3^4 \sin x_1, \tag{4.17}$$

The input probability density functions are assumed as $p_i(x_i) = \frac{1}{2\pi}$, when $-\pi < x_i < \pi$ for $i = 1, 2, 3$. The decomposition of the function is given as

$$f(\mathbf{x}) = f_0 + f_1 + f_2 + f_{12} + f_3 + f_{13} + f_{23} + f_{123}, \tag{4.18}$$

Thus,

$$f_0 = \int\int\int f(x_1, x_2, x_3) p_1(x_1) p_2(x_2) p_3(x_3) dx_1 dx_2 dx_3 = \frac{a}{2}, \tag{4.19}$$

$$f_1 = \int\int f(x_1, x_2, x_3) p_2(x_2) p_3(x_3) dx_2 dx_3 - f_0 = (1 + \frac{1}{5} b\pi^4) \sin(x_1), \tag{4.20}$$

$$f_2 = \int\int f(x_1, x_2, x_3) p_1(x_1) p_3(x_3) dx_1 dx_3 - f_0 = a \sin^2(x_2) - \frac{a}{2}, \tag{4.21}$$

$$f_3 = \int\int f(x_1, x_2, x_3) p_1(x_1) p_2(x_2) dx_1 dx_2 - f_0 = 0, \tag{4.22}$$

The term $f_{ij}(x_i, x_j)$ can be computed as

$$f_{12} = \int\int f(x_1, x_2, x_3) p_3 dx_3 - f_1 - f_2 - f_0 = 0, \tag{4.23}$$

$$f_{13} = \int\int f(x_1, x_2, x_3) p_2 dx_2 - f_1 - f_3 - f_0 = (b x_3^4 - \frac{1}{5} b\pi^4) \sin x_1, \tag{4.24}$$

$$f_{23} = \int\int f(x_1, x_2, x_3) p_1 dx_1 - f_2 - f_3 - f_0 = 0, \tag{4.25}$$

In addition, f_{123} can be obtained by difference

$$f_{123} = f(\mathbf{x}) - (f_0 + f_1 + f_2 + f_{12} + f_3 + f_{13} + f_{23}) = 0. \tag{4.26}$$

Now we can calculate the total variance of the function $f(\mathbf{x})$ according Equation 4.12.

$$D = \int\int\int (f(x_1, x_2, x_3) - f_0)^2 dx_1 dx_2 dx_3 \tag{4.27}$$

$$= \frac{1}{(2\pi)^3} \int\int\int (\sin x_1 + a \sin^2 x_2 + b x_3^4 \sin x_1 - \frac{a}{2})^2 dx_1 dx_2 dx_3 \tag{4.28}$$

$$= ... = \frac{1}{2} + \frac{a^2}{8} + \frac{b\pi^4}{5} + \frac{b^2\pi^8}{18}. \tag{4.29}$$

The first order partial variance D_1 can be obtained according to Equation 4.13

$$D_1 = \int (f(x_1)^2 dx_1 = \int [\sin(x1) + \frac{1}{5} b\pi^4 \sin(x_1)]^2 dx_1 = ... = \frac{1}{2} + \frac{b\pi^4}{5} + \frac{b^2\pi^8}{50} \tag{4.30}$$

The rest partial variances are calculated by the same way as

$$D_2 = \frac{a^2}{8} \tag{4.31}$$

$$D_3 = 0 \tag{4.32}$$

$$D_{1,2} = 0 \tag{4.33}$$

$$D_{1,3} = \frac{b^2\pi^4}{18} - \frac{b^2\pi^8}{50} \tag{4.34}$$

$$D_{2,3} = 0 \tag{4.35}$$

$$D_{1,2,3} = 0 \tag{4.36}$$

The sum of the partial variances is

$$D_1 + D_2 + D_3 + D_{1,2} + D_{1,3} + D_{2,3} + D_{1,2,3} = \frac{1}{2} + \frac{b\pi^4}{5} + \frac{b^2\pi^8}{50} + \frac{a^2}{8} + \frac{b^2\pi^8}{18} - \frac{b^2\pi^8}{50} \tag{4.37}$$

$$= \frac{1}{2} + \frac{a^2}{8} + \frac{b\pi^4}{5} + \frac{b^2\pi^8}{18}. \tag{4.38}$$

The sum of all partial variances in Equation 4.38 is equal to the variance in Equation 4.29, which satisfies the Sobol variance decomposition according to Equation 4.16, Hence, the sensitivity index can be expressed in a normalised form (of between 0 and 1). The example shows that the total variance D can be partitioned into partial variances related to individual inputs or their interactions. The sensitivity index based on the partial variances and total variance is a model independent as it shows the effects of parameters in terms of their variance.

4.1.3 Monte Carlo Simulation of Sobol Method

The Sobol's indices can be approximated using Monte Carlo simulation. The mean value of function $f(\mathbf{x})$ can be approximated using N_{sim} samples as follows:

$$\widehat{f_0} = \frac{1}{N_{sim}} \sum_{m=1}^{N_{sim}} f(\mathbf{x_m}). \tag{4.39}$$

The total variance in Equation 4.12 can be derived (Sobol, 1990) (Saltelli et al., 2000):

$$\widehat{D} = \frac{1}{N_{sim}} \sum_{m=1}^{N_{sim}} f^2(\mathbf{x_m}) - \widehat{f_0}^2, \tag{4.40}$$

To obtain the partial variance in Equation 4.13, two independent samples, $\mathbf{x}^1$ and $\mathbf{x}^2$, are generated. Let us consider the partial variance of a input x_i, the variance can be approximated as

$$\widehat{D_i} = \frac{1}{N_{sim}} \sum_{m=1}^{N_{sim}} f(\mathbf{x}^{(\mathbf{1})}_{(\sim\mathbf{i})\mathbf{m}}, \mathbf{x}^{(\mathbf{1})}_{(\mathbf{i})\mathbf{m}}) f(\mathbf{x}^{(\mathbf{2})}_{(\sim\mathbf{i})\mathbf{m}}, \mathbf{x}^{(\mathbf{1})}_{(\mathbf{i})\mathbf{m}}) - \widehat{f_0}^2 \tag{4.41}$$

where $\mathbf{x}_m$ is the m_{th} samples point. $\mathbf{x}_{(\sim i)m}$ is all the m_{th} sample points except the i_{th} input, which is $\mathbf{x}_{(\sim i)m} = (x_{1m}, x_{2m}, ..., x_{(i-1)m}, x_{(i+1)m}, ..., x_{nm})$. Sobol method calculates the partial variance of a set of inputs α, and $\mathbf{x} = [\alpha, \beta]$. Two independent samples, $\mathbf{x}^1 = [\alpha^1, \beta^1]$ and $\mathbf{x}^2 = [\alpha^2, \beta^2]$. A quasi-Monte Carlo estimation of D_α is shown as

$$\widehat{D}_\alpha = \frac{1}{N_{sim}} \sum_{m=1}^{N_{sim}} f(\alpha^1_m, \beta^1_m) f(\alpha^1_m, \beta^2_m) - \widehat{f_0}^2 \tag{4.42}$$

Where $\widehat{D}_\alpha$ is the estimated total variance of the input set α. Any individual variance component of D_α can be obtained by removing the other components. For example, for $\alpha = \{x_1, x_2\}$, the total variance is expressed as $\mathrm{D}_\alpha = \mathrm{D}_1 + \mathrm{D}_1 + \mathrm{D}_{1,2}$, where $\mathrm{D}_{1,2}$ is the second order interaction between x_1 and x_2. The second order variance $\mathrm{D}_{1,2}$ can be calculated using D_α, D_1 and D_2. The first order partial variances D_1 and D_2 are obtained from Equation 4.42.

The pseudocode of the Sobol algorithms is shown Algorithm 1. The algorithm shows the calculation of the subset α within the range $\mathbf{x_0} \pm 0.2\mathbf{x_0}$. If the input α is a scalar, The Sobol method returns a first order sensitivity index (return the index $\mathrm{S_i}$ when $\alpha = x_i$). For vector input α, the Sobol method returns the total index of the subset α which contains the first order indices and higher order indices. For example, when $\alpha = \{\mathrm{x_1}, \mathrm{x_2}\}$, the total index $\mathrm{S}_\alpha = \mathrm{S}_1 + \mathrm{S}_1 + \mathrm{S}_{1,2}$ as discussed before. $\mathrm{S}_{1,2}$ is obtained calculated using $\mathrm{S}_{1,2} = \mathrm{S}_\alpha$ - S_2 - S_1. Second order Sobol indices are calculated by this way in this work. The input $\mathbf{X_0}$ is the default ion channel conductances and N is the number of samples.

In the initialization, two n × N dimensional Sobol quasi-random sequences $\mathbf{X^1}$ and $\mathbf{X^2}$ with random shift $\varphi \sim \mu(0, 1)$ are generated. The Sobol sequences can be generated using the Matlab function *sobolset*. The algorithm draws two independent samples $\mathbf{X^1} = [\alpha^{(1)}, \beta^{(1)}]$ and $\mathbf{X^2} = [\alpha^{(2)}, \beta^{(2)}]$ from $K^n = [0, 1]^n$. The samples of $\mathbf{X^1}$, $\mathbf{X^2}$ are scaled to the parameters' true values $\mathrm{X}^{1*} = [\alpha^{(1*)}, \beta^{(2*)}]$ and $\mathrm{X}^{2*} = [\alpha^{(2*)}, \beta^{(2*)}]$. X^{1*} and X^{2*}, N × n dimensional matrixes, are the samples inputs. $\mathbf{y}$ is the outputs with respect to X^{1*}. The total variance D can be approximated with $\mathbf{y}$. $\mathbf{y}^\alpha$ is obtained by solving $\mathrm{y}^\alpha_\mathrm{m} = f(\alpha^{(1m*)}, \beta^{(2m*)})$, where m = 1,..., N. We can evaluate the partial variance D_α with two independent samples $\mathbf{y}^\alpha$ and $\mathbf{y}$. The sensitivity index for subset α is approximated as $\widehat{\mathrm{S}}_\alpha$. In the following section, an example is presented to explain the implementation of Algorithm 1.

4.1.4 A Toy Example of Sobol Analysis

Here we introduce a toy example of predatorprey model which is also know as Lotka-Volterra equations to illustrate the Sobol method. The equations of a case of predator-prey model are given as

$$\frac{\mathrm{d}y_1}{\mathrm{d}t} = \alpha y_1 - \beta y_1 y_2, \tag{4.43}$$

$$\frac{\mathrm{d}y_2}{\mathrm{d}t} = -\alpha y_1 + \beta y_1 y_2. \tag{4.44}$$

Where y_1 is the number of prey (e.g. rabbit) and y_2 is the number of predator (e.g. fox). α and β are parameters describing the growth and the interaction of the two species. The default values of α and β are 0.4 and 0.01 respectively. The state variables y_1

Algorithm 1 Sobol method

1: **Input**:
2: $\mathbf{X_0}$: default values of inputs, n×1 dimensional vector
3: N: Number of samples
4: ΔX: Perturbation range
5: **Initialize**:
6: Generate two independent Sobol sequences $\mathbf{X^1}$ and $\mathbf{X^2}$ // sequence dimension: n×N
7: $\mathbf{X^{1*}} = 0.4\mathbf{X_0}(\mathbf{X^1}) + 0.8\mathbf{X_0}$ // ΔX = 0.2
8: $\mathbf{X^{2*}} = 0.4\mathbf{X_0}(\mathbf{X^2}) + 0.8\mathbf{X_0}$
9: **FOR** m = 1,..., N
10: $\mathrm{y_m} = f(\mathbf{X^{1*}_{:,m}})$ // obtain outputs from ODE solver
11: $\widehat{\mathrm{f}}_0 = \mathrm{E}(\mathbf{y})$ // calculate the mean of outputs
12: $\mathbf{y} = \mathbf{y} - \widehat{\mathrm{f}}_0$ // normalised output value
13: $\widehat{\mathrm{D}} = 1/\mathrm{N}\sum_{m=1}^{\mathrm{N}} \mathrm{y_m}^2 - \widehat{\mathrm{f}}_0^2$ // calculate the total variance
14: **FOR** m = 1,..., N
15: $\mathrm{y}_\mathrm{m}^\alpha = f(\alpha^{(1m*)}, \beta^{(2m*)})$ // obtain outputs from ODE solver
16: $\widehat{\mathrm{D}}_\alpha = 1/\mathrm{N}\sum_{\mathrm{m}=1}^{\mathrm{N}} \mathrm{y_m y}_\mathrm{m}^\alpha - \widehat{\mathrm{f}}_0^2$ // calculate the partial variance
17: $\widehat{\mathrm{S}}_\alpha = \widehat{\mathrm{D}}_\alpha / \widehat{\mathrm{D}}$
18: **RETURN** $\widehat{\mathrm{S}}_\alpha$

and y_2 can be obtained by solving function $f(\alpha, \beta)$. In this example, the output y, the period of rabbit population, is measured from the state variable y_1 as shown by Figure 4.1. The global sensitivity analysis based on the inputs (α and β) and output y can explain how the parameters (input) impact the population of rabbit y. The input space

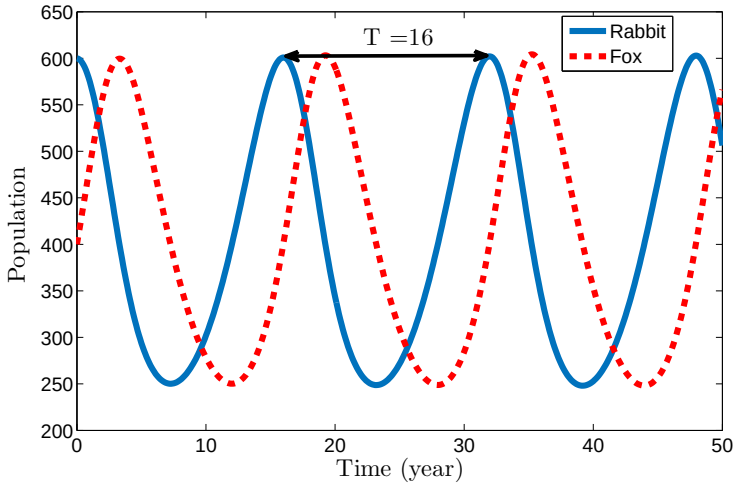

FIGURE 4.1: The population of predator and prey (fox and rabbit). The simulation are based on the inputs, α =0.4 and β = 0.01. The period of rabbit population is T = 16 which is the model output y, $y = f(0.4, 0.1) = 16$.

of the function $y = f(\mathbf{x})$ is $\mathbf{x} \pm 0.2\mathbf{x}$, i.e. $\alpha \in (0.32,\ 0.48)$ and $\beta \in (0.008,\ 0.012)$ as we choose the perturbation size $\Delta X = 0.2$ (line 7 of Algorithm 1). The input space is the ranges of parameters in which we are interested, and the results of the sensitivity

analysis are to explain the roles of parameter in the range. The samples of X^1 and X^2 are obtained from Sobol sequences, which is shown by Figure 4.2. The samples in

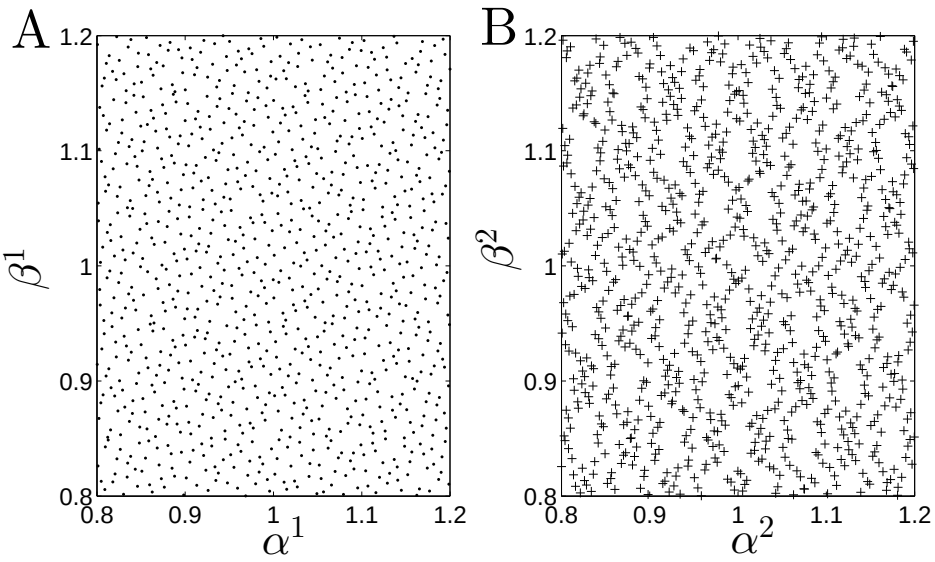

FIGURE 4.2: Two unscaled independent Sobol quasi-random sequences X^1 (Figure A) and X^2 (Figure B). The sampling of α and β is within 1 ± 0.2 (we assume $\Delta X = 0.2$). The 1000 samples are uniformly distributed over the input space. The implementation of the sampling is based on line 6 of Algorithm 1.

Figure 4.2 can be mapped to the true values of inputs as shown by Figure 4.3. The mapping of the samples is by scaling the sample value with the default values of 0.4 (for α) and 0.1 (for β) respectively. The scaled samples can be assigned to ODE solver

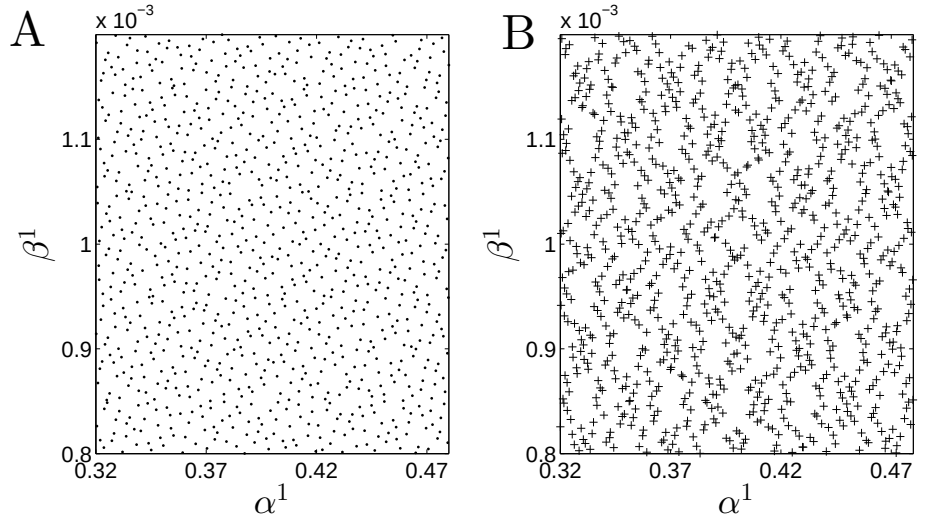

FIGURE 4.3: Two scaled independent Sobol quasi-random sequences X^{1*} (Figure A) and X^{2*} (Figure B). The sampling of α and β is within ±20 % perturbation of the default values. The X^1 (shown by Figure 4.2) are mapped to true parameter values. Any sample of X^1 is scaled by their default value 0.4 (for α) and 0.1 (for β) respectively. The implementation of the sampling is based on line 7 and 8 of Algorithm 1.

TABLE 4.1: The Sobol indices of the parameter α, β and their interaction. The test is based on 1000 sample points.

Input	α	β	interaction
Index	0.981	0.014	0.005

for corresponding outputs, which is presented by Figure 4.4. These returned outputs are used for variance decomposition. In Figure 4.4, the mean $\widehat{f}_0$ (the mean number of

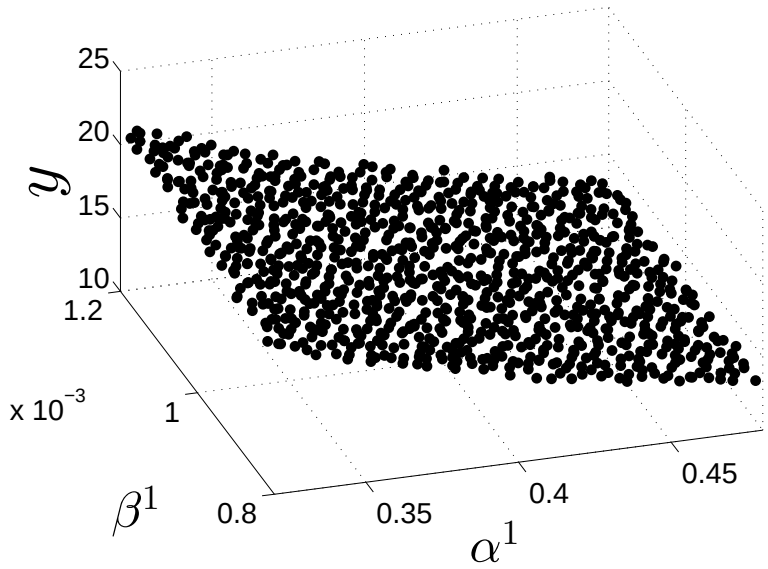

FIGURE 4.4: The output y with respect to the given inputs $\mathbf{x}\pm 0.2\mathbf{x}$ (line 10 of Algorithm 1). The scaled samples are assigned to ODE solver. The returned outputs of ODE solver are shown as y. This simulation results is based on 1000 samples points.

animals) of the 1000 samples is 16.32 animals by the calculation of line 11 of Algorithm 1. The corresponding variance is 4.46 animals (line 13 of Algorithm 1). The variance is a total variance contributed by both α and β. In the following content, the total variance can be attributed to each input by a partial variance. Therefore, the roles of inputs can be quantified. In order to quantify the partial variance D_α of input α, a new sequence X^{3*} is obtained from α^1 in X^{1*} and the β^2 in X^{2*}. Similarly, the new sequence X^{3*} is scaled by the default values which is explained in Figure 4.4. Figure 4.5 shows the scaled new sequence X^{3*}. By assigning the values of X^{3*} to ODE solver, the simulation results y_α is shown in Figure 4.6. In Figure 4.6, the variance of y_α is 4.37 (line 16 of Algorithm 1). By implementing Line 16 of Algorithm 1, the approximated Sobol index of the parameter α is given as $\widehat{\mathrm{S}}_\alpha = 4.37/4.46 \approx 0.98$ (line 17 of Algorithm 1). Similarly, we can also obtain the Sobol index of the parameter β. In addition, the interaction term $\widehat{\mathrm{S}}_{\alpha,\beta}$ can be calculated by using $\widehat{\mathrm{S}}_{\alpha,\beta} = 1 - \widehat{\mathrm{S}}_\alpha - \widehat{\mathrm{S}}_\beta = 0.005$. The sensitivity indices is shown as Table 4.1. The sensitivity indices are 0.981 and 0.014 for α and β respectively, which shows that α accounts for 98 % variance of the total variance and the effect of β and input interaction is very limited.

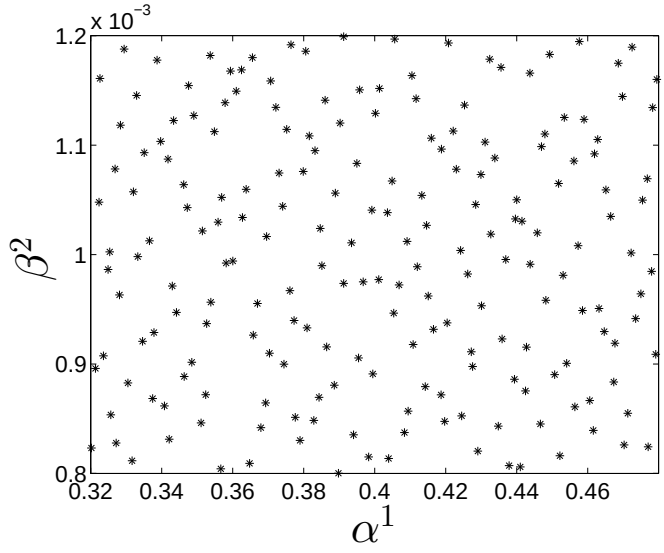

FIGURE 4.5: The samples of the sequence X^{3*} which is used to quantify the contribution of the parameter α. The implementation is $X^{3*} = [\alpha^1, \beta^2]$ (line 15 of Algorithm 1).

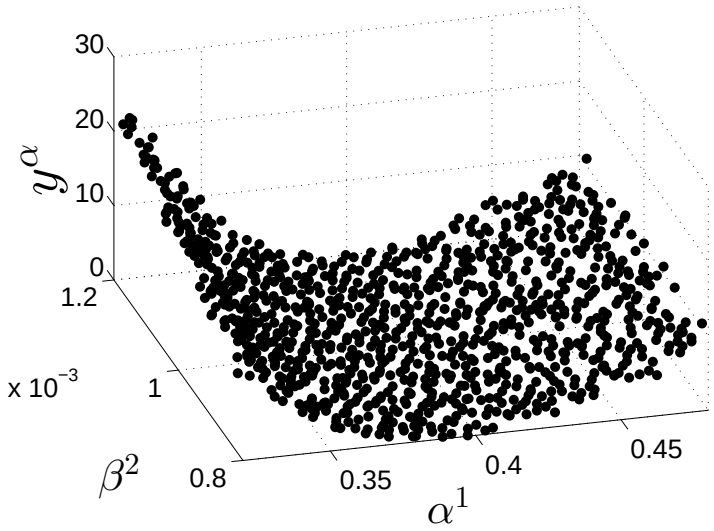

FIGURE 4.6: The simulation results y_α of the sequence X^{3*} obtained by solving ODE and measuring the period (line 15 of Algorithm 1). The variance of y_α is the partial variance contributed by α to the total variance.

4.2 Fourier Amplitude Sensitivity Test (FAST)

The FAST method is developed by (Cukier et al., 1973) to investigate the sensitivity of the large sets of nonlinear equations to uncertainties in inputs (or parameters). The basic idea of the method is that by relating model parameters to a set of frequencies, each parameter is varied at the given frequency simultaneously, the importance of a parameter can quantified by the Fourier coefficient of the given frequency.

FAST method considers a function $f(\mathbf{x})$ with the n-dimensional input $\mathbf{x}$, where $\mathbf{x} = [x_1, ..., x_n]$. The n-dimensional input $\mathbf{x}$ can be assigned to a set of frequency ω, where $\omega = [\omega_1, ..., \omega_n]$. The implement of the FAST approach is to relate an input x_i $(1 \leq i \leq n)$ to a corresponding frequency ω_i by introduce a one-dimensional variable s. The values of inputs are regulated by s, and all inputs are periodic functions of s.

This implement is based on ergodic theorem (Weyl, 1938) which states that if the entire n-dimensional input space is covered densely when s varies, the integrals over the n-dimensional space is equal to the integrals over the one-dimensional input space. By the application of the ergodic theorem, the n-dimensional Fourier coefficients of the function $f(\mathbf{x})$ can be projected into one-dimensional space of the function $f(\mathbf{s})$. The sensitivity indices are obtained from the one-dimensional Fourier coefficients. The effect of each input x_i is quantified by the Fourier coefficient A_{ω_i}. A large value of A_{ω_i} indicates a large influence of x_i. Conversely, a small value of A_{ω_i} indicates the small effect of x_i. The FAST index is defined by Fourier coefficients, and it has been proven that the FAST index is equivalent to the first order Sobol sensitivity index (Chan et al., 2000).

The function $f(\mathbf{x})$ with the n-dimensional input $\mathbf{x}$ can be expressed in Fourier series

$$f(\mathbf{x}) = \sum_{k_1=-\infty}^{\infty} \sum_{k_2=-\infty}^{\infty} ... \sum_{k_n=-\infty}^{\infty} C_{k_1,k_2,...,k_n} e^{j2\pi(k_1x_1+k_2x_2+...+k_nx_n)}, \tag{4.45}$$

The Fourier coefficients $C_{k_1,k_2,...,k_n}$ is a n-dimensional integer which is given as

$$C_{k_1,k_2,...,k_n} = \int_{I^n} f(\mathbf{x}) e^{j2\pi(k_1x_1+k_2x_2+...+k_nx_n)} d\mathbf{x}. \tag{4.46}$$

The n-dimensional inputs $\mathbf{x}$ can be projected into one-dimensional variable s. The function G_i for $i = 1, ...,$ n transform $\mathbf{x}$ into s, namely

$$x_i = G_i(\sin \omega_i s), \tag{4.47}$$

where ω_i is an assigned integer frequency for input x_i, and $s \in (-\pi, \pi)$. The function $f(\mathbf{x})$ can be expressed as

$$f(\mathbf{x}) = f(s) = f(G_1(\sin \omega_1 s), G_2(\sin \omega_2 s), ..., G_n(\sin \omega_n s)) \tag{4.48}$$

By using Parseval's theorem, the variance of function $f(s)$ can be given as

$$D^{\text{FAST}} = \frac{1}{2\pi}\int_{-\pi}^{\pi} f^2(s)ds - [E(f(s))]^2 \tag{4.49}$$

$$= \sum_{j=-\infty}^{\infty} (C_j^2) - (C_0^2) \tag{4.50}$$

$$= \sum_{j=-\infty}^{\infty} (A_j^2 + B_j^2) - (A_0^2 + B_0^2) \tag{4.51}$$

$$= 2\sum_{j=1}^{\infty}(A_j^2 + B_j^2), \tag{4.52}$$

where C_j is the Fourier coefficients in one-dimensional space, and A_j and B_j are the Fourier coefficients which are obtained as follows:

$$A_j = \frac{1}{2\pi}\int_{-\pi}^{\pi} f(s)\cos(js)ds, \tag{4.53}$$

$$B_j = \frac{1}{2\pi}\int_{-\pi}^{\pi} f(s)\sin(js)ds, \tag{4.54}$$

where j is the frequency for coefficients A_j and B_j which are relevant to ω_i assigned to each inputs. The Equation 4.53, Equation 4.54 and Equation 4.52 show that the variance D^{FAST} is related to the Fourier coefficients A_j and B_j, and the calculation of A_j and B_j involves ωi and G_i. The variance from input the x_i which is assigned with the frequency ω_i is measured as

$$D_{\omega_i}^{\text{FAST}} = 2\sum_{p=1}^{\infty}(A_{p\omega_i}^2 + B_{p\omega_i}^2). \tag{4.55}$$

D_{ω_i} denotes the variance contribution of input x_i. Equation 4.55 shows that the Fourier coefficients $A_{p\omega_i}$ and $B_{p\omega_i}$ are measured as the harmonic frequencies of ω_i. This requires that the harmonics of different inputs cannot be mixed. If not, $D_{\omega_i}^{\text{FAST}}$ is overestimated as the contribution of other parameters are measured at the same frequency. This require that any assigned frequencies of ω should be incommensurate. The FAST sensitivity index of the input x_i is defined as

$$S_i^{\text{FAST}} = \frac{D_{\omega_i}^{\text{FAST}}}{D^{\text{FAST}}}. \tag{4.56}$$

Equation 4.56 gives the definition of FAST sensitivity index which is a dimensionless ratio a partial variance $D_{\omega_i}^{\text{FAST}}$ and total variance D^{FAST}. $D_{\omega_i}^{\text{FAST}}$ is the variance contributed by input x_i. The total variance, D^{FAST} is the variance from all inputs and their interactions. As the calculation of $D_{\omega_i}^{\text{FAST}}$ requires an infinite number of harmonics of ω_i, it is computationally impossible. The index S_i^{FAST} can be approximated by a finite

number of harmonics, which is discussed in the following section.

4.2.1 FAST Sampling

The FAST method uses the ergodic theorem to convert the n-dimensional Fourier coefficient integral into a one-dimensional integral using the transform function $G_i(s)$. However, the ergodic theorem requires that the n-dimensional input space is covered densely when the s varies. Hence, the transform function should provide uniformly distributed samples for inputs in the n-dimensional input space as s varies in one-dimensional space.

Various transformation functions have been proposed to sample the n-dimensional input space. These functions are given in Table 4.2. Each function oscillates over a range of 0 and 1. The transfer function was first proposed by Cukier et al. (1973), which does not satisfy the requirement that samples should be uniformly distributed. Saltelli et al. (1999) suggested two new functions (function C and D in Table 4.2) to achieve a better distribution. Based on function C, function D introduce a random shift φ_i which applies a random starting point for sampling, as illustrated by Figure 4.8. The corresponding

TABLE 4.2: FAST transformation functions

No.	**transformation functions G_i**	**Reference**
A	$x_i = \overline{x_i}\exp\left(\overline{v_i}\sin(\omega_i s)\right)$	(Cukier et al., 1973)
B	$x_i = \overline{x_i}(1 + \overline{v_i}\sin(\omega_i s))$	(Koda et al., 1979)
C	$x_i = \frac{1}{2} + \frac{1}{\pi}\arcsin(\sin(\omega_i s)))$	(Saltelli et al., 1999)
D	$x_i = \frac{1}{2} + \frac{1}{\pi}\arcsin(\sin(\omega_i s + \varphi_i)))$	(Saltelli et al., 1999)

waveforms and histograms of the transformation functions are listed in Figure 4.7. Figure 4.7 (a) shows an example of the transformation function A with $\overline{x_i} = \exp(-5)$, $\overline{v_i} = 5$ and $\omega = 11$. Figure 4.7 (b) shows the transformation function B with $\overline{x_i} = 1/2$, $v_i = 1$ and $\omega = 11$. Figure 4.7 (c) shows the function C with $\omega = 11$. All the examples are implemented with 1000 samples. As can be seen, the sample points in Figure 4.7 (d) is more uniformly distributed than the samples of Figure 4.7 (a), (b) and (c). According to the ergodic theorem, the transformation function D (used in Figure 4.7 (d)) in Table 4.2 has a better approximation of the Fourier integers than transformation function A, B and C. As shown in these figures, the transfer function D samples uniformly in the input space. This transfer function is introduced in an extended FAST (eFAST) method. The eFAST method is suggested by Zi (2011) as it provides a better transformation function. In our global sensitivity analysis of cardiac models, eFAST is used because of this advantage.

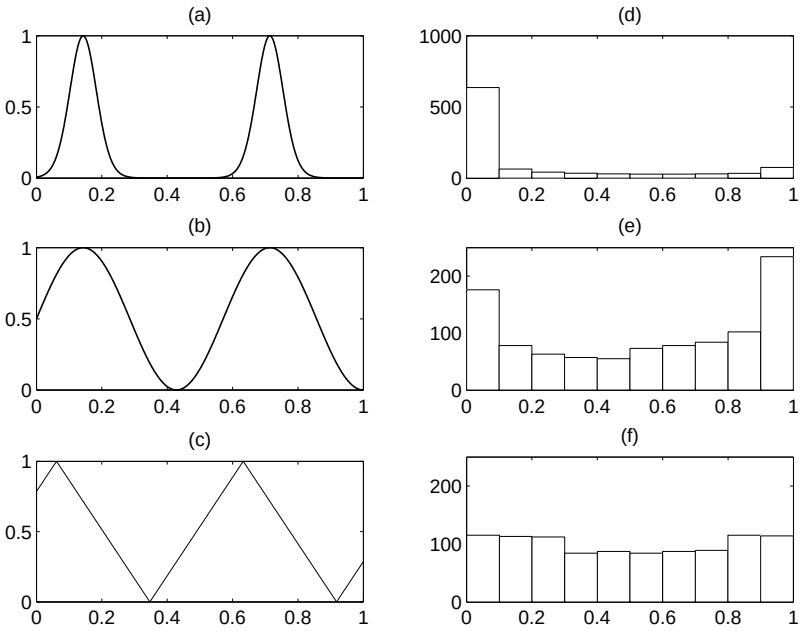

FIGURE 4.7: Waveforms and histograms of FAST transformation functions. Plots (a), (b) and (c) are the waveforms of the transformation function (A), (B) and (C) respectively. The corresponding histograms (1000 samples) of (a), (b) and (c) are given in plot (d), (e) and (f) respectively.

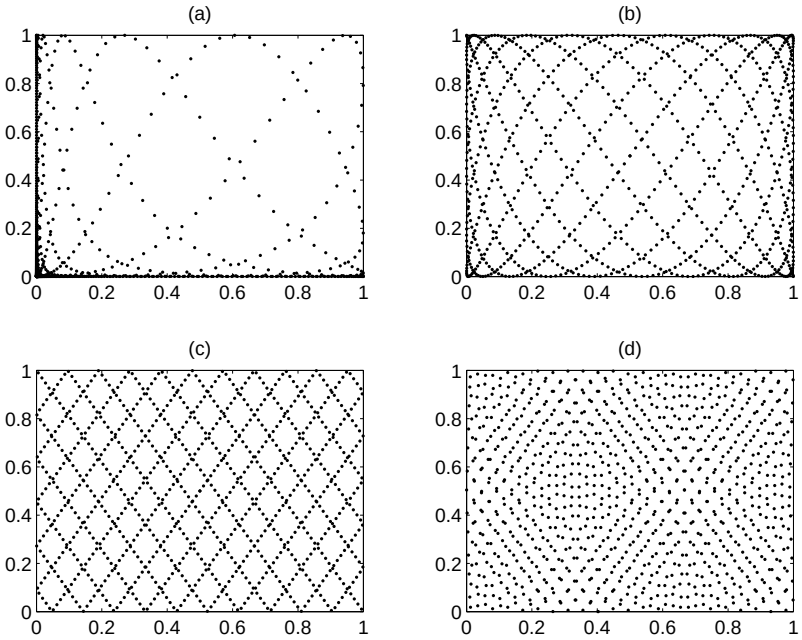

FIGURE 4.8: Scatter plot of transformation functions (1000 samples). Plots (a), (b), (c) and (d) are the waveforms of the transformation function (A), (B), (C) and (D) respectively

4.2.2 FAST Index

The FAST method calculates the first order sensitivity index by evaluating the Fourier coefficients A_j and B_j as shown in Equation 4.53 and Equation 4.53. The i_{th} input parameter is assigned with ω_i. The implementation of the FAST method requires the evaluation of A_j and B_j at the fundamental frequency ω_i and its harmonics. The corresponding variance is shown by Equation 4.55. Equation 4.55 considers an infinite number of harmonics, which is computationally impossible. Here, only a finite number of the harmonics are considered. The approximated variance $\hat{D}_{\omega_i^{FAST}}$ is given as

$$\hat{D}_{\omega_i^{FAST}} = 2\sum_{p=1}^{M}(A_{p\omega_i}^2 + B_{p\omega_i}^2), \tag{4.57}$$

where M is the maximum harmonic which is normally chosen to be 4 or 6 (Saltelli et al., 1999). The evaluation of the $\hat{D}_{\omega_i^{FAST}}$ requires a minimum sample size (or sample frequency) with respect to M and $\omega_{\max}$. According to the Nyquist sampling theorem, the sampling frequency should be at leat twice the highest frequency of the signal to avoid aliasing. The highest frequency contained in the output is $\omega_{\max}$. The harmonic considered is M which is chosen to be 4. Hence, the minimum sample size $\mathrm{N_s}$ is given as (Saltelli et al., 1999)

$$\mathrm{N_s} = 2\mathrm{M}\omega_{\max} + 1. \tag{4.58}$$

$\omega_{\max}$ is the maximum component of the n-dimensional vector ω. The minimum sample size is used to avoid aliasing. Aliasing is where the harmonics of D_i^{FAST} and $D_{\sim i}^{FAST}$ are mixed at a same frequency (assume the input of interest is x_i), which leads to the overestimation of D_i^{FAST}. In the following content, we are going to discuss the selection of the frequency.

4.2.3 Selection of frequency

As introduced, an input x_i varies with a corresponding assigned frequency ω_i, and any assigned frequencies of ω should be incommensurate. Let us assume that the input x_i is of interest, then the corresponding assigned frequency ω_i should be the highest among all frequencies. This is because the highest frequency and its harmonics can easily measured when the maximum harmonic of the second highest frequency is less than ω_i. The low frequencies of $\omega_{\sim i}$ are assigned to all the other $x_{\sim i}$. As we discussed above, the harmonics of theses frequencies can be mixed and lead to overestimation of the partial variance of interest. When we set the considered number of harmonics as M, the frequency range of the $x_{\sim i}$ is within [1 max$\{\omega_{\sim i}\}$], A algorithm is proposed to select

ω_i and $\omega_{\sim i}$ (Saltelli et al., 2000).

$$\max\{\omega_{\sim i}\} = \frac{\omega_i}{2M} \tag{4.59}$$

The selection of the complementary frequency sets is within the range [1 $\max\{\omega_{\sim i}\}$]. The following rules are given to select the sets:

- The step between two consecutive frequencies should be maximised
- The number of inputs with the same frequency should be minimised

TABLE 4.3: Sets of complementary frequencies obtained by automated algorithm. The table assume the number of factors is 8 and the interested one is factor X_4, ω_4 is the factor for X_4 (Saltelli et al., 2000).

N_s	**Frequency** ω_4	max $\{\omega_{\sim 4}\}$	$\{\omega_1, \omega_2, \omega_3, \omega_5, \omega_6, \omega_7, \omega_8\}$	Step size
65	8	1	{ 1, 1, 1, 1, 1, 1, 1}	0
129	16	2	{1, 2, 1, 1, 2, 1, 2}	1
257	32	4	{ 1, 2, 3, 1, 2, 3, 4}	1
513	64	8	{1, 2, 3, 5, 6, 7, 8}	1
1025	128	16	{1, 3, 5, 9, 11, 13, 15}	2
2049	256	32	{1, 5, 9, 17, 21, 25, 29}	4
4097	512	64	{ 1, 9, 17, 33, 41, 49, 57}	8
8193	1024	128	{1, 17, 33, 65, 81, 97, 113}	16

Table 4.3 shows examples of frequency selections for eight inputs. The complementary frequencies are given according to the sample size. The frequency of interest $\omega_{\max}$ is chosen according to Equation 4.58, then we can choose the $\max\{\omega_{\sim i}\}$ according to the number of inputs and the $\omega_{\max}$. The step size is then obtained from $\max\{\omega_{\sim i}\}$ and the number of inputs. For examples, if the N_s is given as 8193, then $\omega_{\max} = (N_s - 1)/8$ =1024, then $\max\{\omega_{\sim i}\}$ =$\omega_{\max}/2M$ = 1024/8 =128. The step size is given as 128/8=16. Finally, we obtain the complementary sets {1, 17, 33, 65, 81, 97, 113}. When we consider the eight number of inputs, the minimum sample size is 65 to implement the FAST method because $\omega_{\max}/2M$= 2M*max$\{\omega_{\sim i}\}$ when we set all other seven frequencies as 1.

4.2.4 Symmetry properties

The Fourier coefficients can be estimated by Equation 4.53 and Equation 4.54. The computational cost of the coefficients can be decreased by the use symmetry properties (Koda et al., 1979). The symmetry properties of the spectrum with 2π period can be helpful to reduce the number of evaluations of the model. The function $f(s)$ has a symmetric property at $s = \pm\pi/2$. From the periodic property of the distribution of the spectrum, the range (-π, π) contains all the information of the signal. We can restrict the

range to (-$\pi/2, \pi/2$). Hence, the number of model evaluations points are halved because of the symmetry property. The use of the search frequency set, $\{\omega_i\}$, is odd integer frequencies. In Koda's procedure (Koda et al., 1979), the sampling of function $f(s)$ is in the range (-$\pi/2, \pi/2$). The sampling points is $s_k = \pi/2(2k - N'_s - 1)/N'_s, \forall k = 1, 2, ..., N'_s$, where $N'_s = (N_s + 1)/2$. The expression for Fourier coefficients A_j and B_j are

$$A_j = \begin{cases} \frac{1}{N'_s}\{f(S_{N^o}) + \sum_{q=1}^{N_q}[f(S_{No+q}) + f(S_{No-q})] \times \cos(j\frac{\pi}{N'_s q})\} \text{ if } j \text{ even} \\ 0 \quad \text{if } j \text{ odd} \end{cases} \tag{4.60}$$

$$B_j = \begin{cases} 0 \quad \text{if } j \text{ even} \\ \frac{1}{N'_s}\{f(S_{N^o}) + \sum_{q=1}^{N_q}[f(S_{No+q}) + f(S_{No-q})] \times \cos(j\frac{\pi}{N'_s q})\} \text{ if } j \text{ odd} \end{cases} \tag{4.61}$$

where $N_q = (N'_s - 1)/2$ and $N_o = (N'_s + 1)/2$. S_{No} is the $\mathrm{N^o{}_{th}}$ number of samples of function $f(s)$ in unit hypercube [0, 1] as shown by Equation 4.47.

4.2.5 Implementation of FAST Method

The FAST algorithm implemented in our work is an extended FAST (eFAST) (Saltelli et al., 1999). The features of this method include better transformation function and re-samples curve. The transfer function of eFAST is shown in Table 4.2 and Figure 4.8. The re-sample curve is the repeated samples of the input space with different initial starting sample points. The eFAST algorithm re-samples the function $f(\mathbf{x})$ with a number of $\mathrm{N_r}$ times. This re-sample scheme is illustrated in Algorithm 2. In addition, eFAST introduces an index, total index $\mathrm{TS_i^{FAST}}$, to compute the overall effect of input $\mathrm{x_i}$. $\mathrm{TS_i^{FAST}}$ denotes the effects with all different orders of the input $\mathrm{x_i}$. $\mathrm{TS_i}$ is defined as

$$TS_i = 1 - \frac{D_{\sim i}^{\mathrm{FAST}}}{D^{\mathrm{FAST}}} \tag{4.62}$$

where $D_{\sim i}^{\mathrm{FAST}}$ is the measurement of all order effects which do not involve the input $\mathrm{x_i}$. $D_{\sim i}^{\mathrm{FAST}}$ is measured as

$$D_{\sim i}^{\mathrm{FAST}} = 2\sum_{p=i}^{M}(A_{p\omega_{\sim i}^2} + B_{p\omega_{\sim i}^2}) \tag{4.63}$$

$D_{\sim i}^{\mathrm{FAST}}$ measures all effects which do not involve the input $\mathrm{x_i}$, and $\mathrm{TS_i}$ shows the all order effects which involve the input $\mathrm{x_i}$. For many models, the first order effects are the main effects, and the interactions account for a very small fraction of output variance. In this case, the values of $\mathrm{TS_i^{FAST}}$ and $\mathrm{S_i^{FAST}}$ are very close.

The pseudocodes of the eFAST is given in Algorithm 2. Algorithm 2 shows how the eFAST algorithm calculates the FAST indices of the function $y = f(\mathbf{x})$ within the input

space $\mathbf{x^0} \pm 0.2\mathbf{x^0}$. In Algorithm 2, the input $\mathbf{X^0}$ are the ODE default ion channel conductances.

The eFAST algorithm samples the function $f(\mathbf{x})$ with $\mathrm{N_r}$ search curves. There are $\mathrm{N_s}$ samples of $f(\mathbf{x})$ on each curve. The total computational cost C to evaluate the function $y = f(\mathbf{x})$ is $\mathrm{C} = \mathrm{n}\times\mathrm{N_r}\times\mathrm{N_s}$. The eFAST algorithm returns the FAST index $\mathrm{S_i}$ which is the i_{th} parameter's contribution to the total variance of output y over the input space.

Initialization of the eFAST method generates an n dimensional frequency vector ω. The maximum frequency, $\omega_{\max}$, is assigned to the $\mathrm{i_{th}}$ parameter for quantification of the $\mathrm{i_{th}}$ input. The rest frequency components of ω are assigned to the other inputs in order. The values of vector ω and the sample size $\mathrm{N_s}$ are obtained from (Saltelli et al., 1999). The $\mathrm{n}\times\mathrm{N_r}\times\mathrm{N_s}$ dimensional samples $\mathbf{X}$ are generated over the unit hypercube, then the samples $\mathbf{X}$ are mapped to the true parameter values $\mathbf{X}^*$ with respect to $\mathbf{X^0}$. A set of action potential pulses can be generated by solving an ODE with the inputs $\mathrm{X^*_{i,r,j}}$, where $f(\mathrm{X^*_{i,r,j}})$ returns the output $\mathrm{Y}_{i,r,j}$ by measuring the last action potential pulse generated.

For $\mathrm{r_{th}}$ search curve, the first order variance $\widehat{\mathrm{D}}^{\mathrm{FAST}}_{\mathrm{i,r}}$ of the $\mathrm{i_{th}}$ parameter is obtained from the summation of the Fourier coefficients $\widehat{\mathrm{A}}_{\mathrm{p}\omega_{\mathrm{i}}}$ and $\widehat{\mathrm{B}}_{\mathrm{p}\omega_{\mathrm{i}}}$, ω_i is the fundamental frequency, $p\omega_i$ is harmonics when $4 \geq p \geq 2$, M indicates the number of harmonics considered, and M is taken to be 4. $E(Y)$ is the mean value of the $\mathrm{N_s}$ numbers of $Y_{i,r,j}$ at given r and j. $\widehat{\mathrm{D}}^{\mathrm{tot}}_{\mathrm{i,r}}$ is the totoal variance for the i_{th} input. The total variance in $\mathrm{r_{th}}$ search curve is given as $\mathrm{D}^{\mathrm{FAST}}_{\mathrm{r}}$. $\widehat{\mathrm{S}}_{\mathrm{i,r}}$ is the approximated sensitivity index for the $\mathrm{i_{th}}$ parameter in the $\mathrm{r_{th}}$ curve. $\bar{\mathrm{S}}^{\mathrm{FAST}}_{\mathrm{i}}$ is the average value over $\mathrm{N_r}$ curves. The algorithm output $\widehat{\mathbf{S}}$ is an n-dimensional vector of first order sensitivity indices.

The default setting of Algorithm 2 is based on Table 4.3. We select the number of sample $\mathrm{N_s} = 8192$ and the number of search curve $\mathrm{N_r} = 1$. According to Table 4.3, ω is given as {1, 17, 33, 65, 81, 97, 113, 1024} and the maximum frequency $\omega_{\max}$ is 1024. The number of harmonics M is selected as 4 and the perturbation size $\Delta\mathrm{X}$ =0.2. The inputs of the algorithm, X^0, are ion channel conductances, and the output Y is a matrix of SAN features obtained from ODE solver. In the following content, if the analysis setting is not claimed, the setting is based on the default setting. If it is claimed, please refer to Table 4.3 for details.

In the literature, the FAST method has been applied to analyse systems biology models, especially ODE based models. For example, Chu et al. (2007) applied the FAST method to a signal transduction pathway model. This work identified the key components of the model for determining signal transduction. Dresch et al. (2010) examined the construction of gene expression models by the eFAST method. Their results suggested that sensitivity analysis is helpful to determine how modeling results can be understood correctly. This is because some simulation results would be artifacts and the insight from sensitivity analysis can show the importance of model driven effects. Instead of the analysis single model, we apply the eFAST method to identify the general effects

Algorithm 2 eFAST method

Input:
  $\mathbf{X^0}$: default values of inputs, n×1 dimensional vector
  $\mathrm{N_r}$: Number of search curves
  ΔX: Perturbation range
Initialize:
  Generate a n×1 dimensional frequency vector ω
  $\mathrm{N_s} = (2\mathrm{M}\omega_{\max} + 1)\mathrm{N_r}$
  FOR r = 1,..., $\mathrm{N_r}$
    $\omega_i^* \leftarrow \omega_{\max}$ // Assign the maximum frequency to the target parameter
    $\omega_{\sim i}^* \leftarrow \omega_{\sim i}$ // Assign the complementary frequencies to the others
    $\mathrm{X}_{i,r,j} = 1/2 + 1/\pi \arcsin(\sin(\omega_i^* \mathrm{s_j} + \varphi))$, $\varphi \sim \mu(0, 2\pi), \mathbf{s} = 1, 2, \ldots, \mathrm{N_s}$
    $\mathrm{X}^*_{\mathrm{i,r,j}} = 0.4X_i^0 \mathrm{X_{i,r,j}} + 0.8X_i^0$ //Perturbation size $\Delta\mathrm{X} = 0.2$
    FOR j = 1,..., $\mathrm{N_s}$
      $\mathrm{Y}_{i,r,j} = f(\mathrm{X}^*_{\mathrm{i,r,j}})$ // obtain outputs from ODE solver
    $\widehat{\mathrm{D}}^{\mathrm{FAST}}_{\mathrm{i,r}} = 2\sum_{p=1}^{M} \widehat{\mathrm{A}}^2_{\mathrm{p}\omega_\mathrm{i}^*} + \widehat{\mathrm{B}}^2_{\mathrm{p}\omega_\mathrm{i}^*}$ // $\widehat{A}$ and $\widehat{B}$ obtained from Fourier transform of Y
    $\widehat{\mathrm{D}}^{\mathrm{tot}}_{\mathrm{i,r}} = 2\sum_{k=1}^{(\mathrm{N_s}-1)/2} \widehat{\mathrm{A}}^2_{\mathrm{k}} + \widehat{\mathrm{B}}^2_{\mathrm{k}}$
$\widehat{\mathrm{D}}_{\mathrm{i}} = 1/\mathrm{N_r} \sum_{\mathrm{r}=1}^{\mathrm{N_r}} \widehat{\mathrm{D}}_{\mathrm{i,r}}$
$\widehat{\mathrm{D}}^{\mathrm{tot}}_{\mathrm{i}} = 1/\mathrm{N_r} \sum_{\mathrm{r}=1}^{\mathrm{N_r}} \widehat{\mathrm{D}}_{\mathrm{i,r}}$
$\widehat{\mathrm{S}}^{\mathrm{FAST}}_{\mathrm{i}} = \widehat{\mathrm{D}}^{\mathrm{FAST}}_{\mathrm{i}} / \widehat{\mathrm{D}}^{\mathrm{tot}}_{\mathrm{i}}$
RETURN $\widehat{\mathrm{S}}^{\mathrm{FAST}}_{\mathrm{i}}$

on several cardiac models. This is because the variance-based method is independent of the model in question.

In the following sections, the global sensitivity methods are applied to cardiac models. Ion channel conductances are considered as the input parameters of the global methods as we discussed in Section 3.2.1.

4.3 Time Varying Global Sensitivity Analysis

The cardiac models produce action potentials which are time-dependent model outputs. The time based sensitivity analysis is a usual approach to calculate sensitivity indices (Sumner, 2010). The analysis is performed at each discrete time point, and the effects of inputs at each time point is evaluated. In the literature, many applications of global sensitivity analysis is time based (Sumner, 2010) (Chu et al., 2007) (Liu et al., 2005).

4.3.1 Sensitivity Analysis Results of A Peripheral SAN Model

We first implement the eFAST method on a cardiac model. Figure 4.9 shows time-based random samples of action potentials. Here, we select 200 samples to illustrate action potential phase shift. There are 200 action potentials with random input values in the

figure over the input space $\mathbf{X} \pm 0.2\mathbf{X}$. It is noticeable that there is a shift of action potential phases among these samples due to the different action potential durations. During the sharp depolarization of action potentials, the shift of the phase may increase the variance of the voltage considerably because the voltage values of 200 samples at a time point may be from different stages. The eFAST method relates output variance to parameters. The variance which cannot be attributed to any parameters are considered as the interaction of parameters. At a given time, the variance caused by the shift of action potential cannot be related to any parameter. The unrelated variance is calculated as interactions by eFAST method, which increases the total variance and increases the values of first order indices. Therefore, the returned eFAST index is inaccurate. In order to obtain accurate eFAST sensitivity index, the implementation of time varying analysis requires a small shift of action potential to keep the sensitivity index accurate, or a large interaction effect appears due to the phase shift. The Zhang peripheral SAN model is

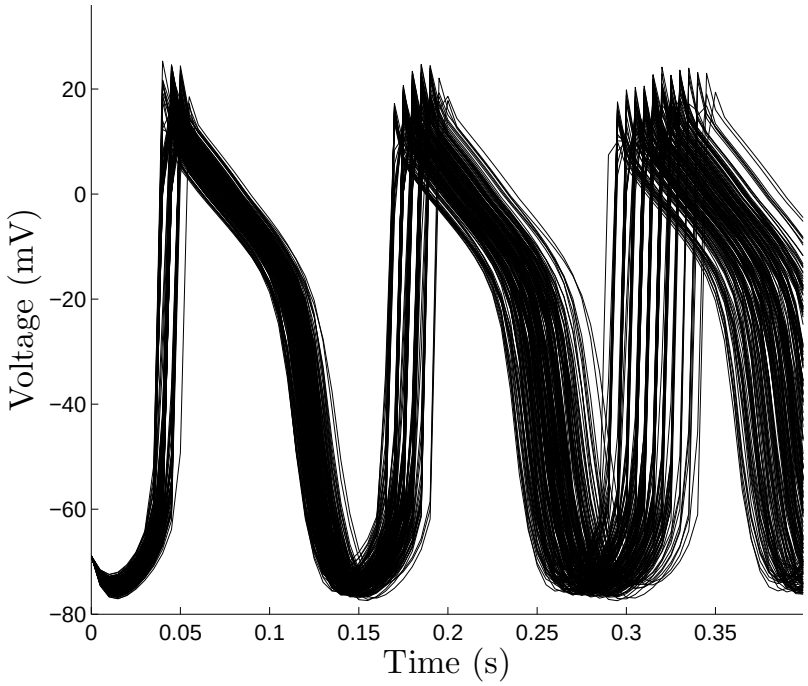

FIGURE 4.9: 200 samples of SAN peripheral action potentials. The Zhang peripheral SAN model is used to produce the samples (Zhang et al., 2000). The 200 outputs are respect to 200 random samples of inputs over the input space $\mathbf{X} \pm 0.2\mathbf{X}$.

considered to perform the eFAST sensitivity test because the period of the peripheral SAN action potential is small with respect to the other SAN models as shown in Chapter 2. We performed global sensitivity analysis on the first action potential pulses of these outputs within the space $\mathbf{X} \pm 0.2\mathbf{X}$. There are 8192 action potential outputs obtained by running ODE models. The potential values at time interval between 0 and 0.15 s with 0.0015 intervals (100 time points) are used to calculate eFAST indices. The eFAST indices obtained from these time points show the effects of inputs at specific time.

Figure 4.10 shows the first order sensitivity indices of individual ion conductances based on eFAST sensitivity analysis. The contributions of individual ionic channels at time points are presented. The main effects of g_{Na}, $g_{Ca,L}$, g_{to}, $g_{K,r}$ and $g_{b,Na}$ occur at different stages of the action potential. The main effects of $g_{K,r}$ and $g_{b,Na}$ take place at the stage of slow depolarization ($0.01 \sim 0.04$s). The contribution of $g_{K,r}$ dominates the slow depolarization stage. In the stage of rapid depolarization ($0.04 \sim 0.05$s), a large contribution from g_{Na} occurs while the contributions from the other five are small. $g_{Ca,L}$ and g_{to} largely contribute greatly to the re-polarization stage ($0.05 \sim 0.13$s). The variation effects of ion channel at different stages can be explained by the activation and de-activation of ion channels with respect to the membrane voltage. Individual contributions of the ion channels experience a considerable decrease near the peak of the action potential as interactions take places at these points. These interactions are further explained by Figure 4.10. Figure 4.10 only presents the five indices with largest

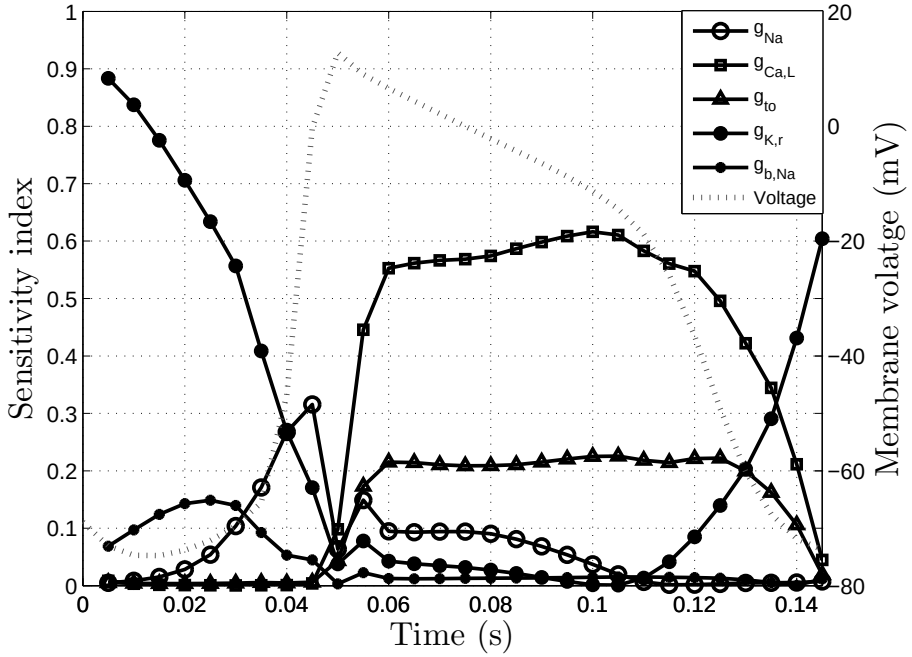

FIGURE 4.10: First order time varying eFAST indices (the five largest indices) of eFAST on peripheral SAN action potential. The number of samples N_s is 8192 and the other FAST implementation details are according to the default setting (shown in Section 4.2.5). The y-axis shows the dimensionless FAST sensitivity indices representing the parameter contributions to output (voltage (mV)) variance. The index is an estimate of the proportion of variance contributed by single input as shown by Equation 4.56. The x-axis is time in second.

value. The remaining seven parameters with comparative small values are presented in Figure 4.11 using a small scale. It is noticeable that the values of eFAST indices have a good correlation with absolute conductances. The five inputs with large sensitivity index values are g_{Na}, $g_{Ca,L}$, g_{to}, $g_{K,r}$ and $g_{b,Na}$. The five parameters with the largest values of conductance are $g_{Ca,L}$, g_{to}, $g_{K,r}$, $g_{K,s}$ and g_{sus}. The parameter values of the model are shown in the Appendix.

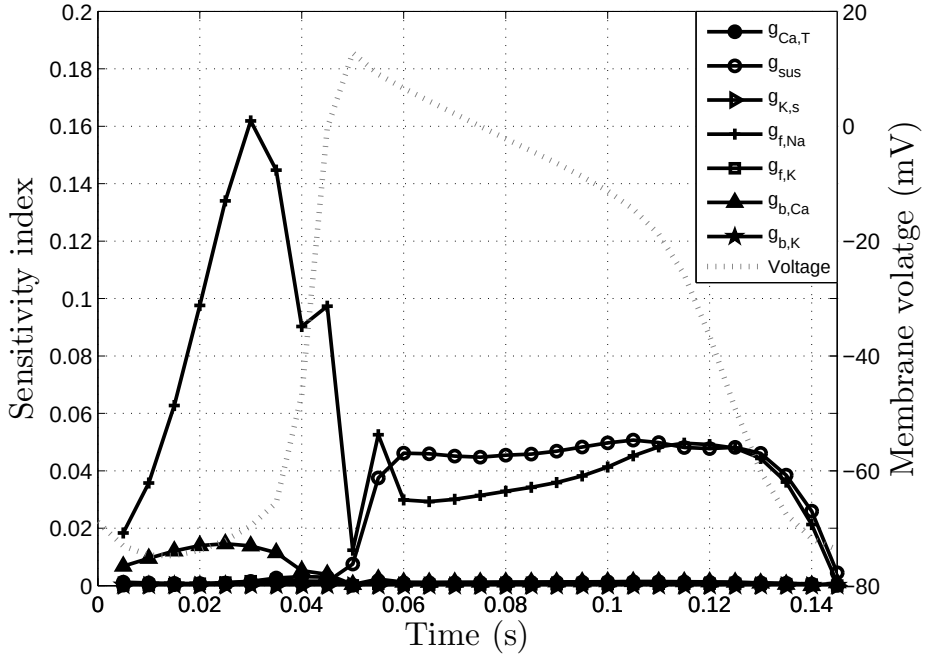

FIGURE 4.11: First order time varying eFAST indices (the less effective inputs) of eFAST on peripheral SAN action potential. The number of samples N_s is 8192 and the other FAST implementation details are according to the default setting (shown in Section 4.2.5). The y-axis are the sensitivity indices of individual ion conductances and the membrane voltage of the SAN.

Figure 4.13 presents the overall first and second order sensitivity effects. The first order effects dominate the action potential variance during slow depolarization stage. In the rapid depolarization stage, first order effects dramatically decrease to 0.25 at the peak (0.05s), which means that 75% of the variation is from higher order interactions (second order or greater). We calculated the overall second order effect (66 second order terms involved). Figure 4.12 shows that the individual second order effect takes place at the rapid depolarization and final stage of an action potential. The most influential interaction indices are $S_{g_{Na},g_{K,r}}$, $S_{g_{Na},g_{f,Na}}$, $S_{g_{K,r},g_{f,Na}}$, $S_{g_{Ca,L},g_{to}}$, $S_{g_{Ca,L},g_{K,r}}$ and $S_{g_{to},g_{K,r}}$. The maximum of these interaction indices are all comparatively small (less than 10% of total variance). The overall effects of these interaction are shown in Figure 4.13. As shown in Figure 4.13, the overall second order effect takes place at the rapid depolarization stage and contributes to 37% variation at most. The sum of the overall first and second order effect does not account for 100% of the variation during the depolarization stage: hence higher order interactions are involved in this stage. Higher order sensitivity indices (third order or higher) are not presented as shown by Figure 4.13, indicating that the interaction can be mainly explained the second order effects. The total effects of first and second order indices account for over 95% of the total variance at most time points. This suggests that the calculation of the higher order sensitivity indices might also be unnecessary. The limitation of this method is that there is the shift of the action potential involved in the evaluation of sensitivity indices,

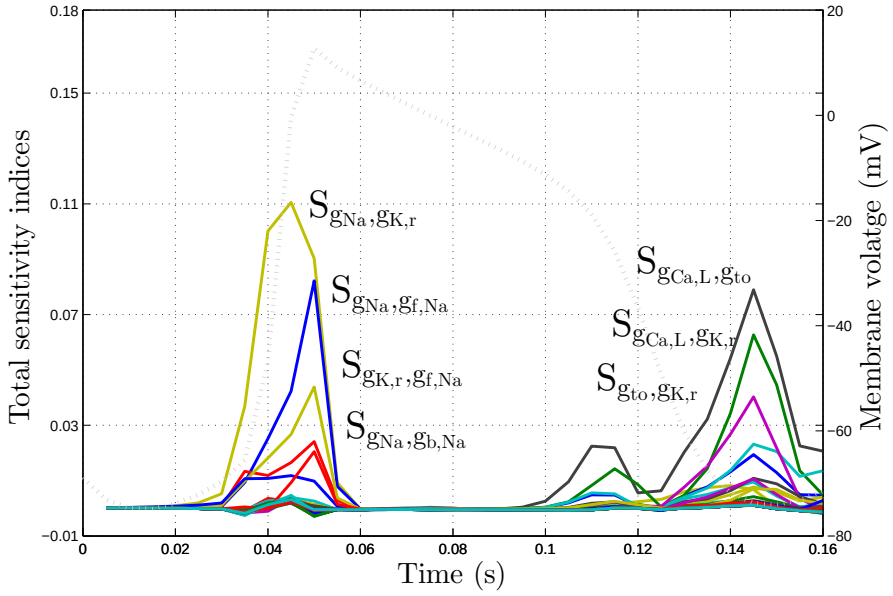

FIGURE 4.12: Second order time varying Sobol indices of the peripheral SAN action potential with 2048 samples. The second order sensitivity index shows the interactions of two inputs. e.g. $S_{g_{Na},g_{K,r}}$ is the interaction index of g_{Na} and $g_{K,r}$.

as shown by Figure 4.9. The values of inputs vary the action potential durations, which makes the synchronization of all stages of an action potential impossible. For example, the 200 samples in Figure 4.9 are synchronised by the starting time point but the inputs vary the durations of action potentials which leads to a shift of the peak values.

At a given time point, a large variation of outputs can be observed due to the shift, which is not cause by input variation but by unsynchronised action potential waveform. The explanation can be verified by a feature based sensitivity analysis on the peak value. As shown in Figure 4.13, the interactions accounts for over 50% of the action potential variation. Here, we perform eFAST sensitivity analysis with the same sampling of inputs, but measure the peak value as a scalar output from the results. The eFAST sensitivity indices of the sensitivity analysis are given in Table 4.4. The results in Table

TABLE 4.4: eFAST indices of of the peripheral SAN action potential peak value. The number of sample , N_s, is 4096. The number of search curve, N_r, is 1.

Input	$g_{Ca,L}$	$g_{Ca,T}$	$g_{K,r}$	g_{to}	g_{sus}	$g_{h,Na}$	$g_{h,K}$	$g_{b,Na}$	interaction
Index	0.80	0.01	0.02	0.09	0.07	0.00	0.00	0.00	0.03

4.4 are distinct from Figure 4.13. Input $g_{Ca,L}$ accounts for 80% peak variation, and the iterations contribution is 0.00 in Table 4.4, which demonstrates that time varying sensitivity analysis was corrupted by the phase shift. The sensitivity index at a given at cannot quantify the roles of inputs on action potential characters of interest due to the phase shift.

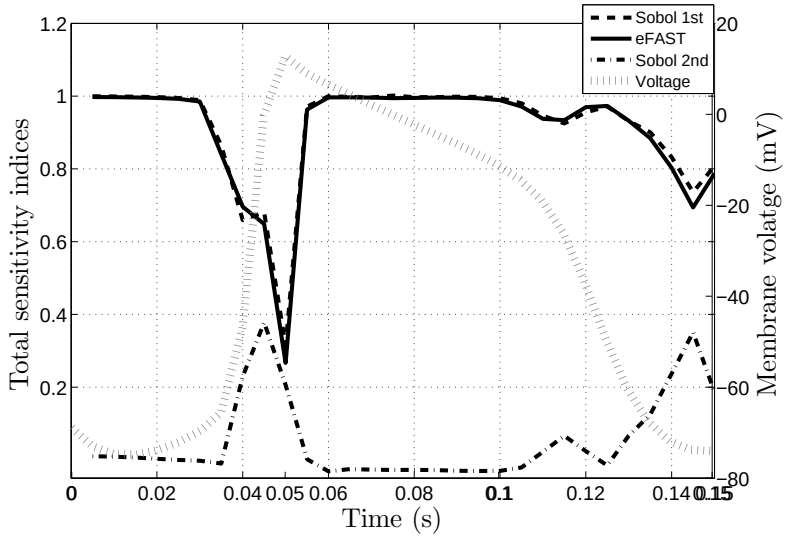

FIGURE 4.13: Overall first and second order effects of the peripheral SAN action potential. The first order effect is calculated by Sobol and eFAST method. The second order effect is calculated by Sobol method. The overall first order effect are the sum of all 12 first order indices as shown in Figure 4.10 and Figure 4.11. The overall second order effect is the sum of all the 66 second order interaction indices as shown in Figure 4.12.

4.3.2 Sensitivity Analysis Results of A Central SAN Model

We also perform a time based sensitivity analysis on a central SAN model (Zhang et al., 2000). As discussed in the previous content, the time varying global sensitivity analysis cannot accurately determine the sensitivity indices of the peripheral SAN model due to the phase shift of action potentials. In order to calculate the sensitivity index accurately, we only select four significant parameters ($g_{Ca,L}$, g_{to}, $g_{f,Na}$ and $g_{f,K}$) as eFAST inputs. Figure 4.14 shows the first order effects of the eFAST analysis. The results shows that the values of the first order indices all dramatically decrease to near zero at the action potential peak. Large interaction effects appear near the action potential peak. A further test was performed based on the Sobol method to determine the high order interactions of these parameters, as shown in Figure 4.15. Figure 4.15 shows that the fourth order effect is the main effect near the action potential peak, which means all of the parameters are involved into the variation of the peak value.

We believe that the results are inaccurate due to the phase shift, which can be proved by use feature-based sensitivity analysis. A feature based sensitivity analysis, specifically on the feature of peak value, is performed. Table 4.5 gives the index values of all of the first order effects and the overall effect of interactions. It was found that first order effect accounts for 97 % of output variance, which does not agree with the results of the time-based sensitivity analysis.

From the results of the central and peripheral SAN models, we conclude that the time based sensitivity analysis which is widely used in systems biology model is not suitable

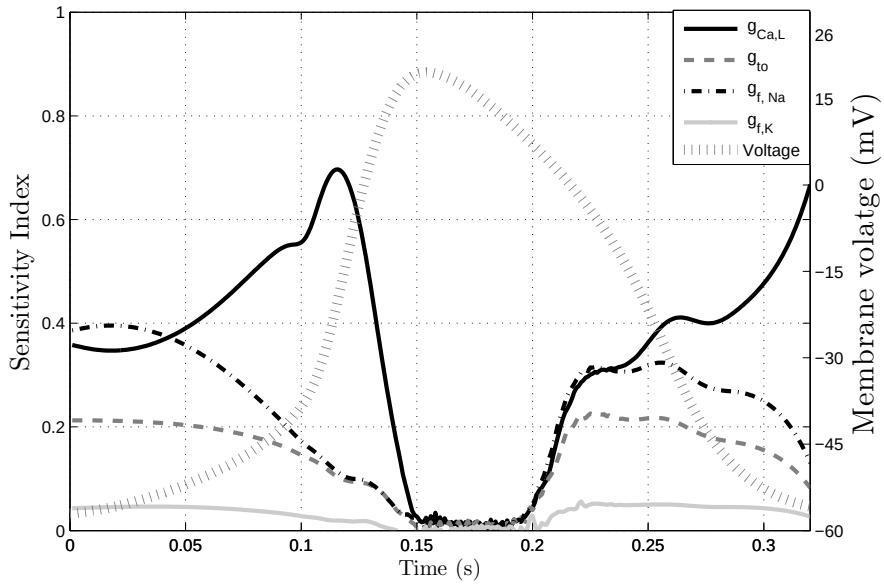

FIGURE 4.14: Time varying Sobol indices of the central SAN action potential (Zhang et al., 2000).

to be used in cardiac models. It is suggested that feature-based sensitivity analysis can avoid the error introduced by the action potential phase shift. In the following section, feature-based sensitivity analysis of cardiac models is discussed.

TABLE 4.5: The eFAST index of of the central SAN action potential peak value. The number of sample, N_s, is 4096. The number of search curve, N_r, is 1.

Input	$g_{Ca,L}$	$g_{Ca,T}$	$g_{K,r}$	g_{to}	g_{sus}	$g_{h,Na}$	$g_{h,K}$	$g_{b,Na}$	interaction
Index	0.16	0.21	0.34	0.08	0.08	0.08	0.00	0.04	0.03

4.4 Feature Based Global Sensitivity Analysis Results

As discussed for varying global sensitivity analysis, the sensitivity analysis based on each time point cannot accurately measure the effects of inputs on characters of an action potential due to the phase shift. Feature-based sensitivity analysis extracts the action potential characters of interest from the action potentials, then measures the corresponding sensitivity indices so that the phase shift does not bias the results. In the literature, researchers have implemented feature-based global sensitivity analysis on different types of cardiac models (Kharche et al., 2009), (Chang et al., 2015).

In this section, the results of feature-based global sensitivity analysis are presented. eFAST sensitivity analysis is implemented on Kurata model and Zhang's central and peripheral SAN models. The Kurata model and Zhangs central SAN model both describe the central SAN cell behaviour. Zhangs peripheral SAN model describes peripheral SAN

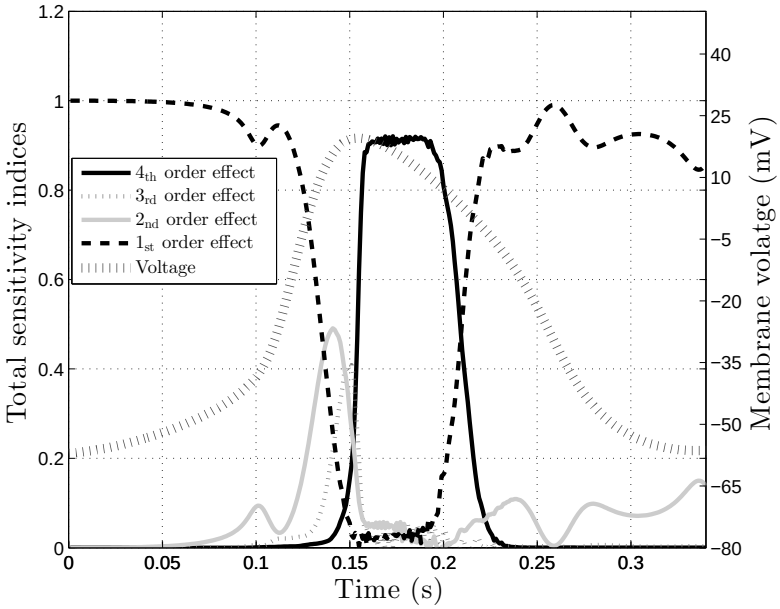

FIGURE 4.15: Time varying Sobol indices of the central SAN action potential (Zhang et al., 2000). The Sobol sensitivity analysis are performed based 8192 samples of the input space. The overall first order, second order, third order and fourth order indices are presented.

cell behaviour. Seven features (CL, APO, MDP, APA, APD_{90}, $\frac{dv}{dt}_{max}$ and DDR) are considered as the model outputs in the eFAST sensitivity analysis.

The results of the eFAST tests on three models are given in Table 4.7, Table 4.8 and Table 4.6. As shown in Table 4.6 and Table 4.7, CL is largely dependent on $g_{Ca,T}$ and $g_{K,r}$, while in the periphery SAN model the CL is more sensitive to $g_{h,Na}$ and $g_{Ca,L}$. In the three models, inputs g_{st} and g_{sus} all affect the CL, though no input has a large effect.

In the three models, the input $g_{Ca,L}$ is largely responsible for the APO variance. $g_{Ca,L}$ generates at leat 50% of the APO variation. $g_{K,r}$ is a comment input for MDP for all three models. The eFAST tests show that $g_{K,r}$ contributes over 34% MDP variance.

The indices of the APA for the central SAN model and the peripheral SAN model do not agree. In the two central SAN models, $g_{K,r}$ greatly regulates the APA with index values 0.51 and 0.64 respectively. On the other hand, in the Zhang periphery model, the index value of $g_{K,r}$ is only 0.02 and $g_{Ca,L}$ is the main effective input of APA with a value of 0.78 . Several parameters are involved in deciding the value of ADP_{90}. The inputs $g_{Ca,L}$, $g_{K,r}$ and $g_{Na,h}$ are important inputs in the regulation of ADP_{90}, though none of the parameters dominates the contribution. For output dv/dt_{max}, the input $g_{Ca,L}$ is the key factor to determine dv/dt_{max} for all the three models.

The effects of inputs on DDR vary from model to model. For the Kurata model, $g_{K,r}$ is the most important input. In the Zhang central SAN model, $g_{Ca,L}$ and $g_{K,r}$ contribute to a large degree to the DDR, while $g_{h,Na}$ is the key input determining the DDR in the

peripheral SAN model.

TABLE 4.6: eFAST sensitivity indices for Kurata model (Kurata et al., 2002). The FAST sensitivity index of each input parameter and AP output, describing the proportion of output variance which can be attributed by individual inputs (the first order effects). The summation of all the second and higher order effect is shown as *interaction*. The eFAST sensitivity analysis are performed based on 4096 samples, one search curve and ±20 % perturbation range of the default input values (N_s = 4096, N_r = 1 and $\Delta X = \pm 20$).

Input	CL	APO	MDP	APA	APD_{90}	$\frac{dv}{dt}_{max}$	DDR
$g_{Ca,L}$	0.01	**0.80**	0.00	0.13	0.00	**0.77**	0.00
$g_{Ca,T}$	**0.24**	0.01	0.00	0.01	**0.27**	0.01	0.09
$g_{K,r}$	0.22	0.02	**0.64**	**0.51**	0.14	0.09	**0.60**
g_{to}	0.00	0.10	0.00	0.02	0.01	0.01	0.00
g_{sus}	0.02	0.04	0.00	0.02	0.02	0.00	0.00
$g_{h,Na}$	0.20	0.00	0.00	0.00	0.19	0.00	0.08
$g_{h,K}$	0.08	0.00	0.00	0.00	0.09	0.00	0.03
g_{st}	0.15	0.01	0.04	0.04	0.22	0.01	0.04
$g_{b,Na}$	0.08	0.02	0.31	0.27	0.04	0.10	0.13
interaction	0.02	0.01	0.00	0.00	0.02	0.01	0.02

TABLE 4.7: eFAST sensitivity indices for the Zhang central model (Zhang et al., 2000). The eFAST sensitivity analysis are performed based on 4096 samples, one search curve and ±20 % perturbation range of the default input values (N_s = 4096, N_r = 1 and $\Delta X = \pm 20$).

Input	CL	APO	MDP	APA	APD_{90}	$\frac{dv}{dt}_{max}$	DDR
$g_{Ca,L}$	0.16	**0.50**	0.03	0.26	0.28	**0.57**	**0.44**
$g_{Ca,T}$	0.21	0.00	0.02	0.01	0.21	0.00	0.08
$g_{K,r}$	**0.34**	0.41	**0.85**	**0.64**	0.20	0.37	0.35
g_{to}	0.08	0.01	0.00	0.00	0.10	0.00	0.03
g_{sus}	0.08	0.01	0.00	0.00	0.10	0.00	0.00
$g_{h,Na}$	0.02	0.00	0.00	0.00	0.02	0.00	0.01
$g_{h,K}$	0.00	0.00	0.00	0.00	0.00	0.00	0.00
$g_{b,Na}$	0.04	0.03	0.09	0.05	0.01	0.03	0.00
interaction	0.03	0.03	0.00	0.02	0.03	0.01	0.08

The results described above demonstrate that there are common sets of inputs determining the outputs of the two central SAN models. There are nine common inputs ($g_{Ca,L}$, $g_{Ca,T}$, $g_{K,r}$, $g_{K,s}$, g_{to}, g_{sus}, $g_{f,Na}$, $g_{f,K}$ and $g_{b,Na}$) for the three SAN models. These common inputs have corresponding common sensitivity indices for feature outputs. Figure 4.16, Figure 4.17 and Figure 4.18 show the correlation of the common eFAST indices of the models. There is a good agreement between the results of the Kurata model and the Zhang central SAN model, as shown in Figure 4.16. Figure 4.16 shows that the two models have the same inputs determining the outputs DMP, APA, APO, DDR, and dv/dt_{max}. The Kurata model and the Zhang central SAN model both describe the central SAN cell behavior. The results suggest that the two models have the similar intrinsic mechanism on determining the action potential characters. Figure 4.17 shows

TABLE 4.8: eFAST sensitivity indices for the Zhang peripheral model (Zhang et al., 2000). The eFAST sensitivity analysis are performed based on 4096 samples, one search curve and ±20 % perturbation range of the default input values ($N_s = 4096$, $N_r = 1$ and $\Delta X = \pm 20$).

Input	CL	APO	MDP	APA	APD_{90}	$\frac{dv}{dt}_{max}$	DDR
$g_{Ca,L}$	0.26	**0.80**	**0.45**	**0.78**	0.29	**0.92**	0.20
$g_{Ca,T}$	0.09	0.01	0.01	0.01	0.08	0.01	0.18
$g_{K,r}$	0.00	0.02	0.34	0.02	0.03	0.02	0.03
g_{to}	0.05	0.09	0.02	0.07	0.04	0.03	0.10
g_{sus}	0.21	0.07	0.14	0.11	0.23	0.01	0.14
$g_{h,Na}$	**0.33**	0.00	0.00	0.00	0.28	0.00	**0.62**
$g_{h,K}$	0.02	0.00	0.00	0.00	0.02	0.00	0.05
$g_{b,Na}$	0.03	0.00	0.04	0.00	0.03	0.00	0.01
interaction	0.00	0.00	0.01	0.00	0.00	0.00	0.01

the eFAST index comparison between the Kurata model and the Zhang peripheral SAN model. The test suggests that there is no significant correlation. Only the outputs dv/dt_{max} and APO have same significant contributors. The other small value indices show no strong correlation either. The results demonstrate that the two models have distinct intrinsic mechanism determining the same action potential characters. Figure 4.18 shows the eFAST index comparison between the Zhang central SAN model and the Zhang peripheral SAN model. Again, the figure suggests that there is no significant correlation. The Zhang central and peripheral SAN models are described by the same differential equations but different ion channel conductances. The Kurata model and the Zhang central SAN model are described with different equations but have a common set of inputs. Figure 4.18 and Figure 4.16 suggest that the default ion channel conductances largely determines the action potential characteristics. For all the SAN models, only a small fraction of output variance (less than 8%) is from parameter interactions. No strong correlation of ion channel is observed. The variation of SAN model outputs is mainly from the first order contribution of input parameters.

In the literature, Chang et al. (2015) state that a strong ion channel interaction exists in the ventricular cell behavior. The interactions account for 74 % and 0.15 % output variances of DI_{min} and Slope respectively (Chang et al., 2015). We performed the eFAST test on the ventricular cell model (Luo and Rudy, 1991). The eFAST sensitivity analysis results are given in Table 4.9. Table 4.9 shows the eFAST sensitivity indices of the Luo-Rudy ventricular model. The APO indices show that 93% of APO variation is from input $g_{Na,f}$. The inputs g_K and g_b are mainly responsible for the MDP variation. APD_{90} is regulated by inputs g_K and g_{Si} with index values of 0.24 and 0.58 respectively. The input $g_{Na,f}$ is the only effective input on determining the variance of dv/dt_{max}. The output DP is dependent on g_b and g_{Si} with eFAST index values of 0.35 and 0.57, respectively. $g_{Na,f}$ and g_{K1} are relevant to the variation of DI_{min}. All of these outputs are determined by the individual inputs and no large interaction is involved. The results also suggest that *Slop* is greatly dependent on the input interactions. 57% of variation of *Slop* comes

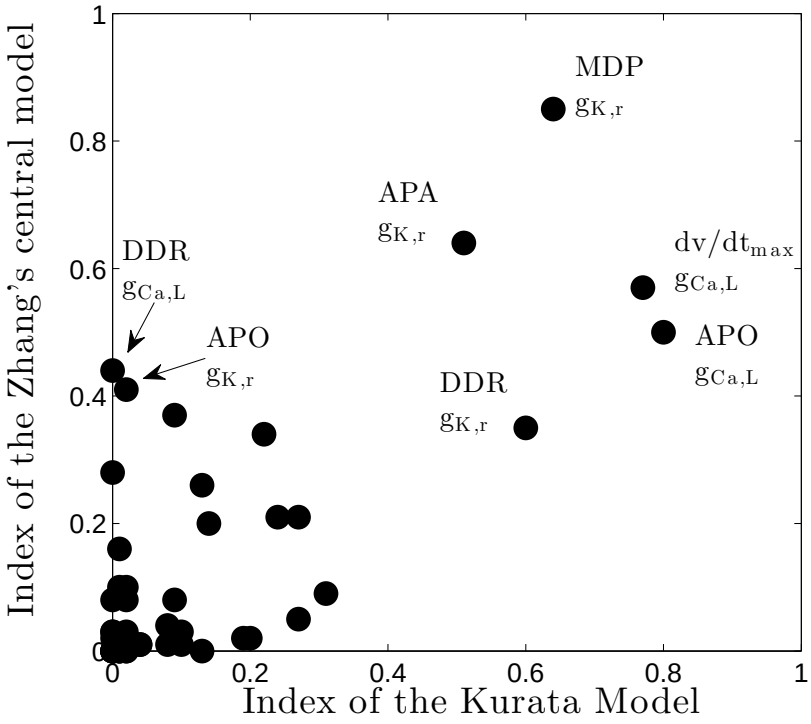

FIGURE 4.16: Pairwise comparisons of global sensitivity indices of Kurata model and Zhangs central SAN model. The spread of the indices illustrate the agreement of the two models. If they are widely spread over the space, the indices of the two models disagree. If not, there is agreement on the roles of the ion channels in determining outputs. The label of sensitivity index shows the corresponding input and output, and the index value is given in Table 4.6 and Table 4.7. In the two tables, there is a common set inputs between the Kurata model and the Zhang's central SAN model which are $g_{Ca,L}$, $g_{Ca,T}$, $g_{K,r}$,$g_{K,s}$, g_{to}, g_{sus}, $g_{h,Na}$, $g_{h,K}$ and $g_{b,Na}$ respectively. There are seven outputs for a given input. The common index of the two models is with common parameters and outputs. Hence, there are 63 common types of eFAST indices between the Kurata model and the Zhang's central SAN model. The x and y axis show index values of two models respectively.

from interaction.

In order to understand the interaction of ion channels, we perform Sobol sensitivity on the Luo-Rudy ventricular model. We obtained very close index values with respect to eFAST indices. The Sobol results are shown in Table 4.10. The correlation of the eFAST indices and Sobol indices of the Luo-Rudy ventricular model is illustrated by Figure 4.19. Figure 4.19 shows that the results obtained from eFAST sensitivity analysis with 2048 samples of parameter values can be replicated well by Sobol sensitivity analysis. Figure 4.20 shows is an comparison between Bayesian sensitivity indices and eFAST sensitivity indices. The Bayesian sensitivity analysis uses Gaussian process emulation, a dominant approach for the statistical modelling of computer model functions. The approach also returns variance based sensitivity indices. Theoretically, the values of Bayesian indices should be identical to the values of both Sobol and FAST indices. Figure 4.20 demon-

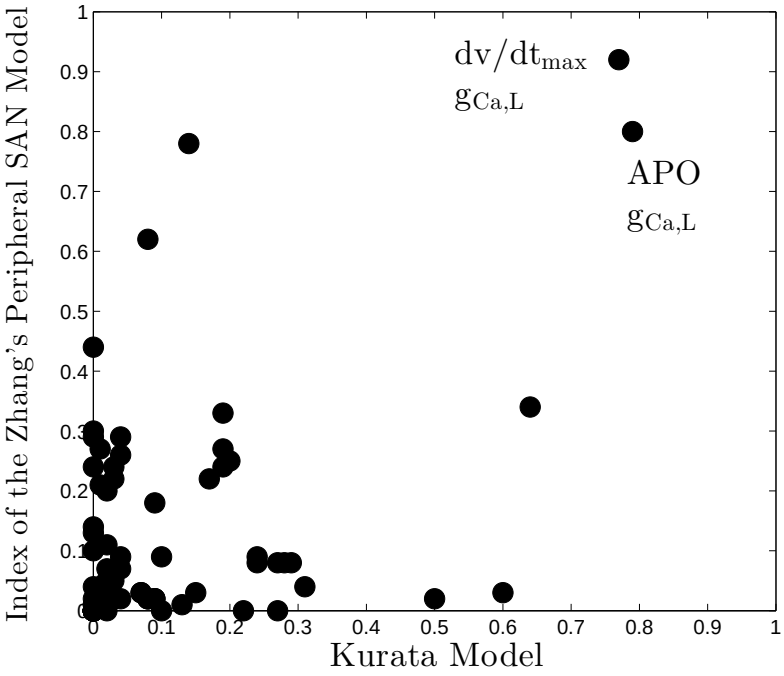

FIGURE 4.17: Pairwise comparisons of global sensitivity indices of Kurata model and Zhangs peripheral SAN model. The spread of the indices illustrate the agreement of the two models. If they are widely spread over the space, the indices of the two models disagree. If not, there is agreement on the roles of the ion channels in determining outputs. The label of sensitivity index shows the corresponding input and output, and the index value is given in Table 4.6 and Table 4.8. In the two tables, there is a common set inputs between the Kurata model and the Zhang's central SAN model which are $g_{Ca,L}$, $g_{Ca,T}$, $g_{K,r}$,$g_{K,s}$, g_{to}, g_{sus}, $g_{h,Na}$, $g_{h,K}$ and $g_{b,Na}$ respectively. There are seven outputs for a given input. Hence, there are 63 common types of eFAST indices between the Kurata model and the Zhang's peripheral SAN model. In this figure, x and y axis show index values of two models respectively.

strates that the results show a good agreement except the indices of APDR Slop and DI_{min}. As Slop and DI_{min} are the features both obtained from fitting APDR curve, the disagreement of the indices between Bayesian indices and eFAST indices may be caused by implementation of data fitting as we discussed in Section 2.8.2. Figure 4.20 shows the indices of inputs g_K, g_{K1} and $g_{Na,f}$ for outputs DI_{min} have difference values in the two tests. The difference of the two tests can be further shown by Figure 4.21. Figure 4.21 shows the all the index values of DI_{min} and Slop. There is a difference between the eFAST indices and of Bayesian sensitivity indices of output the Slop. However, eFAST index values of output Slop are all comparatively small as a large interaction effect exists in the output. The indices of DI_{min} are matched comparatively accurately. The Bayesian indices of DI_{min} are very small due to large interaction effect, while eFAST indices of DI_{min} are comparatively large, with the interaction only accounting for 3% of output variance (shown in Table 4.10). Both Bayesian indices and eFAST indices show that strong interaction effects involved in the feature, Slop. In the following context, interaction effects are analysed by the Sobol sensitivity analysis.

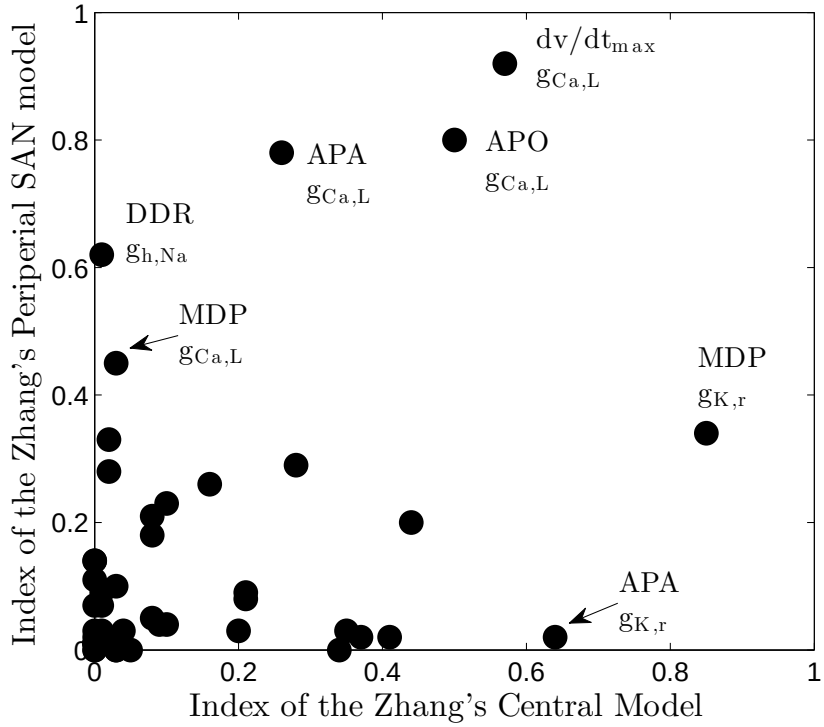

FIGURE 4.18: Pairwise comparisons of global sensitivity indices of Zhangs models of central and peripheral. The spread of the indices illustrate the agreement of the two models. If they are widely spread over the space, the indices of the two models disagree. If not, there is agreement on the roles of the ion channels in determining outputs. The label of sensitivity index shows the corresponding input and output, and the index value is given in Table 4.7 and Table 4.8. As shown by the two tables , Zhangs models of central and peripheral has same type of eFAST indices. In this figure, x and y axis show index values of two models respectively.

TABLE 4.9: eFAST sensitivity indices for Luo-Rudy ventricular model (Luo and Rudy, 1991). The eFAST sensitivity analysis are performed based on 4096 samples, one search curve and ±20 % perturbation range of the default input values ($N_s = 4096$, $N_r = 1$ and $\Delta X = \pm 20$).

Input	APO	MDP	APD_{90}	$\frac{dv}{dt}_{max}$	DP	DI_{min}	Slope
$g_{Na,f}$	**0.93**	0.00	0.00	**1.00**	0.00	**0.36**	0.00
g_K	0.00	0.00	0.24	0.00	0.01	0.01	0.23
g_{K1}	0.06	**0.57**	0.02	0.00	0.00	0.35	0.01
g_{Kp}	0.00	0.00	0.00	0.00	0.06	0.00	0.00
g_{Si}	0.01	0.41	0.14	0.00	0.35	0.24	0.03
g_b	0.00	0.01	**0.58**	0.00	**0.57**	0.02	0.15
interaction	0.00	0.01	0.02	0.00	0.01	0.02	**0.57**

Table 4.9 shows that first order effects only account for 43% of APDR *Slop* variance. The majority of the variance is from the interaction terms. Sobol sensitivity analysis is performed on the Luo-Rudy model to analyse the second order effects. Table 4.12 presents all the second order sensitivity indices of APDR *Slop*. The results show that the combination between g_b and g_{Si}, g_b and g_{K1}, g_b and g_{Kp} have a large impact on the APDR *Slop* value. First order and second order effects account for 98% variance in

TABLE 4.10: Sobol sensitivity indices for Luo-Rudy ventricular model (Luo and Rudy, 1991). The results are based on 2048 samples.

Input	APO	MDP	APD_{90}	$\frac{dv}{dt}_{max}$	DP	DI_{min}	Slope
$g_{Na,f}$	**0.95**	0.00	0.00	**1.00**	0.00	**0.35**	0.00
g_K	0.00	0.00	0.24	0.00	0.01	0.01	0.23
g_{K1}	0.05	**0.57**	0.02	0.00	0.00	0.35	0.02
g_{Kp}	0.00	0.00	0.00	0.00	0.06	0.00	0.01
g_b	0.00	0.41	0.14	0.00	0.35	0.23	0.05
g_{Si}	0.00	0.01	**0.58**	0.00	**0.57**	0.02	0.15
interaction	0.00	0.01	0.02	0.00	0.01	0.03	**0.55**

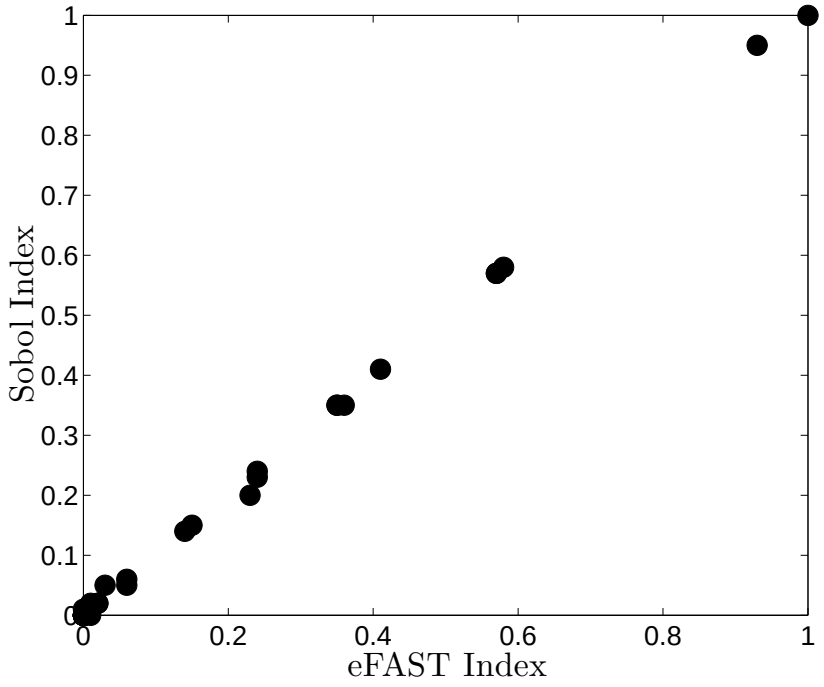

FIGURE 4.19: Pairwise comparisons of eFAST indices and Sobol first order indices of Luo-Rudy ventricular model. The index values are based on Table 4.10 and Table 4.9. As eFAST sensitivity index is equivalent to Sobol first order index, the eFAST indices and Sobol first order indices of a same model should agree with each other. The spread of the indices illustrate the agreement of the two models. If they are widely spread over the space, the indices of the two models disagree. If not, there is agreement on the roles of the ion channels in determining outputs.

total. The other 2% variance is from third or higher order effects. The results show the second order effects dominate in the interactions.

4.5 Discussion

In this chapter, two global sensitivity analysis techniques (eFAST and Sobol methods) were applied. Both of the two methods are capable of systematically searching over a wide range in the parameter space. Based on the literature, there are two common approaches to implement global sensitivity analysis on systems biology models, (1) feature

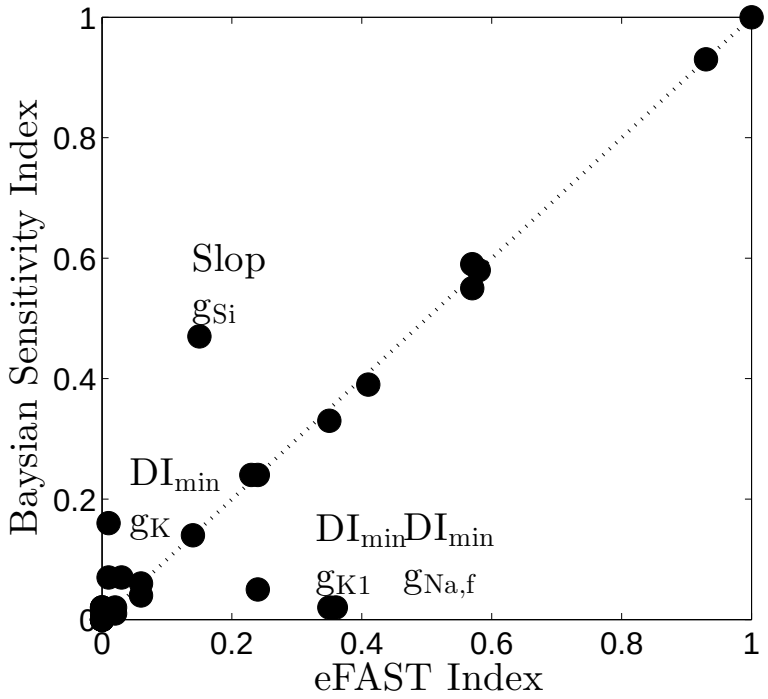

FIGURE 4.20: Pairwise comparisons of eFAST indices and first order Bayesian sensitivity indices of Luo-Rudy ventricular model. Bayesian sensitivity indices are obtained from Chang et al. (2015). The spread of the indices illustrate the agreement of the two models. The eFAST indices and Bayesian sensitivity indices of a same model should agree with each other. The disagreement of the indices of DI_{min} and Slop may duo to different fitting methods of APDR curve used in this work and Chang et al. (2015).

TABLE 4.11: Second order Sobol sensitivity indices for the output *Slop* Luo-Rudy ventricular model. All the 2-combinations from the 6 inputs are listed. The row and column of a index represent the combination of two inputs. The 15 second order sensitivity indices are based on Sobol test with 1024 samples. The total variance contribution of the second order terms is 0.55 out of 1.

Input	g_{Si}	g_K	g_{K1}	g_{Kp}	g_b
$g_{Na,f}$	0.016	0.000	0.019	0.006	0.049
g_{Si}		0.000	0.000	0.081	**0.202**
g_K			0.027	0.000	0.000
g_{K1}				0.044	**0.103**
g_{Kp}					**0.127**

based sensitivity analysis and (2) time varying sensitivity analysis. We compared the two approaches on cardiac models. The feature based approach evaluates the variation of features of action potentials. The time varying sensitivity analysis presents the effects of parameters at each time points of action potentials. We showed that the feature based sensitivity analysis is better since it avoids the error introduced by the phase shift of action potential as we explained in the discussion of Section 4.3.

By carrying out feature based eFAST analysis, we observed a common set of important parameters among several SAN models, which shows that the global methods are able

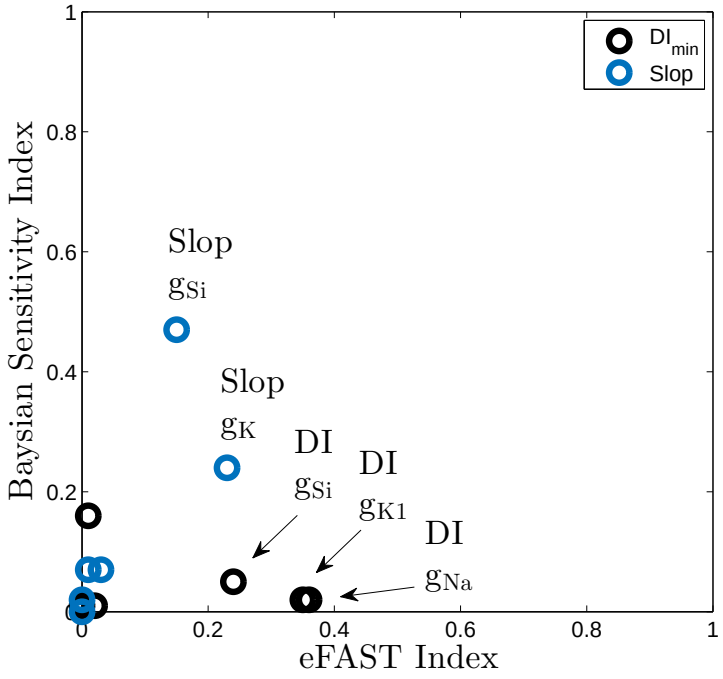

FIGURE 4.21: Pairwise comparisons of sensitivity indices of DI_{min} and Slop between Sobol and Bayesian sensitivity analysis. The spread of the indices illustrate the agreement of the two models. If they are widely spread over the space, the indices of the two models disagree. If not, there is agreement on the roles of the ion channels in determining outputs. The Sobol indices are based on Table 4.10. The Bayesian indices are obtained from Chang et al. (2015). x and y axis show index values of the two methods respectively. A disagreement with the indices of DI_{min} and Slop is found in this case.

TABLE 4.12: Second order Sobol sensitivity indices for the output *Slop* Luo-Rudy ventricular model. All the 2-combinations from the 6 inputs are listed. The row and column of a index represent the combination of two inputs. The 15 second order sensitivity indices are based on Sobol test with 1024 samples and ±20 % perturbation range of the default input values. The total variance contribution of the second order terms is 0.55 out of 1.

Input	g_{Si}	g_K	g_{K1}	g_{Kp}	g_b
$g_{Na,f}$	0.016	0.000	0.019	0.006	0.049
g_{Si}		0.000	0.000	0.081	**0.202**
g_K			0.027	0.000	0.000
g_{K1}				0.044	**0.103**
g_{Kp}					**0.127**

to provide model independent evaluation of the effects of ion channels, and that the models with different descriptions show the SAN mechanism in a similar way. The results also suggest that the first order effects of ion channels are the main effects of action potential features. Among all the SAN models, the interactions of ion channels account less 10 % of the variation of the features. In the ventricular cell model, a large interaction was observed. The feature based Sobol analysis was used to uncover the iteration terms. We also found a strong interaction influencing action potential duration curve, which achieves a good agreement with Chang et al. (2015). We further explained

this interaction by Sobol sensitivity analysis, and presented that the interaction is mainly contributed by the second order effects, which agree with an experimental observation of an pairwise interaction (Guo et al., 2011).

As we shown in Figure 2.5, the action potential is associated with contractile response via excitation-contraction coupling. The action potential amplitude and duration regulates contraction force and duration respectively. The results of the sensitivity analysis can possibly be applied to understand and to vary cardiac cell behavior. For example, our results reveal that Ca^{2+} currents plays a leading role on action potential duration (i.e. APD_{90}) in every SAN model. In the literature, experimental measurements also show the age related Ca^{2+} concentration variation impacts cardiac muscle duration (Froehlich et al., 1978), and the blocking Ca^{2+} with nifedipine lead to a great variations in cardiac contraction force (Schouten, 1990). There is a agreement of the roles of Ca^{2+} currents on the regulation of the contractile behavior between analysis and these experimental works. These works further suggest that cardiac contractile response can be regulated by cellular ion currents. Hence, the knowledge obtained from sensitivity analysis is useful to relate these currents to cardiac muscle contraction.

Chapter 5

Multi-scale Stochastic SAN Model

In this chapter, we propose single cell SAN models and 1D SAN models based on stochastic differential equation (SDE). We achieve SDE based single cell SAN models by reformulations of ODE based SAN models and estimations of the number of ion channels. The results of single cell SDE models agree with experimental observation of single SAN cell variability. The 1D SAN models are based on the coupled single cell SDE models employed to analyse the cell coupling effects on the SAN action potential variability. We note that cell coupling increases the action potential variability, which agrees with existing experimental data.

5.1 Intact SAN Behavior and Single Cell SAN Behavior

Zhang et al. (2000) published the first 1D SAN model and suggested that there is a difference between the CL of intact SAN and the CL of single SAN cells. The characteristics of action potentials is dependent on the cell location in the SAN tissue, which is the results of regional differences in membrane properties, such as cell size and ion channel densities (Boyett et al., 2007a). They mentioned that the rabbit SAN CL observed experimentally at 37 °C is 348 ± 50 ms (Kirchhof et al., 1987), which is greater than the single central SAN cell CL (331 ± 13 ms) and the single peripheral SAN cell CL (298± 8 ms). These observation shows that the characteristics of the CL of intact SAN cells are distinct from those of isolated single SAN cells. In this chapter, the regional difference of SAN cells is addressed.

In addition, there are also differences between the CL coefficient of variation of single cells and intact SAN tissue. Yaniv et al. (2014) used the coefficient of variation to describe the the CL variation. The variation coefficient is defined as the ratio of the

standard deviation to the mean. They found that the coefficient of intact isolated SAN tissue is 2.8 ± 0.6 (n = 8), while the coefficient of isolated single SAN cells is 8.9 ± 0.5 (n = 64). This result shows that the CL variability of intact SAN is distinct from single SAN cells. To our best knowledge, the reason for this phenomenon is still unknown.

At cellular level, Wilders and Jongsma (1993) concluded that the variation of CL (Cycle Length) of a isolated SAN cell is due to the stochastic open-close kinetics of ion channels. In the literature, the intact SAN tissue is considered as a strand of coupled SAN cells (Zhang et al., 2000) (Oren and Clancy, 2010). Hence, a stochastic SAN tissue model can be achieved by the incorporation of stochastic open-close kinetics of ion channels. The CL variability of intact SAN tissue can be shown with a stochastic SAN tissue model. The stochastic model must be computationally efficient because a large number of cells may be involved in the simulation (as shown in Table 2.2). Walmsley et al. (2010) used a channel-level SDE formulation to capture stochastic behaviours of isolated ventricular myoctes. The variability of cardiac cells are modelled by fitting experimental data with the SDE formulation. They further applied this formulation to explain the tissue level variability between cardiac cells (extrinsic variability) and beat-to-beat variability of each cell (intrinsic variability) (Walmsley et al., 2015). These two works discuss the variability by fitting experimental data instead of modeling ion channel gating mechanisms. In this chapter, we compare several SDE hypothesises of intrinsic ion channel modelling. The best hypothesis is used to modelling extrinsic and intrinsic SAN tissue variability.

5.2 Markov Chain Ion Channel Model

We consider Hodgkin-Huxley (HH) scheme-based cardiac model throughout this work. The cardiac models discussed in our work are deterministic HH scheme based. HH scheme-based models assume that the activity of ion channels is governed by the transition between a number of possible channel states, which leads to intrinsically stochastic models behavior. The most wildly used stochastic ion channel model is the Markov chain (MC) model (Goldwyn et al., 2011b).

The MC model assumes that the ion channel states are discrete, continuous-time Markov chain, and that each state describes a particular configuration of the ion channel. The Markov chain simulates the ion channel transition from one state to the next state with respect to the current state and membrane voltage. Wilders and Jongsma (1993) applied the Markov chain SAN model to explain the variability of action potential cycle length (CL) and suggested the the stochastic transition of ion channel states is responsible for the variability of action potential CL.

However, the ion channel simulations based on MC models are computationally expensive. Hence, a lot of researchers are interested in formulating SDE ion channel models,

especially in neuroscience. Fox and Lu (1994) published the first SDE ion channel model of Hodgkin-Huxley equations. This research has been widely applied in HH type neuron models. The SDE based Hodgkin-Huxley model reduces the computational time by about two orders of magnitude (Fox, 1997). Goldwyn et al. (2011b) later proved that a certain SDE type ion channel model could accurately approximate the ion channel noise even with a small number of ion channels. In this chapter, we first start with the Markov chain model of ion channels. SDE models are discussed later in this section.

According to the HH scheme, an ion channel is formed by channel subunits. For examples, in the standard HH model, the current I_{K} of K^+ channel is constituted of four independent identical subunits which is shown as:

$$I_{\mathrm{K}} = \overline{g}_{\mathrm{K}} \mathrm{n}^4 (V - E_{\mathrm{K}}) \tag{5.1}$$

E_{K} is the reversal potential at which there is no current across the membrane. n is the state variable of a ion channel subunit. There are four identical ion channel subunits in a K^+ channel. The kinetics of of an K^+ subunit can be described as a two-state process:

$$\text{Closed} \underset{\beta_n}{\overset{\alpha_n}{\rightleftharpoons}} \text{Open} \tag{5.2}$$

The transition of the four K^+ ion channel subunits can be modelled as a five-state Markov chain. Each Markov state represents the number of open subunits at a given time:

$$0 \underset{1\beta_n}{\overset{4\alpha_n}{\rightleftharpoons}} 1 \underset{2\beta_n}{\overset{3\alpha_n}{\rightleftharpoons}} 2 \underset{3\beta_n}{\overset{2\alpha_n}{\rightleftharpoons}} 3 \underset{4\beta_n}{\overset{1\alpha_n}{\rightleftharpoons}} 4, \tag{5.3}$$

where the diagram has five Markov states and corresponding transition rates. As shown by Equation 5.1, a K^+ channel has four subunits and the channel conducts only under the condition that all the four subunits are open. The state 4 in the Markov state diagram represents the open state of the channel. The constant $1\alpha_n$ is the transition rate from state 3 to 4 because there is only one closed subunit at state 3. Similarly, the $4\beta_n$ is the rate from state 4 to 3 as four open subunits have the same probability to transit to be closed. For a Markov chain model, let $\mathbf{P}$ be a vector where the i_{th} element presents the probability that the channel has i open subunits at a given time. The evaluation of $\mathbf{p}$ then can be shown as

$$\frac{\mathrm{d}\mathbf{p}}{\mathrm{d}t} = A\mathbf{p}, \tag{5.4}$$

where the transition matrix A is

$$A = \begin{bmatrix} -4\alpha_n & \beta_n & 0 & 0 & 0 \\ 4\alpha_n & -(3\alpha_n + \beta_n) & 2\beta_n & 0 & 0 \\ 0 & 3\alpha_n & -2(\alpha_n + \beta_n) & 3\beta_n & 0 \\ 0 & 0 & 2\alpha_n & -(\alpha_n + \beta_n) & 4\beta_n \\ 0 & 0 & 0 & \alpha_n & -4\beta_n \end{bmatrix} \tag{5.5}$$

The conductance of K^+ channel is determined by the number of open channels. Let $f = N_o/N$ be the ratio of open channel, where N_o is the number of channel in the open state and N is the total number of ion channels. The HH scheme K^+ current then can be rewritten as $i_{\mathrm{K}} = g_{\mathrm{K}} f(E - E_{\mathrm{K}})$.

5.3 SDE Ion Channel Models

Markov chain model is considered to be the gold standard for the simulation of ion channel kinetics (Goldwyn and Shea-Brown, 2011). The Markov process can be simulated by the Gillespie type algorithm. The Markov ion channel model is computationally intensive to simulate and is difficult to analyze mathematically (Goldwyn et al., 2011b). In this section, three SDE ion channel models are considered. An illustration of the three SDE ion channel models is shown in Figure 5.1. In the following content, we use the classic HH K^+ ion channel as an examples to illustrate the difference between the three SDE ion channel models.

5.3.1 Channel Based SDE Model

Fox and Lu (1994) formulated the first SDE HH model with system-size expansion. The system size expansion enables us to derive an SDE model from the master equation. In Equation 5.7, P is a function $P(x,t)$ is a function of x and t, where x is the number of ion channel in state x, $0 \leq x \leq$ N. In the system size expansion, a scaled process $x = x/N$ is considered ($0 \leq x \leq 1$), which can be further used in stochastic differential equation. The system size expansion method is a scaled process to resemble the channel states behavior. Fox and Lu showed that the channel based SDE K^+ model can be expressed as:

$$\frac{\mathrm{d}\mathbf{x}}{\mathrm{d}t} = A\mathbf{x} + S\xi, \tag{5.6}$$

where $\mathbf{x}$ is a vector with five components and the i_{th} component stands for the proportion of K^+ with i open subunits. A is the transition matrix in Equation 5.6. For example, x_1 is equal to 0.2, which means that 20% of the total number of ion channels have only one open subunit. ξ is a vector of five independent Gaussian white noise processes

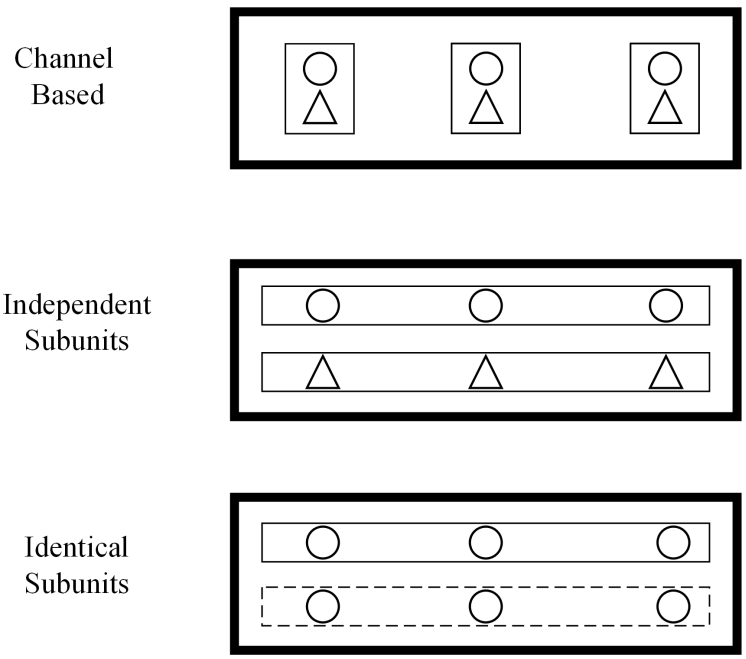

FIGURE 5.1: Illustration of the difference between channel-based and subunit based ion channel models (recreation from (Goldwyn et al., 2011b)). ◯ and △ stand for two different type subunits. (a) In channel based model, the two subunits are grouped together to form channels, and Gaussian white noise is added into a **channel level variable** which is related to the ratio of the number of open ion channels to the total number of ion channels as shown by Equation 5.6. (b) In the independent subunits model, Gaussian white noise is added into independent **subunit level variables** which are related to the ratio of the number of open subunits to the total number of subunits as shown by Equation 5.7. As two gates involved, the independent subunits model requires two stochastic differential equations. (c) In the identical subunits model, there is only one subunit been modelled. The identical subunits model assumes that the two subunits are identical. The SDE of the identical subunits model is also shown as shown by Equation 5.7, but only a stochastic differential equation is used.

$N \in (0, 1)$. The fluctuation term S is the matrix square root of the K^+ diffusion matrix D which is defined as

$$D = \frac{1}{N}\begin{bmatrix} 4\alpha_n x_0 + \beta_n x_1 & -(4\alpha_n x_0 + \beta_n x_1) & 0 & 0 & 0 \\ -(4\alpha_n x_0 + \beta_n x_1) & 4\alpha_n x_0 + (3\alpha_n + \beta_c)x_1 + 2\beta_n x_2 & -(3\alpha_n x_1 + 2\beta_n x_2) & 0 & 0 \\ 0 & (3\alpha_n x_1 + 2\beta_n x_2) & 3\alpha_n x_1 + 2(\alpha_n + \beta_n)x_2 & -2(\alpha_n x_2 + 3\beta_n)x_3) & 0 \\ 0 & 0 & -2(\alpha_n x_2 + 3\beta_n x_3) & -2\alpha_n x_2 + (\alpha_n + 3\beta_n)x_3 + 4\beta_n x_4 & -2(\alpha_n x_3 + 4\beta_n x_4) \\ 0 & 0 & 0 & -(\alpha_n x_3 + 4\beta_n x_4) & \alpha_n x_3 + 4\beta_n x_4 \end{bmatrix}$$

5.3.2 Independent Subunit SDE Model

The subunit-based SDE model is derived from the subunit based structure of the HH model. The stochastic behavior of opening and closing of the HH ion channel subunit is approximated by the SDE model. In the classic HH model, the stochastic behavior exists in the opening and closing of ion channel subunits as shown in Equation 5.3. For example, a K^+ channel is composed of four n subunits which represent the faction of open subunits. A subunit can open and close randomly with respect to the transition

rates α_n and β_n, respectively. In addition, it is typically assumed that all the subunits behave identically. Some studies have suggested that it is appropriate to add noise into subunit variable n.

$$\frac{\mathrm{d}n}{\mathrm{d}t} = \alpha_n(1-n) + \beta_n n + \sigma_n(V)S\xi(t), \tag{5.7}$$

where $\xi(t)$, a time varying stochastic term, is a Gaussian white noise with zero mean and unit variance. In Equation 5.7, $\xi(t)$ is scaled by $\sigma_n(V)$ which is determined as

$$\sigma_n^2(V) = \frac{\alpha_n(1-n) + \beta_n n}{N} \tag{5.8}$$

Shuai and Jung (2002) introduced the independent subunit model and the K^+ channel conductance is defined as $g_{\mathrm{K}} = \overline{g}_K n_1 n_2 n_3 n_4$. Four subunit variables n_1, n_2, n_3 and n_4 are introduced to describe the four independent subunits, as expressed by Equation 5.8.

5.3.3 Identical Subunit SDE Model

The identical subunit SDE model is a simplified model in contrast to independent subunit SDE model. The identical subunit SDE model was firstly introduce by Fox and Lu (1994). This model also realizes the stochastic channel behavior by Equation 5.7 and Equation 5.8, though the K^+ channel conductance is described as $g_{\mathrm{K}} = \overline{g}_K n^4$. Only one single SDE is used to realize the K^+ channel, and the open fraction of the four K^+ channel subunits is described with a same value n.

5.3.4 The Distinction Among Channel Based SDE Model, Identical and Independent Subunit Based Models

In the previous section, the channel-based SDE model, identical subunit SDE model and independent subunit SDE K^+ channel model is introduced. We use K^+ channel as to illustrate the differences between the three models. These three SDE model can also be used to model the stochastic behaviors of other classic HH scheme ion channels. For example, Na^+ channel can also be modelled using identical subunit model and independent subunit model. The identical subunit Na^+ channel model can be expressed as $g_{\mathrm{Na}} = \overline{g}_{Na} m^3 h$, where m and h are two SDE subunit variables. The corresponding independent subunit Na^+ channel model is given as $g_{\mathrm{Na}} = \overline{g}_{Na} m_1 m_2 m_3 h$, where m_1, m_2, m_3 are three independent h subunit variables.

Goldwyn et al. (2011b) analysed the three SDE models to discuss their approximation to the Markov chain model. Their results suggest that the **channel-based approach** is the best approximation of the three SDE models for Hodgkin-Huxley description-based model, but the two subunit based ion channel models cannot capture the Markov chain model behavior. Their results also show that Markov chain ion channel models can

be accurately approximated by SDE models. The stochastic behavior of the Markov chain based HH model with even as few as 60 Na^+ channels and 18 K^+ channels can be well approximated by SDE model. The recreation of the numerical results based on the HH model is given the Figure 5.2, Figure 5.3 Figure 5.2 and Figure 5.3 (Goldwyn et al., 2011b). Figure 5.2 and Figure 5.3 show the mean and standard deviation of

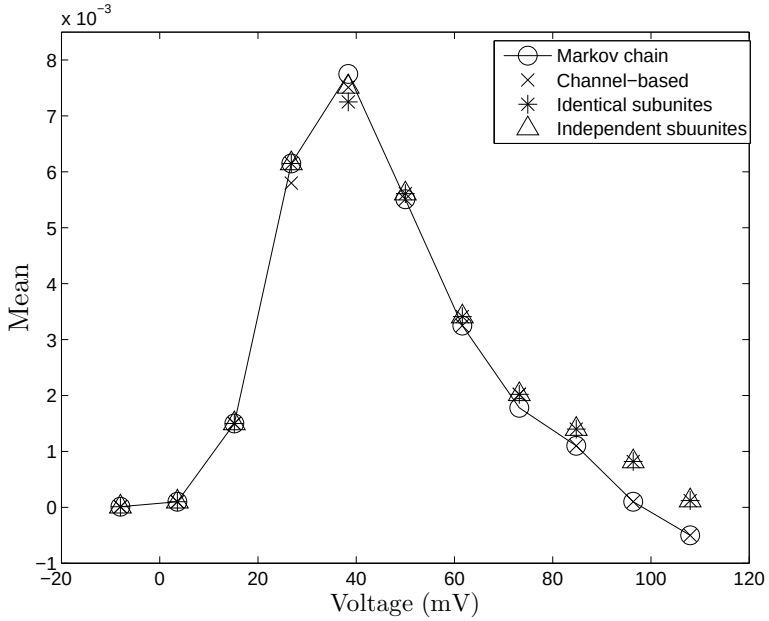

FIGURE 5.2: Mean value of fraction of open Na^+ channels. The y axis is the proportion of open channels. The x axis is the corresponding voltage. The channel-based SDE perfectly approximates Markov chain model. The number of Na^+ channel is 600. The number of K^+ channel is 180. This figure is recreated based on Goldwyn et al. (2011b).

the fraction of open Na^+ channel of the three Na^+ channel SDE models. The mean of Na^+ channel behavior can be accurately captured by all the three SDE models, but the standard deviations of the two subunit based SDE models are distinct from the Markov chain model. Only the channel based model captures the standard deviation of the Na^+ Markov chain model.

Figure 5.4 and Figure 5.5 illustrate the mean and standard deviation of the fraction of open K^+ channel. The mean of K^+ channel behavior can be captured well by all of the SDE models, but the two subunit-based SDE models still fail to capture the behavior of the standard deviation of the Markov chain model. The channel based model still captures the standard deviation of the K^+ Markov chain model.

These results suggest that the channel based SDE model provides an accurate approximation to the Markov chain model. In the following section, we reformulate the SAN ion channel model using the channel-based SDE ion channel model to build stochastic single cell SAN models and stochastic multi-scale SAN models. Based on the accurate approximation of the channel-based model, the stochastic single cell models and stochastic multi-scale models should capture the variability of ion channel noise at the cellular

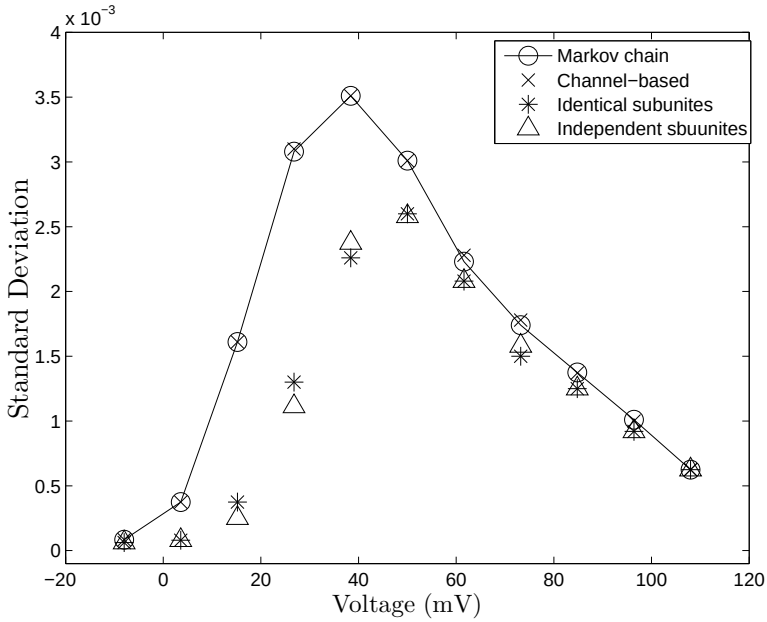

FIGURE 5.3: Standard deviation of fraction of open Na^+ channels. The y axis is the standard deviation of the open channel fraction. The x axis is the corresponding voltage. The channel-based SDE perfectly approximates Markov chain model. The number of Na^+ channel is 600. The number of K^+ channel is 180. This figure is recreated based on Goldwyn et al. (2011b).

and tissue level.

5.4 Simulation of Channel-based SDE Model

In this section, we consider classic HH model (Hodgkin and Huxley, 1952) as an example to illustrate the formulation of the channel-based SDE model from an ODE model. The simulation details of the channel-based SDE HH model is also introduced in this section. In the later section, we only introduce ion channel reformulations of the SAN ion channel.

In HH model, the Markov state diagram of the Na^+ channel is shown as

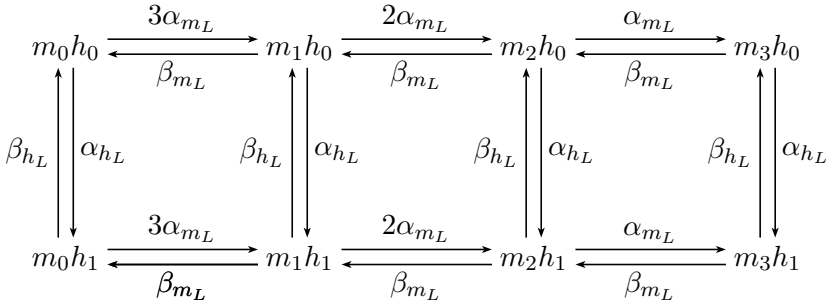

In the Na^+ channel, there are eight states in the diagram. Each state can be shown as m_ih_j which stands for i open m subunits and j open h subunits. For instance, m_3h_1 indicates that three m subunits are all open and one h subunit is open, so m_3h_1 is the

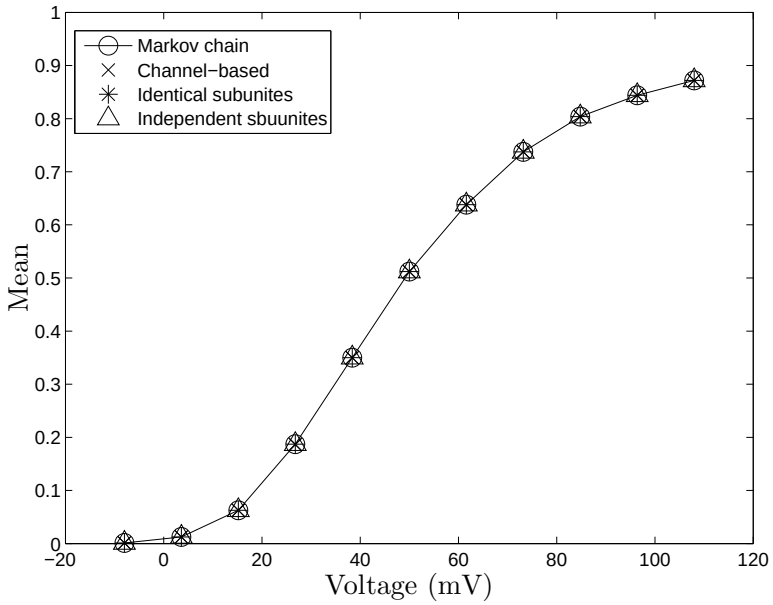

FIGURE 5.4: Mean value of fraction of open K^+ Channels. The y axis is the proportion of open channels. The x axis is the corresponding voltage. All SDE approaches approximates Markov chain model well. The number of Na^+ channel is 600. The number of K^+ channel is 180. This figure is recreated based on Goldwyn et al. (2011b).

open state of a Na^+ channel. The channel based SDE HH model can be shown as

$$C\frac{\mathrm{d}\mathbf{V}}{\mathrm{d}t} = -g_{\mathrm{Na}}y_{31}(V - E_{\mathrm{Na}}) - g_{\mathrm{K}}x_4(V - E_{\mathrm{K}}) - g_{\mathrm{L}}(V - E_{\mathrm{L}}) + I \tag{5.9}$$

$$\frac{\mathrm{d}\mathbf{x}}{\mathrm{d}t} = A_{\mathrm{K}}\mathbf{x} + S_{\mathrm{K}}\xi_{\mathrm{K}} \tag{5.10}$$

$$\frac{\mathrm{d}\mathbf{y}}{\mathrm{d}t} = A_{\mathrm{Na}}\mathbf{y} + S_{\mathrm{Na}}\xi_{\mathrm{Na}}. \tag{5.11}$$

The vector $\mathbf{y}$ denoted as y_{ij} and represents the proportion of the open Na^+ channels with i open m subunits and j open h subunits, where $i = 0, 1, 2, 3$ and $j = 0$ or 1. The vector $\mathbf{y}$ satisfies the fact that $\sum_{i=0}^{3}\sum_{j=0}^{1} y_{ij} = 1$. The entries of $\mathbf{x}$ are denoted as x_i represents the proportion of the open K^+ channels with i open n subunits, where $i = 0, 1, 2, 3, 4$. The vector $\mathbf{x}$ satisfies the fact that $\sum_{i=0}^{4} x_i = 1$. The transition matrix A_{K} and A_{Na} are derived from the Markov state diagram of Na^+ and K^+ ion channel, respectively. The Markov state diagram of K channel has been shown previously by Equation 5.3. The corresponding transition matrix A_{K} is given in Equation 5.5. The diffusion matrix D_{K} has also been introduced. Let us define that $\mathbf{y} = [y_{10}, y_{20}, y_{30}, y_{01}, y_{21}, y_{31}]^T$. The transition matrix A_{Na} is

$$A_{\mathrm{Na}} = \begin{bmatrix} -(2\alpha_m + \beta_m + \alpha_h) & 2\beta_m & 0 & 0 & \beta_h & 0 & 0 \\ 2\alpha_m & -(\alpha_m + 2\beta_m + \alpha_m) & 3\beta_m & 0 & 0 & 0 & 0 \\ 0 & \alpha_m & -(3\beta_m + \alpha_h) & 0 & 0 & 0 & \beta_h \\ & 0 & 0 & -(3\alpha_m + \beta_h) & \beta_m & 0 & 0 \\ & 0 & 0 & 2\alpha_m & -(3\alpha_m + \beta_m + \beta_h) & 2\beta_h & 0 \\ & 0 & 0 & 0 & 2\alpha_m & -(\alpha_m + 2\beta_m + \beta_h) & 3\beta_m \\ & 0 & 0 & 0 & 0 & \alpha_m & -(3\beta_m + \beta_h)0 \end{bmatrix}$$

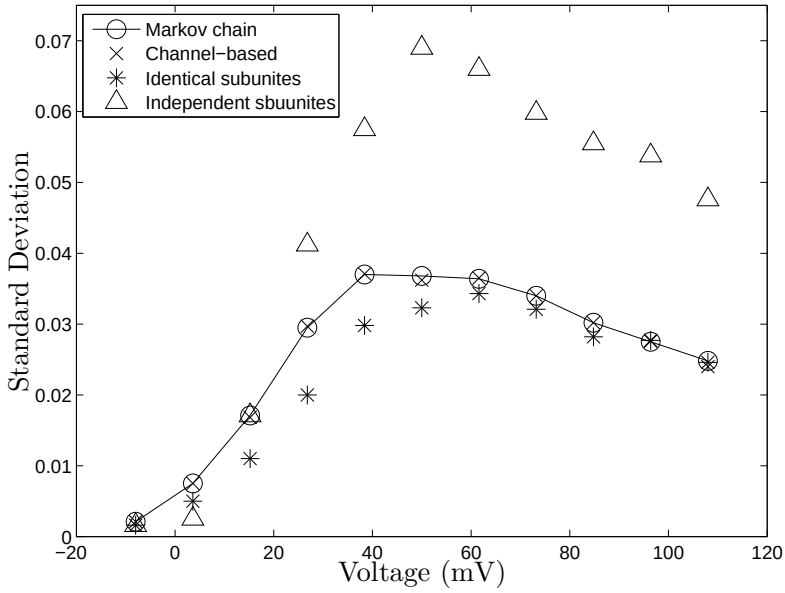

FIGURE 5.5: Standard deviation of fraction of open K^+ Channels. The y axis is the standard deviation of the open channel fraction. The x axis is the corresponding voltage. Only the channel-based SDE perfectly approximates Markov chain model. The number of Na^+ channel is 600. The number of K^+ channel is 180. This figure is recreated based on Goldwyn et al. (2011b).

where the diffusion matrix D_{Na} is

$$D_{\mathrm{Na}} = \frac{1}{N}\begin{bmatrix} \mathrm{d}_1 & -2(\alpha_m y + \beta_m y_{20}) & 0 & 0 & (\alpha_h y_{10} + \beta_h y_{11}) & 0 & 0 \\ -2(\alpha_m y_{10} + \beta_m y_{20}) & \mathrm{d}_2 & -(\alpha_m y_{20} + 3\beta_m y_{30}) 0 & 0 & 0 & (\alpha_h y_{20} + \beta_h y_{22}) & 0 \\ 0 & -(\alpha_m y_{20} + 3\beta_m y_{30}) & 0 & 0 & 0 & 0 & -(\alpha_h y_{30} + \beta_h y_{31}) \\ 0 & 0 & 0 & \mathrm{d}_4 & -(3\alpha_m y_{01} + \beta_m y_{11}) & 0 & 0 \\ -(\alpha_h y_{10} + \beta_h y_{11}) & 0 & 0 & -(3\alpha_m y_{01} + \beta_m y_{11}) & \mathrm{d}_5 & -2(\alpha_m y_{11} + \beta_m y_{21}) & 0 \\ 0 & -(\alpha_h y_{20} + \beta_h y_{21}) & 0 & 0 & -2(\alpha_m y_{11} + \beta_m y_{21}) & \mathrm{d}_6 & -(\alpha_m y_{21} + 3\beta_m y_{31}) \\ 0 & 0 & -(\alpha_h y_{30} + \beta_h y_{31}) & 0 & 0 & -(\alpha_m y_{21} + 3\beta_m y_{31}) & \mathrm{d}_7 \end{bmatrix}$$

where the elements in the matrix $\mathrm{D_{Na}}$ can be expressed as

$$\mathrm{d}_1 = 3\alpha_m y_{00} + (2\alpha_m + \beta_m + \alpha_h) y_{10} + 2\beta_m y_{20} + 2\beta_h y_{11} \tag{5.12}$$

$$\mathrm{d}_2 = 2\alpha_m y_{10} + (\alpha_m + 2\beta_m + \alpha_h) y_{30} + 3\beta_m y_{30} + 2\beta_h y_{21} \tag{5.13}$$

$$\mathrm{d}_3 = \alpha_m y_{20} + (3\beta_m + \alpha_h) y_{30} + \beta_h y_{31} \tag{5.14}$$

$$\mathrm{d}_4 = \alpha_h y_{00} + (3\alpha_h + \beta_h) y_{01} + \beta_m y_{11} \tag{5.15}$$

$$\mathrm{d}_5 = \alpha_h y_{10} + 3\alpha_m y_{01} + (2\alpha_m + 2\beta_m + \beta_h) y_{11} + 2\beta_m y_{21} \tag{5.16}$$

$$\mathrm{d}_6 = \alpha_h y_{20} + 2\alpha_m y_{11} + (\alpha_m + 2\beta_m + \beta_h) y_{21} + 3\beta_m y_{31} \tag{5.17}$$

$$\mathrm{d}_7 = \alpha_h y_{30} + \alpha_h y_{21} + (3\beta_m + \beta_h) y_{31} \tag{5.18}$$

The example of the channel-based SDE HH model shows that the reformulation of a classic HH scheme ion channel requires the Markov state diagram, the corresponding transition matrix A and the diffusion matrix D. A stochastic version of the HH model can be easily obtained from the ODE HH model, but the number of ion channels, N, is

an extra input needed for the stochastic model. The channel noise is simulated by the noise term S and ξ. In order to construct the channe-based SDE stochastic Zhang SAN model and Kurata model. For each type of ion channel, the following is necessary

1. obtain transition matrix A and the diffusion matrix D.

2. estimate of the number of ion channels N

In the following section, the reformulation of channel-based SDE model is presented.

5.5 Ion Channel Reformulation of SAN Models

As we shown in Section 5.3, channel-based SDE model is the best approximation to Markov chain model of ion channel. Goldwyn et al. (2011a) provide a formal method for obtaining a channel-based SDE model from master equation. However, they only derived the channel-based SDE models of I_{K} and I_{Na}. In order to build SDE SAN models, the ODE based cardiac ion channels need to be reformulated. Here we list these cardiac ion channels in Table 5.1. In this section, the reformulations of key SAN model ion channels are introduced. In this section, ODE SAN models (Zhang et al., 2000) (Kurata et al., 2002) are reformulated into corresponding SDE SAN models.

The reformation of ion channels Ca^{2+}involves the L-type Ca^{2+} ion current $I_{\mathrm{Ca,L}}$, the T-type ion current $I_{\mathrm{Ca,T}}$, the rapid delayed rectifying current $I_{\mathrm{K,r}}$, the 4-AP-sensitive currents I_{to} and I_{sus}, the slow delayed rectifying current $I_{\mathrm{K,s}}$ and the hyperpolarization-activated current I_{h}. The seven ion currents consist of ion channel gates which regulate the stochastic behavior of the ion currents. The background currents, ion pumps and the exchanger currents do not consist of ion channel subunits, so these currents are not reformulated.

5.5.1 L-Type Ca^{2+} Ion Channel Reformulation

The L-type Ca^{2+} ion current is expressed as (Zhang et al., 2000)

$$I_{\mathrm{Ca,L}} = g_{\mathrm{Ca,L}}[f_{\mathrm{L}}d_{\mathrm{L}} + \frac{0.006}{1+\exp -(V+14.1)/6}](V - E_{\mathrm{Ca,L}}) \tag{5.19}$$

$$= g_{\mathrm{Ca,L}}f_{\mathrm{L}}d_{\mathrm{L}}(V - E_{\mathrm{Ca,L}}) + g_{\mathrm{Ca,L}}\frac{0.006}{1+\exp -(V+14.1)/6}(V - E_{\mathrm{Ca,L}}) \tag{5.20}$$

Equation 5.20 shows that only the first term on the right side of the equation has the gating variables. The second term can be considered as a constant at a given membrane voltage.

TABLE 5.1: Ion Currents involved in the SDE reformulation of the Zhang SAN model and the Kurata model. ✓ stands for the incorporation of a current.

Ion Current	Zhang central SAN model	Zhang peripheral SAN model	Kurata model
I_{Na}	-	✓	-
$I_{\mathrm{Ca,L}}$	✓	✓	✓
$I_{\mathrm{Ca,T}}$	✓	✓	✓
$I_{\mathrm{K,r}}$	✓	✓	✓
I_{to}	✓	✓	✓
I_{sus}	✓	✓	✓
I_{st}	-	-	✓
I_{h}	✓	✓	✓

The Markovian state diagram of L-type Ca^{2+} ion current is given as

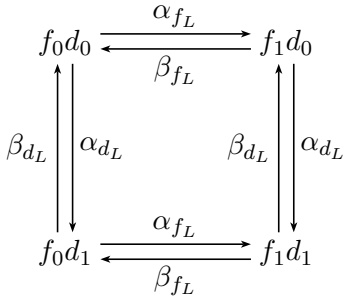

The transition matrix $A_{\mathrm{Ca,L}}$ of L-type Ca^{2+} ion current is

$$A_{\mathrm{Ca,L}} = \begin{bmatrix} -(\alpha_{f_L}+\alpha_{d_L}) & \beta_{f_L} & \beta_{d_L} & 0 \\ \alpha_{f_L} & -(\beta_{f_L}+\alpha) & 0 & \beta_{d_L} \\ \alpha_{d_L} & 0 & -(\alpha_{f_L}+\beta_{d_L}) & \beta_{f_L} \\ 0 & \alpha_{d_L} & \alpha_{f_L} & -(\beta_{d_L}+\beta_{f_L}) \end{bmatrix} \tag{5.21}$$

The diffusion matrix $D_{\mathrm{Ca,L}}$ of the L-type Ca^{2+} ion channel is

$$D_{\mathrm{Ca,L}} = \frac{1}{N}\begin{bmatrix} x_{00}(\alpha_{f_L}+\alpha_{d_L})+x_{10}\beta_{f_L}+x_{01}\beta_{d_L} & -(x_{00}\alpha_{f_L}+x_{10}\beta_{f_L}) & -(x_{00}\alpha_{d_L}+x_{10}\beta_{d_L}) & 0 \\ -(x_{00}\alpha_{f_L}+x_{10}\beta_{f_L}) & x_{00}\alpha_{f_L}+x_{10}(\beta_{f_L}+\alpha_{d_L})+x_{11}\beta_{d_L} & 0 & -(x_{11}\beta_{d_L}+x_{10}\alpha_{d_L}) \\ -(x_{00}\alpha_{d_L}+x_{01}\beta_{d_L}) & 0 & x_{00}\alpha_{d_L}+x_{11}\beta_{f_L}+x_{01}(\beta_{d_L}+\alpha_{f_L}) & -(x_{11}\beta_{f_L}+x_{01}\alpha_{f_L}) \\ 0 & -(x_{10}\alpha_{d_L}+x_{11}\beta_{d_L}) & -(x_{01}\alpha_{f_L}+x_{11}\beta_{d_L}) & x_{10}\alpha_{d_L}+x_{01}\alpha_{f_L}+x_{11}(\beta_{f_L}+\beta_{d_L}) \end{bmatrix}$$

The vector $\mathbf{x}$ denoted as x_{ij} represents the proportion of the open channels with i open f_{L} subunits and j open d_{L} subunits.

5.5.2 T-Type Ca^{2+} Ion Channel Reformulation

The T-type Ca^{2+} ion current is given as (Zhang et al., 2000)

$$I_{\mathrm{Ca,T}} = g_{\mathrm{Ca,T}} f_{\mathrm{T}} d_{\mathrm{T}} (V - E_{\mathrm{Ca,T}}) \tag{5.22}$$

The corresponding Markovian state diagram of T-type Ca^{2+} ion current is given as

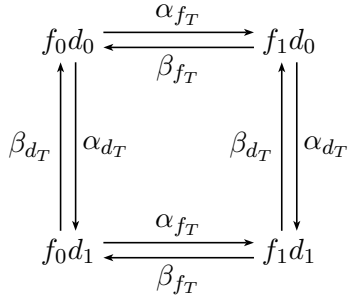

The transition matrix $A_{\mathrm{Ca,T}}$ of T-type Ca^{2+} ion current is

$$A_{\mathrm{Ca,T}} = \begin{bmatrix} -(\alpha_{f_T} + \alpha_{d_T}) & \beta_{f_T} & \beta_{d_T} & 0 \\ \alpha_{f_T} & -(\beta_{f_T} + \alpha_{d_T}) & 0 & \beta_{d_T} \\ \alpha_{d_T} & 0 & -(\alpha_{f_T} + \beta_{d_T}) & \beta_{f_T} \\ 0 & \alpha_{d_T} & \alpha_{f_T} & -(\beta_{d_T} + \beta_{f_T}) \end{bmatrix} \tag{5.23}$$

The diffusion matrix D of T-type Ca^{2+} ion channel is

$$D_{\mathrm{Ca,T}} = \frac{1}{N} \begin{bmatrix} x_{00}(\alpha_{f_T} + \alpha_{d_T}) + x_{10}\beta_{f_T} + x_{01}\beta_{d_T} & -(x_{00}\alpha_{f_T} + x_{10}\beta_{f_T}) & -(x_{00}\alpha_{d_T} + x_{10}\beta_{d_T}) & 0 \\ -(x_{00}\alpha_{f_T} + x_{10}\beta_{f_T}) & x_{00}\alpha_{f_T} + x_{10}(\beta_{f_T} + \alpha_{d_T}) + x_{11}\beta_{d_T} & 0 & -(x_{11}\beta_{d_T} + x_{10}\alpha_{d_T}) \\ -(x_{00}\alpha_{d_T} + x_{01}\beta_{d_T}) & 0 & x_{00}\alpha_{d_T} + x_{11}\beta_{f_T} + x_{01}(\beta_{d_T} + \alpha_{f_T}) & -(x_{11}\beta_{f_T} + x_{01}\alpha_{f_T}) \\ 0 & -(x_{10}\alpha_{d_T} + x_{11}\beta_{d_T}) & -(x_{01}\alpha_{f_T} + x_{11}\beta_{d_T}) & x_{10}\alpha_{d_T} + x_{01}\alpha_{f_T} + x_{11}(\beta_{f_T} + \beta_{d_T}) \end{bmatrix}$$

The vector $\mathbf{x}$ denoted as x_{ij} represents the proportion of the open channels with i open f_{T} subunits and j open d_{T} subunits.

5.5.3 Transient and Sustained Components of 4-AP-sensitive Ion Channel (i_{to} and i_{sus}) Reformulation

The expression of the transient and sustained components of 4-AP-sensitive currents (i_{to} and i_{sus}) is given as (Zhang et al., 2000)

$$I_{\mathrm{to}} = g_{\mathrm{to}} qr(V - E_{\mathrm{K}}), \tag{5.24}$$

$$I_{\mathrm{sus}} = g_{\mathrm{sus}} r(V - E_{\mathrm{K}}), \tag{5.25}$$

where q and r are the subunit variables, and the variable r regulates i_{to} and i_{sus} simultaneously.

The Markovian state diagram of the transient component of 4-AP-sensitive ion channel

(i_{to} current) is given as

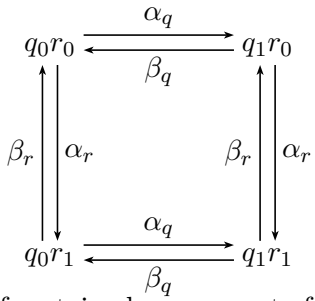

The Markovian state diagram of sustained component of 4-AP-sensitive ion channel (i_{sus} current) is given as

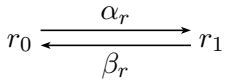

The transition matrix A of the transient component of 4-AP-sensitive ion channel is

$$A_{\text{to}} = \begin{bmatrix} -(\alpha_q + \alpha_r) & \beta_q & \beta_r & 0 \\ \alpha_q & -(\beta_q + \alpha_r) & 0 & \beta_r \\ \alpha_r & 0 & -(\alpha_q + \beta_r) & \beta_q \\ 0 & \alpha_r & \alpha_q & -(\beta_r + \beta_q) \end{bmatrix} \tag{5.26}$$

The transition matrix A_{sus} of the sustained component of 4-AP-sensitive ion channel is

$$A_{\text{sus}} = \begin{bmatrix} -\alpha_r & \beta r \\ \alpha_r & -\beta r \end{bmatrix} \tag{5.27}$$

The diffusion matrix D_{to} of the transient component of 4-AP-sensitive ion channel is

$$D_{\text{to}} = \frac{1}{N} \begin{bmatrix} x_{00}(\alpha_q + \alpha_r) + x_{10}\beta_q + x_{01}\beta_r & -(x_{00}\alpha_q + x_{10}\beta_q) & -(x_{00}\alpha_r + x_{10}\beta_r) & 0 \\ -(x_{00}\alpha_q + x_{10}\beta_q) & x_{00}\alpha_q + x_{10}(\beta_q + \alpha_r) + x_{11}\beta_r & 0 & -(x_{11}\beta_r + x_{10}\alpha_r) \\ -(x_{00}\alpha_r + x_{01}\beta_r) & 0 & x_{00}\alpha_r + x_{11}\beta_q + x_{01}(\beta_r + \alpha_q) & -(x_{11}\beta_q + x_{01}\alpha_q) \\ 0 & -(x_{10}\alpha_r + x_{11}\beta_r) & -(x_{01}\alpha_q + x_{11}\beta_r) & x_{10}\alpha_r + x_{01}\alpha_q + x_{11}(\beta_q + \beta_r) \end{bmatrix}$$

The vector $\mathbf{x}$ in the matrix D_{to} denoted as x_{ij} represents the proportion of the open channels with i open q subunits and j open r subunits.

The diffusion matrix D_{sus} of the sustained component of 4-AP-sensitive ion channel is

$$D_{\text{sus}} = \frac{1}{N} \begin{bmatrix} x_0\alpha_r + x_1\beta_r & -(x_0\alpha_r + r_1\beta_r) \\ -(x_0\alpha_r + x_1\beta_r) & x_0\alpha_r + r_1\beta_r \end{bmatrix}$$

The vector $\mathbf{x}$ denoted as $[x_0,\ x_1]$ represents the proportion of the close and the open channel respectively.

5.5.4 Rapid Delayed Rectifying K^+ Ion Channel Reformulation

The rapid delayed rectifying K^+ current $i_{K,r}$ is given as (Zhang et al., 2000)

$$I_{K,r} = g_{K,r}[(1 - F_{K,r})p_{a,f} + F_{K,r}p_{a,s}]p_i(V - E_K), \tag{5.28}$$

where $p_{a,f}$ and $p_{a,s}$ are the subunit variables, and $F_{K,r}$ is a constant. We consider $F_{K,r}$ = 0.4. The Equation 5.28 can be rewritten as

$$I_{K,r} = 0.6g_{K,r}p_{a,f}p_i + 0.4g_{K,r}p_{a,s}p_i(V - E_K). \tag{5.29}$$

Hence, we can consider that $I_{K,r}$ consist two ion currents $I_{K,r1} = 0.6g_{K,r}p_{a,f}p_i$ and $I_{K,r2} = 0.4g_{K,r}p_{a,s}p_i(V - E_K)$. $I_{K,r1}$ is gated by subunit variable $p_{a,f}$ and p_i. $I_{K,r2}$ is gated by subunit variable $p_{a,s}$ and p_i.

The Markovian state diagram of $I_{K,r1}$ current is given as

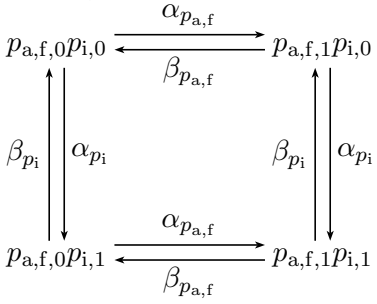

The Markovian state diagram of $I_{K,r2}$ current is given as

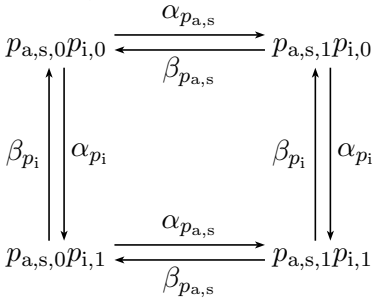

The transition matrix $A_{K,r1}$ of the $I_{K,r1}$ current is

$$A_{K,r1} = \begin{bmatrix} -(\alpha_{p_{a,f}} + \alpha_d) & \beta_{p_{a,f}} & \beta_{p_i} & 0 \\ \alpha_{p_{a,f}} & -(\beta_{p_{a,f}} + \alpha_{p_i}) & 0 & \beta_{p_i} \\ \alpha_{p_i} & 0 & -(\alpha_{p_{a,f}} + \beta_{p_i}) & \beta_{p_{a,f}} \\ 0 & \alpha_{p_i} & \alpha_{p_{a,f}} & -(\beta_{p_i} + \beta_{p_{a,f}}) \end{bmatrix} \tag{5.30}$$

The diffusion matrix $D_{K,r1}$ of the $I_{K,r1}$ current is

$$D_{K,r1} = \frac{1}{N} \begin{bmatrix} x_{00}(\alpha_{p_{a,f}} + \alpha_{p_i}) + x_{10}\beta_{p_{a,f}} + x_{01}\beta_{p_i} & -(x_{00}\alpha_{p_{a,f}} + x_{10}\beta_{p_{a,f}}) & -(x_{00}\alpha_{p_i} + x_{10}\beta_{p_i}) & 0 \\ -(x_{00}\alpha_{p_{a,f}} + x_{10}\beta_{p_{a,f}}) & x_{00}\alpha_{p_{a,f}} + x_{10}(\beta_{p_{a,f}} + \alpha_{p_i}) + x_{11}\beta_{p_i} & 0 & -(x_{11}\beta_{p_i} + x_{10}\alpha_{p_i}) \\ -(x_{00}\alpha_{p_i} + x_{01}\beta_{p_i}) & 0 & x_{00}\alpha_{p_i} + x_{11}\beta_{p_{a,f}} + x_{01}(\beta_{p_i} + \alpha_{p_{a,f}}) & -(x_{11}\beta_{p_{a,f}} + x_{01}\alpha_{p_{a,f}}) \\ 0 & -(x_{10}\alpha_{p_i} + x_{11}\beta_{p_i}) & -(x_{01}\alpha_{p_{a,f}} + x_{11}\beta_{p_i}) & x_{10}\alpha_{p_i} + x_{01}\alpha_{p_{a,f}} + x_{11}(\beta_{p_{a,f}} + \beta_{p_i}) \end{bmatrix}$$

The vector $\mathbf{x}$ denoted as x_{ij} represents the proportion of the open channels with i open $p_{\mathrm{a,f}}$ subunits and j open p_{i} subunits.

The transition matrix $A_{\mathrm{K,r2}}$ of the $I_{\mathrm{K,r2}}$ current is

$$A_{\mathrm{K,r2}} = \begin{bmatrix} -(\alpha_{p_{\mathrm{a,s}}} + \alpha_{p_{\mathrm{i}}}) & \beta_{p_{\mathrm{a,s}}} & \beta_{p_{\mathrm{i}}} & 0 \\ \alpha_{p_{\mathrm{a,s}}} & -(\beta_{p_{\mathrm{a,s}}} + \alpha_{p_{\mathrm{i}}}) & 0 & \beta_{p_{\mathrm{i}}} \\ \alpha_{p_{\mathrm{i}}} & 0 & -(\alpha_{p_{\mathrm{a,s}}} + \beta_{p_{\mathrm{i}}}) & \beta_{p_{\mathrm{a,s}}} \\ 0 & \alpha_{p_{\mathrm{i}}} & \alpha_{p_{\mathrm{a,s}}} & -(\beta_{p_{\mathrm{i}}} + \beta_{p_{\mathrm{a,s}}}) \end{bmatrix} \tag{5.31}$$

The diffusion matrix D of the $I_{\mathrm{K,r2}}$ current is

$$D_{\mathrm{K,r2}} = \frac{1}{N} \begin{bmatrix} x_{00}(\alpha_{p_{\mathrm{a,s}}} + \alpha_{p_{\mathrm{i}}}) + x_{10}\beta_{p_{\mathrm{a,s}}} + x_{01}\beta_{p_{\mathrm{i}}} & -(x_{00}\alpha_{p_{\mathrm{a,s}}} + x_{10}\beta_{p_{\mathrm{a,s}}}) & -(x_{00}\alpha_{p_{\mathrm{i}}} + x_{10}\beta_{p_{\mathrm{i}}}) & 0 \\ -(x_{00}\alpha_{p_{\mathrm{a,s}}} + x_{10}\beta_{p_{\mathrm{a,s}}}) & x_{00}\alpha_{p_{\mathrm{a,s}}} + x_{10}(\beta_{p_{\mathrm{a,s}}} + \alpha_{p_{\mathrm{i}}}) + x_{11}\beta_{p_{\mathrm{i}}} & 0 & -(x_{11}\beta_{p_{\mathrm{i}}} + x_{10}\alpha_{p_{\mathrm{i}}}) \\ -(x_{00}\alpha_{p_{\mathrm{i}}} + x_{01}\beta_{p_{\mathrm{i}}}) & 0 & x_{00}\alpha_{p_{\mathrm{i}}} + x_{11}\beta_{p_{\mathrm{a,s}}} + x_{01}(\beta_{p_{\mathrm{i}}} + \alpha_{p_{\mathrm{a,s}}}) & -(x_{11}\beta_{p_{\mathrm{a,s}}} + x_{01}\alpha_{p_{\mathrm{a,s}}}) \\ 0 & -(x_{10}\alpha_{p_{\mathrm{i}}} + x_{11}\beta_{p_{\mathrm{i}}}) & -(x_{01}\alpha_{p_{\mathrm{a,s}}} + x_{11}\beta_{p_{\mathrm{i}}}) & x_{10}\alpha_{p_{\mathrm{i}}} + x_{01}\alpha_{p_{\mathrm{a,s}}} + x_{11}(\beta_{p_{\mathrm{a,s}}} + \beta_{p_{\mathrm{i}}}) \end{bmatrix}$$

The vector $\mathbf{x}$ denoted as x_{ij} represents the proportion of the open channels with i open $p_{\mathrm{a,s}}$ subunits and j open p_{i} subunits.

5.5.5 Slow Delayed Rectifying K^+ Ion Channel Reformulation

The rapid delayed rectifying K^+ current $i_{\mathrm{K,s}}$ is given as (Zhang et al., 2000)

$$I_{\mathrm{K,s}} = g_{\mathrm{K,s}} x_{\mathrm{s}}^2 (V - E_{\mathrm{K,s}}), \tag{5.32}$$

The Markovian state diagram of the $i_{\mathrm{K,s}}$ current is given as

$$x_{\mathrm{s0}} \underset{\beta_{\mathrm{x_s}}}{\overset{2\alpha_{\mathrm{x_s}}}{\rightleftharpoons}} x_{\mathrm{s1}} \underset{2\beta_{\mathrm{x_s}}}{\overset{\alpha_{\mathrm{x_s}}}{\rightleftharpoons}} x_{\mathrm{s2}}$$

The transition matrix $A_{\mathrm{K,s}}$ of the ion channel is

$$A_{\mathrm{K,s}} = \begin{bmatrix} -2\alpha_{\mathrm{x_s}} & \beta_{\mathrm{x_s}} & 0 \\ 2\alpha_{\mathrm{x_s}} & -\beta_{\mathrm{x_s}} & 2\beta_{\mathrm{x_s}} \\ 0 & \alpha_{\mathrm{x_s}} & -2\beta_{\mathrm{x_s}} \end{bmatrix} \tag{5.33}$$

The diffusion matrix $D_{\mathrm{K,s}}$ of the ion channel is

$$D_{\mathrm{K,s}} = \frac{1}{N} \begin{bmatrix} x_0 2\alpha_{\mathrm{x_s}} + x_1\beta_{\mathrm{x_s}} & -(x_0 2\alpha_{\mathrm{x_s}} + x_1\beta_{\mathrm{x_s}}) & 0 \\ -(x_0 2\alpha_{\mathrm{x_s}} + x_1\beta_{\mathrm{x_s}}) & x_0 2\alpha_{\mathrm{x_s}} + x_1(\beta_{\mathrm{x_s}} + \alpha_{\mathrm{x_s}}) + x_2 2\beta_{\mathrm{x_s}} & -(x_1\alpha_{\mathrm{x_s}} + x_2 2\beta_{\mathrm{x_s}}) \\ 0 & -(x_1\alpha_{\mathrm{x_s}} + x_2 2\beta_{\mathrm{x_s}}\beta_{\mathrm{x_s}}) & x_1\alpha_{\mathrm{x_s}} + x_2\beta_{\mathrm{x_s}} \end{bmatrix}$$

The vector **x** is expressed as [x_0, x_1, x_2]. The term x_i represents the proportion of the open channels with i open x_s subunits.

5.5.6 Hyperpolarization-activated Channel Reformulation

The hyperpolarization-activated current i_h consists of two currents $I_\mathrm{h,Na}$ and $I_\mathrm{h,K}$ which are shown as (Zhang et al., 2000)

$$I_\mathrm{h,Na} = g_\mathrm{h,Na} y (V - E_\mathrm{Na}) \tag{5.34}$$

$$I_\mathrm{h,K} = g_\mathrm{h,K} y (V - E_\mathrm{K}), \tag{5.35}$$

where y is the subunit variable of the two variable. The subunit variable y controls both $i_\mathrm{h,Na}$ and $i_\mathrm{h,K}$. The Markovian state diagram of $i_\mathrm{h,Na}$ and $i_\mathrm{h,K}$ is given as

$$y_0 \underset{\beta_y}{\overset{\alpha_y}{\rightleftharpoons}} y_1$$

The transition matrix A_h of the current $i_\mathrm{h,Na}$ and $i_\mathrm{h,K}$ is

$$A_\mathrm{h} = \begin{bmatrix} -\alpha_h & \beta_h \\ \alpha_h & -\beta_h \end{bmatrix} \tag{5.36}$$

The diffusion matrix D_h of the $i_\mathrm{h,Na}$ and $i_\mathrm{h,K}$ currents is given as

$$D_\mathrm{h} = \frac{1}{N} \begin{bmatrix} x_0\alpha_y + x_1\beta_y & -(x_0\alpha_y + x_1\beta_y) \\ -(x_0\alpha_r + x_1\beta_y) & x_0\alpha_r + x_1\beta_y \end{bmatrix}$$

The vector **x** denoted as [x_0, x_1] The term x_0 and x_1 represents the proportion of the close and the open channels respectively.

5.5.7 Kurata SAN Model Reformulation

A channel-based SDE Kurata SAN model is reformulated from the original ODE model (Kurata et al., 2002). The ODE SAN model are reformulated into corresponding SDE SAN models. In Kurata model, the reformation of ion channels involves the L-type Ca^{2+} ion current $I_\mathrm{Ca,L}$, the T-type Ca^{2+} ion current $I_\mathrm{Ca,T}$, the rapid delayed rectifying current $I_\mathrm{K,r}$, the sustained inward current I_st, the 4-AP-sensitive currents I_to and I_sus, the slow delayed rectifying current $I_\mathrm{K,s}$ and the hyperpolarization-activated current I_h.

The currents $I_{\mathrm{Ca,T}}$, I_{to}, I_{sus}, ,$I_{\mathrm{K,r}}$, $I_{\mathrm{K,s}}$ and I_{h} have the same channel-based SDE formulations as the Zhang SAN model. Therefore, only three currents I_{st}, $I_{\mathrm{Ca,L}}$ and I_{h} are reformulated in the following content.

5.5.7.1 Reformulation of the Sustained Inward Channel

The sustained inward current I_{st} is a novel current incorporated by the Kurata model. The expression of the current is given as

$$I_{\mathrm{st}} = g_{\mathrm{st}} q_{\mathrm{a}} q_{\mathrm{i}} (V - E_{\mathrm{st}}), \tag{5.37}$$

The Markovian state diagram of the sustained inward ion channel is given as

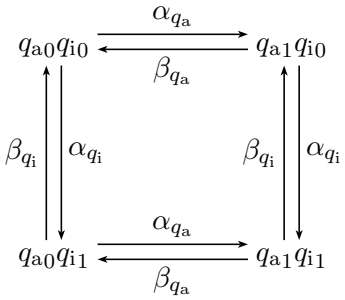

The transition matrix A_{st} of the sustained inward ion channel is

$$A_{\mathrm{st}} = \begin{bmatrix} -(\alpha_{q_{\mathrm{a}}} + \alpha_{q_{\mathrm{i}}}) & \beta_{q_{\mathrm{a}}} & \beta_{q_{\mathrm{i}}} & 0 \\ \alpha_{q_{\mathrm{a}}} & -(\beta_{q_{\mathrm{a}}} + \alpha) & 0 & \beta_{q_{\mathrm{i}}} \\ \alpha_{q_{\mathrm{i}}} & 0 & -(\alpha_{q_{\mathrm{a}}} + \beta_{q_{\mathrm{i}}}) & \beta_{q_{\mathrm{a}}} \\ 0 & \alpha_{q_{\mathrm{i}}} & \alpha_{q_{\mathrm{a}}} & -(\beta_{q_{\mathrm{i}}} + \beta_{q_{\mathrm{a}}}) \end{bmatrix} \tag{5.38}$$

The diffusion matrix D_{st} of the sustained inward ion channel is

$$D_{\mathrm{st}} = \frac{1}{N} \begin{bmatrix} x_{00}(\alpha_{q_{\mathrm{a}}} + \alpha_{q_{\mathrm{i}}}) + x_{10}\beta_{q_{\mathrm{a}}} + x_{01}\beta_{q_{\mathrm{i}}} & -(x_{00}\alpha_{q_{\mathrm{a}}} + x_{10}\beta_{q_{\mathrm{a}}}) & -(x_{00}\alpha_{q_{\mathrm{i}}} + x_{10}\beta_{q_{\mathrm{i}}}) & 0 \\ -(x_{00}\alpha_{q_{\mathrm{a}}} + x_{10}\beta_{q_{\mathrm{a}}}) & x_{00}\alpha_{q_{\mathrm{a}}} + x_{10}(\beta_{q_{\mathrm{a}}} + \alpha_{q_{\mathrm{i}}}) + x_{11}\beta_{q_{\mathrm{i}}} & 0 & -(x_{11}\beta_{q_{\mathrm{i}}} + x_{10}\alpha_{q_{\mathrm{i}}}) \\ -(x_{00}\alpha_{q_{\mathrm{i}}} + x_{01}\beta_{q_{\mathrm{i}}}) & 0 & x_{00}\alpha_{q_{\mathrm{i}}} + x_{11}\beta_{q_{\mathrm{a}}} + x_{01}(\beta_{q_{\mathrm{i}}} + \alpha_{q_{\mathrm{a}}}) & -(x_{11}\beta_{q_{\mathrm{a}}} + x_{01}\alpha_{q_{\mathrm{a}}}) \\ 0 & -(x_{10}\alpha_{q_{\mathrm{i}}} + x_{11}\beta_{q_{\mathrm{i}}}) & -(x_{01}\alpha_{q_{\mathrm{a}}} + x_{11}\beta_{q_{\mathrm{i}}}) & x_{10}\alpha_{q_{\mathrm{i}}} + x_{01}\alpha_{q_{\mathrm{a}}} + x_{11}(\beta_{q_{\mathrm{a}}} + \beta_{q_{\mathrm{i}}}) \end{bmatrix}$$

The vector $\mathbf{x}$ denoted as x_{ij} represents the proportion of the open channels with i open q_{a} subunits and j open q_{i} subunits.

5.5.7.2 Reformulation of L-type Ca^{2+} Ion Channel of Kurata Model

The formulation of the current $I_{\mathrm{Ca,L}}$ is distinct from the Zhang SAN model. The L-type Ca^{2+} ion current is expressed as (Zhang et al., 2000)

$$I_{\mathrm{Ca,L}} = g_{\mathrm{Ca,L}} f_{\mathrm{L}} d_{\mathrm{L}} f_{\mathrm{Ca}} (V - E_{\mathrm{Ca,L}}), \tag{5.39}$$

where f_{L}, d_{L} and f_{Ca} are gate variables. As three types of ion gates are consisted in the ion channel, the corresponding Markov diagram should be a three dimensional diagram has not been discussed in the literature of the SDE reformulation of ion channels. Hence, we only consider the stochastic behavior of two ion gates, the stochastic behavior of f_{Ca} is ignored. The corresponding ion current equation is

$$I_{\mathrm{Ca,L}} = g_{\mathrm{Ca,L}} x_{11} f_{\mathrm{Ca}} (V - E_{\mathrm{Ca,L}}), \tag{5.40}$$

where x_{11} is the proportion of the open channels with both open f_{L} subunit and open d_{L} subunit. The corresponding transition matrix $A_{\mathrm{Ca,L}}$ and the diffusion matrix $D_{\mathrm{Ca,L}}$ are same to the SDE Zhang $I_{\mathrm{Ca,L}}$ current.

5.5.7.3 Reformulation of the hyperpolarization-activated current I_{h}

In Kurata's model, the formulation of current I_{h} is distinct from the Zhang SAN model. The ion current equation is given as

$$I_{\mathrm{h}} = g_{\mathrm{h,K}} y^2 (V - E_{\mathrm{K}}) + g_{\mathrm{h,Na}} y^2 (V - E_{\mathrm{Na}}), \tag{5.41}$$

The Markovian state diagram of the hyperpolarization ion channel is given as

$$y_0 \underset{\beta_{\mathrm{y}}}{\overset{2\alpha_{\mathrm{y}}}{\rightleftarrows}} y_1 \underset{2\beta_{\mathrm{y}}}{\overset{\alpha_{\mathrm{y}}}{\rightleftarrows}} y_2$$

The transition matrix A_{h} of the the hyperpolarization ion channel is

$$A_{\mathrm{h}} = \begin{bmatrix} -2\alpha_{\mathrm{y}} & \beta_{\mathrm{y}} & 0 \\ 2\alpha_{\mathrm{y}} & -\beta_{\mathrm{y}} & 2\beta_{\mathrm{y}} \\ 0 & \alpha_{\mathrm{y}} & -2\beta_{\mathrm{y}} \end{bmatrix} \tag{5.42}$$

The diffusion matrix D_{h} of the hyperpolarization ion channel is

$$D_{\mathrm{h}} = \frac{1}{N} \begin{bmatrix} x_0 2\alpha_{\mathrm{y}} + x_1 \beta_{\mathrm{y}} & -(x_0 2\alpha_{\mathrm{y}} + x_1 \beta_{\mathrm{y}}) & 0 \\ -(x_0 2\alpha_{\mathrm{y}} + x_1 \beta_{\mathrm{y}}) & x_0 2\alpha_{\mathrm{y}} + x_1(\beta_{\mathrm{y}} + \alpha_{\mathrm{y}}) + x_2 2\beta_{\mathrm{y}} & -(x_1 \alpha_{\mathrm{y}} + x_2 2\beta_{\mathrm{y}}) \\ 0 & -(x_1 \alpha_{\mathrm{y}} + x_2 2\beta_{\mathrm{y}} \beta_{\mathrm{y}}) & x_1 \alpha_{\mathrm{y}} + x_2 \beta_{\mathrm{y}} \end{bmatrix}$$

The vector $\mathbf{x}$ is expressed as $[x_0, x_1, x_2\ ]$. The term x_{i} represents the proportion of the open channels with i open y subunits.

5.6 Estimation of The Number of Ion Channels

In this section, the estimation of the number of ion channels is presented. The ion channel numbers of Zhangs central and peripheral SAN models and the Kurata model are also calculated. These three models are converted to their corresponding SDE models.

The stochastic simulation of a SDE model demands the estimation of the number of individual ion channel, N, to approximate the channel noise. In the simulation of a SDE model, the number N scales the value of the diffusion matrix which regulates the noise level of the channel-based model. This value of N can be obtained by dividing the channel conductances g by the single ion channel conductance γ. A summary of the single channel conductances present in the literature is given in Table 5.2.

TABLE 5.2: Single channel conductance records. The literature of the measurement of single channel conductances are listed here. The currents I_{sus} and I_{st} are not listed, because we failed to find proper experimental measurements of single channel conductances of I_{sus} and I_{st}.

Current	Single channel conductance (pS)	Reference
I_{Na}	20	Wilders and Jongsma (1993)
	20.1	Ono et al. (1993)
$I_{\text{Ca,L}}$	3.3	Wilders and Jongsma (1993)
	3.0	Guia et al. (2001)
	8.2	Lemay et al. (2011a)
$I_{\text{Ca,T}}$	5.8	Wilders and Jongsma (1993)
	8.5	Hagiwara et al. (1988b)
	8.0	Nilius et al. (1985)
I_{f}	0.5	Wilders and Jongsma (1993)
	0.98	DiFrancesco (1986)
I_{K}	2.9	Wilders and Jongsma (1993)
$I_{\text{K,s}}$	4.5	Yang and Sigworth (1998)
	3.11	Lemay et al. (2011a)
$I_{\text{K,r}}$	2.25	Veldkamp et al. (1993)
	2.31	Lemay et al. (2011a)
I_{to}	13.0	Fedida and Giles (1991)

5.6.1 Single Cell SDE Kurata Model

In order to obtain the stochastic version of the Kurata Model, proper single ion channel conductances need to be elected. In the literature, the estimation of the numbers of ion channels in cardiac cells has been estimated. Wilders and Jongsma (1993) evaluated the numbers of ion channels for the single cell SAN model. Lemay et al. (2011b) and Heijman et al. (2013) caudated the numbers of ion channels and corresponding gap junctional channels based on a ventricular cell model. We use values of the single channel conductances from the three references in our work. The numbers of ion channels of

$I_{h,Na}$, $I_{h,K}$, $I_{Ca,L}$, $I_{Ca,T}$, I_{to}, $I_{K,s}$ and $I_{K,r}$ are calculated. The results are listed in Table 5.3. As the published value of the Kurata model's Na^+ channel conductance is zero, the SDE Na^+ ion channel is not presented in our SDE Kurata model. Table 5.4 lists the

TABLE 5.3: The estimation of the number of ion channel of the Kurata model. In the literature, the single channel conductances of $I_{h,Na}$ and $I_{h,K}$ are considered to be same (Wilders and Jongsma, 1993) (Lemay et al., 2011b). We consider the single channel conductances of $I_{h,Na}$ and $I_{h,K}$ both as 0.5 here. The number of ion channels is proportion to the capacitance. The membrane capacitance is 32pF (Kurata et al., 2002). γ is single channel conductance. N is the number of ion channel estimated. The total number of ion channel is 34405.

Ion Channel	Conductance Density (nS/pF)	Conductance (nS)	γ (pS)	N
$I_{h,Na}$	0.14	4.48	0.5 (Wilders and Jongsma, 1993)	9199
$I_{h,K}$	0.23	7.36	0.5 (")	14801
$I_{Ca,L}$	0.58	18.56	3.6 (")	6187
$I_{Ca,T}$	0.46	14.72	5.8 (")	2572
$I_{K,s}$	0.026	0.83	3.11 (Lemay et al., 2011b)	266
$I_{K,r}$	0.068	2.18	2.31 (")	937
I_{to}	0.18	5.76	13 (Heijman et al., 2013)	443
I_{Na}	0	-	-	-

number of ion channels for the Zhang central SAN model and peripheral SAN model. The evaluation of the number of ion channels of the two models are same to the Kurata model. The central SAN model does not consist of any Na^+ ion channel. The peripheral SAN model consists of a Na^+ ion channel with a conductance value of 0.0012 nS which is smaller than a single Na^+ ion channel conductance (0.02 nS) as shown in Table 5.2. Hence, in our SDE Zhang peripheral SAN model we still use the deterministic Na^+ ion channel.

TABLE 5.4: The estimation of the number of ion channel for Zhang central SAN model and peripheral SAN model. The Zhang central SAN model does not present the Na^+ current I_{Na}. The Zhang peripheral SAN model sets the Na^+ channel conductance as 1.2 pS which is smaller than single Na^+ channel conductance (Wilders and Jongsma, 1993) (Ono et al., 1993). γ is single channel conductance. N_C is the number of ion channel estimated for the central SAN model. N_P is the number of ion channel estimated for the peripheral SAN. The total numbers of ion channel of central and peripheral models are 5688 and 64932 respectively.

Ion Channel	Central Conductance (nS)	Peripheral Conductance (nS)	γ (pS)	N_C	N_P
$I_{h,Na}$	0.547	6.9	0.5 (Wilders and Jongsma, 1993)	1093	13750
$I_{h,K}$	0.547	6.9	0.5 (")	1093	13750
$I_{Ca,L}$	5.80	65.9	3.6 (")	1931	21962
$I_{Ca,T}$	4.30	13.9	5.8 (")	738	2393
$I_{K,s}$	0.311	10.4	3.11 (Lemay et al., 2011b)	111	3344
$I_{K,r}$	0.797	16.0	2.31 (")	345	6926
I_{to}	4.90	36.5	13 (Heijman et al., 2013)	377	2807
I_{Na}	0	0.0012	-	-	-

5.7 Results of Single Cell SDE Model

Based on the estimated number of ion channels in Table 5.3, the stochastic simulation of SDE ion channel models (based on Equation 5.6) can be performed. Simulations of the single cell SDE system were performed by Euler-Maruyama method following the work of Goldwyn et al. (2011a), We simulated the SDE channel-based SDE Kurata model. Table 5.5 presents the model results based on the CL mean $\overline{\text{CL}}$ and standard deviation σ_{CL}, and the corresponding box plots are given in Figure 5.6. Table 5.5 shows that the

TABLE 5.5: Action potential CL mean and standard deviation with respect to different perturbation size. The results are based on the channel-based SDE Kurata model. The numbers of ion channels are based estimated values in Table 5.3. The CL coefficient C_{CL} is obtained according to $C_{\text{CL}} = \sigma_{\text{CL}}/\overline{\text{CL}}$, where $\overline{\text{CL}}$ is the mean of CL and σ_{CL} is the standard deviation of CL.

ΔT (ms)	N	CL (ms)	C_{CL} (%)
2×10^{-2}	170	364.0 ± 35.41	9.72
1×10^{-2}	124	351.2 ± 19.60	5.58
1×10^{-3}	130	344.4 ± 19.88	5.77
2×10^{-4}	116	348.9 ± 17.54	5.03

CL coefficient C_{CL} converges at around $\Delta T = 1 \times 10^{-2}$. The corresponding data is shown as box plots in Figure 5.6. Table 5.6 shows that the CL mean, standard deviation

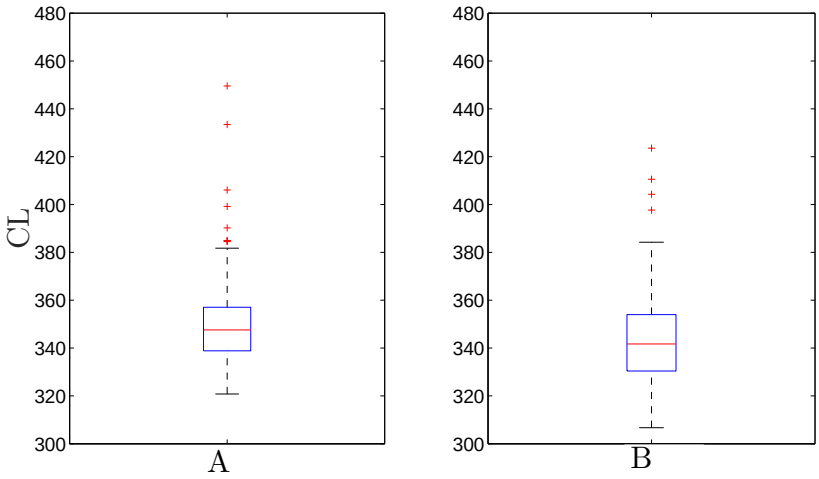

FIGURE 5.6: Box plot of the CL of the Kurata SAN SDE model. The data details are shown in Table 5.5. Figure A: $\Delta T = 1 \times 10^{-2}$ ms. Figure B: $\Delta T = 1 \times 10^{-3}$ ms.

and the coefficient C_{CL} of the Zhang central SAN SDE model. Table 5.6 shows that the CL mean, standard deviation and the coefficient C_{CL} of the peripheral SAN SDE model. Figure 5.8 show the corresponding box plots of Table 5.7. Table 5.8 shows the experimental measurement of the single rabbit SAN cell CL. The data in the tables includes the mean, standard deviation and the coefficient of the CL. The mean value of the CL varies from 298 to 358.4, and the ratio of standard deviation (C_{CL}) is in the

TABLE 5.6: CL mean and standard deviation of the Zhang central SAN SDE model with respect to various perturbation size.

ΔT (ms)	N	CL (ms)	C_{CL} (%)
1×10^{-2}	65	319.32 ± 26.20	8.21
1×10^{-3}	120	318.43 ± 25.97	8.16

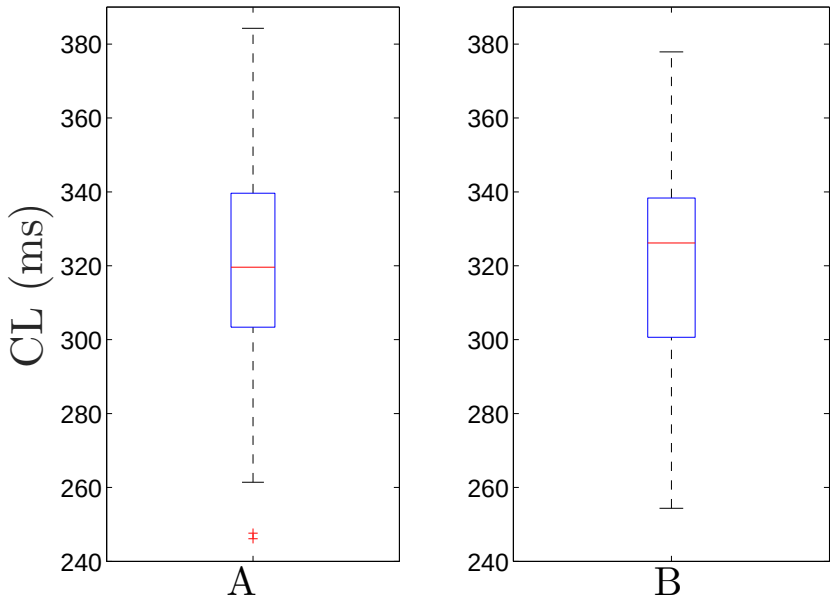

FIGURE 5.7: Box plot of the CL of the Zhang central SAN SDE model. The data details are shown in Table 5.6. Figure A: $\Delta T = 1 \times 10^{-2}$ ms. Figure B: $\Delta T = 1 \times 10^{-3}$ ms.

range of 2.35 to 16.05. Kodama and Boyett (1985) presents the central and peripheral SAN cell measurements respectively.

As shown in Table 5.6, the coefficient of the SDE Zhang central SAN model is 8.16 % which is considerably bigger than Wilders and Jongsma's experimental measurement (3.93 %), but close to the measurement of Yaniv (8.9%). The coefficient of the SDE Kurata model is 5.03 % which is between 3.93 % and 8.16%. Therefore, we believe that the results of the Kurata model and the Zhang central SAN model agree with experimental measurements.

The CL coefficient of the Zhang peripheral SAN model is 0.79 %, significantly smaller than the experimental measurements. This may be due to the large default capacitance of the peripheral model of 65 pF (Zhang et al., 2000). A large cell capacitance results in a small mean CL value of 159.46 ms compared with the experimental observations of 390 (Yaniv) and 273 ms (Wilders). In addition, under the condition that the ion channel densities are constants, the large or small capacitances determine corresponding large or small number of ion channels, respectively. This considerable difference comes from the default parameter values of the Zhang peripheral model not from the SDE reformulation.

TABLE 5.7: CL mean and standard deviation of the Zhang peripheral SAN SDE model.

ΔT (ms)	N	CL (ms)	C_{CL} (%)
1×10^{-2}	206	159.35 ± 1.50	0.94
1×10^{-3}	106	159.18 ± 1.40	0.88
1×10^{-4}	153	159.46 ± 1.26	0.79

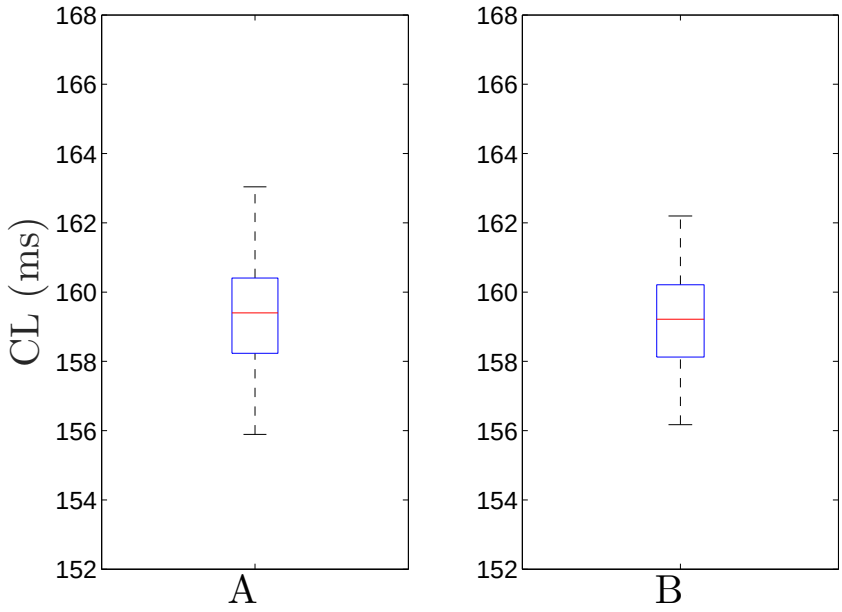

FIGURE 5.8: Box plot of the CL of the Zhang peripheral SAN SDE model. The data details are shown in Table 5.7.

In addition, the discrepancy may also be caused by the absence of the Na^+ ion channel, but as we discussed previously the estimated number of Na^+ ion channel is less than one. A very small number of ion channels is unlikely to produce the large variation. Hence, we assume that the Na^+ ion channel cannot add large variation into the results.

TABLE 5.8: Experimental measurements of rabbit SAN CL.

Reference	Tissue Type	n	CL (ms)	C_{CL} (%)
(Hagiwara et al., 1988b)	single cell	5	296.4 ± 47.5	-
(Van Ginneken and Giles, 1991)	single cell	20	335.4 ± 15.0	-
(Denyer and Brown, 1990)	single cell	12	358.2 ± 39.5	-
(Wilders and Jongsma, 1993)	single cell	100	273 ± 7.7	2.8
(Yaniv et al., 2014)	single cell	64	390 ± 9	8.9 ± 0.5
(Yaniv et al., 2014)	SAN tissue	8	324 ± 11	2.8 ± 0.6
(Satoh, 1995)	tissue size of 1.0-0.5 mm	14	298 ± 7	-
(Kodama and Boyett, 1985)	central SAN tissue	22	331 ± 13	-
(Kodama and Boyett, 1985)	peripheral SAN tissue	21	298 ± 8	-

TABLE 5.9: Experimental measurement of the intact SAN CL.

Reference	CL (ms)	C_{CL} (%)
(Oren and Clancy, 2010)	361 ± 38	11
(Kirchhof et al., 1987)	348 ± 50	14.37

5.8 One-dimensional SDE Model

5.8.1 One-dimensional Uniform SDE Model

In order to understand the coupling effects on the CL behavior of the SAN action potential, we construct a 1D SDE Kurata model. The 1D model consists of 30 cells whose schematic diagram is shown in Figure 5.9. This 1D model is uniform model which only consists of a type of single cell SDE Kurata models. A linear gradient of cell-to-cell coupling is applied in the model, which is based on the experimental studies of SAN cell coupling strength (Bleeker et al., 1980) (Masson-Pévet et al., 1979). We use a 15-fold coupling strength gradient (Oren and Clancy, 2010) which is 7.5 nS at the SAN centre and 112.5 nS at the SAN periphery. In the 1D SAN model, the atrial cells are not incorporated into the simulation in order to test the coupling effects from SAN cells only. A regional difference of gap junction proteins exists in the SAN tissue (Boyett et al., 2000). The junction proteins are intercellular connections which allow the propagation of action potentials between cells. The junction protein density determines the coupling strength between cells. The difference of the coupling strength is based on the experimental observation that there is a gradient of cell-to-cell coupling strength from central SAN to peripheral SAN (Bleeker et al., 1980). This regional difference of is incorporated in our 1D SAN model. Table 5.10 shows the variations of $\overline{\mathrm{CL}}$, σ_{CL} and

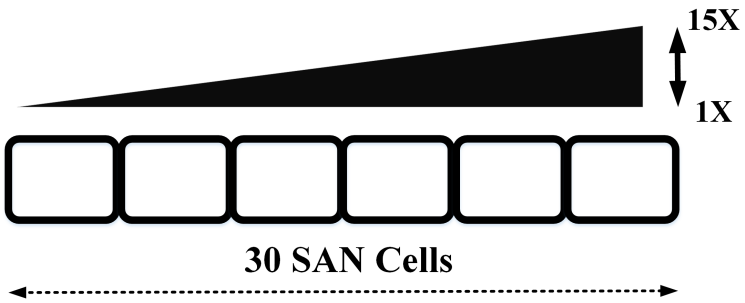

FIGURE 5.9: The schematic diagram of 1D SDE Kurata model (uniform model). The 1D model consists of 30 cells, and each cell is simulated as a single cell SDE Kurata model. This model incorporates a linear gradient of cell-to-cell coupling from the SAN centre to the SAN periphery. The central intercellular coupling is 7.5 nS (the 1_{st} cell). The peripheral intercellular coupling is 112.5 nS (the 30_{th} cell).

C_{CL} with respect to the increase of coupling strength. The results show that the $\overline{\mathrm{CL}}$ remains unchanged from the central SAN cell to the peripheral SAN cell. The σ_{CL} and C_{CL} decrease with respect to the increase of the coupling strength. The CL coefficient C_{CL} declines from 6.91 % to 5.70 %, which means that the rising coupling strength of

cells can reduce the CL fluctuation. As shown in Table 5.5, the single cell coefficient σ_{CL} at Δ T of 0.01 ms is 5.58 % which is smaller than the σ_{CL} of the central SAN cells (6.91 %) and is very close to the σ_{CL} of the peripheral SAN cells (5.70 %). The results indicate the the small coupling strength in the central SAN cells may lead to an increase of σ_{CL} in the 1D uniform SAN model. These results is a detailed example based on a fixed gradient of coupling strength. A further discussion in the following is presented in Figure 5.11. The corresponding box plot of Table 5.10 is shown in Figure

TABLE 5.10: CL mean and standard deviation of the one-dimensional 30 cell Kurata SDE model. The results are based on 167 CL samples of the one-dimensional model. The σ_{CL} and $\overline{\mathrm{CL}}$ of seven cells (the 1_{st}, 5_{th}, 10_{th}, 15_{th}, 20_{th}, 25_{th}, 30_{th}) are listed together with C_{CL}. The time step is chosen as 10^{-2} ms.

	Cell_1	Cell_5	Cell_{10}	Cell_{15}	Cell_{20}	Cell_{25}	Cell_{30}
$\overline{\mathrm{CL}}$	356.10	356.06	356.37	356.33	356.32	356.33	356.34
σ_{CL}	24.61	24.72	24.75	20.25	20.16	20.24	20.31
C_{CL}	6.91	6.94	6.94	5.68	5.66	5.68	5.70

5.10. Furthermore, we did a test on the σ_{CL} of the 1D model with respect to several

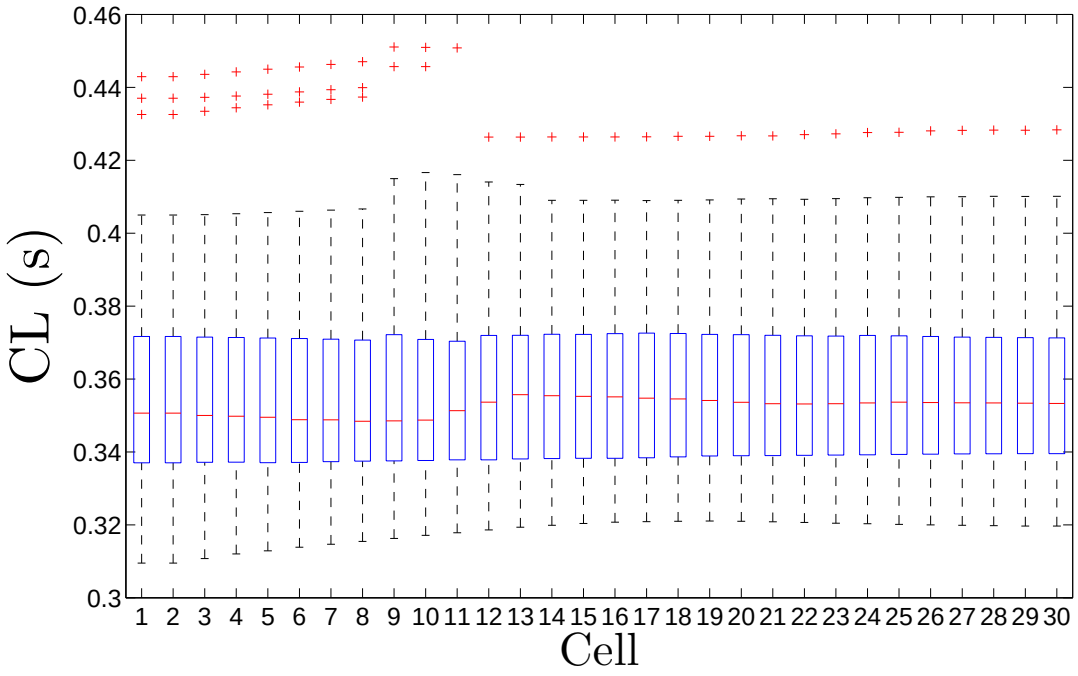

FIGURE 5.10: Box plot of the CL of the 1D SDE Kurata model. The results are based on 167 CL samples of each cell.

increase peripheral coupling strengthes (i.e. 5×, 10× and 15×). The results are shown in Figure 5.11 (see Appendix for box plots). As shown in Figure 5.11, the converged values of σ_{CL} at the peripheral SAN cells vary with respect to the increased peripheral coupling strength. The curve of 5× increased strength reaches the minimum of σ_{CL} which is at the value of 2.8. The σ_{CL} of the central SAN cells are comparatively large.

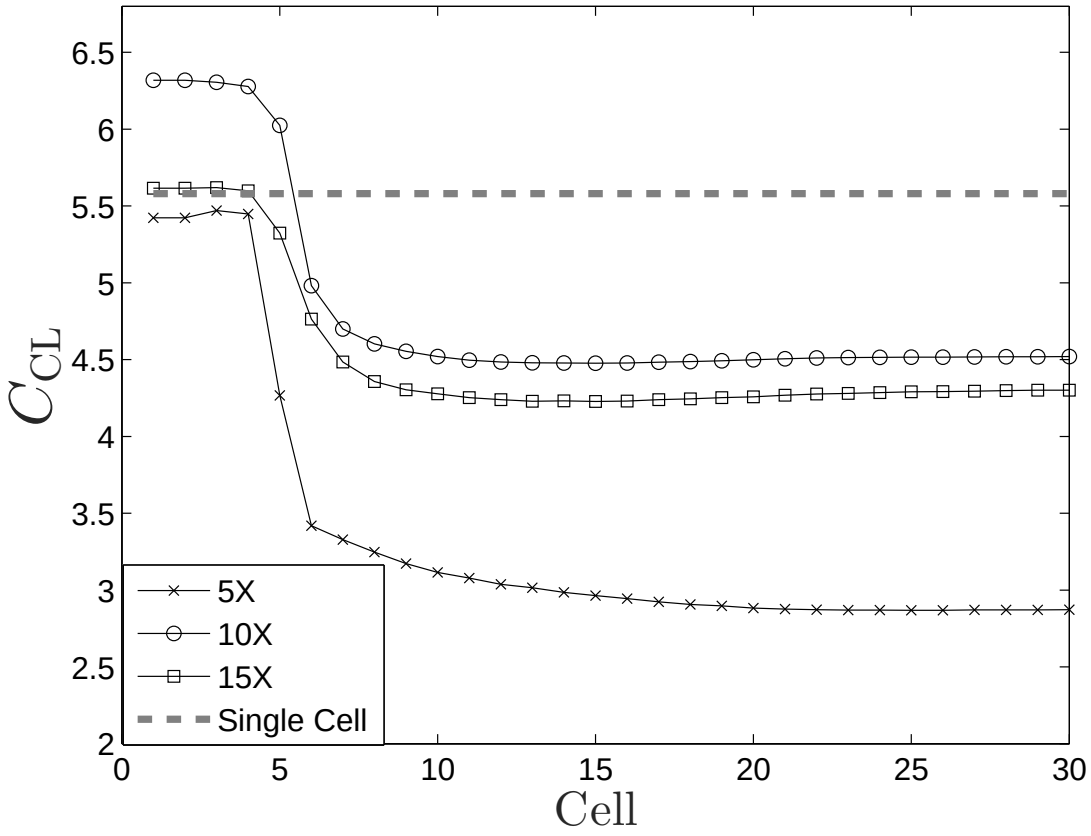

FIGURE 5.11: The effects of various coupling increased peripheral coupling strength of the C_{CL} for 1D SDE Kurata model. The 1D Kurata model consists of 30 central cells. The C_{CL} is computed at 5×, 10× and 15× increased peripheral coupling. The C_{CL} of single central cell is given as a reference.

The maximum is archived by the curve of 10× increased strength, and the value of σ_{CL} is 6.3 % which is bigger than the single cell. All the results have a comparatively large value of σ_{CL} in the central SAN, which is due to the small coupling strength of the centre. These indicate that the coupling gradient decrease variance coefficient with respect to the regional difference of the SAN.

5.8.2 One-dimensional Non-uniform SDE Model

The one-dimensional Zhang SAN SDE models discussed in this section are a non-uniform model which incorporates different types of SAN cells. The schematic diagrams of the 1D models with 30 cells whose are shown in Figure 5.12 and Figure 5.13. The two schematic diagrams shows two different descriptions of the SAN heterogeneity. The first diagram is a 1D model is based on an increase of the capacitance from 20 to 65 pF as shown in Figure 5.12. The implementation details of this model is based on Zhang et al. (2000). The model in the second diagram has 15 central and 15 peripheral SAN cells as

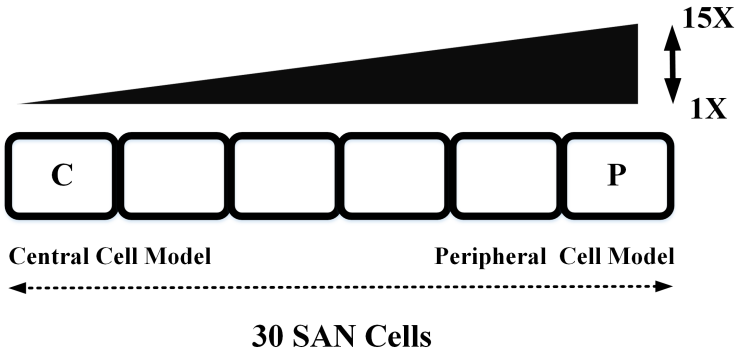

FIGURE 5.12: Schematic diagram of a 1D SDE Zhang SAN model (non-uniform model). The central intercellular coupling is 7.5 nS (the 1_{st} cell). The peripheral intercellular coupling is 112.5 nS (the 30_{th} cell). This model incorporates a linear increase of cell-to-cell coupling from the SAN centre to the SAN periphery. The gradient model which is based on the 1D model of the intact SAN Zhang et al. (2000).

shown in Figure 5.12. The capacitances of the central and peripheral cells are 20 and 65 pF, respectively. The linear gradient of cell-to-cell coupling strength are also applied to the two 1D models as used for the 1D SDE Kurata model. Table 5.11 shows the $\overline{\text{CL}}$,

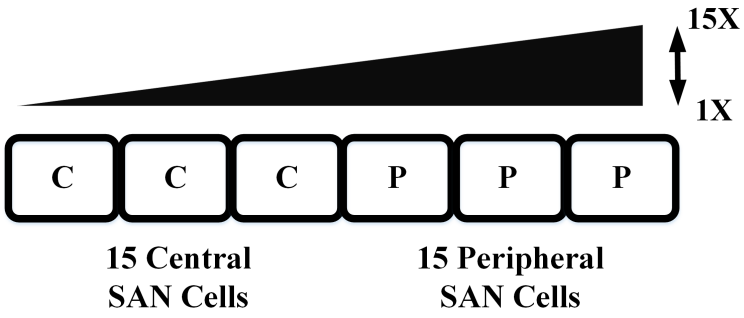

FIGURE 5.13: Schematic diagram of a 1D SDE Zhang SAN model (non-uniform model). The central intercellular coupling is 7.5 nS (the 1_{st} cell). The peripheral intercellular coupling is 112.5 nS (the 30_{th} cell). The 1D model has 15 central SAN cells and 15 peripheral SAN cells. This model incorporates a linear gradient of cell-to-cell coupling from the first SAN cell to the last SAN cell. The schematic diagram of the 1D model is based on Oren and Clancy (2010).

σ_{CL} and C_{CL} of with respect to the coupling strength. The results show that the $\overline{\text{CL}}$ remains at 174 ms from the central SAN cell to the peripheral SAN cell, which shows that the firing rate of the 30 cells are synchronised. As shown in Table 5.6 and Table 5.7, the $\overline{\text{CL}}$ for isolated central SAN cells and peripheral SAN cells are 319.32 and 158.72 ms, respectively.

The σ_{CL} and C_{CL} decrease as the coupling strength increases. The CL coefficient C_{CL} declines from 6.91 % to 5.70 %, which means that the rising coupling strength of cells can reduce the CL fluctuation. As shown in Table 5.5, the single cell coefficient σ_{CL} at Δ T of 0.01 ms is 5.58 % which is smaller than the σ_{CL} of the central SAN cells (6.91 %) and is very close to the σ_{CL} of the peripheral SAN cells (5.70 %). The results

suggests that the coupling strength of the central SAN cells may lead to the increase of the fluctuations of the action potential CL. These results is an example based on a fixed gradient of coupling strength. A further discussion in the following is presented in Figure 5.16. The corresponding box plot of Table 5.11 is shown in Figure 5.14 which

TABLE 5.11: CL mean and standard deviation of the one-dimensional 30 cell Zhang SDE model. The results are based on 167 CL samples of the one-dimensional model. The σ_{CL} and $\overline{CL}$ of seven cells (the 1_{st}, 5_{th}, 10_{th}, 15_{th}, 20_{th}, 25_{th}, 30_{th}) are listed together with C_{CL}. The simulation time step is chosen as 10^{-2} ms.

	Cell_1	Cell_5	Cell_{10}	Cell_{15}	Cell_{20}	Cell_{25}	Cell_{30}
$\overline{\mathrm{CL}}$	173.99	174.00	174.04	174.07	174.08	174.08	174.08
σ_{CL}	4.06	2.85	2.31	2.24	2.92	0.92	0.91
C_{CL}	2.33	1.64	1.33	1.29	1.68	0.53	0.53

shows the CL variation of each cells in details. We also performed a test with respect to

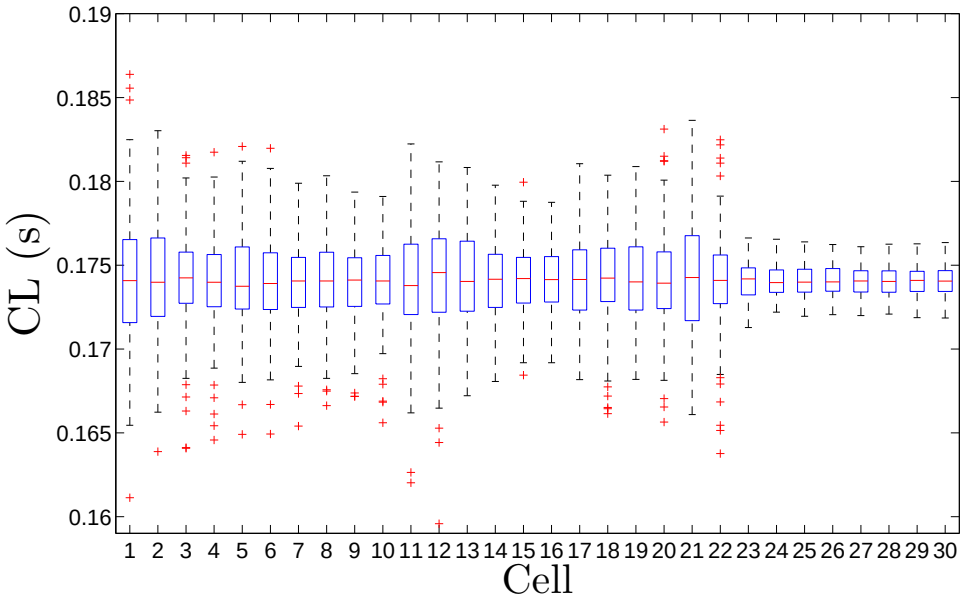

FIGURE 5.14: Box plot of the CL of the 1D SDE Zhang SAN Model. The results are based on 150 CL samples of each cell.

various increased peripheral coupling strength of the two 1D non-uniform models. The results are shown in Figure 5.15 and Figure 5.16 (see Appendix for box plots).

Figure 5.15 and Figure 5.16 both show that the non-uniform 1D models have comparatively small C_{CL} compared with 1D uniform model. The C_{CL} for all the SAN cells is around 0.9 which is very close to the coefficient of single peripheral SAN cells as shown in Figure 5.15. In Figure 5.16, the coefficients of central SAN cells are only slightly larger than the single peripheral SAN cells, and the coefficients of peripheral SAN cells also very close to the single peripheral SAN cells. These results show that the 1D models with heterogeneity (the two non-uniform 1D models) have very small variance coefficients of cycle length. Based on the results in Figure 5.11, Figure 5.15 and Figure 5.16,

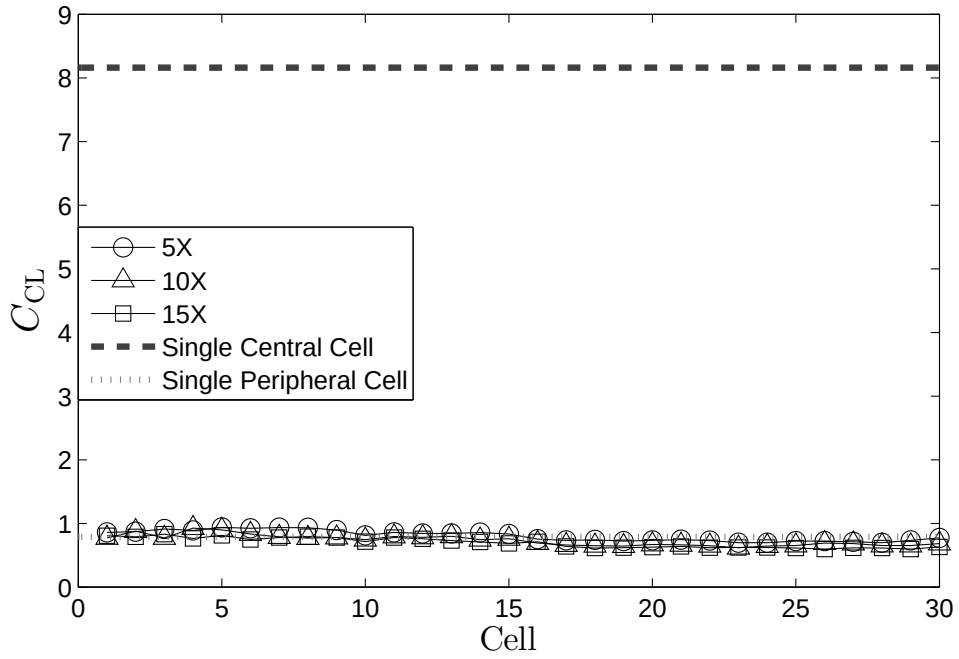

FIGURE 5.15: The effects of various coupling increased peripheral coupling strength of the C_{CL} for a Zhang's non-uniform model. The corresponding schematic diagram of the model is shown by Figure 5.13. The 1D SDE Zhang model has 15 central cells and 15 peripheral cells. The C_{CL} is computed at 5×, 10× and 15× increased peripheral coupling. The C_{CL} of single central and peripheral cells are give as references.

we can conclude that the heterogeneity of the intact SAN could reduce the variability of action potentials.

The experimental observation shows that have the value of variance coefficient is 8.9±0.5 (n = 64) for the single isolated SAN cells while the value of the intact SAN is 2.8±0.6 (n = 8) Yaniv et al. (2014), which also shows a dramatic decrease of variance coefficient when the SAN cells are coupled. In addition, the non-uniform 1D models with heterogeneity have a synchronised variance coefficients compared with the uniform 1D model. Figure 5.15 and Figure 5.16 also show that the converged variance coefficients of 1D models are related to the peripheral SAN cells because the converged values are very close to the values of single peripheral cells. Therefore, we suggest that non-uniform 1D models match the experimental observations better and the heterogeneity of the SAN is capable to reduce action potential variability at tissue level.

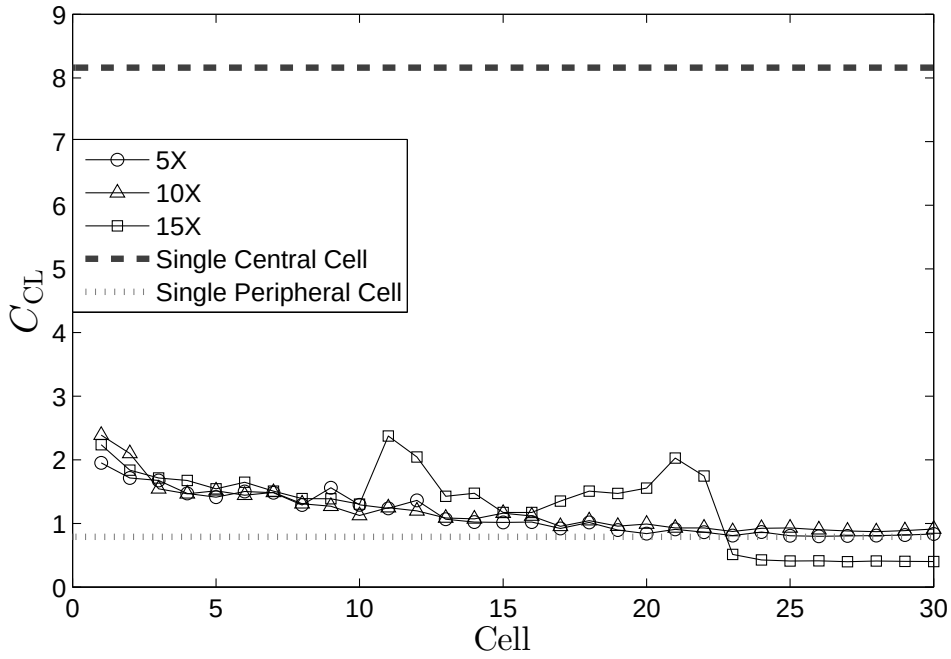

FIGURE 5.16: The effects of various coupling increased peripheral coupling strength of the C_{CL} for a 1D SDE Zhang model. The corresponding schematic diagram of the model is shown by Figure 5.12. The 1D SDE Zhang model is a gradient model (non-uniform model) which is based on the 1D model of the intact SAN Zhang et al. (2000). The C_{CL} is computed at 5×, 10× and 15× increased peripheral coupling. The C_{CL} of single central and peripheral cells are give as references.

5.9 Discussion

5.9.1 Roles of SAN Heterogeneity and Coupling Strength

In the chapter, we discussed the stochastic modeling of the intact SAN tissue. We reformulated the ODE based ion channel of single cell SAN models into SDE based descriptions, and therefore the stochastic versions of Zhang SAN models and the Kurata model were achieved. Simulations of the single cell SDE system were performed by Euler-Maruyama method following the work of Goldwyn et al. (2011a), which achieves a good agreement with experimental measurements of Wilders and Jongsma (1993) and Yaniv et al. (2014). Based the single cell SDE model, we modelled intact SAN tissue with 30 cells. We first tested the effect of several coupling gradients. The result indicates that the coupling gradient decrease variance coefficient with respect to the regional difference of the SAN. The heterogeneity of stochastic intact SAN tissue was also incorporated into the model to explain the controversial SAN heterogeneity. The action potential variabilities of uniform model (with heterogeneity) and non-uniform model (without heterogeneity) were simulated and discussed. We showed that the heterogeneity greatly reduces the action potential variability, and the variability is determined by the behavior of peripheral SAN cells. The results reproduced the experimental observations of the

small action potential variability of intact SAN tissue with respect to the large variability of single cells (Yaniv et al., 2014). The SAN heterogeneity assumption (the non-uniform model) of Boyett et al. (2000) is supported by our results.

Our results present the variabilities of various increased peripheral coupling strengthes (5X, 10X and 15X). This coupling strength shows the cell-cell conductivity near SAN-atria boundary. In one-dimensional uniform SDE model, the coefficient of variance largely varies with respect to the coupling strengthes (Figure 5.11). In one-dimensional non-uniform SDE models, the coefficients show no variation for various coupling strengthes (Figure 5.16 and Figure 5.15). The effectiveness of conductivity near SAN-atria boundary is reduced by SAN heterogeneity. The limitation of our test is the absence of the variability from the coupling of atrial cells. We assume there is no voltage coupling from atrial cells. As this research addresses the heterogeneity of the SAN tissue, the atrial cells are not incorporated in order to simplify the problem. The assumption can be interpreted as a complete blockage of SAN-atria boundary.

5.9.2 Intrinsic and Extrinsic Variability

The sources of variability in SAN cells are intrinsic variability (beat to beat variability in a single SAN cell) and extrinsic variability (variability arising from heterogeneity of coupled cells). In the chapter, we observe that the intrinsic variability varies greatly among the three SAN models we considered due to the number of ion channels of each model. The CL variance coefficients of Kurata model, Zhang central and peripheral SAN model are 5.77, 8.16 and 0.88 % respectively (as shown in Table 5.5, 5.6 and 5.7), and the corresponding total number of ion channels are 34405, 5688 and 64932 (Table 5.3 and 5.4). The CL variability decreases with respect to the growth of the total number of ion channels, which shows the total number of ion channels determines the intrinsic variability.

Furthermore, we show that extrinsic variability is dependent on intrinsic variability when the SAN heterogeneity is considered. When SAN cells are coupled, the variability of the SAN cells decreases significantly due to the induced of extrinsic variability and cell to cell coupling; the minimum variability are relevant to single cell variability (intrinsic variability). In non-uniform models, the minimum variability of coupled cells is largely affected by the peripheral SAN cells in various cell to cell coupling strengths (shown in Figure 5.15 and 5.16). In contrast, non-uniform model has no heterogeneity of SAN cells; the variability of each cell is varied only by the increased coupling strength from central to peripheral SAN. As shown by the variability, the influence of the coupling strength is not as great as the heterogeneity, and the extrinsic variability has a larger effect than the intrinsic variability in SAN cells, but minimum variability of the SAN

tissue is relevant to intrinsic variability. In the literature, (Walmsley et al., 2015) also observed that the extrinsic variability implies a greater effects than intrinsic variability in ventricular myocytes. In this work, we further show the interaction between intrinsic and extrinsic variabilities in the environment of SAN heterogeneity.

Chapter 6

Conclusions and Future Work

6.1 Conclusions

This dissertation is about the analysis of computational models of cardiac cells, we considered several single cell models. By sensitivity analysis of deterministic models of single cells (both local and global sensitivity analysis) and a stochastic differential equation approach of modeling coupled cells we derived a number of key observations about their properties. The results obtained from sensitivity analysis and stochastic modelling are based on the assumption that these models are adequate to capture real cardiac cell behaviors. The behaviors, such as cell coupling strength, ion channel functions and densities, are important for the results.

Firstly (Chapter 3), we analysed these models of rabbit sinoatrial node (SAN) cells, the Zhang central and peripheral SAN models (Zhang et al., 2000) and the Kurata model (Kurata et al., 2002), and quantified sensitivities of several features of the pacemaker waveform with respect to variations in ion channel conductances of the models. Local sensitivity indices were found to be model dependent, similarly to the observation made by previous authors, e.g. Dresch et al. (2010). Moreover, the results of local sensitivities may vary among different SAN models; though in the most important parameter there is agreement in the global sensitivities which could be found in a computationally efficient way (shown by Table 3.5, Table 4.6, Table 4.7 and Table 4.8). Based on these results, we conclude that the local method is able to identify the key parameter but validity of the index interpretation is undermined, because the local indices are unnormalised therefore cannot be compared between different models (discussed in Section 3.5). Hence, a global method with normalised index and model independence is required.

In Chapter 4, global sensitivity analysis was carried out using two techniques (eFAST and Sobol methods), systematically searching over a wide range in the parameter space. We compared two approaches of implementing global sensitivity analysis on cardiac models, (i) feature based sensitivity analysis and (ii) time varying sensitivity analysis.

We showed that the time based approach fails to present accurate sensitivity index at the depolarisation stage due to the phase shift of action potential, and the feature based analysis accurately quantifies the roles of ion channels. By carrying out feature based eFAST analysis, a common set of important parameters was discovered among several cardiac models, which shows that the global methods are able to provide model independent evaluation of the effects of ion channels, and that the models with different descriptions of ion channels have a agreement on the SAN mechanism. We suggest that the individual effects of ion channels are the determinants of the SAN action potential and there is no great interactions between ion channels. Moreover, the feature based Sobol analysis uncover important interaction terms contributing to output variability. As shown by Table 4.10, we found a strong interaction (55 % of variance) of ion channels influencing action potential duration curve of a ventricular model, which maintains relative consistency with previous authors (Chang et al., 2015). Based on these results, we conclude that there is a interaction in pairs of ion channels in ventricular cell model, which shows that the interaction is mainly from the second order effects of ion channels.

In the final part of the work (Chapter 5), analysing coupled cells, we considered stochastic modeling of the intact SAN tissue, because the action potential variability of the intact SAN tissue is largely different from isolated single SAN cells (Boyett et al., 2000) (Yaniv et al., 2014), and the reasons for this phenomenon is still unknown. We reformulated the ODE based single cell SAN models, the Zhang SAN models and the Kurata model, into SDE based descriptions. Simulations of the single cell SDE system were performed by Euler-Maruyama method following the work of Goldwyn et al. (2011a), which achieves a good agreement with experimental measurements of Wilders and Jongsma (1993) and Yaniv et al. (2014). By stochastic modeling of the intact SAN tissue based on the SDE single cell models, the heterogeneity of stochastic intact SAN tissue is modelled to explain the controversial SAN heterogeneity (Oren and Clancy, 2010). We showed that the heterogeneity greatly reduces the action potential variability, and the variability is largely determined by the peripheral SAN cells. We also show that total number of ion channels determines the intrinsic variability and extrinsic variability is dependent on intrinsic variability when the SAN heterogeneity is considered. According to an experimental observation of the variability of the intact SAN tissue (Yaniv et al., 2014), the simulation results presented by intact heterogeneity models have better agreement with the observation in contrast to the intact non-heterogeneity model (discussed in Section 5.9.1). Thus, the hypothesis of the SAN heterogeneity Boyett et al. (2000) is supported by our results.

In the literature, there are experimental measurements which relate to our results. Yaniv et al. (2014) provide a good support for our work. They isolated the rabbit SAN from the heart and gave many heart beat measurements for both intact SAN tissue and single SAN cells. Yaniv et al. (2014) show a great difference coefficient of variance (C_{CL}) between single cells and SAN tissue, which is 8.9 $\pm$ 0.5 (single SAN cell) and 2.8 $\pm$

0.6 (intact isolated SAN). In our simulation work, only the 1D SAN models with the cell heterogeneity show the similar variance difference (shown in Figure 5.15 and Figure 5.16). This experimental measurement observed the difference between the intact SAN and the single SAN cell, which strongly support our work, and this experiment can be further modified to directly demonstrate cell heterogeneity by measuring the coefficient of variance. As we shown the CL coefficient of variance relate to the SAN heterogeneity, an experiment work based on measuring the coefficient of variance can verify our results. If two small size SAN tissues with around 30 cells can be isolated from the central and peripheral SAN, we can measure the effects of cell coupling on C_{CL}, which are the control groups. A treatment group with a same cell size tissue which incorporates both central and peripheral cells can shows the effects of cell heterogeneity. By comparing the C_{CL} of these groups, the cell heterogeneity can be quantified.

6.2 Future Work

In this thesis, we quantified the effects of the ion channels of several single cell cardiac models by both local and global sensitivity analysis. We also proposed stochastic single cell and tissue level SAN models to explain the variability in action potentials.

As a next step, the global sensitivity analysis can be further applied to age-related function decline of tissue level SAN models. The function of the SAN declines with age, and the mechanisms underlying the age-related decline in SAN function are still unclear (Dobrzynski et al., 2007). Older animals have slower SAN action potential rates, which may be caused by the decrease of ion channel densities and a structural remodelling of the SAN tissue Yanni et al. (2010). The age-related decrease of ion channel densities can be considered by global sensitivity analysis as the covariation of ion channels conductances, and the structural remodelling of the SAN tissue could be presented by tissue level models. Therefore, the global sensitivity analysis of tissue level SAN models could provide insights into ageing-related function changes.

Furthermore, the sensitivity analysis of the tissue level SAN model is computationally intensive as a large number of cardiac cells are involved. Some studies used different approaches to build a statistical model based on a number of cardiac cell model outputs, which can also return the sensitivity of the parameters (Sobie, 2009). Chang et al. (2015) further showed that a surrogate statistical model of a cardiac model can be built with Gaussian process emulators with a small number of model runs. Therefore, we can use the surrogate statistical model to implement global sensitivity analysis of multi-scale SAN models.

In Chapter 5, we modelled the variability of action potential based on the stochastic simulation of cardiac models. The cell-to-cell coupling strength was considered as a constant gradient from SAN centre to periphery. However, this coupling is determined

by the number of gap junctions which undergo a continuous turnover. The coupling strength also varies with respect to the number of gap junctions. Lemay et al. (2011b) considered this variation of the coupling strength as a stochastic variable and showed that its distribution could strongly impact the variability of action potential conduction. We did not consider the randomness of the cell-to-cell coupling strength. In future work, the distribution of the coupling strength can be incorporated into our stochastic SAN models.

Appendix A

Single Cell Cardiac Model

A.1 Noble Model

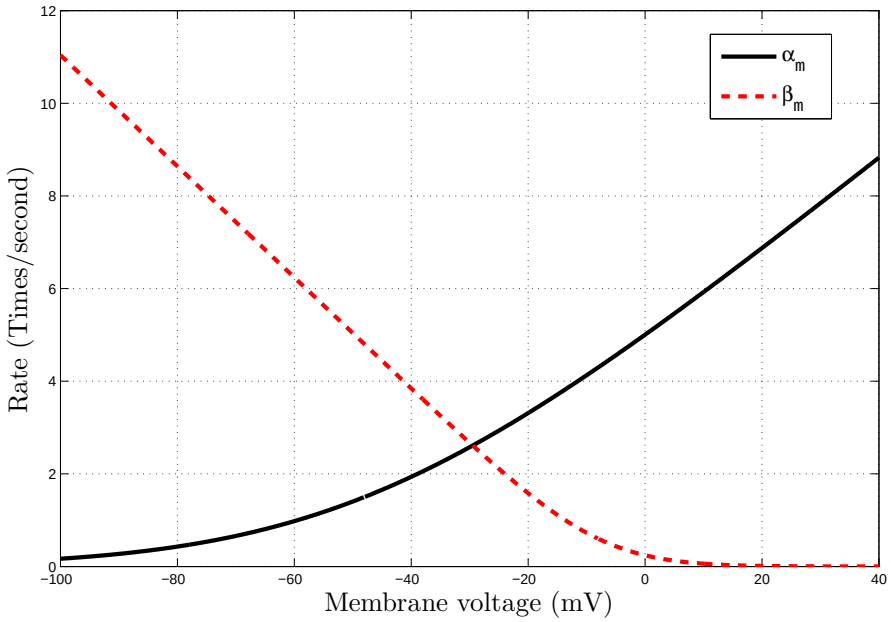

FIGURE A.1: The transition rates (α_m and β_m) of the gate m of Na^+ channel (Noble, 1962). The constants regulate fluctuations of ion channel gates with respect to the membrane voltage.

The transition rates, α_m and β_m, are the functions of the membrane voltage as shown in Section 2.4. The relationship between transition rates and the membrane voltage is explained by FigureA.1.

TABLE A.1: The initial values of state variables of Noble model (Noble, 1962).

Variable Name	Initial Value
V_{m}	-81.6 mV
m	0.0434
n	0.6089
h	0.8522

TABLE A.2: Parameter values of Noble model (Noble, 1962).

Parameter Name	Value
E_{Na}	40 mV
E_{K}	-100 mV
E_{An}	-60 mV
C_{m}	10 μF/cm^2
g_{An}	0.075

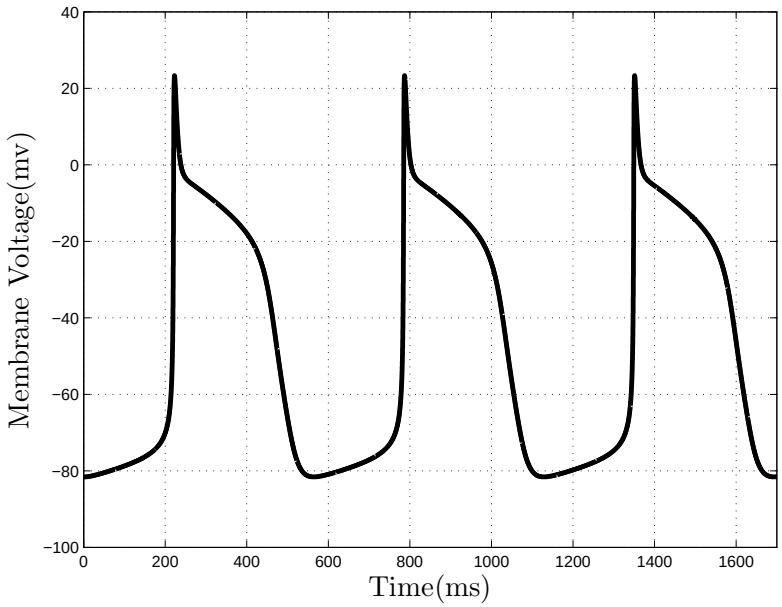

FIGURE A.2: The membrane voltage of Noble model. The model details are presented in Section 2.4.

A.2 Zhang SAN Model

The parameter values of Zhang's central and peripheral SAN models are given in Table A.3. The default input values used in the local and global sensitivity analysis of these models are based on these values.

TABLE A.3: Parameter Values for central and peripheral SAN models (Zhang et al., 2000).

Parameter Name	Peripheral SA Node Cell Value	Central SA Node Cell Value
C_{m}	65 pF	20 pF
d_{NaCa}	0.0001	0.0001
$E_{\mathrm{Ca,L}}$	46.4 mV	46.4 mV
$E_{\mathrm{Ca,T}}$	44 mV	45 mV
$g_{\mathrm{Ca,L}}$	$6.59 \times 10^{-2}\mu$S	$0.58 \times 10^{-2}\mu$S
$g_{\mathrm{Ca,T}}$	$1.39 \times 10^{-2}\mu$S	$0.43 \times 10^{-2}\mu$S
g_{to}	$36.49 \times 10^{-3}\mu$S	$0.49 \times 10^{-3}\mu$S
g_{sus}	$1.14 \times 10^{-2}\mu$S	$6.65 \times 10^{-5}\mu$S
$g_{\mathrm{K,r}}$	$1.60 \times 10^{-2}\mu$S	$7.97 \times 10^{-4}\mu$S
$g_{\mathrm{K,s}}$	$1.04 \times 10^{-2}\mu$S	$5.18 \times 10^{-4}\mu$S
$g_{\mathrm{f,Na}}$	$0.69 \times 10^{-2}\mu$S	$0.0548 \times 10^{-2}\mu$S
$g_{\mathrm{f,K}}$	$0.69 \times 10^{-2}\mu$S	$0.0548 \times 10^{-2}\mu$S
$g_{\mathrm{b,Na}}$	$1.89 \times 10^{-4}\mu$S	$5.8 \times 10^{-5}\mu$S
$g_{\mathrm{b,Ca}}$	$4.3 \times 10^{-5}\mu$S	$1.32 \times 10^{-5}\mu$S
$g_{\mathrm{b,K}}$	$8.19 \times 10^{-5}\mu$S	$2.52 \times 10^{-5}\mu$S
$\overline{i_{\mathrm{p}}}$	0.16 nA	$2.46 \times 10^{-2}n$A
k_{NaCa}	$0.88 \times 10^{-5}n$A	$0.27 \times 10^{-5}n$A

TABLE A.4: Glossary A for SAN model

Parameter Name	Meaning
4-AP	4-Aminopyridine
AM	Atrial muscle
APD	Action potential duration
CL	Spontaneous cyuccle length
C_{m}	Cell capacitance
$C_{\mathrm{m}}^{a}(x)$,$C_{s}^{m}(x)$	Capacitance of atrial muscle cell in one-dimensional model of intact SA node at distnace xfrom center of SA node
$d_{\mathrm{L}}, d_{\mathrm{T}}$	Activation variables for $i_{\mathrm{Ca,L}}$ and$i_{\mathrm{Ca,T}}$
d_{NaCa}	Denominator constant for i_{NaCa}
$\frac{\mathrm{d}V}{\mathrm{d}t_{\mathrm{max}}}$	Maximum upstroke velocity of action potential
D^{a}, D^{s}	Diffusion coefficient beween atrial muscle cells or SA node cells in one-dimensional model of the intact SA node
$E_{\mathrm{K,s}}$	Resersal potential for $i_{\mathrm{K,s}}$
E_{Na},E_{K},E_{Ca}	Equilibrium potentials for Na^{+},K^{+},and Ca^{2+}
$E_{\mathrm{Ca,L}}$,$E_{\mathrm{Ca,T}}$	Reversal potentials for $i_{\mathrm{Ca,L}}$ and $i_{\mathrm{Ca,T}}$
F	Faraday's constant
$F_{\mathrm{K,r}}$	Faction of activation of $i_{\mathrm{K,r}}$ that occurs slowly
F_{Na}	Fraction of inactivation of i_{Na} that occurs slowly
$f_{\mathrm{L}}, f_{\mathrm{T}}$	Inativation variables for $i_{\mathrm{Ca,L}}$ and $i_{\mathrm{Ca,T}}$
g_{p}^{a}, g_{c}^{s}	Conductance of a current in atrial muscle cell or SA node cell in one-dimensional model of intact SA node at distance x from conter of SA node
g_{Na}	Conductance of i_{Na}
$g_{\mathrm{Ca,L}}, g_{\mathrm{Ca,T}}$	Conductance of $i_{\mathrm{Ca,L}}, i_{\mathrm{Ca,T}}$
$g_{\mathrm{to}}, g_{\mathrm{sus}}$	Conductance of $i_{\mathrm{to}}, i_{\mathrm{sus}}$
$g_{\mathrm{K,r}}, g_{\mathrm{K,s}}$	Conductance of $i_{\mathrm{K,r}}, i_{\mathrm{K,s}}$
$g_{\mathrm{f,Na}}, g_{\mathrm{f,K}}$	Conductance of $i_{\mathrm{f,Na}}, i_{\mathrm{f,K}}$
$g_{\mathrm{b,Na}}, g_{\mathrm{b,K}}, g_{\mathrm{b,Ca}}$	Conductance of $i_{\mathrm{b,Na}}, i_{\mathrm{b,K}} and i_{\mathrm{b,Ca}}$
h_1, h_2	Fast and slow inactivation variables for i_{Na}
h	Net fractional availabiity of i_{Na}
i_{Na}	TTX-sensitive Na^{+} current
$i_{\mathrm{Ca,L}}, i_{\mathrm{Ca,T}}$	L- and T-type Ca^{2+} currents
$i_{\mathrm{to}}, i_{\mathrm{sus}}$	Transient and sustained components of 4-AP-sensitive current
$i_{\mathrm{K,r}}, i_{\mathrm{K,s}}$	Rapid and slow delayed rectifying K^{+} currents
i_{K}	Sum of $i_{\mathrm{K,r}}$ and $i_{\mathrm{K,s}}$
i_{f}	Funny current (also known as hyperpolarization-activated current)
i_{h}	Hyperpolarization-activated current
$i_{\mathrm{f,Na}}, i_{\mathrm{f,K}}$	Na^{+} and K^{+} components of i^{f}
$i_{\mathrm{b,Na}}, i_{\mathrm{b,Ca}}, i_{\mathrm{b,K}}$	Background Na^{+}, Ca^{2+}, and K^{+} currents
i_{NaCa}	Na^{+}/Ca^{2+} exchanger current
i_{p}	$Na^{+} - K^{2+}$ pump current
$\overline{i_{p}}$	Maximum i_{p}
i_{tot}	Totoal ionic current in a cell
$i_{\mathrm{tot}}^{a}(x), i_{\mathrm{tot}}^{s}(x)$	Total ionic current in atrial muscle cell or SA node cell in one-dimensional model of intact SA node at distance x from center of SA node
i_{st}	Sustained current
$i_{\mathrm{K,ACh}}$	ACh-activated K^{+} current
$i_{\mathrm{K,ATP}}$	ATP-sensitive K^{+} current
k_{NaCa}	Scaling factor for i_{NaCa} current

TABLE A.5: Glossary B for SAN model

Parameter Name	Meaning
$K_{\mathrm{m,Na}}, K_{\mathrm{m,K}}$	Dissociation constants for Na^+ and K^+ activation of i_{p}
L	Length of string of SA node and atrial tissue in one-dimensional model of intact SA node
L^s	Length of string of SA node tissue in one-dimensional model of intact SA node
m	Activation variable for i_{Na}
MDP	Maximum diastolic potential
n_∞	Steady-state value of n
p_{a}	General activation variable for $i_{\mathrm{K,r}}$
$p_{\mathrm{a,f}}, p_{\mathrm{a,s}}$	Fast and slow activation variables for $i_{\mathrm{K,r}}$
p_{i}	Inactivation variable for $i_{\mathrm{K,r}}$
Q_{10}	Fractional change in a variable with a 10^oC increase in temperature
r	Activation variable for i_{to}
R	Universal gas constant
q	inactivation variable for i_{to}
SA node, SAN	Sinoatrial node
t	Time
T	Absolute temperature
TOP	Takeoff potential
V	membrane potential
V^a, V^s	Membrane potential of atrial muscle cell or SA node in one-dimensional model of intact SA node
$V^a(x), V^s(x)$	Membrane potential of atrial muscle cell or SA node in one-dimensional model of intact SA node at distance x from center SA node
x	Distance from center of SA node in one-dimensional model of intact SA node
x_{s}	Activation variable for $i_{\mathrm{K,s}}$
y	Activation vrable of i_{f}
z	Valency of ion
$[\mathrm{Na}^+]_{\mathrm{i}}, [\mathrm{Ca}^{2+}]_{\mathrm{i}}, [K^+]_i$	Intracellular $[\mathrm{Na}^+]$, $[\mathrm{Ca}^{2+}]$, and $[\mathrm{K}^+]$ concentrations
$[\mathrm{Na}^+]_{\mathrm{o}}, [\mathrm{Ca}^{2+}]_{\mathrm{o}}, [\mathrm{K}^+]_{\mathrm{o}}$	Extracellular $[\mathrm{Na}^+]$, $[\mathrm{Ca}^{2+}]$, and $[\mathrm{K}^+]$ concentrations
α_n	Voltage-dependent opening rat constant of n
β_n	Voltage-dependent closing rat constant of n
γ_{NaCa}	Position of Erying rate theory energy barrier controlling voltage dependence of i_{NaCa}
τ_n	Time constant of n
λ	Space constant

Appendix B

1D Uniform Model

In Chapter 5, we presented the action potential variability of the 1D uniform model. The box plots of the cycle length corresponding to Figure 5.9 are given as follows.

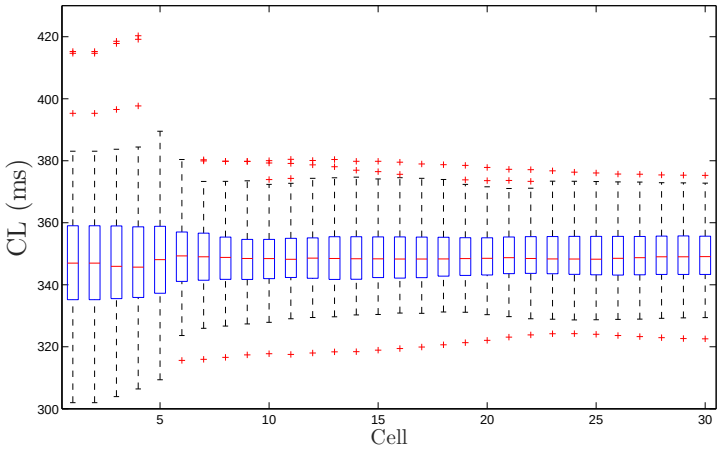

FIGURE B.1: Box plot of the uniform SED model with 5× increased peripheral coupling (n = 117). The corresponding variance coefficients of this figure are given in Figure 5.11. The schematic diagram of the is shown in Figure 5.9.

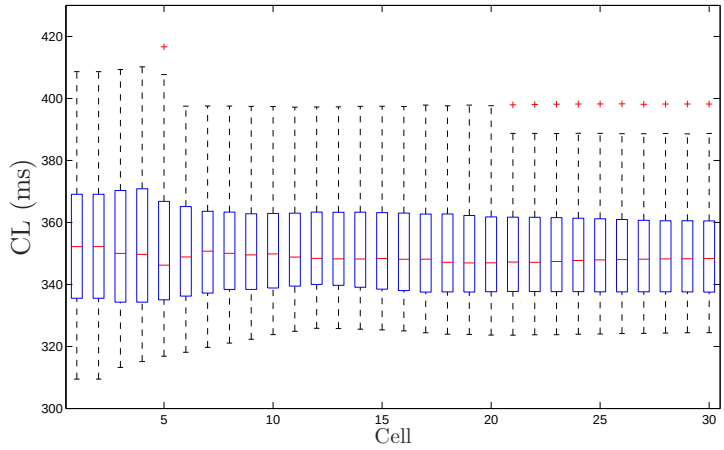

FIGURE B.2: Box plot of the uniform SED model with 10× increased peripheral coupling (n = 109). The corresponding variance coefficients of this figure are given in Figure 5.11. The schematic diagram of the is shown in Figure 5.9.

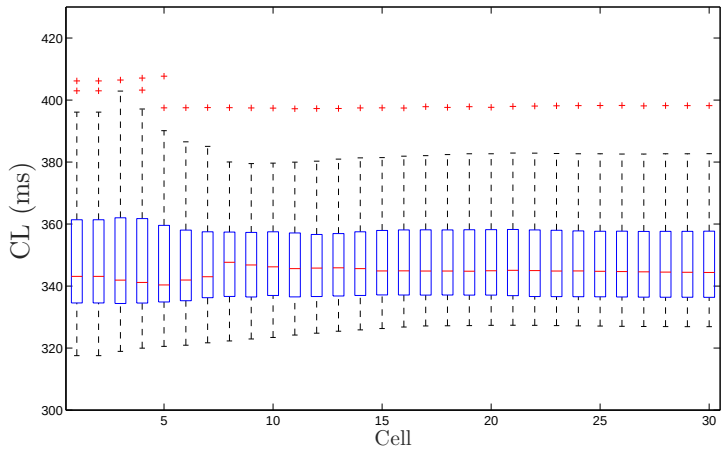

FIGURE B.3: Box plot of the uniform SED model with 15× increased peripheral coupling (n = 106). The corresponding variance coefficients of this figure are given in Figure 5.11. The schematic diagram of the is shown in Figure 5.9.

Appendix C

1D Non-Uniform Model

We showed the effects of SAN heterogeneity on the action potential variability based on two 1D non-uniform models in Chapter 5. The box plots of cycle length corresponding to Figure 5.16 and Figure 5.15 are given as follows.

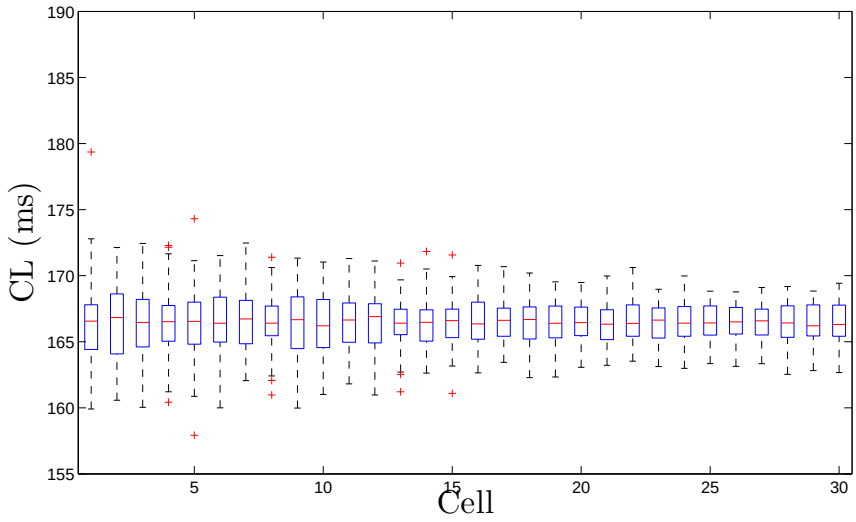

FIGURE C.1: Box plot of the 1D SDE Zhang SAN model with 5× increased peripheral coupling (n = 252). The corresponding variance coefficients of this figure are given in Figure 5.16. The schematic diagram is shown in Figure 5.12.

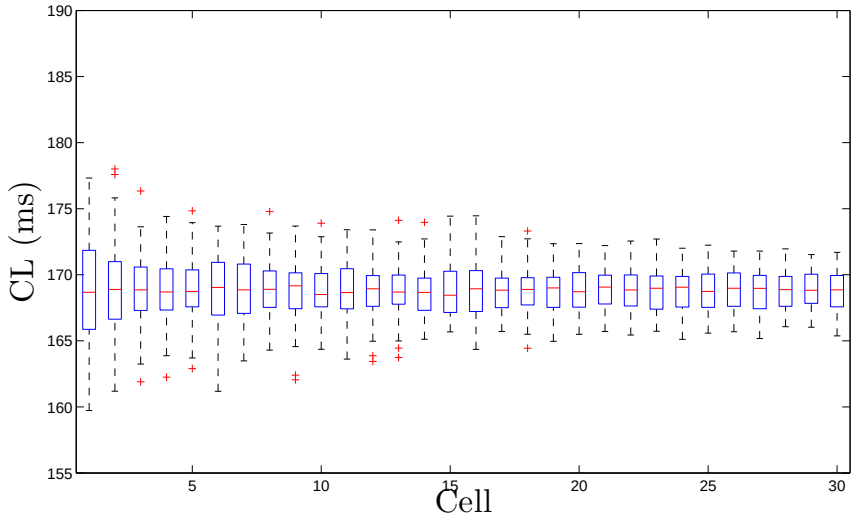

FIGURE C.2: Box plot of the 1D SDE Zhang SAN model with 10× increased peripheral coupling (n = 191). The 1D model consists of 15 central and 15 peripheral SAN cells. The corresponding variance coefficients of this figure are given in Figure 5.16. The schematic diagram is shown in Figure 5.12.

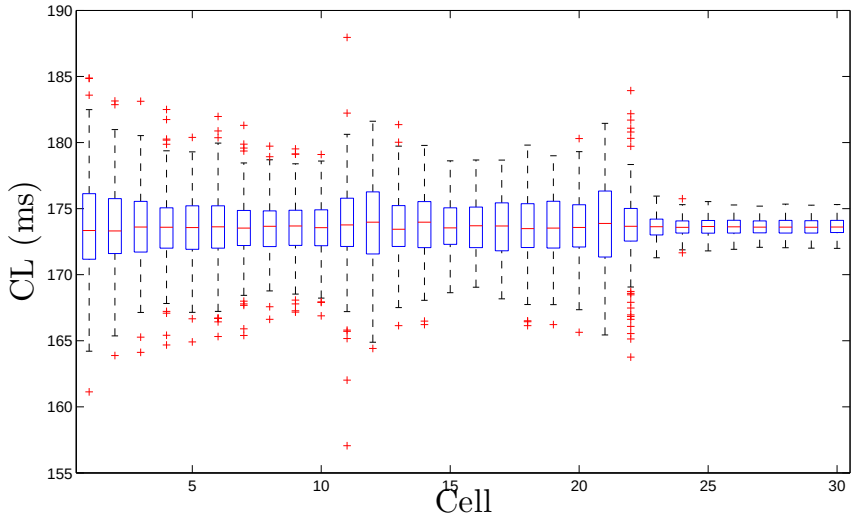

FIGURE C.3: Box plot of the 1D SDE Zhang SAN model with 15× increased peripheral coupling (n = 166). The corresponding variance coefficients of this figure are given in Figure 5.16. The schematic diagram is shown in Figure 5.12.

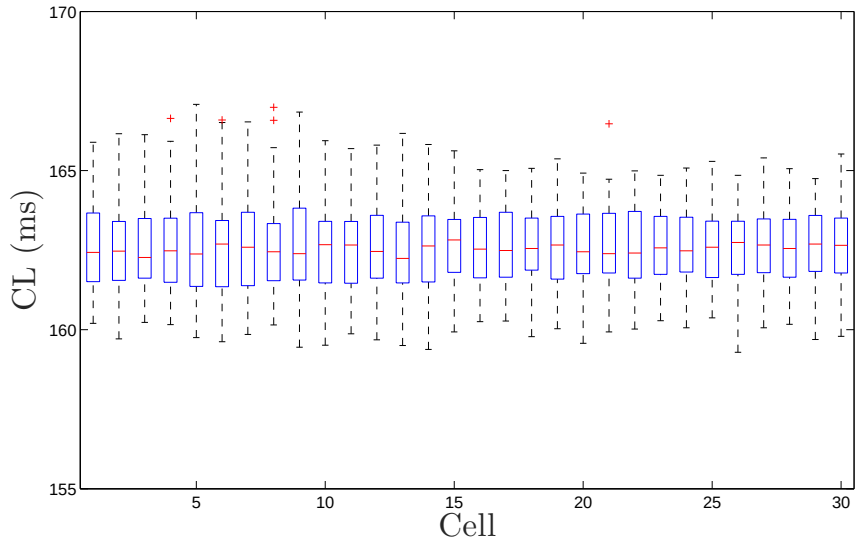

FIGURE C.4: Box plot of the 1D SDE Zhang SAN model with 5× increased peripheral coupling (n = 128). The 1D model consists of 15 central and 15 peripheral SAN cells. The corresponding variance coefficients of the box plot are given in Figure 5.15. The schematic diagram is shown in Figure 5.13.

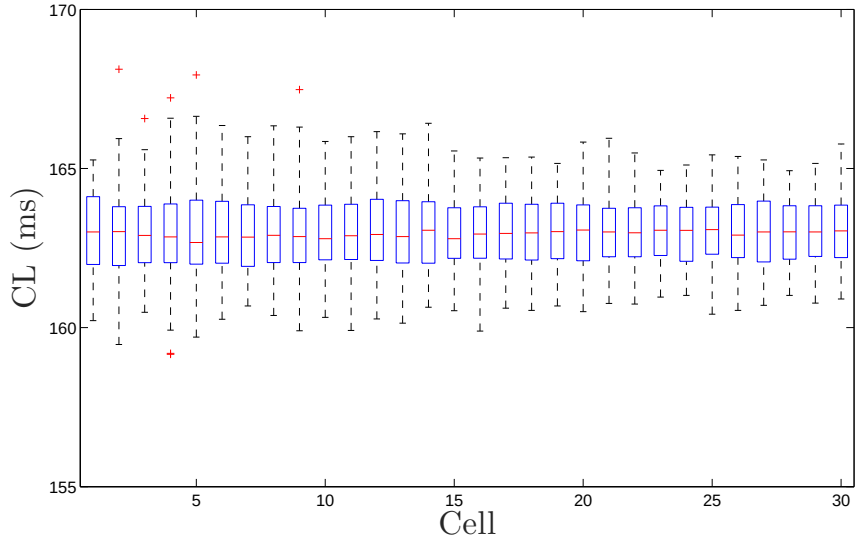

FIGURE C.5: Box plot of the 1D SDE Zhang SAN model with 10× increased peripheral coupling (n = 108). The 1D model consists of 15 central and 15 peripheral SAN cells. The corresponding variance coefficients of this figure are given in Figure 5.15. The schematic diagram is shown in Figure 5.13.

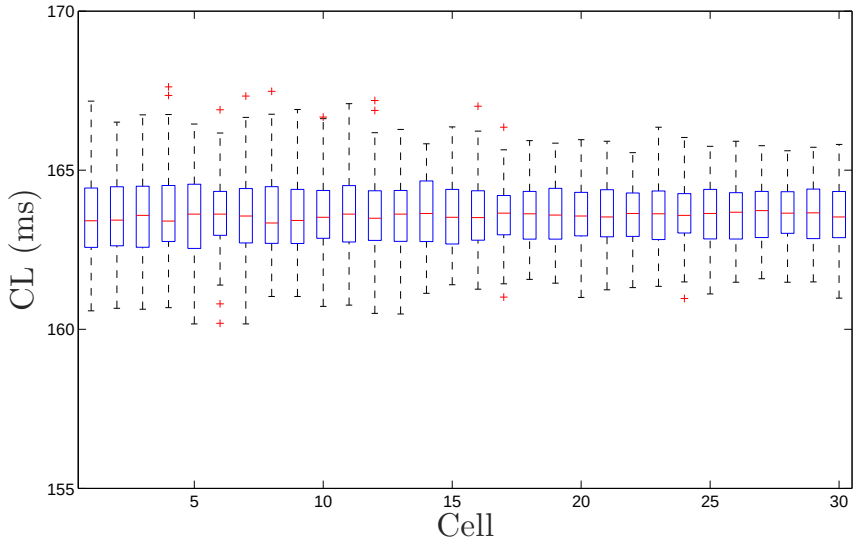

FIGURE C.6: Box plot of the 1D SDE Zhang SAN model with 15× increased peripheral coupling (n = 101). The 1D model consists of 15 central and 15 peripheral SAN cells. The corresponding variance coefficients of this figure are given in Figure 5.15. The schematic diagram is shown in Figure 5.13.

Bibliography

A. P. Arkin and D. V. Schaffer. Network news: innovations in 21st century systems biology. *Cell*, 144(6):844–849, 2011.

R. W. Atherton, R. B. Schainker, and E. R. Ducot. On the statistical sensitivity analysis of models for chemical kinetics. *AIChE Journal*, 21(3):441–448, 1975.

G. W. Beeler and H. Reuter. Reconstruction of the action potential of ventricular myocardial fibres. *The Journal of Physiology*, 268:177–210, 1977.

D. A. Beneski and W. A. Catterall. Covalent labeling of protein components of the sodium channel with a photoactivable derivative of scorpion toxin. *Proceedings of the National Academy of Sciences*, 77(1):639–643, 1980.

D. L. Beres and D. M. Hawkins. Plackett–burman technique for sensitivity analysis of many-parametered models. *Ecological Modelling*, 141(1):171–183, 2001.

W. K. Bleeker, A. J. Mackaay, M. Masson-Pévet, L. N. Bouman, and A. E. Becker. Functional and morphological organization of the rabbit sinus node. *Circulation Research*, 46(1):11–22, 1980.

M. R. Boyett, I. Kodama H. Honjo, M. K. Lancaster, M. Lei, H. Musa, and H. Zhang. The sinoatrial node: Cell size does matter. *Circulation Research*, 101:81–82, 2007a.

M. R. Boyett, H. Honjo, and I. Kodama. The sinoatrial node, a heterogeneous pacemaker structure. *Cardiovascular Research*, 47(4):658–687, 2000.

M. R. Boyett, H. Honjo, I. Kodama, M. K. Lancaster, M. Lei, H. Musa, and H. Zhang. The sinoatrial node: cell size does matter. *Circulation Research*, 101(7):e81–e82, 2007b.

D. G. Bristow and J. W. Clark. A mathematical model of primary pacemaking cell in sa node of the heart. *American Journal of Physiology-Heart and Circulatory Physiology*, 243(2):H207–H218, 1982.

J. D. Bronzino and D. R. Peterson. *Biomedical engineering fundamentals*. CRC Press, 2014.

W. A. Catterall. Voltage-gated sodium channels at 60: structure, function and pathophysiology. *The Journal of Physiology*, 590(11):2577–2589, 2012.

K. Chan, S. Tarantola, A. Saltelli, and I. M Sobol. Variance-based methods. *Sensitivity Analysis*, 45:167–197, 2000.

E. T. Y. Chang, M. Strong, and R. H. Clayton. Bayesian sensitivity analysis of a cardiac cell model using a gaussian process emulator. *PloS One*, 10:e0130252, 2015.

Y Chu, A Jayaraman, and J Hahn. Parameter sensitivity analysis of il-6 signalling pathways. *IET Systems Biology*, 1(6):342–352, 2007.

C. E. Clancy and Y. Rudy. Linking a genetic defect to its cellualr phenotype in a cardiac arrhythmia. *Nature*, 400:566–569, 1999.

G. D. Clifford. *Singal Processing Methods for Heart Rate Variablitiy*. PhD thesis, University of Oxford, 2002.

R. I. Cukier, C. M. Fortuin, K. E. Petschek, and J. H. Schaibly. Study of the sensitivity of coupled reaction system to uncertainties in rate coeffeicients. i. theory. *The Journal of Chemical Physics*, 59:3873–3879, 1973.

D. J.W. De Pauw and P. A. Vanrolleghem. Practical aspects of sensitivity analysis for dynamic models. In *Proceedings of the* 4_{th} *IMACS Symposium on Mathematical Modelling (MATHMOD). Vienna, Austria*, volume 47, 2003.

D Degenring, C Froemel, G Dikta, and R Takors. Sensitivity analysis for the reduction of complex metabolism models. *Journal of Process Control*, 14(7):729–745, 2004.

S.S. Demir, J.W. Clark, C.R. Murphey, and W.R. Giles. A mathematical model of a rabbit sinoatrial node cell. *American Journal of Physiology-Cell Physiology*, 266(3): C832–C852, 1994.

J. C. Denyer and H. F. Brown. Rabbit sino-atrial node cells: isolation and electrophysiological properties. *The Journal of Physiology*, 428:405, 1990.

R. P Dickinson and R. J Gelinas. Sensitivity analysis of ordinary differential equation systemsa direct method. *Journal of Computational Physics*, 21(2):123–143, 1976.

D. DiFrancesco. Characterization of single pacemaker channels in cardiac sino-atrial node cells. *Nature*, 1986.

D. DiFrancesco and D. Noble. A model of cardiac electrical activity incorporating ionic pumps and concentration changes. *Philos Trans R Soc Lond B Biol Sci*, 307:353–98, 1985.

H. Dobrzynski, M. R. Boyett, and R. H. Anderson. New insights into pacemaker activity promoting understanding of sick sinus syndrome. *Circulation*, 115(14):1921–1932, 2007.

S. Dokos, B. Celler, and N. Lovell. Ion currents underlying sinoatrial node pacemaker activity: a new single cell mathematical model. *Journal of Theoretical Biology*, 181 (3):245–272, 1996.

J. M Dresch, X. Liu, D. N. Arnosti, and A. Ay. Thermodynamic modeling of transcription: sensitivity analysis differentiates biological mechanism from mathematical model-induced effects. *BMC Systems Biology*, 4(1):1, 2010.

D. Fedida and W. R. Giles. Regional variations in action potentials and transient outward current in myocytes isolated from rabbit left ventricle. *The Journal of Physiology*, 442:191, 1991.

M. Fink and D. Noble. Markov models for ion channels: versatility versus identifiability and speed. *Philosophical Transactions of the Royal Society of London A: Mathematical, Physical and Engineering Sciences*, 367(1896):2161–2179, 2009.

R. F. Fox. Stochastic versions of the hodgkin-huxley equations. *Biophysical Journal*, 72 (5):2068–2074, 1997.

R. F. Fox and Y. Lu. Emergent collective behavior in large numbers of globally coupled independently stochastic ion channels. *Physical Review E*, 49:3421–3431, 1994.

M. Frenklach. Modeling. In *Combustion Chemistry*, pages 423–453. Springer, 1984.

J. P. Froehlich, E. G. Lakatta, E. Beard, H. A. Spurgeon, M. L. Weisfeldt, and G. Gerstenblith. Studies of sarcoplasmic reticulum function and contraction duration in young adult and aged rat myocardium. *Journal of Molecular and Cellular Cardiology*, 10(5):427–438, 1978.

A. Garny, K. Kohl, P. J. Hunter, M. R. Boyett, and D. Noble. One-dimensional rabbit sinoatrial node models. *Journal of Cardiovascular Electrophysiology*, 14(s10):S121–S132, 2003.

A. Garny, D. Noble, and P. Kohl. Dimensionality in cardiac modelling. *Progress in Biophysics and Molecular Biology*, 87(1):47–66, 2005.

A. L. Goldin. Mechanisms of sodium channel inactivation. *Current Opinion in Neurobiology*, 13(3):284–290, 2003.

J. H. Goldwyn, N. S. Imennov, M. Famulare, and E. S. Brown. Stochastic differential equation models for ion channel noise in Hodgkin-Huxley neurons. *Physical Review E*, 83:041908, 2011a.

J. H. Goldwyn, N. S. Imennov, M. Famulare, and E. Shea-Brown. Stochastic differential equation models for ion channel noise in hodgkin-huxley neurons. *Physical Review E*, 83(4):041908, 2011b.

J. H. Goldwyn and E. Shea-Brown. The what and where of adding channel noise to the hodgkin-huxley equations. *PLoS Computational Biology*, 7:e1002247, 2011.

A. Guia, M. D. Stern, E. G. Lakatta, and I. R. Josephson. Ion concentration-dependence of rat cardiac unitary l-type calcium channel conductance. *Biophysical Journal*, 80 (6):2742–2750, 2001.

J Guo, T. Wang, T. Yang, J. Xu, W. Li, M. D. Fridman, J. T. Fisher, and S. Zhang. Interaction between the cardiac rapidly (i_{Kr}) and slowly (i_{Ks}) activating delayed rectifier potassium channels revealed by low k+-induced herg endocytic degradation. *Journal of Biological Chemistry*, 286(40):34664–34674, 2011.

R. N. Gutenkunst, J. J. Waterfall, F. P. Casey, K. S Brown, C. R. Myers, and J. P. Sethna. Universally sloppy parameter sensitivities in systems biology models. *PLOS Computational Biology*, 3(10):e189, 2007.

N. Hagiwara, H. Irisawa, and M. Kameyama. Contribution of two types of calcium currents to the pacemaker potentials of rabbit sino-atrial node cells. *The Journal of Physiology*, 395:233–253, 1988a.

N. Hagiwara, H. Irisawa, and M. Kameyama. Contribution of two types of calcium currents to the pacemaker potentials of rabbit sino-atrial node cells. *The Journal of Physiology*, 395(1):233–253, 1988b.

J. Heijman, A. Zaza, D. M Johnson, Y. Rudy, R. L. M. Peeters, P. G. A. Volders, and R. L. Westra. Determinants of beat-to-beat variability of repolarization duration in the canine ventricular myocyte: a computational analysis. *PLoS Computational Biology*, 9(8):e1003202, 2013.

J. Hetherington, I. D. Lockhart Bogle, P. Saffrey, O. Margoninski, L. Li, M. V. Rey, S. Yamaji, S. Baigent, J. Ashmore, K. Page, et al. Addressing the challenges of multiscale model management in systems biology. *Computers & Chemical Engineering*, 31(8):962–979, 2007.

D. W. Hilgemann and D. Noble. Excitation-contraction coupling and extracellular calcium transients in rabbit atrium:reconstruction of basic cellular mechanisms. *Proceedings of the Royal Society of London. Series B, Biological Sciences*, 230(1259):163–205, 1987.

A. L. Hodgkin and A. F. Huxley. A quantitative description of membrane current and its application to conduction and excitation in nerve. *The Journal of Physiology*, 117: 500–544, 1952.

A. E. C. Ihekwaba, D. S. Broomhead, R. L. Grimley, N Benson, and D. B. Kell. Sensitivity analysis of parameters controlling oscillatory signalling in the nf-kb pathway: the roles of ikk and ikba. *Syst Biol*, 1:93–103, 2004.

H. Irisawa and A. Noma. Pacemaker mechanisms of rabbit sinoatrial node cells. In *Cardiac Rate and Rhythm*, pages 35–51. Springer, 1982.

S. Kharche, N. Lüdtke, S. Panzeri, and H. Zhang. A global sensitivity index for biophysically detailed cardiac cell models: a computational approach. In *Functional Imaging and Modeling of the Heart*, pages 366–375. Springer, 2009.

K. A. Kim, S. L. Spencer, J. G. Albeck, J. M. Burke, P. K. Sorger, S. Gaudet, et al. Systematic calibration of a cell signaling network model. *BMC Bioinformatics*, 11(1): 1, 2010.

C. J. Kirchhof, F. I. Bonke, M. A. Allessie, and W. J. Lammers. The influence of the atrial myocardium on impulse formation in the rabbit sinus node. *Pflügers Archiv*, 410(1-2):198–203, 1987.

M. Koda, G. J. McRae, and J. H. Seinfeld. Automatic sensitivity analysis of kinetic mechanisms. *International Journal of Chemical Kinetics*, 11:427–444, 1979.

I. Kodama and M. R. Boyett. Regional differences in the electrical activity of the rabbit sinus node. *Pflügers Archiv*, 404(3):214–226, 1985.

I. Kodama, M. R. Nikmaram, M. R. Boyett, R. Suzuki, H. Honjo, and J. M. Owen. Regional differences in the role of the Ca^{2+} and Na^{+} currents in pacemaker activity in the sinoatrial node. *Am J Physiol Heart Circ Physiol*, 272:2793–2806, 1997.

Y. Kurata, I. Hisatome, S. Imanishi, and T. Shibamoto. Dynamical description of sinoatrial node pacemaking: improved mathematical model for primary pacemaker cell. *The American Journal of Physiology - Heart and Circulatory Physiology*, 283: 2074–2101, 2002.

Y. Kurata, H. Matsuda, I. Hisatome, and T. Shibamoto. Regional difference in dynamical property of sinoatrial node pacemaking: Role of na^{+} channel current. *Biophysical Journal*, 95:951–977, 2008.

M. Lemay, E. de Lange, and J. P. Kucera. Effects of stochastic channel gating and distribution on the cardiac action potential. *Journal of Theoretical Biology*, 281(1): 84–96, 2011a.

M. Lemay, E. Lange, and J. P. Kucera. Effects of stochastic channel gating and distribution on the cardiac action potential. *Journal of Theoretical Biology*, 281:84–96, 2011b.

G. Liu, M. T. Swihart, and S. Neelamegham. Sensitivity, principal component and flux analysis applied to signal transduction: the case of epidermal growth factor mediated signaling. *Bioinformatics*, 21(7):1194–1202, 2005.

C. Luo and Y. Rudy. A model of the ventricular cardiac action potential. depolarization, repolarization, and their interaction. *Circulation Research*, 68(6):1501–1526, 1991.

C. H. Luo and Y. Rudy. A dynamic model of the cardiac ventricular action potential. i. simulations of ionic currents and concentration changes. *Circulation Research*, 74: 1071–1096, 1994a.

C. H. Luo and Y. Rudy. A dynamic model of the cardiac ventricular action potential. ii. afterdepolarizations, triggered activity, and potentiation. *Circulation Research*, 74: 1097–1113, 1994b.

A. E. Lyashkov, M. Juhaszova, H. Dobrzynski, T. M. Vinogradova, V. A. Maltsev, O. Juhasz, H. A. Spurgeon, S. J. Sollott, and E. G. Lakatta. Calcium cycling protein density and functional importance to automaticity of isolated sinoatrial nodal cells are independent of cell size. *Circulation Research*, 100(12):1723–1731, 2007.

S. Marino, I. B. Hogue, C. J. Ray, and D. E. Kirschner. A methodology for performing global uncertainty and sensitivity analysis in systems biology. *Journal of Theoretical Biology*, 254(1):178–196, 2008.

M. Masson-Pévet, W. K. Bleeker, and D. Gros. The plasma membrane of leading pacemaker cells in the rabbit sinus node. a qualitative and quantitative ultrastructural analysis. *Circulation Research*, 45(5):621–629, 1979.

V. Maupoil, C. Bronquard, J. L. Freslon, P. Cosnay, and I. Findlay. Ectopic activity in the rat pulmonary vein can arise from simultaneous activation of α_1 and β_1 adrenoceptors. *British Journal of Pharmacology*, 150:899–905, 2007.

R. E. McAllister, D. Noble, and R. W. Tsien. Reconstruction of the electrical activity of cardiac purkinje fibres. *The Journal of Physiology*, 251:1–59, 1975.

M. D. McKay. *Evaluating prediction uncertainty.* US Nuclear Regulatory Commission, 1995.

D. C Michaels, E. P. Matyas, and J. Jalife. Mechanisms of sinoatrial pacemaker synchronization: a new hypothesis. *Circulation Research*, 61(5):704–714, 1987.

L. T. H. Newham, J. P. Norton, I. P. Prosser, B. F. W. Croke, and A. J. Jakeman. Sensitivity analysis for assessing the behaviour of a landscape-based sediment source and transport model. *Environmental Modelling & Software*, 18(8):741–751, 2003.

B. Nilius, P. Hess, J. B. Lansman, and R. W. Tsien. A novel type of cardiac calcium channel in ventricular cells. 1985.

D. Noble. A modification of the hodgkinhuxley equations applicable to purkinje fibre action and pacemaker potentials. *The Journal of Phyiology*, 160:317–352, 1962.

D. Noble. Modeling the heart-from genes to cells to the whole organ. *Science*, 295: 1678–1682, 2002.

D. Noble, D. DiFrancesco, and J. C. Denyer. Ionic mechanisms in normal and abnormal cardiac pacemaker activity. *Neuronal and Cellular Oscillators*, pages 59–85, 1989.

D. Noble and R. W. Tsien. Outward membrane currents activated in the plateau range of potentials in cardiac purkinje fibres. *The Journal of Physiology*, 192:479–492, 1967.

K. Ono, H. A Fozzard, and D. A. Hanck. Mechanism of camp-dependent modulation of cardiac sodium channel current kinetics. *Circulation Research*, 72(4):807–815, 1993.

R. V. Oren and C. E. Clancy. Determinants of heterogeneity, excitation and conduction in the sinoatrial node: a model study. *PLoS Computational Biology*, 6(12):e1001041, 2010.

B. Phibbs. Paroxysmal atrial tachycardia with block around the ectopic pacemaker. *Circulation*, 28(5):949–950, 1963.

C. Port. *Pathophysiology: Concepts of Altered Health States (7th ed.).* Lippincott Williams & Wilkins, 2005.

H. Reuter. The dependence of slow inward current in purkinje fibers on the extracellular calcium-concentration. *The Journal of Physiology*, 192:479–492, 1967.

G. J. Rozanski. Atrial ectopic pacemaker escape mediated by phasic vagal nerve activity. *American Journal of Physiology-Heart and Circulatory Physiology*, 260(5): H1507–H1514, 1991a.

G. J. Rozanski. Atrial ectopic pacemaker escape mediated by phasic vagal nerve activity. *The American Journal of Physiology*, 260:1507–1514, 1991b.

A. Saltelli, T. H. Andres, and T. Homma. Sensitivity analysis of model output: an investigation of new techniques. *Computational Statistics & Data Analysis*, 15(2): 211–238, 1993.

A. Saltelli, K. Chan, and E. M. Scott. *Sensitivity Analysis*. Wiley, 2000.

A. Saltelli, M. Ratto, T. Andres, F. Campolongo, J. Cariboni, D. Gatelli, M. Saisana, and S. Tarantola. *Global Sensitivity Analysis*. The Primer, John Wiley & Sons, 2008.

A. Saltelli, S. Tarantola, and KP-S. Chan. A quantitative model-independent method for global sensitivity analysis of model output. *Technometrics*, 41:39–56, 1999.

N. Sarai, S. Matsuoka, S. Kuratomi, K. Ono, and A. Noma. Role of individual ionic current systems in the sa node hypothesized by a model study. *The Japanese Journal of Physiology*, 53(2):125–134, 2003.

H. Satoh. Role of t-type ca^{2+} channel inhibitors in the pacemaker depolarization in rabbit sino-atrial nodal cells. *General Pharmacology: The Vascular System*, 26(3): 581–587, 1995.

V. J. Schouten. Interval dependence of force and twitch duration in rat heart explained by ca2+ pump inactivation in sarcoplasmic reticulum. *The Journal of Physiology*, 431:427, 1990.

A. A Sher, K. Wang, A. Wathen, P. J. Maybank, G. R. Mirams, D. Abramson, D. Noble, and D. J. Gavaghan. A local sensitivity analysis method for developing biological models with identifiable parameters: Application to cardiac ionic channel modelling. *Future Generation Computer Systems*, 29(2):591–598, 2013.

L. Sherwood. *Human Physiology: From Cells to Systems*. CENGAGE Learning, 2008.

J. W. Shuai and P. Jung. Optimal intracellular calcium signaling. *Physical Review Letters*, 88(6):068102, 2002.

E. A. Sobie. Parameter sensitivity analysis in electrophysiological models using multivariable regression. *Biophysical Journal*, 96(4):1264–1274, 2009.

I. Sobol. Sensitivity estimates for nonlinear mathematical models. *Matematicheskoe Modelirovanie*, 2:112118, 1990.

I. Sobol. Sensitivity estimates for nonlinear mathematical models. *Math Modeling Comput Exp*, 1:407414, 1993.

T. Sumner. *Sensitivity analysis in systems biology modelling and its application to a multi-scale model of blood glucose homeostasis*. PhD thesis, UCL (University College London), 2010.

P. Valko and S. Vajda. An extended ode solver for sensitivity calculations. *Computers & Chemistry*, 8(4):255–271, 1984.

A. C. Van Ginneken and W. Giles. Voltage clamp measurements of the hyperpolarization-activated inward current i (f) in single cells from rabbit sino-atrial node. *The Journal of Physiology*, 434:57, 1991.

N. A. W. Van Riel. Dynamic modelling and analysis of biochemical networks: mechanism-based models and model-based experiments. *Briefings in Bioinformatics*, 7(4):364–374, 2006.

M. W. Veldkamp, A. C. Van Ginneken, and L. N. Bouman. Single delayed rectifier channels in the membrane of rabbit ventricular myocytes. *Circulation Research*, 72 (4):865–878, 1993.

E. E. Verheijck, A. Wessels, A. C. G. van Ginneken, J. Bourier, M. W. M. Markman, J. L. M. Vermeulen, J. M. T. de Bakker, W. H. Lamers, T. Opthof, and L. N. Bouman. Distribution of atrial and nodal cells within the rabbit sinoatrial node models of sinoatrial transition. *Circulation*, 97(16):1623–1631, 1998.

J. Walmsley, G. Mirams, M. Bahoshy, C. Bollensdorff, B. Rodriguez, and K. Burrage. Phenomenological modeling of cell-to-cell and beat-to-beat variability in isolated guinea pig ventricular myocytes. In *2010 Annual International Conference of the IEEE Engineering in Medicine and Biology*, pages 1457–1460. IEEE, 2010.

J. Walmsley, G. Mirams, J. M. Pitt-Francis, Rodriguez B., and K. Burrage. Application of stochastic phenomenological modelling to cell-to-cell and beat-to-beat electrophysiological variability in cardiac tissue. *Journal of Theoretical Biology*, 365:325–336, 2015.

H. Weyl. Mean motion. *American Journal of Mathematics*, 60(4):889–896, 1938.

R. Wilders. Computer modelling of the sinoatrial node. *Medical & Biological Engineering & Computing*, 45:189–207, 2007.

R. Wilders and Habo J. Jongsma. Beating irregularity of single pacemaker cells isolated from the rabbit sinoatrial node. *Med Bio Eng Comput*, 65:2601–2613, 1993.

R Wilders, HJ Jongsma, and AC Van Ginneken. Pacemaker activity of the rabbit sinoatrial node. a comparison of mathematical models. *Biophysical journal*, 60(5): 1202, 1991.

B. J. Winer, D. R. Brown, and K. M. Michels. *Statistical principles in experimental design*, volume 2. McGraw-Hill New York, 1971.

Y. Yang and F. J. Sigworth. Single-channel properties of iks potassium channels. *The Journal of General Physiology*, 112(6):665–678, 1998.

Y. Yaniv, I. Ahmet, J. Liu, A. E. Lyashkov, T. R. Guiriba, Y. Okamoto, B. D. Ziman, and E. G. Lakatta. Synchronization of sinoatrial node pacemaker cell clocks and its autonomic modulation impart complexity to heart beating intervals. *Heart Rhythm*, 11(7):1210–1219, 2014.

J. Yanni, J. O. Tellez, P. V. Sutyagin, M. R. Boyett, and H. Dobrzynski. Structural remodelling of the sinoatrial node in obese old rats. *Journal of Molecular and Cellular Cardiology*, 48(4):653–662, 2010.

H. Yue, M. Brown, J. Knowles, H. Wang, D. S. Broomhead, and D. B. Kell. Insights into the behaviour of systems biology models from dynamic sensitivity and identifiability analysis: a case study of an nf-κb signalling pathway. *Molecular BioSystems*, 2(12): 640–649, 2006.

H. Zhang, A. V. Holden, and M. R. Boyett. Gradient model versus mosaic model of the sinoatrial node. *Circulation*, 103(4):584–588, 2001.

H. Zhang, A. V. Holden, I. Kodama, H. Honjo, M. Lei, T. Varghese, and M. R. Boyett. Mathematical models of action potentials in the periphery and center of the rabbit sinoatrial node. *Am J Physiol Heart Circ Physiol*, pages 397–421, 2000.

Y. Zheng and A. Rundell. Comparative study of parameter sensitivity analyses of the tcr-activated erk-mapk signalling pathway. *IEE Proceedings-Systems Biology*, 153(4): 201–211, 2006.

Z. Zi. Sensitivity analysis approaches applied to systems biology models. *Systems Biology, IET*, 5(6):336–346, 2011.